U.S. Department
of Transportation
Federal Railroad
Administration

Office of Research,
Development and Technology
Washington, DC 20590

Detailed Puncture Analyses of Tank Cars - Analysis of Different Impactor Threats and Impact Conditions

Revision 1

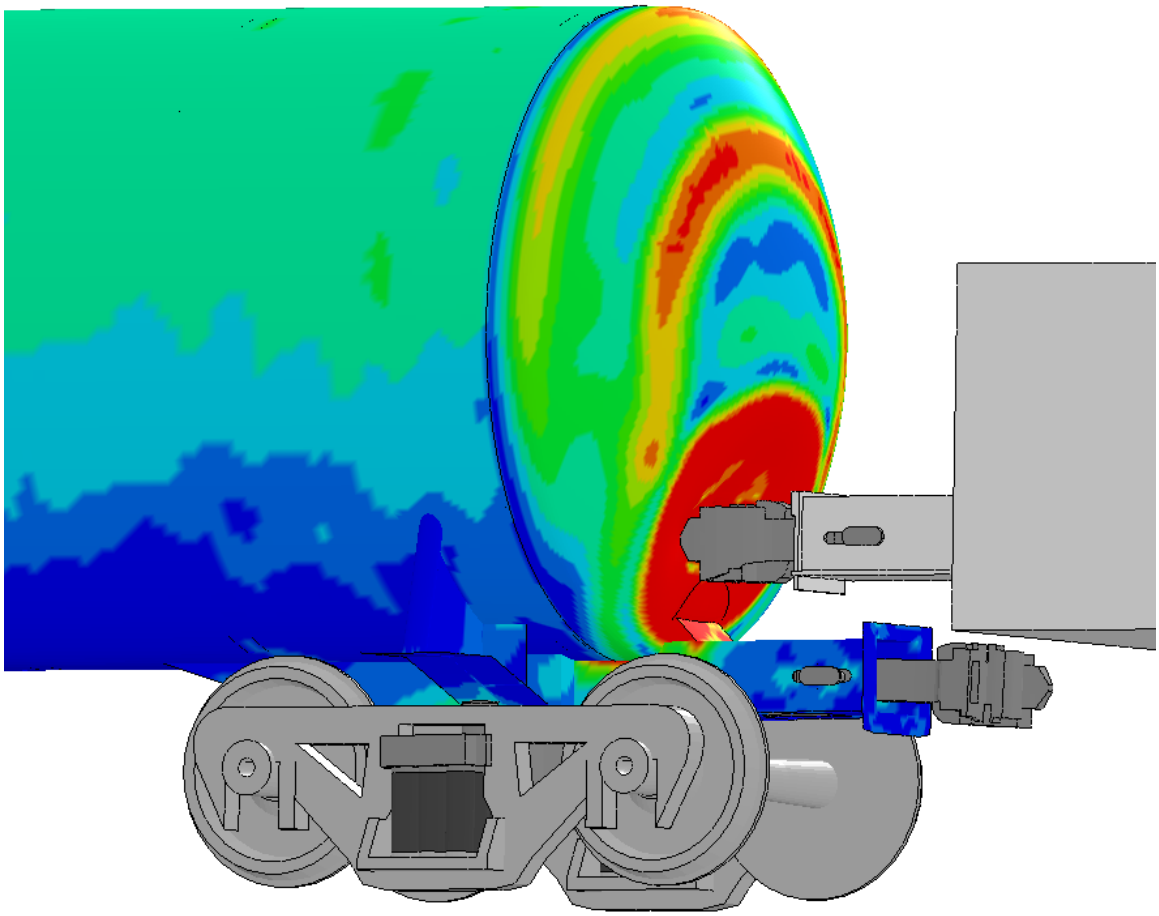

DOT/FRA/ORD-13/17

Final Report | September 2023

REPORT DOCUMENTATION PAGE

Form Approved
OMB No. 0704-0188

1. REPORT DATE *(DD-MM-YYYY)*	2. REPORT TYPE	3. DATES COVERED *(From - To)*
	Final Report	6/20/2022-10/20/2023

4. TITLE AND SUBTITLE

Detailed Puncture Analyses of Tank Cars - Analysis of Different Impactor Threats and Impact Conditions – Revision 1

5a. CONTRACT NUMBER
693JJ622C000002

5b. GRANT NUMBER

5c. PROGRAM ELEMENT NUMBER

6. AUTHOR(S)

Steven W Kirkpatrick: ORCID 0000-0001-9590-7980

5d. PROJECT NUMBER

5e. TASK NUMBER

5f. WORK UNIT NUMBER

7. PERFORMING ORGANIZATION NAME(S) AND ADDRESS(ES)
Applied Research Associates
95 First Street, Suite 100
Los Altos, CA 94022

8. PERFORMING ORGANIZATION REPORT NUMBER

9. SPONSORING/MONITORING AGENCY NAME(S) AND ADDRESS(ES)
U.S. Department of Transportation
Federal Railroad Administration
Office of Railroad Policy and Development
Office of Research, Development, and Technology
Washington, DC 20590

10. SPONSOR/MONITOR'S ACRONYM(S)

11. SPONSOR/MONITOR'S REPORT NUMBER(S)
DOT/FRA/ORD-13/17

12. DISTRIBUTION/AVAILABILITY STATEMENT
This document is available to the public through the FRA website.

13. SUPPLEMENTARY NOTES
COR: Francisco González, III

14. ABSTRACT

This report describes a research program to improve the safety and security of railroad tank cars. The approach used in the research and development program was to apply a tank impact and puncture prediction capability using detailed finite element analyses (FEA). The FEA capability was developed and validated previously in the NGRTC program. The analysis methodologies apply advanced damage and failure models that were validated by series of material tests under various loading conditions. In this study, the analyses were applied to investigate the tank puncture behaviors for a wide range of impact conditions.

15. SUBJECT TERMS
Tank Car, Impact, Puncture, Crash, Derailment, Hazmat Safety

16. SECURITY CLASSIFICATION OF:			17. LIMITATION OF ABSTRACT	18. NUMBER OF PAGES	19a. NAME OF RESPONSIBLE PERSON
a. REPORT	b. ABSTRACT	c. THIS PAGE		273	19b. TELEPHONE NUMBER *(Include area code)*

Standard Form 298 (Rev. 8/98)
Prescribed by ANSI Std. Z39.18

METRIC/ENGLISH CONVERSION FACTORS

ENGLISH TO METRIC	METRIC TO ENGLISH
LENGTH (APPROXIMATE)	**LENGTH (APPROXIMATE)**
1 inch (in) = 2.5 centimeters (cm)	1 millimeter (mm) = 0.04 inch (in)
1 foot (ft) = 30 centimeters (cm)	1 centimeter (cm) = 0.4 inch (in)
1 yard (yd) = 0.9 meter (m)	1 meter (m) = 3.3 feet (ft)
1 mile (mi) = 1.6 kilometers (km)	1 meter (m) = 1.1 yards (yd)
	1 kilometer (km) = 0.6 mile (mi)
AREA (APPROXIMATE)	**AREA (APPROXIMATE)**
1 square inch (sq in, in^2) = 6.5 square centimeters (cm^2)	1 square centimeter (cm^2) = 0.16 square inch (sq in, in^2)
1 square foot (sq ft, ft^2) = 0.09 square meter (m^2)	1 square meter (m^2) = 1.2 square yards (sq yd, yd^2)
1 square yard (sq yd, yd^2) = 0.8 square meter (m^2)	1 square kilometer (km^2) = 0.4 square mile (sq mi, mi^2)
1 square mile (sq mi, mi^2) = 2.6 square kilometers (km^2)	10,000 square meters (m^2) = 1 hectare (ha) = 2.5 acres
1 acre = 0.4 hectare (he) = 4,000 square meters (m^2)	
MASS - WEIGHT (APPROXIMATE)	**MASS - WEIGHT (APPROXIMATE)**
1 ounce (oz) = 28 grams (gm)	1 gram (gm) = 0.036 ounce (oz)
1 pound (lb) = 0.45 kilogram (kg)	1 kilogram (kg) = 2.2 pounds (lb)
1 short ton = 2,000 pounds (lb) = 0.9 tonne (t)	1 tonne (t) = 1,000 kilograms (kg)
	= 1.1 short tons
VOLUME (APPROXIMATE)	**VOLUME (APPROXIMATE)**
1 teaspoon (tsp) = 5 milliliters (ml)	1 milliliter (ml) = 0.03 fluid ounce (fl oz)
1 tablespoon (tbsp) = 15 milliliters (ml)	1 liter (l) = 2.1 pints (pt)
1 fluid ounce (fl oz) = 30 milliliters (ml)	1 liter (l) = 1.06 quarts (qt)
1 cup (c) = 0.24 liter (l)	1 liter (l) = 0.26 gallon (gal)
1 pint (pt) = 0.47 liter (l)	
1 quart (qt) = 0.96 liter (l)	
1 gallon (gal) = 3.8 liters (l)	
1 cubic foot (cu ft, ft^3) = 0.03 cubic meter (m^3)	1 cubic meter (m^3) = 36 cubic feet (cu ft, ft^3)
1 cubic yard (cu yd, yd^3) = 0.76 cubic meter (m^3)	1 cubic meter (m^3) = 1.3 cubic yards (cu yd, yd^3)
TEMPERATURE (EXACT)	**TEMPERATURE (EXACT)**
[(x-32)(5/9)] °F = y °C	[(9/5) y + 32] °C = x °F

QUICK INCH - CENTIMETER LENGTH CONVERSION

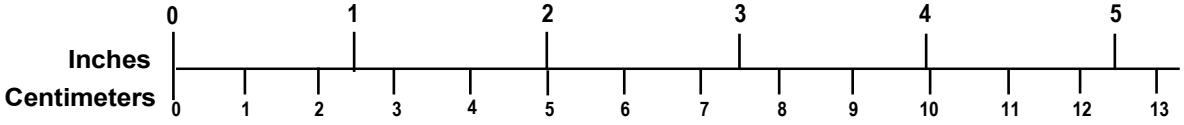

QUICK FAHRENHEIT - CELSIUS TEMPERATURE CONVERSIO

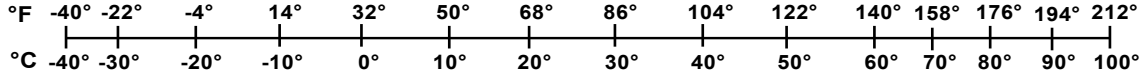

For more exact and or other conversion factors, see NIST Miscellaneous Publication 286, Units of Weights and Measures. Price $2.50 SD Catalog No. C13 10286

Updated 6/17/98

Contents

Illustrations

Tables

Revision Control Table

Revision	Date	Section	Comments
0	March 2015	All	Report No. DOT/FRA/ORD-13/17 - Original Technical Report
1	Sept. 2023	Misc.	Primary change to include assessment of the DOT-113 LNG tank car. Additional edits to update report from 2015 to 2023.
1	Sept. 2023	Acknowledgements	Additional acknowledgements were added for the new research.
1	Sept. 2023	Introduction	The need for assessing DOT-113 LNG tank car was added. Additional relevant research performed since the original report was added to the background section.
1	Sept. 2023	2.2	Sections 2.2 and 2.2.1 were combined into Section 2.2.
1	Sept. 2023	5.7	A new section of the report was generated covering the puncture resistance assessment of the DOT-113 LNG tank car.
1	Sept. 2023	5.2.2, 5.3.5, 5.4.4	Additional information provided on head impact analyses for various tank head designs.
1	Sept. 2023	Conclusions	Discussion on conclusions from new content added.
	Sept. 2023	References	Multiple new references updated or added to the report.

Acknowledgements

This report primarily describes analyses performed under the Federal Railroad Administration (FRA) Contract DTFR53-11-C-00017. The analysis methodologies used in this report build on the work previously performed under Next Generation Rail Tank Car (NGRTC) Project funded by The Dow Chemical Company. The development of the puncture modeling methodologies and the testing used to validate the models and develop the constitutive and failure models were performed under the NGRTC project.

The analyses of Ethylene oxide tank cars in this report were performed under Contract No. 5058 with the American Chemistry Council on behalf of its Ethylene Oxide Panel. The analyses use identical methodologies to those for the other tank car designs included in this study.

Finally, the assessment of the cryogenic DOT-113C120W9 tank car for LNG service was added to Revision 1 of the report in 2023. The evaluation of the DOT-113 tank car was performed under Contract No. 693JJ622C000002 with the FRA. The support and collaboration of Francisco Gonzalez, III and Jeffrey Gordon of the FRA and Michael Carolan of the Volpe National Transportation Systems Center on this phase of the research was greatly appreciated.

Executive Summary

This report describes a research program to improve the safety and security of railroad tank cars. The approach used in the research and development program was to apply a tank impact and puncture prediction capability using detailed finite element analyses (FEA). The FEA capability was developed and validated previously in the NGRTC program. The analysis methodologies apply advanced damage and failure models that were developed using a series of material tests under various loading conditions and validated by full-scale tank car impact and puncture tests. In this study, the analyses were applied to investigate the tank puncture behaviors for a wide range of impact conditions.

Different Size and Shape Impactors

In the initial phase of this program, different size and shape impactors were investigated. The impactors used included square, rectangular, and round impact face geometries. A new parameter was developed to characterize the effective size of the impactor. This impactor characteristic size is the square root of the area of the impactor face. The summary of the puncture forces for the various impactors is plotted against the impactor characteristic size in Figure 1. The figure shows that the impactor characteristic size parameter provides a good correlation for all the different impactor sizes and shapes analyzed. Overall, there is a strong linear correlation of the puncture force with the characteristic size of the impactor.

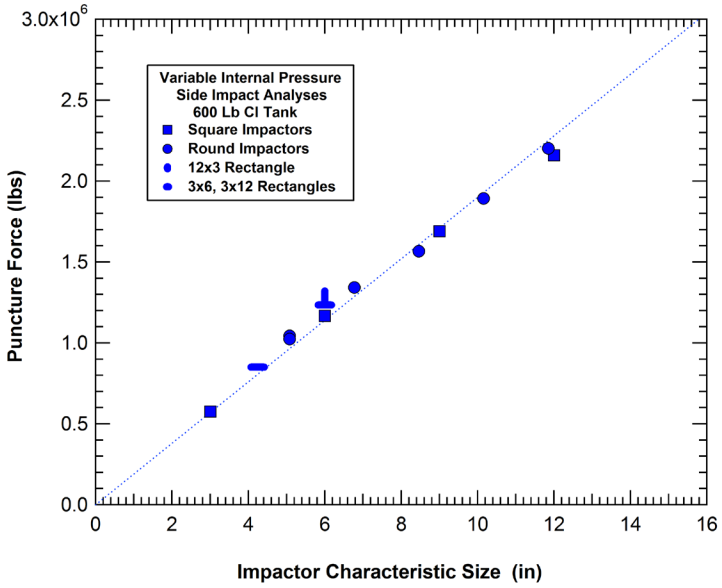

Figure 1. Correlation of side impact puncture forces with ram characteristic size.

A similar summary of the puncture energies for the various impactors is shown in Figure 2. The figure shows that the impactor characteristic size parameter also correlates well to the impact energy for the range of impactors considered. There is more scatter in the correlation of the impact energies but that is expected since various factors such as the impact speed and boundary conditions (BCs) have been shown to introduce variations in the impact energy for different impact scenarios. The comparison of impact energies in Figure 2 show that the correlation is

roughly with the square of the characteristic size of the impactor. This is a result of the linear increase in the puncture force combined with a similar increase in the displacements required to reach the impact force (the puncture energy is obtained by integrating the force-deflection curve of the impact up to the point of the tank puncture).

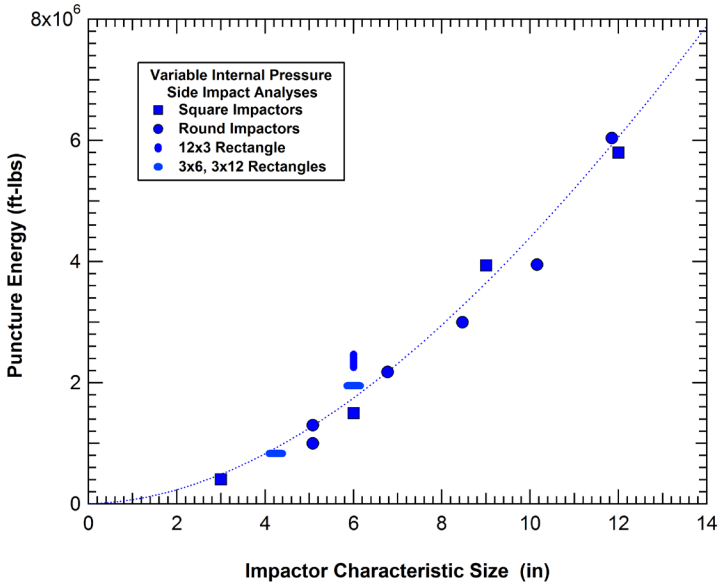

Figure 2. Correlation of side impact puncture energies with ram characteristic size.

The linear correlation between the puncture force and the impactor characteristic size is useful for defining the effective size of complex impactors. For example, the rail section impactor has a cross-sectional profile that includes both convex and concave regions. The puncture force for the rail has corresponds to a characteristic size of approximately 5 inches in a normal side impact. This falls within the expected range of values estimated from the rail profile. Alternatively, a more complex impactor, such as a coupler head can be assessed. Here the behavior is complicated by an impactor face profile that is not flat. As a result, the puncture force was found to vary significantly with relatively small changes in the orientation of the impact. For a limited set of impact orientations analyzed, the coupler head was found to have a characteristic size as small as 5 inches and as large as 12 inches.

Impact Orientation Effects

To investigate the effects of the impactor orientation, as series of analyses was performed with a 12x12 inch square impactor with a 0.1-inch edge radius. A summary of the analyses is provided in Figure 3 where the calculated puncture forces are plotted against the impactor rotation angles. The effects for the pitch rotation are similar to those for the yaw rotation, but with a slight variation in the puncture forces resulting from the relative stiffness of the tank for bending in the longitudinal and radial directions in the impact zone. The analyses where the yaw rotation was maintained at 45 degrees and various levels of pitch rotation were added further concentrates the load and damage at the corner of the impactor.

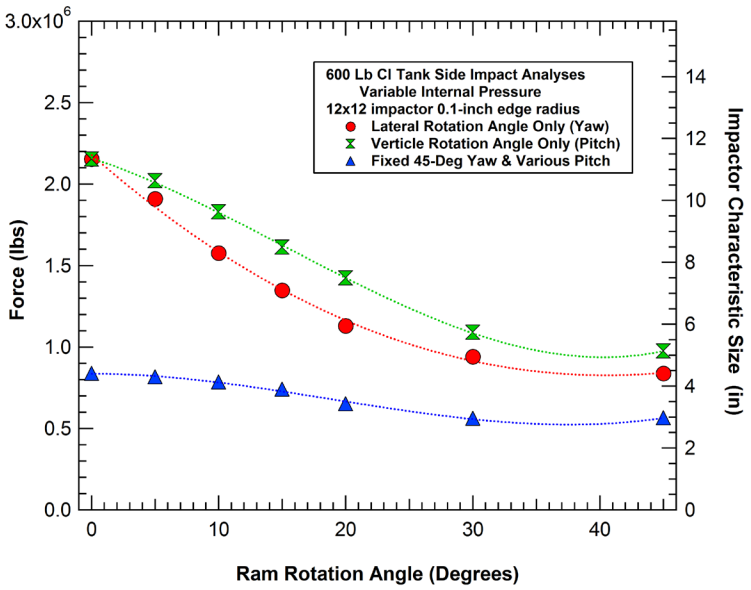

Figure 3. Puncture forces for the 12x12 inch impactor at various orientations.

For comparison, the puncture forces calculated for the rotated 12x12 inch impactor were used to calculate the impactor characteristic size, shown on the right axis of Figure 3. The plot shows that the characteristic size of the impactor decreases rapidly as the rotation increases from 0 to approximately 30 degrees. Between 30 and 45 degrees the contact is primarily with the edge or corner of the impactor and the puncture force (or characteristic size) is relatively constant. The characteristic size of the 12x12 impactor drops from 12 inches in the normal impact to approximately 4.5 to 5 inches in an edge impact. The characteristic size is further reduced to approximately 3 inches for the corner impact. These results show that impacting objects with corners and edges can have the penetration potential of a much smaller object if the orientation of the impactor concentrates the loading to the edge or corner.

An impact condition with similarities to the rotated impactor is where the impact occurs at an oblique angle to the tank. A set of analyses was performed with the full range of impactor sizes and shapes at 15, 30, and 45-degree oblique impact angles. Comparisons of the normal and oblique impact puncture forces and energies are provided in Figure 4 and Figure 5, respectively. The puncture forces are reduced with increasing obliquity angles and at the 45-degree impacts the puncture forces are more than 50 percent lower for the largest impactors. However, as the impactor size is reduced the differences in puncture force are also reduced. At a 6-inch characteristic size the oblique impact puncture force is only reduced by 40 percent compared the normal impact. Finally, for the 3x3 inch impactor there is significantly less difference between the normal and oblique impact puncture forces.

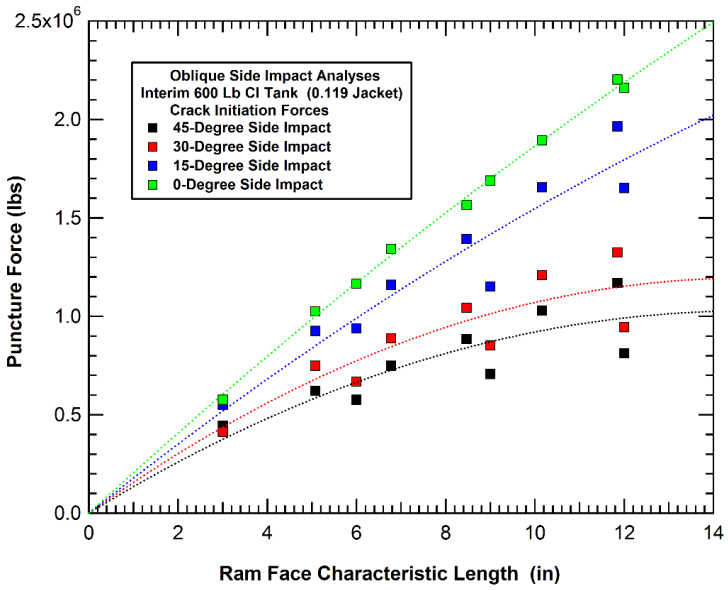

Figure 4. Comparison of puncture forces for normal and oblique impacts.

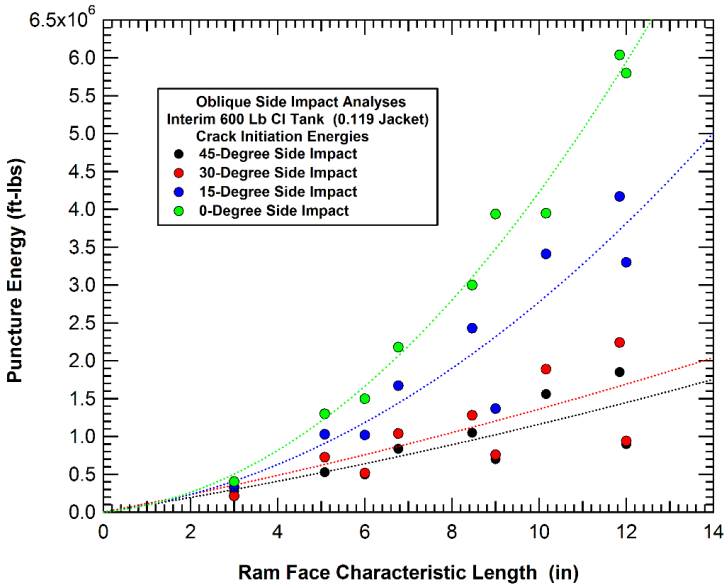

Figure 5. Comparison of puncture energies for normal and oblique impacts.

The puncture energies for the oblique impact show similar trends to the puncture forces. The puncture energies for the largest impactors are reduced by roughly 60 percent. Again, as the impactor size is reduced, the differences in puncture energies are also reduced. At a 6-inch characteristic size, the oblique impact puncture energy is only reduced by 50 percent compared the normal impact. Finally, for the 3x3 inch impactor, there is very little difference between the normal and oblique impact puncture energies.

Head Impacts

A summary of the calculated head impact puncture forces and puncture energies for various size and shape impactors are compared to the side impact forces and energies in Figure 6 and Figure 7, respectively. The slope of the puncture force fit is approximately 10 percent greater than that of the side impact puncture forces. The difference is a combination of two competing factors. First the combined head and head shield thickness is almost 50 percent thicker than the combined thickness of the tank shell and jacket. However, this increase in thickness is partially negated by the fact that the offset head impact scenario produces larger stress and strain concentrations at the top edge of the impactor that reduces the puncture force.

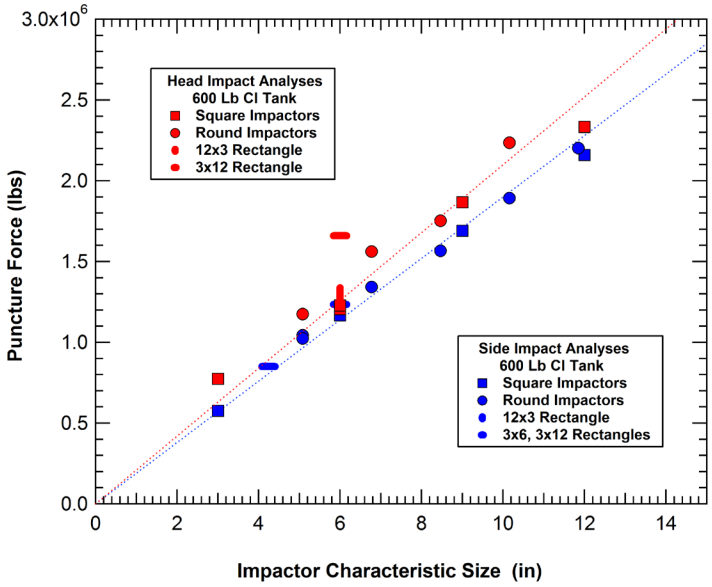

Figure 6. Comparison of the calculated head and side impact puncture forces.

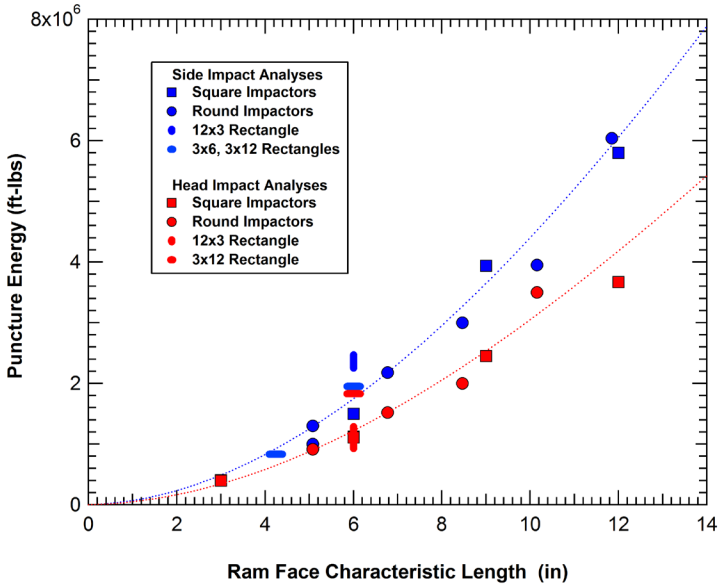

Figure 7. Comparison of the calculated head and side impact puncture energies.

The comparison of the side and head puncture energies in Figure 7 show that again the head impacts have a similar fit to the square of the ram characteristic size, but the puncture energies are 30 percent to 35 percent lower for the head than for the shell. The difference primarily results from the head deformation mode and rigidly constrained impact scenario that are much stiffer than for the shell side impacts. As a result, the puncture forces are reached at significantly lower ram displacements resulting in the reduction of puncture energies.

Side Impact Boundary Condition Effects

A series of analyses were performed to investigate the effects of the constraint level on the tank side impact response. The analyses were for the side impact of the 600 lb chlorine tank car. The impactor selected for these analyses was the 9.55-inch-diameter round impactor. Three different levels of constraint were considered: (1) highly constrained (2) moderately constrained and (3) unconstrained. The highly constrained boundary condition is the tank backed by the rigid impact wall that has been used for the majority of the side impact analyses in this report, as well as the previous NGRTC analyses (Kirkpatrick, 2009a). The unconstrained boundary condition is a single tank that is free to translate. The moderately constrained boundary condition is two deformable tanks sitting side-by-side.

The impactor was prescribed to have a 15-mph constant velocity during the entire impact duration. This is more representative of the loading for an impactor that is attached to a longer section of train in a derailment where the very large mass results in small changes in impactor velocity over the duration of any individual impact event. A comparison of the force-deflection characteristics for the side impact response with the three different constraint conditions (wall, tank, free) is shown in Figure 8. For reference, a corresponding force-deflection curve for a 25-mph impact with the 295,000 lb impactor is also shown on the graph.

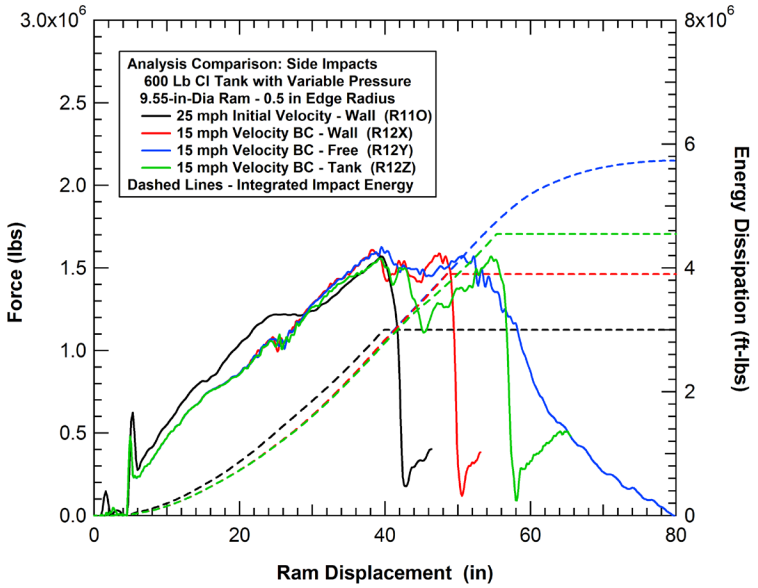

Figure 8. The effects of constraint conditions for the 15 mph constant velocity impacts.

The comparison shows that the initial portion of the force-deflection curves for all three 15 mph impacts are identical (up to approximately 30 inches ram displacement). All three impacts reach

an initial peak force that was very close to the failure level before the dynamic response of the tank results in a temporary drop in the impact force (at approximately 40 inches displacement). Beyond this time, the tank constraint BCs begin to play a large role in the behavior. With the highly constrained (wall) impact scenario the impact force quickly recovers, and the tank is punctured at approximately 48 inches of ram displacement. With the moderately constrained side-by-side tank scenario the impact force more slowly recovers, and the tank is punctured at approximately 56 inches of ram displacement. Finally, with the unrestrained (free) tank the impact force never fully recovers to the puncture force level and the tank does not puncture.

The comparison of the different tank boundary constraints shows that the effects on the late time behavior and puncture energy can be significant. However, the initial portion of the loading is dominated by the inertial resistance of the tank and the puncture will occur in this initial phase of the impact for many combinations of impactor sizes and impact speeds. Thus, for many side impacts, the constraint on the back side of the tank is not significant.

Head Impact Boundary Condition Effects

A series of analyses were performed to investigate the effects of the constraint level on the tank head impact response. The analyses were for the side impact of the 600 lb chlorine tank head with a 0.5-inch-thick head shield. The impactor selected for these analyses was the 9.55-inch-diameter round impactor.

The baseline head impact conditions, adapted from the NGRTC program (Kirkpatrick, 2009a), were for a highly constrained tank head mounted on a test frame that does not allow for any motion at the specimen support. The head impact specimen included the tank head and head shield, supported by a short length of the tank shell and jacket, which were welded to a rigid test frame. To investigate the constraint effects in head impacts an unconstrained tank model was developed. The model includes the entire tank which is free to translate. Gravity was included in the analyses to develop appropriate vertical forces and motions in the offset impact scenario. Without the test frame support, a model of the ground was needed to resist the gravitational free-fall motions of the tank. The tank is free to slide along the ground as a result of the impact.

In the analysis of the unconstrained tank, the mesh-free Smoothed Particle Hydrodynamics (SPH) approach is used to model the lading. This has the advantage of being able to capture the fluid sloshing without mesh distortion effects and possible numerical instability of classical Lagrangian analyses. The SPH methodology is also compatible with the traditional Lagrangian analysis methodologies being used to evaluate the tank response. As a result, it is more computationally efficient than the Arbitrary Lagrangian Eulerian (ALE) methodology.

The comparison of the force-displacement behaviors for 18 mph impacts with the 9.55-inch-diameter round impactor on the constrained and unconstrained tank heads is shown in Figure 9. For the constrained tank head, the force increases approximately linearly with displacement up to approximately a 1.8 million lb force at a displacement of approximately 25 inches. At this point the constrained tank head is punctured. However, the behavior for the head impact on the unconstrained tank is significantly different. The force-displacement curves for the unconstrained tank model start along the same force deflection curve. However, the force levels begin to drop below those of the constrained tank head at early displacement levels. This is because the impact forces push the tank away from the impactor reducing the rate of the

impactor head intrusion (dent formation). The impact forces level off and begin to drop at a force of approximately 1 million lbs and a displacement of 20 inches. The impact severity is well below the level needed to puncture the tank head for the unconstrained tank condition.

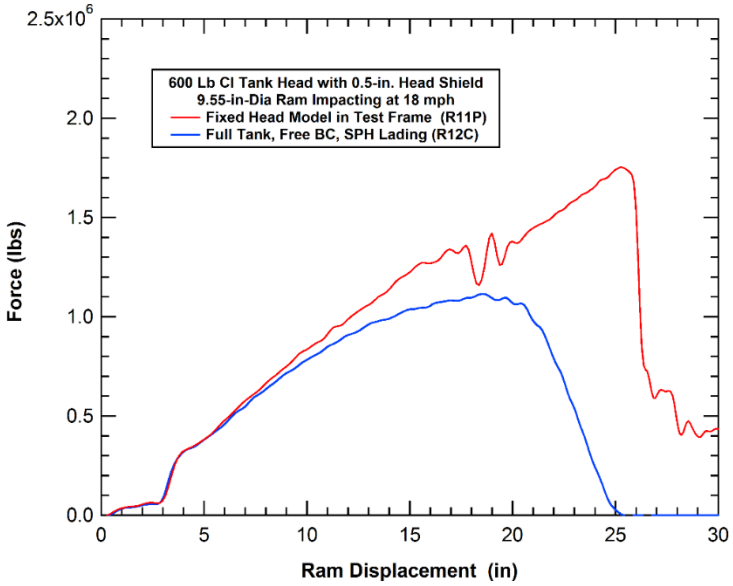

Figure 9. The effects of tank motion BCs on head impact response.

The effect of the tank constraints for head impacts is observed much earlier in the response than for side impacts for two reasons. The first is that the tank cylinder is much stiffer in axial loading compared to lateral loading. Thus, the head impact forces are very rapidly transmitted to translations of the tank center of gravity (CG). The second reason for increased constraint effects in head impacts is the behavior of the lading. During the duration of the impact, only a fraction of the total lading mass is coupled to the motions of the unconstrained tank. This effect is shown by fringes of longitudinal velocity in the lading in Figure 10. The time shown is well past peak load, halfway through unloading. However, the bulk of the lading is still stationary (blue fringes in the figure). Only the regions of the fluid very near to the tank wall or directly behind the impacted tank head are moving.

To investigate the effective weight of the fluid lading contributing to the motion in the head impact, we ran analyses at different smeared lading tank weights and iterated on an approximate equivalent weight of the tank. The value that matched the analysis best was a tank weight of 130 percent of the empty weight. The comparison of the analysis with the 130 percent tank weight with the empty tank model, the full weight model (smeared mass) and the model with SPH lading is shown in Figure 11. The agreement of the SPH model with the 130 percent tank weight model is quite good. Note that the 130 percent weight model increases the tank from an empty weight of 61,300 lbs to a weight of 79,690 lbs. The full weight of the tank is 263,000 lbs which is the empty tank plus approximately 200,000 lbs for the lading. As a result, these analyses show that less than 10 percent of the lading is coupled to the motion of the tank for this head impact scenario.

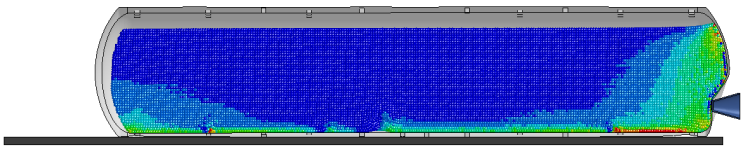

(a) Full tank profile (time=0.18 s)

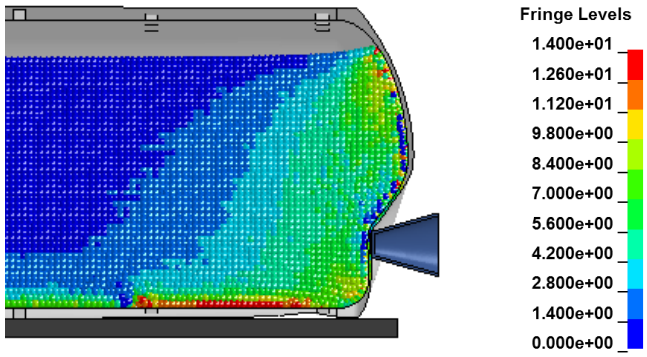

(b) Impact zone (time=0.18 s)

Figure 10. Calculated longitudinal velocity distribution in the SPH lading.

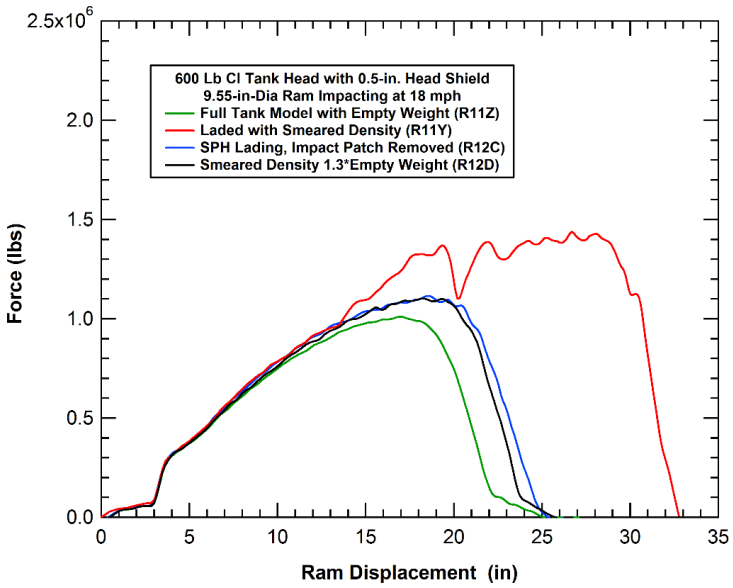

Figure 11. The effects of lading on unconstrained head impact response.

Analysis of Other Tank Conditions and Car Designs

A set of analyses was performed to assess the effects of the tank and lading temperature. As the equilibrium temperature of the tank rises, the vapor pressure increases, and the liquid density is reduced. A decrease in the liquid density will produce an increase in the liquid volume with a corresponding reduction in the outage volume. Both increasing the pressure and reducing the outage can reduce the puncture resistance of a tank car.

The condition analyzed is a 105J600W chlorine tank car at an equilibrium temperature of 105° F. This temperature increases the internal vapor pressure for the tank to 155 psi and lowers the corresponding outage volume for a tank loaded to the specified limit to 7.5 percent. These are compared to the 100-psi internal pressure and outage volume of 10.6 percent at a tank temperature of 78 degrees F.

A summary of results for both normal and oblique side impacts for the tank at higher temperature is given in Figure 12. In the figure, the calculated puncture energies at 105° F are normalized by the puncture energies at 78° F for the corresponding impact conditions. On average, the increase in temperature dropped the puncture energies by 20 percent. However, the puncture energies for smaller impactor sizes are more similar at the two temperatures. This is because the impact response for small impactors is dominated more by the structural stiffness. The internal pressure (and pressure increase) plays a smaller roll for the small dent sizes prior to puncture with the small impactor sizes.

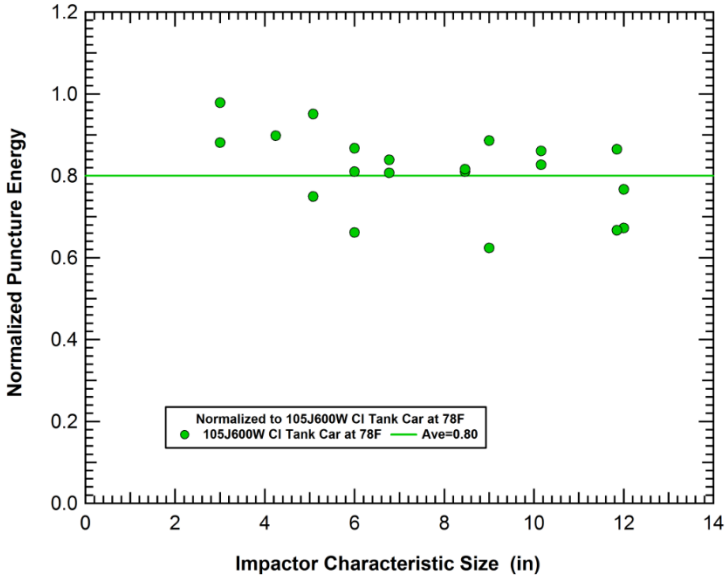

Figure 12. Normalized side impact puncture energies at 105° F.

In addition to the analyses performed on the 105J600 tank car, a series of other tank car types were analyzed. Evaluations were performed for the 500 lb chlorine tank car, the 340 and 500 lb anhydrous ammonia (AA) tank cars, the 300, 400, 500 lb ethylene oxide (EO) tank cars, and the DOT-113 LNG tank car. A full set of normal and 45-degree oblique side impacts were performed for each of the chlorine, EO, AA, and LNG tank car designs considered. For comparison of the various designs, the team normalized the calculated puncture energies all the various designs to those of the 105J500W chlorine tank car. The comparison for these normalized results is provided in Figure 13.

In the comparison, the DOT-113 LNG tank car had the highest average puncture energy, which was 126 percent higher than the 105J500W chlorine tank car. The average puncture energies for the 105J500W EO tank car design was the next highest and had the best puncture resistance for any of the pressure tank cars carrying Toxic Inhalation Hazard (TIH) materials. The EO tanks

had relatively high puncture energies because of the lower tank pressures and larger diameter tanks. The 105J500W, 105J400W, and 105J300W EO tank cars had puncture energies on average 82 percent higher, 17 percent higher, and 12 percent lower, respectively, than the 105J500W chlorine tank car. The puncture energies for the 105J600W chlorine tank car were on average 37 percent higher than the 105J500W chlorine tank car. The 112J500W and 112J340W AA tank cars were on average 10 percent above and 39 percent below the 105J500W chlorine tank car, respectively.

A similar comparison of the relative head impact puncture energies is shown in Figure 14. Again, the DOT-113 LNG tank head had the highest puncture resistance with an average puncture energy 56 percent higher than the 105J500W chlorine tank head.

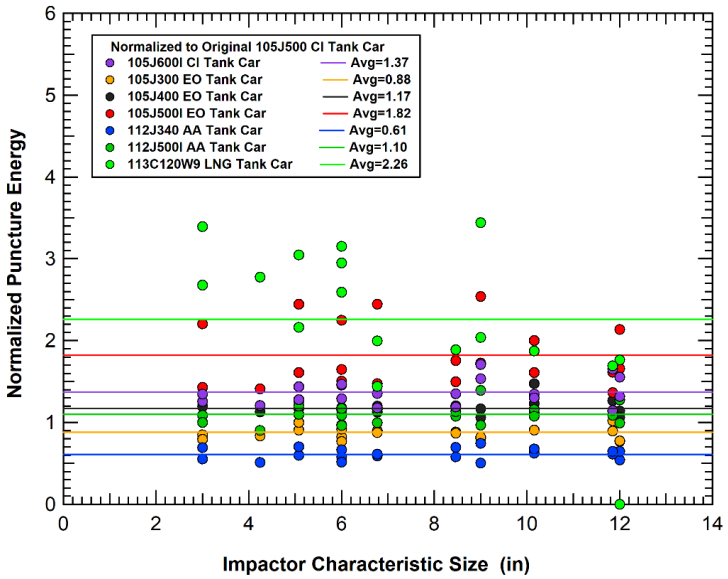

Figure 13. Comparison of relative tank shell puncture performance for different designs.

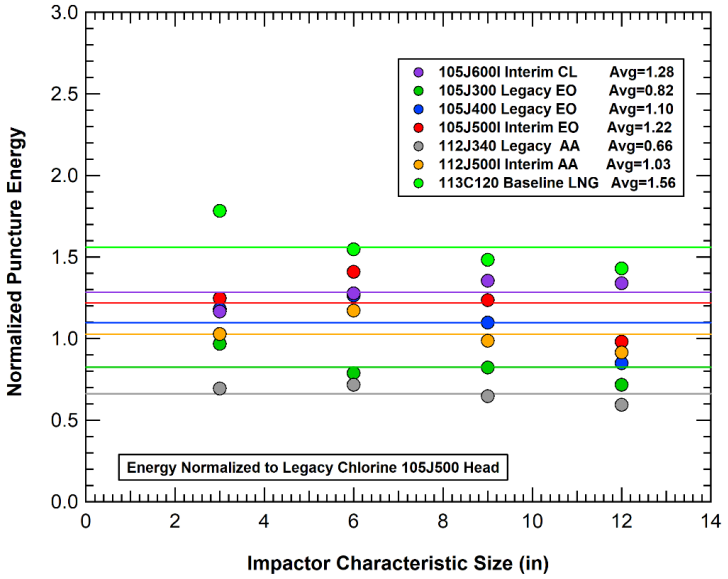

Figure 14. Comparison of relative tank head puncture performance for different designs.

Analytical Models of Tank Car Impacts

The FE modeling approach is very useful for determining the mechanics of tank impacts and punctures. However, at times, a simplified analysis methodology or impact algorithm is useful for the assessment of various factors on tank impact safety. In this study, we developed analytical tank impact algorithms that can be applied for future analyses of tank car safety. When evaluating appropriate analysis methodologies, we examined the response characteristics of both head and side impacts. We found that the behaviors for these two impact conditions are sufficiently unique that different analysis methodologies were appropriate.

The head impact response has several characteristics that influenced the simplified impact algorithm. The tank head is a stiffer structure under impact and the impact behavior for a constrained head is relatively independent of the impact speed. The most common head impact scenario is with the motions and orientations of the impacted and impacting cars nearly aligned with the original direction of travel. As a result, the motions can be assumed to be primarily one dimensional. In addition, the contributions of the lading response are significantly different for head impacts on unconstrained tanks.

A simple 1D algorithm was developed for the head impact tank motions with the different constraint conditions. The algorithm uses a known force-deflection curve of the fully constrained tank head as a characteristic property of the tank structure. The forces are then used to update the tank and impactor motions. The relative displacement of the impactor and tank are used to calculate an updated tank depth and corresponding change in impact force.

The force-deflection behaviors predicted by the simple 1D algorithm for the two unconstrained tank impacts with the empty and full tank weights are compared to the detailed FE analyses in Figure 15. The comparison shows that the simple algorithm accurately reproduces the force versus dent depth interaction and tank motions for the full impact and unloading behavior.

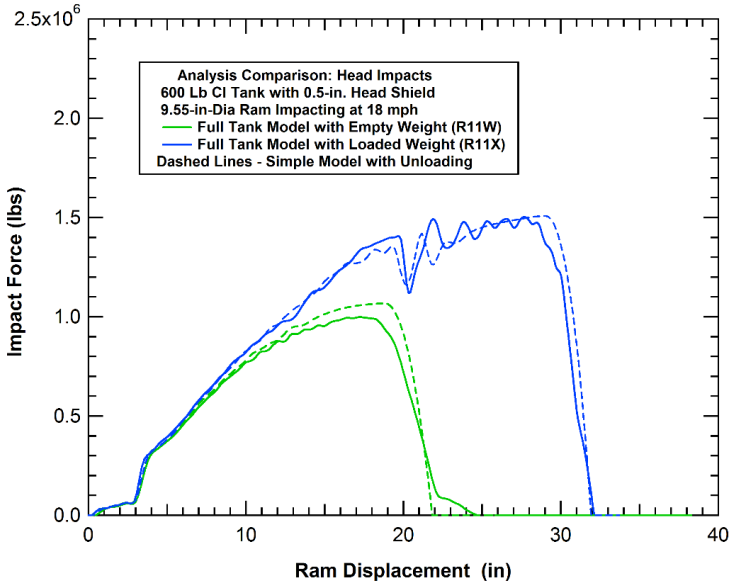

Figure 15. Comparison of the 1D model and FEA of head impact behaviors.

The side impact response also has several characteristics that influenced the methodology applied for the simplified impact algorithm. The tank is a more compliant structure under side impacts and the impact behavior is not independent of the impact speed (dynamic effects – see Section 3.4). The side impact scenarios typically occur as a result of large-scale lateral buckling behaviors in a derailment where the motions of the various cars are chaotic. As a result, the side impacts will include a greater range of variability in impact location and orientation and the motions will be at least two dimensional. These characteristics required a unique analytical methodology for side impacts.

The approach used to develop a side impact analysis algorithm is to develop a spring-mass model for the tank that can replicate the force-deflection characteristics for side loading against various objects (e.g., impactor, reaction wall). These loads can then be applied with equations for the tank kinematics under the combined actions of the loads. A schematic of the spring-mass system used for the side impact algorithm is shown in Figure 16. The tank is represented by a series of five symmetric masses connected by springs. The outer masses (M_1) are small and represent a small region of the tank that is involved with the initial interaction with the impactor or reaction structures. The secondary masses (M_2) represent the region of the tank in the deformation zone around the impactor or reaction structures that become significant as the deformation progresses. The central mass (M_3) is the remainder of the tank mass.

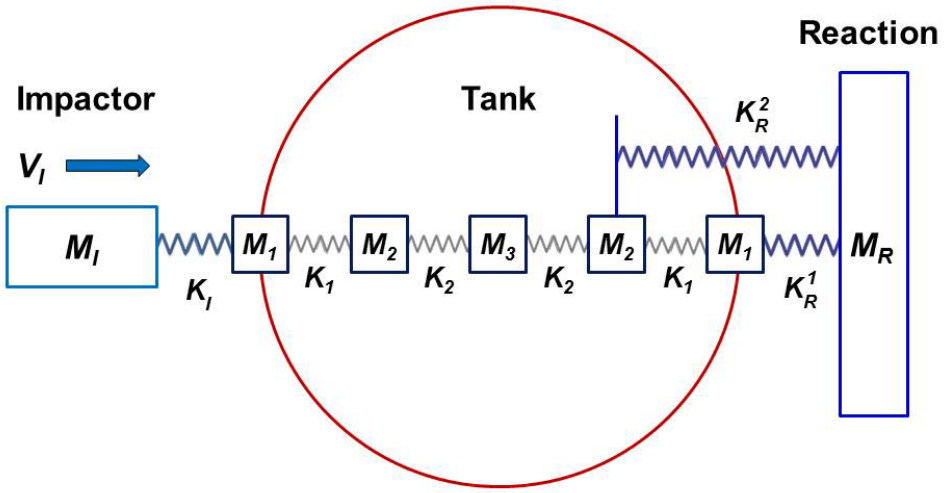

Figure 16. Idealized schematic of the side impact spring mass model.

The values used for the spring-mass model parameters were derived in a two-step fitting process. Initially, a series of Monte-Carlo analyses were performed where the parameters were allowed to vary randomly, within ranges determined by physical constraints. Results were compared to a series of FE impact analyses and the correlation for each set of parameters was determined. Subsequently, the parameters that provided the best fit to the impact data were optimized by finding the minimum error in the parameter space around the initial Monte Carlo parameter set.

The resulting model was then applied to simulate a series of impact behaviors and the results were compared to the corresponding FE analyses. For example, a series of impacts with the 9.55-in-diameter impactor at different impact speeds are compared in Figure 17. The comparison shows that the spring-mass model does a good job of reproducing the variations in impact

behaviors produced by different speed impacts. Note that the spring-mass model does not include puncture prediction, so the comparison of the higher speed impacts is only appropriate up to the point of the calculated tank punctures in the FEA.

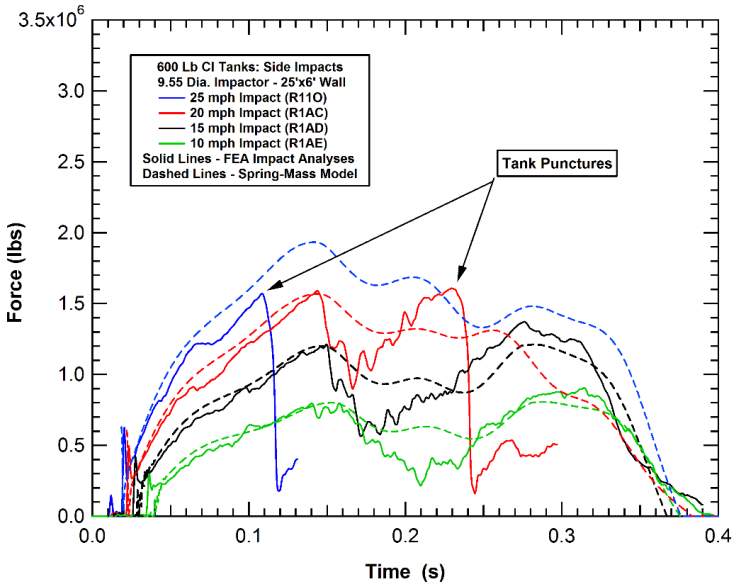

Figure 17. Comparison of the FEA and impact algorithm for different speed impacts.

Development of the Characteristic Puncture Force

The above sections describe analyses that can predict the force-deflection behaviors. However, the point along the force-deflection curve at which the tank is punctured also needs to be determined. This puncture force will be dependent on both tank geometry (materials and thicknesses) and the impact conditions (impactor size and impact orientation).

Our approach to developing a tank puncture criterion for the tank impact algorithm(s) was to use puncture data from all the detailed FE puncture analyses described in this report and develop a "characteristic puncture force" parameter that is a function of the impactor characteristic size. A collection of the calculated puncture forces for various tank and impact conditions is shown in Figure 18. As expected, there is a general trend in the data with increasing puncture loads for increasing ram characteristic size. However, for any given ram characteristic size, there is a large spread in puncture forces. This is because the puncture force for an oblique impact against a 111A100W1 tank car will be much lower than the puncture force for a normal impact against a 105J600 tank car.

To develop a characteristic puncture force, we applied a series of correction factors for the tank thickness, impact orientation, and impactor shape. When we apply all the corrections, we obtain the characteristic puncture force correlation as shown in Figure 19. Using this characteristic puncture force allows us to assess the puncture conditions for a wide range of tank and impact parameters. The uncertainties in the puncture force can be assessed by comparing the range of errors in the corrected data for the detailed FE analyses to the puncture data fitting line.

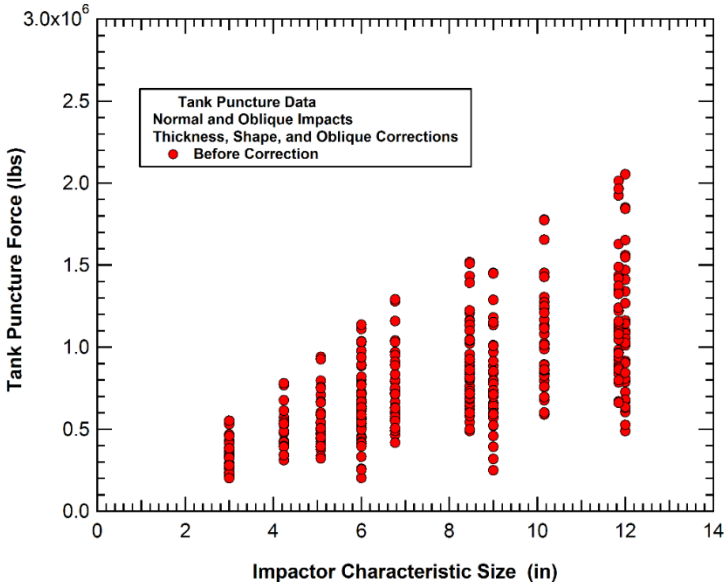

Figure 18. Initial set of tank puncture forces under various impact conditions.

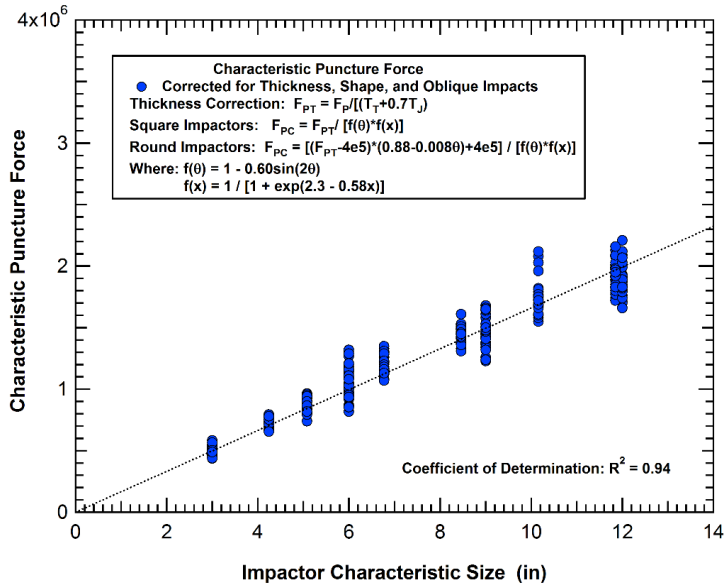

Figure 19. Correlation of characteristic puncture forces for various impact conditions.

Analysis of Real-World Threats

The majority of this study was focused on the safety of tank cars in accidents and derailments. These events that occur as part of normal rail operations are the most common events that lead to releases of hazardous materials in rail operations. However, the security of tank car from an intentional attack is also a consideration for these designs. The Department of Homeland Security (DHS) has done several small- and full-scale tests of components and tank cars subjected to different acts of terrorism. The objective of the analyses performed in this effort was

to assess the puncture performance in impacts (safety) of a protection concept developed by DHS for security against various threats.

The protection system concept analyzed was the punched plate concept. The system consists of two ¼-inch-thick perforated panels made of High Hard Steel (HHS). The perforations were 3/8-inch diameter holes in a hexagonal pattern with ½-inch spacing between the nearest neighbor hole positions. The two panels are used in an offset configuration.

A series of tank side impact puncture analyses was performed on the punched plate protection concept. The analyses showed that the protection concept also performs reasonably well in impact conditions. A comparison to other jacket designs found that the punched plate system provided equal or better impact protection than an equivalent weight TC128B jacket. Thus, this concept looks like a good design alternative that can provide protection for both safety and security concerns.

1. Introduction

There is ongoing research to develop strategies for improving railroad tank cars so they can maintain tank integrity for more severe accident conditions than current equipment. Research results are being used to develop improved tank car designs and to inform rulemaking by the Federal Railroad Administration (FRA).

A significant portion of the tank car research was performed under the Next Generation Railroad Tank Car (NGRTC) Program (Kirkpatrick, 2009a). A key effort in the NGRTC Program was the development and validation of detailed finite element (FE) models of tank car equipment which can accurately predict the puncture resistance under different impact conditions. To date, these analysis tools have been developed and validated for the puncture of the baseline tank cars for both side and head impact conditions. These validated tools are being applied in this study to assess the puncture resistance of various tank car designs under various impact conditions.

This report describes the application of the validated puncture analysis capabilities to assess the effects of different impactor threats and impact conditions. The scope of this effort includes the development of detailed FE models for tank cars and impactors, and the use of those models for various impact scenarios to assess puncture conditions.

1.1 Background

Accident statistics show that the rail industry's safety performance has generally improved over the last few decades. The FRA's Railroad Accident and Incident Reporting System (RAIRS) show that the number of accidents per year with at least one car releasing hazardous materials has decreased significantly over the past 25 years, as shown in Figure 20 (FRA, 2023). However, a series of three recent accidents or derailments involving the release of hazardous material have focused attention on the structural integrity of railroad tank cars. These events include (1) Minot, ND, on January 18, 2002 (NTSB, 2004); (2) Macdona, TX, on June 28, 2004 (NTSB, 2006); and (3) Graniteville, SC, on January 6, 2005 (NTSB, 2005).

Following these incidents, a series of research programs were initiated to develop strategies for improving railroad tank cars to maintain their structural integrity for more severe accident conditions. A significant portion of this research was performed under the Next Generation Railroad Tank Car (NGRTC) Program (Kirkpatrick, 2009a) (2009b) (2009c) that was performed from 2006 through 2010. The NGRTC program was initiated by The Dow Chemical Company, Union Pacific Railroad, and Union Tank Car Company, working with the FRA and Transport Canada (TC). The NGRTC program included full-scale tank car impact testing, material and component testing, development and application of tank car impact and puncture modeling, and efforts to design and evaluate advanced tank car impact protection concepts. A key outcome of the NGRTC Program was the development and validation of detailed FE models of tank car equipment that can accurately predict the puncture resistance under specified impact conditions. These tank car impact and puncture modeling capabilities have supported all the subsequent tank car safety research efforts.

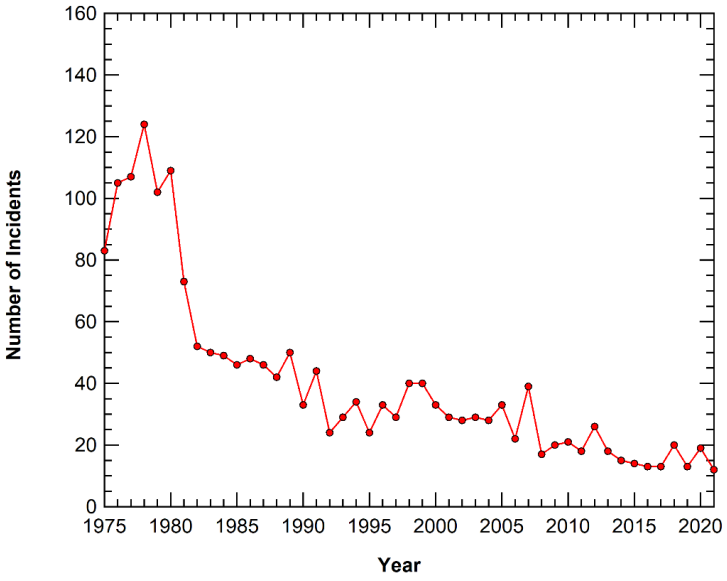

Figure 20. Number of Rail Accidents Releasing Hazardous Materials (FRA, 2023).

In collaboration with the NGRTC efforts, FRA initiated a significant research program to improve tank car safety, which is still ongoing. An important contribution of this FRA research has been a series of full-scale impact tests on tank cars and the related analyses of the impact test conditions. A summary of the full-scale tank car impact tests and associated analyses (2007-2019) is provided by Krishnamurthy et al. (2022).

One limitation of the effort in the NGRTC program is a primary focus on a few idealized impact conditions such as a normal impact (an impact that is perpendicular to the tank surface) with a 6-inch by 6-inch square impactor. Similarly, most of the subsequent full-scale tests performed by FRA were conducted using a 12-inch by 12-inch square impactor (Krishnamurthy, et al., 2022). However, there is uncertainty as to how representative these idealized impact conditions are as surrogates for the real-world critical impact threat environment.

In a parallel research effort, the Railway Supply Institute (RSI) and Association of American Railroads (AAR) have an ongoing project to evaluate the safety of tank cars. The RSI-AAR Railroad Tank Car Safety Research and Test Project used an alternate approach of collecting and analyzing extensive information about tank car performance in train accidents [e.g., (Barkan, Ukkusuri, & Waller, 2005), (Saat & Barkan, 2005)]. In over 50 years, the effort has collected data on more than 50,000 damaged tank cars and 31,000 accidents (Saat & Barkan, 2005). Analysis of these accident data allows for the assessment of the Conditional Probability of Release (CPR) of a tank car carrying hazmat in a train accident for a given tank car design. The CPR is available for the existing tank car types in the database, allowing for an assessment of the change of CPR when the hazmat shipment is moved by a tank car with different design features. However, this approach cannot provide information on CPR for a novel tank car design that varies from existing practices.

The initial set of research projects above had addressed two fundamental and separate aspects of tank car safety, as illustrated in Figure 21. The research performed by NGRTC and FRA included deterministic analyses and testing of tank cars under ideal conditions. This included

both traditional tank car designs as well as novel tank car concepts proposed for enhanced impact protection. However, there was not a capability to quantitatively show how the increased puncture resistance obtained in these idealized impact conditions would result in reduced releases under service conditions.

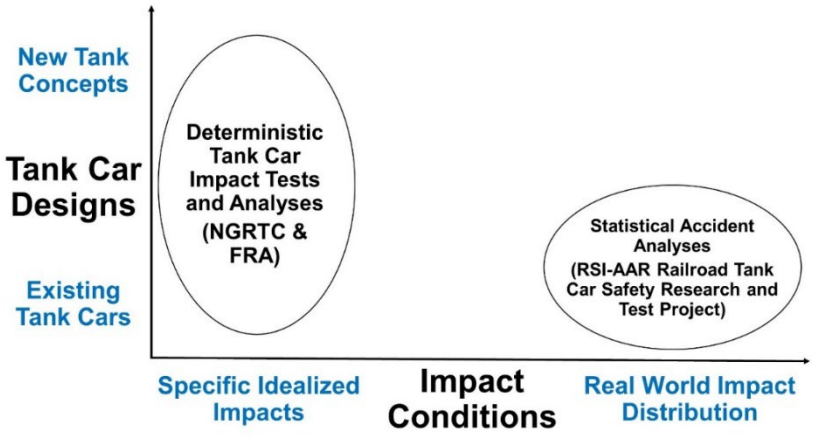

Figure 21. A graphical illustration of the initial tank car safety research areas.

In contrast, the RSI-AAR Railroad Tank Car Safety Research and Test Project was focused on the performance of existing tank car designs under the impact threat environments produced by real-world service conditions. However, since the program was based on the statistical performance of tank cars in service, there was no way to predict how a novel tank car design would perform when introduced into the freight rail fleet.

After the completion of the NGRTC program, additional research for tank car safety improvements was performed under the Advanced Tank Car Cooperative Research Program (ATCCRP), which was initiated to coordinate research efforts to enhance the safety and security of rail tank car shipments of Toxic Inhalation Hazard (TIH) materials. The ATCCRP was built on prior and ongoing research conducted by the NGRTC Project, the Chlorine Institute tank car safety research (Anderson & Kirkpatrick, 2006) (2007), and the RSI-AAR Tank Car Safety Research and Test Project (Railway Supply Institute, 2009), (Treichel, et al., 2019). The ATCCRP was a joint effort of shippers of tank cars, railroads that transport hazmat, and railroad tank car builders and lessors. In addition, Memoranda of Cooperation were developed to formalize cooperation agreements between ATCCRP participants and USDOT - FRA, TC, the U.S. Department of Homeland Security (DHS) - Transportation Security Administration, and the DHS Science and Technology Directorate.

The ATCCRP was organized by first collecting a wide range of topics for Technical White Papers (TWP) on potential technologies that could improve the safety and security of tank cars. These topics included the following (some numbers are missing because similar topics were combined):

- TWP-1: Effect of Pressure on Puncture Resistance – Chlorine and Anhydrous Ammonia

- TWP-3: Reducing Dispersion Effects by Lading Temperature Reduction
- TWP-4: Sandwich Tank Car Design
- TWP-5: Composite Materials for Protection Systems
- TWP-6: Structural Foams and Adhesives
- TWP-9: Coupler Modifications
- TWP-10: Correlating Material Properties to Puncture Resistance
- TWP-11: Relating Conditional-Probability-of-Release to Modeling and Tests
- TWP-13: Other TIH Materials
- TWP-14: Analysis of Different Impactor Threats and Impact Conditions
- TWP-15: Development of Performance-Based Testing Requirements for Railroad Tank Cars
- TWP-16: Application Study for Perforated Armor Plating
- TWP-17: Revising and Updating Conditional Release Probability Estimates
- TWP-18: Forensic Analyses and Elimination of Real-World Failures
- TWP-19: Improvements in Tank Car Weld Safety
- TWP-20: Investigation of Impactors in Past Accidents
- TWP-21: Demonstrate Approval Protocols on Candidate Technologies
- TWP-22: Development of Advanced Head Protection Concepts

The ATCCRP participant organizations reviewed and ranked the merits of the TWPs including anticipated commercial feasibility, estimated costs, and proposed schedules. Each organization identified the five TWP projects they believed were most important and likely to provide meaningful results. A system was worked out and used to identify interdependencies between projects and rate the proposed TWP research against the following ATCCRP objectives:

- Improved puncture resistance
- Reduce releases at top fittings
- Mitigate potential security threats
- Provide a basis for possible use in establishing regulatory standards and protocols for performance tests
- Enhance security, situational awareness, and tools for emergency responders

Following this evaluation and rating process, the ATCCRP Committee decided to perform projects TWP-4, 5, 10, 11, 14, 15, 17, and 22 (Kirkpatrick, 2018).

Among these TWPs, two were selected to form a connection between the two thrust areas of tank car safety research, shown previously in Figure 21. The expansion in the areas of research

developed by these two projects is illustrated in Figure 22. The TWP-11 project was initiated with the objective to better define the collision threat under real-world service conditions (Kirkpatrick, et al., 2023). To support this goal, the TWP-11 project developed and applied detailed FE methodologies to analyze the kinematics of freight trains in derailments and collisions [e.g., (Kirkpatrick, et al., 2023), (Kirkpatrick, et al., 2022)]. The models were then validated by quantitative comparisons to real world derailments. An example derailment simulation is shown in Figure 23 for the October 7, 2011, derailment in Tiskilwa, IL (NTSB, 2013). Evaluation of the derailments and collisions has shown that these are complex events with a wide range of collisions between the various cars and equipment in the train.

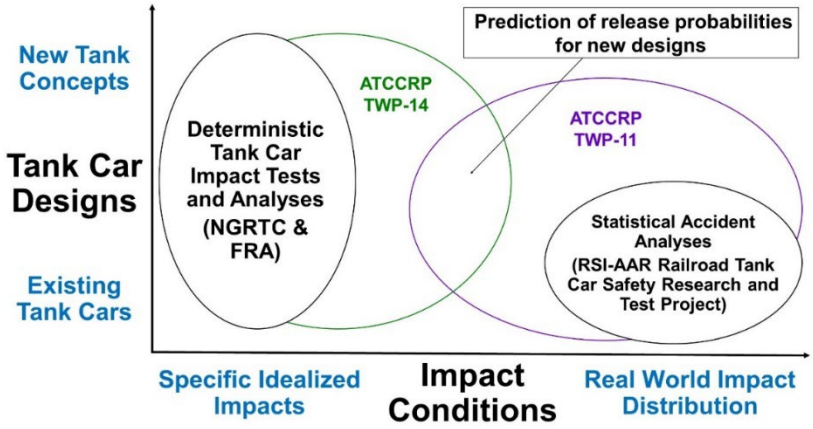

Figure 22. Summary of tank car safety research including ATCCRP Projects.

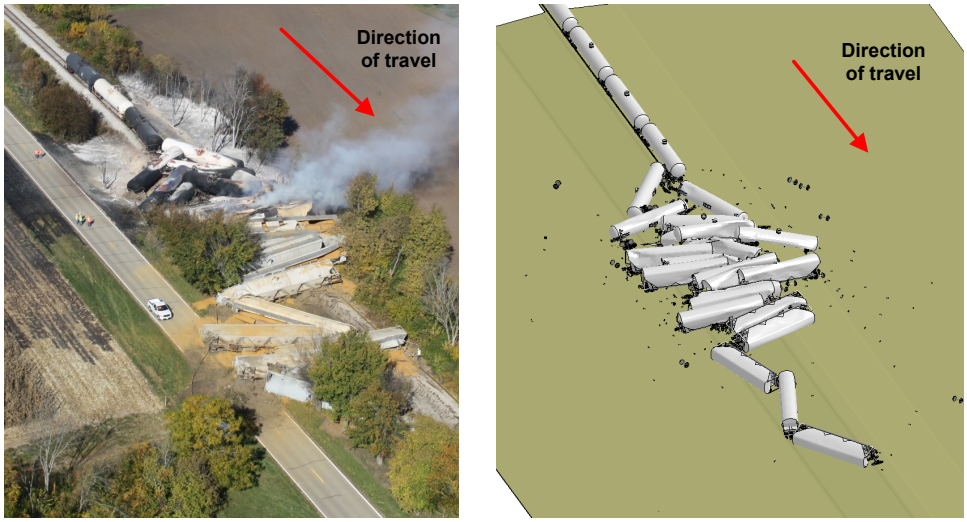

Figure 23. Detailed FE simulation evaluation for the Tiskilwa, IL derailment.

The second project was the TWP-14 project performed under FRA sponsorship. This project applied deterministic tank car impact analyses under a much wider range of impact conditions including various shape and size impactors, offset impact conditions, and oblique impacts. This project was carried out in 2013 and is the study documented in the initial revision of this report

(Kirkpatrick, 2013). With the TWP-14 methodology, the tank impact resistance was not limited to a single idealized impact condition but rather evaluated over a wide range of potential impact scenarios.

After the completion of this initial TWP-14 research project in 2013 (Kirkpatrick, 2013), an FRA ruling was made that allows transport of LNG in DOT-113C120W9 tank cars. This will likely result in an increase in shipments of LNG by rail in the near future. FRA has an ongoing full-scale test program to address the puncture resistance of these tank cars. However, these tests are being performed under ideal impact conditions and to date have applied a relatively large 12-inch by 12-inch impactor. Since these are novel tank designs, there is a risk that under different impact conditions (e.g., smaller impactors) the puncture resistance displayed with these tests of the DOT-113C120W9 tank cars relative to other designs may not be proportional. It was important to identify if this type of vulnerability exists in the design before a significant fleet is put into service. As a result, the study is revised in this report to assess the puncture resistance of the DOT-113C120W9 under a variety of impactors and impact conditions and compare the relative puncture resistance to other designs.

In addition to the assessment of the DOT-113C120W9 tank car, this report was also revised to include relevant ATCCRP impact results that were completed subsequent to the original TWP-14 study [e.g., (Kirkpatrick & McKeighan, 2018), (Kirkpatrick, 2017)]. The results included are primarily additional head impact assessments of the various tank car designs.

1.2 Material Damage and Failure Behaviors

A necessary component of the predictive tank car puncture modeling capability applied in this study is a detailed model that can be used to determine the impact damage and failure of the tank and protective system materials. An extensive program of laboratory materials testing was performed in the NGRTC Program (Kirkpatrick, 2009a) to characterize the tank car materials of interest. The tests included various material characterization tests, such as notched tensile tests and combined tension/shear tests, used to calibrate the material constitutive and failure behavior. Strain rate effects on the tank car materials were investigated and found to not have a significant effect on the tank puncture behavior. Additional component tests, such as punch tests and bend tests, were performed to validate the constitutive models.

The material damage and failure model applied is the Bao-Wierzbicki (BW) model that defines the material damage development based on the current stress state in the material and the plastic strain increments. The critical strain function is that proposed in the BW criterion and contains multiple branches depending on the range of stress state. For completeness, the NGRTC material testing and failure model development efforts are summarized in Section 2 of this report.

1.3 Tank Car Puncture Modeling

The BW failure modeling capability was combined with the tank car model to complete the tank car puncture prediction capability. This combined tank car impact and puncture modeling capability was applied in the NGRTC program (Kirkpatrick, 2009a) to evaluate a wide range of tank/jacket and head/head shield geometries. The side impact condition was a normal impact centered on the belt line of the tank. The head impact condition was an offset impact point approximately 29 inches vertically downward from the center of the head.

An example head impact and puncture analysis is shown in Figure 24. The head impact analyses included the head, head shield, and a sufficient length of the side shell and jacket to allow for buckling to initiate in the jacket support from the loads transmitted by the head shield, as seen in Figure 24.

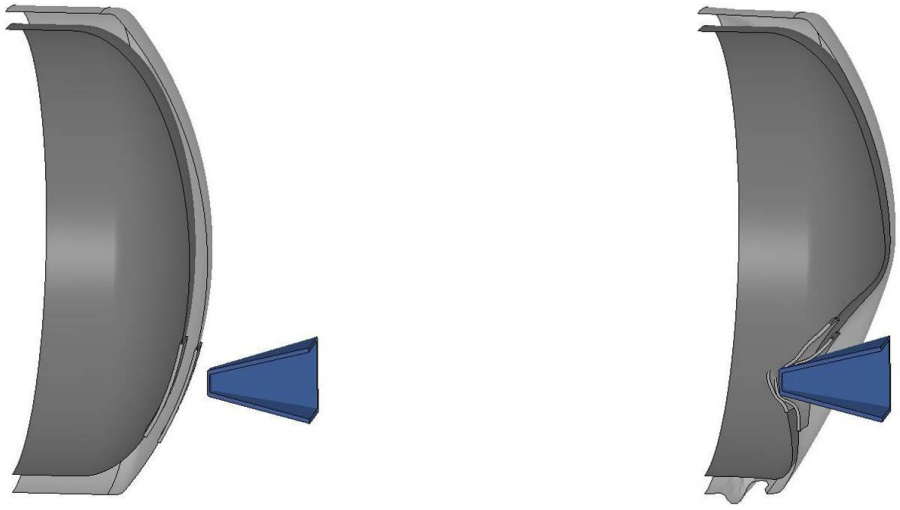

(a) Initial impact conditions **(b) Puncture response of the head**

Figure 24. Calculated puncture behavior of a head and head shield.

The calculated head and shell puncture forces as a function of the combined tank and jacket (or head shield) thickness is shown in Figure 25. All the analyses included in the figure are performed with the 6x6 inch impactor with a ½-inch edge radius (the standard impactor in the NGRTC program). The figure shows the analyses are mostly consistent with a linear relationship between puncture force and total thickness of the protective layers.

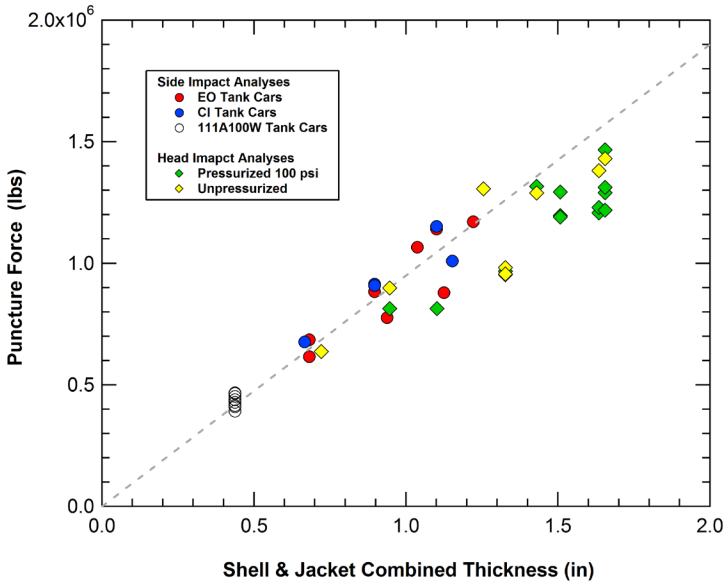

Figure 25. Calculated puncture forces as a function of system thickness.

The linear relationship between the puncture force and total tank system thickness provides an indication of the primary failure mechanism initiating the tank puncture. The geometry of the ram impacting and indenting a pressurized tank shell is shown in Figure 26(a). A force balance analysis in the direction of the impact on a patch of tank shell material is shown in Figure 26(b). The forces resisting the impact loads are the pressure on the inside surface of the contact patch and the shear stress around the perimeter of the contact patch. For a 100-psi tank pressure and a 6x6 inch impactor, the resultant force from the pressure is less than 4 kips on the contact patch. Thus, the average shear stress is approximately equal to the impact force divided by the product of the impactor face perimeter and tank thickness.

The slope of the linear fit in Figure 25 corresponds to an average shear stress in the tank layers around the perimeter of the impactor of 39 ksi. By comparison, the yield and ultimate stress levels of the TC128B in pure shear are 33 ksi and 49 ksi, respectively (approximately 58 percent of the stress values in pure tension using a Von Mises yield criterion). Thus, the force balance indicates that the failure mode is primarily exceeding the shear capacity around the perimeter of the impact patch.

The calculated puncture forces for pressurized heads and the thicker head systems tended to fall slightly below the linear fit in Figure 25. The proposed mechanism for these lower forces is that, for the stiffer head systems, the offset impact creates a larger stress concentration along the upper edge of the impactor face and the failure initiates at that location at a lower total force. The more compliant head systems allow for a larger dent to form, and the impactor develops a more uniform stress distribution in the impact patch around the ram face perimeter.

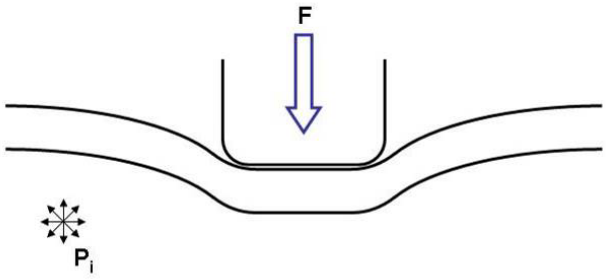

(a) Geometry of the tank indentation

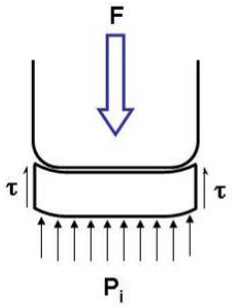

(b) Free body diagram for the tank contact patch

Figure 26. Loading and failure mechanism for the tank impact and puncture.

2. Material Constitutive and Damage Models

2.1 Introduction

The tank car impact analyses require a model for the material constitutive and damage behaviors to accurately predict the puncture threshold under various impact conditions. A piecewise linear elastic-plastic constitutive model was modified for this purpose to include a version of the Bao-Wierzbicki (BW) failure criterion [(Bao & Wierzbicki, 2004a), (2004b), (Lee & Wierzbicki, 2004)]. This model has been applied by other researchers to assess tank car puncture conditions (Tang Y. , Yu, Gordon, Jeong, & Perlman, 2008) and is capable of reproducing both the nonlinear stress-strain behavior of the material as it deforms into the plastic regime and the fracture and failure behavior that depends on the state of stress and plastic strain history in the material. The material parameters used in these constitutive models were developed from the material test data on TC128B steel, developed under the NGRTC program [e.g., (McKeighan, 2007a), (2007b) (2007c)].

The following sections describe the development of the constitutive and damage parameters used in the subsequent tank car puncture analyses.

2.2 TC128B Material Properties

The first step in the development of a constitutive model is the development of the nonlinear stress-strain behavior. This governs the mechanical response of the material and prescribes the internal forces (stress) that are developed as the material is deformed (strained).

A tabular stress-strain curve was developed based on testing of different samples of TC128B (McKeighan, 2007a). A series of standard tensile tests were performed on different batches of TC128B, as shown in Figure 27. The data is consistent within each batch of material, but significant variation can be found in tank car material obtained from different sources. The new material that was tested was at the upper range of strength for TC128B and the material recovered from the tank cars used in the test were more consistent with previous test data [e.g., (NTSB, 2003)]. As a result, the material recovered from the tank car used as the Test 2 target vehicle was used as the baseline material for the analyses in this report.

The data shown in Figure 27 is the measured engineering stress-strain behavior. Engineering stress was obtained by dividing the measured loads by the original cross-sectional area of the specimen. Similarly, engineering strain was obtained by dividing the change in the specimen gauge-section length by the original length.

The constitutive model in the finite element analyses requires that the engineering data be converted to true stress and true strain. This conversion accounts for the changing cross section of the specimen as it was deformed. The specimen cross section changes (shrinks) significantly during the test, and the engineering stress does not yield the “true” stress in this cross section. Similarly, the engineering strain is not representative of the material behavior, especially when a general three-dimensional state of strain exists. As a result, the engineering stress decreases as some materials approach failure, implying a weakening of the material. In reality, the stress in the cross section is increasing due to the reduction in the cross-sectional area (i.e., necking).

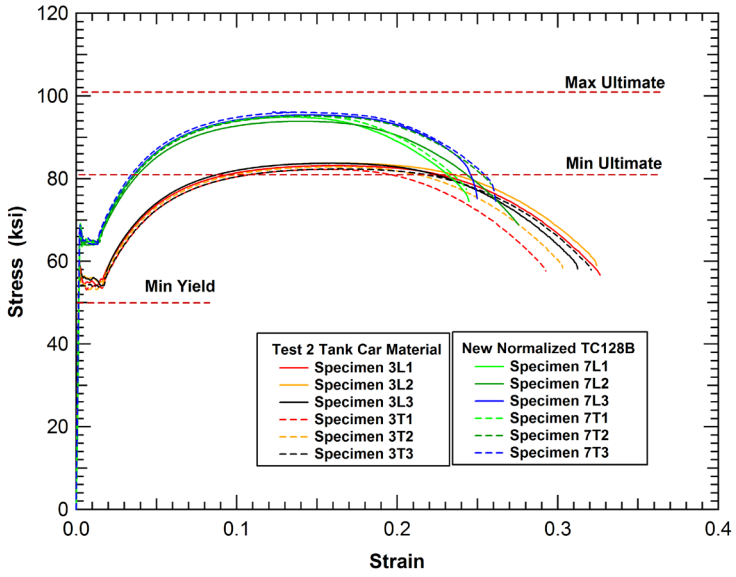

Figure 27. Material testing data for different TC128B materials.

There are several different ways to measure stress and strain based on the coordinate system used (Malvern, 1969). Some are based on material (Lagrangian) coordinates and some on spatial (Eulerian) coordinates. These give rise to terms such as "Green" and "Almansi" strain tensors. These are important in writing a computer code to solve large strain problems. An alternate approach is to define a "true" or "natural" stress and strain. The true stress is based on the load divided by the actual cross-sectional area of the specimen and is equal to the engineering stress multiplied by a term to correct for the change in cross section.

$$\sigma_T = \sigma_{eng}(1 + e) \tag{1}$$

where σ_T and σ_{eng} are the true and engineering stresses, respectively, and e is the engineering strain.

Prior to the onset of localization (necking), the natural or true strain, ε_T, is defined as

$$\varepsilon_T = ln(\frac{l}{l_o}) = ln(1 + e) \tag{2}$$

This definition comes about from defining the incremental true or "natural" strain as the current "change in length" divided by the current length, or

$$d\varepsilon_T = \frac{dl}{l} \tag{3}$$

This is in contrast with the definition of engineering strain that references the change in length, Δl, divided by the original length, l_0, or

$$e = \frac{\Delta l}{l_0} \tag{4}$$

After the onset of localization, the determination of the true strain in the necked region becomes more complex and requires measurement of the local neck geometry.

The TC128B engineering test results are compared to the converted true stress and true strain data in Figure 28. The true stress curves from the tests do not include a correction for the necking behavior. As a result, they are only valid up to the onset of necking at a true strain of approximately 15 percent. The actual true stress and true strain curves for the material continue to strain harden throughout the loading if the effects of necking were corrected. An extrapolated true stress curve that corrects for the effects of the necking behavior is added to Figure 28 (solid black line). It is this extrapolated curve that is used in the material constitutive model.

The final step in obtaining the tabular stress-strain parameters for the TC128B constitutive model was to fit a smooth set of points to the extrapolated true stress data. This final tabular fit for the TC128B is shown in the true stress versus plastic strain curve in Figure 29. The specific values for the tabular stress-strain curve are also listed in Table 1. As a validation that this curve accurately captures the true stress-strain behavior of the material, a tensile specimen model was generated, and the constitutive parameters were applied to simulate the tensile test response. The calculation was analyzed to determine the engineering stress-strain behavior consistent to the tests (e.g., using equivalent gauge section length). A plot of the calculated engineering behavior compared to the test data is shown in Figure 30. The data shows that the constitutive parameters accurately reproduce the material behaviors including the onset and development of necking in the specimen.

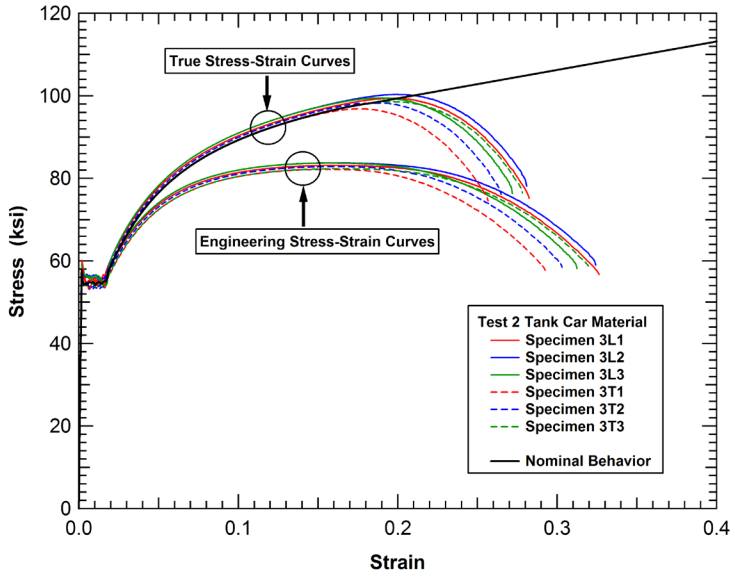

Figure 28. Comparison of engineering and true stress-strain data for TC128B.

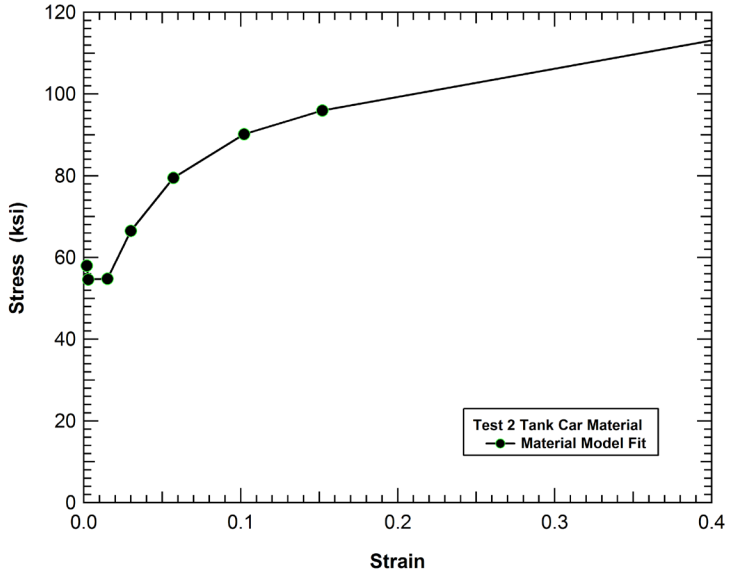

Figure 29. Tabular true stress curve developed for the TC128B constitutive model.

Table 1. Tabular TC128B stress-strain curve values

Point No.	Plastic Strain (in/in)	True Stress (ksi)
1	0.00e+00	58.0
2	8.22e-04	54.6
3	1.30e-02	54.8
4	2.76e-02	66.5
5	5.41e-02	79.5
6	9.87e-02	90.2
7	1.49e-01	96.0
8	1.15e+00	165.0

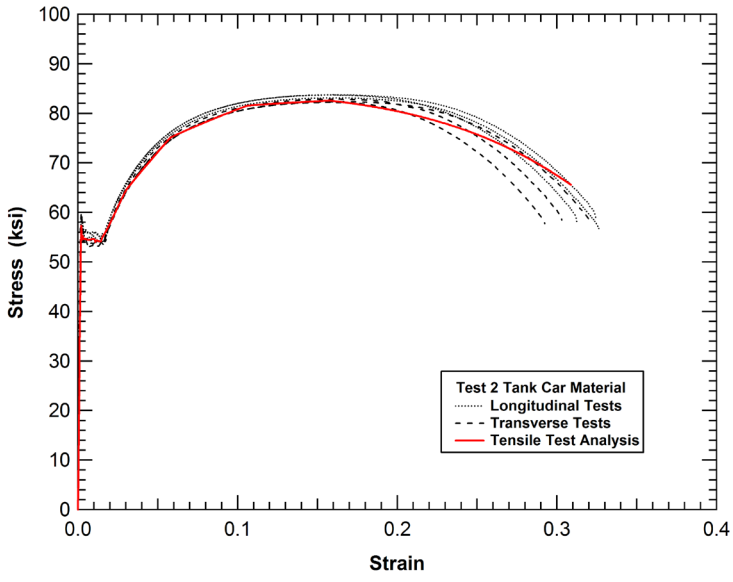

Figure 30. Comparison of the measured and calculated TC128B tensile test.

2.3 Bao-Wierzbicki Failure Surface

Accurate prediction of the puncture energies of tank cars for various impact conditions requires the addition of a detailed damage and failure assessment capability to the material model. These damage mechanics, or so-called local fracture mechanics (LFM) approaches, provide enhanced capabilities for tank car design and puncture assessment. Local fracture mechanics models the microstructural deformation and failure processes leading to fracture in terms of continuum parameters averaged over a small volume of material [e.g., (Beremin, 1981), (Lemaitre, 1986), (Mudry, 1985), (Hancock & Mackenzie, 1976)]. In contrast to classical linear elastic and elastic-plastic fracture mechanics (LEFM and EPFM, respectively), which characterize fracture in terms of the conditions at the boundary of the fracture process zone while ignoring the details of the processes occurring in that zone, LFM focuses on the evolution of the process zone itself. Although LFM may initially seem more complex to formulate and more difficult to apply than LEFM/EPFM, it is more versatile and more general than the latter approaches. Local fracture mechanics methodologies are also ideally suited to implementation into finite element analyses where damage can be evaluated at the local element level.

The key mechanism that needs to be included in the ductile local fracture model for tank car puncture analyses is the influence of the stress state on the rate of damage development as the material is undergoing plastic deformation. The primary stress state factor that controls the rate of damage development is the stress triaxiality, defined as the ratio of the mean stress to the equivalent stress ($\sigma_{mean}/\sigma_{eq}$). The mean stress (or hydrostatic stress) is the average of the three principal stresses (stresses on 3 orthogonal axes perpendicular to the principal planes upon which no shear stress exists). The equivalent stress, also referred to as the effective stress or the Von Mises stress is defined as

$$\sigma_{eq} = \frac{1}{\sqrt{2}}[(\sigma_1 - \sigma_2)^2 + (\sigma_2 - \sigma_3)^2 + (\sigma_3 - \sigma_1)^2]^{1/2} \quad (5)$$

where σ_1, σ_2, and σ_3 are the three principal stresses.

There are many models that include the effects of stress triaxiality on damage development and ductility. Several of these have previously been applied within LS-DYNA to analyze various ductile fracture problems [e.g. (Giovanola & Kirkpatrick, 1992), (1993), (Giovanola, Kirkpatrick, & Crocker, 1996)] including the use of the Gurson-Tvergaard model [(Gurson, 1977), (Tvergaard, 1982), (1990)] for the puncture assessment of pressure tank cars (Anderson & Kirkpatrick, 2006). These models include the stress triaxiality effects on ductility for tensile loading as illustrated in Figure 31. The deficiency with many of these previous local damage models is that they do not include the changes in damage development and failure for low triaxiality where the tensile damage and failure behavior transitions into a shear dominated fracture behavior. The concern that shear loads are important for tank car puncture assessments led to the selection of the Bao-Wierzbicki (BW) model in this effort.

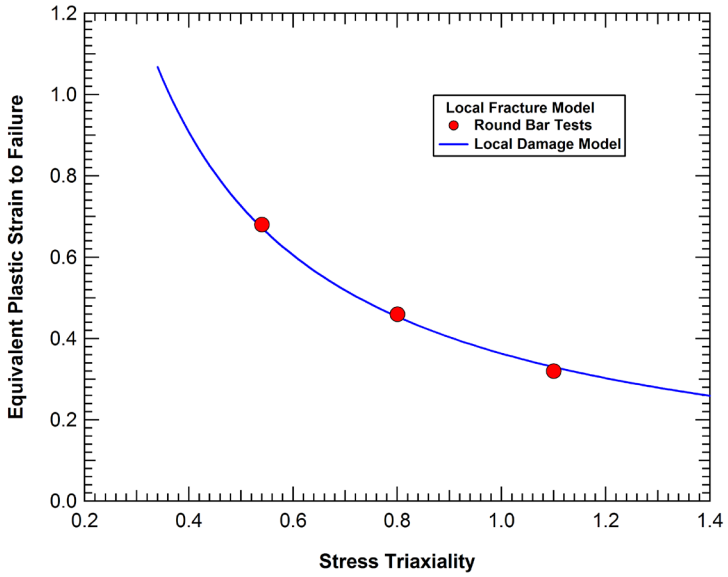

Figure 31. Local damage criterion for tensile ductile fracture analyses.

As implemented, the BW model is a basic form of a ductile fracture criterion (Mudry, 1985). It assumes that failure at a material location occurs when the damage within a surrounding characteristic volume (VMIC) exceeds a critical value. The damage development and failure criterion can be written in the form:

$$D = \int \frac{d\varepsilon_{eq}^{p}}{\varepsilon_c(\sigma_{mean}/\sigma_{eq})} = 1 \quad \text{over } V_{MIC} \tag{6}$$

where D is the normalized damage parameter; $d\varepsilon_{eq}^{p}$ is an increment in equivalent plastic strain; and $\varepsilon_c(\sigma_{mean}/\sigma_{eq})$ is the critical failure strain as a function of the stress triaxiality. The characteristic volume (VMIC) in this application is the element size which was maintained with a characteristic element length of approximately 0.040 inch (1 mm) in the fracture zone. Damage accumulation occurs with plastic deformations and the damage is tracked locally in each element in the model. When the damage level in any element exceeds the failure criterion (D=1), the local failure is propagated in the model by element erosion.

The critical strain function is that proposed in the BW criterion and contains multiple branches depending on the range of stress state as shown in Figure 32. The critical strain in each branch is governed by the equation:

$$\varepsilon_c(\sigma_{mean}/\sigma_{eq}) = \begin{cases} \infty & (\sigma_{mean}/\sigma_{eq}) \le -\frac{1}{3} \\ \dfrac{A}{1+3(\sigma_{mean}/\sigma_{eq})} & -\frac{1}{3} \le (\sigma_{mean}/\sigma_{eq}) \le 0 \\ 9(B-A)\left[(\sigma_{mean}/\sigma_{eq})\right]^2 + A & 0 \le (\sigma_{mean}/\sigma_{eq}) \le \frac{1}{3} \\ \dfrac{B}{3(\sigma_{mean}/\sigma_{eq})} & \frac{1}{3} \le (\sigma_{mean}/\sigma_{eq}) \end{cases} \tag{7}$$

The parameters A and B in Equation 7 can be determined by a series of tests under different stress conditions including notched tensile tests with specimens of varying notch radii (Mackenzie, Hancock, & Brown, 1977) and tensile-shear tests with different ratios of tension to shear stress.

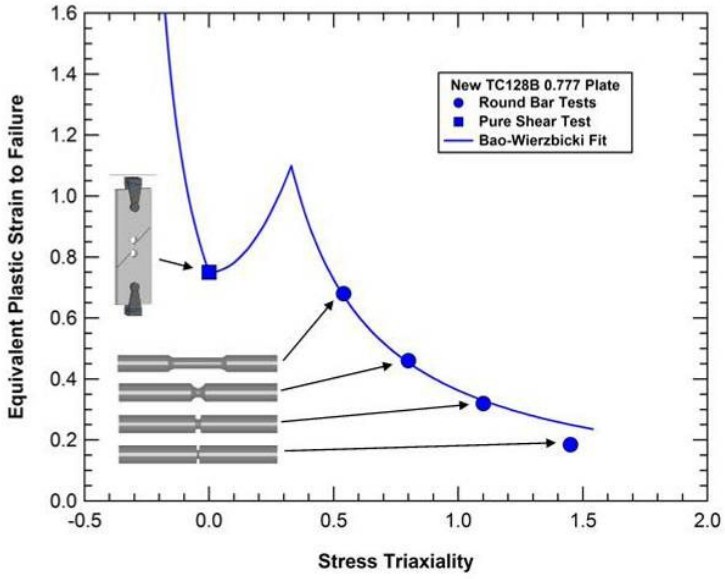

Figure 32. Bao-Wierzbicki failure surface and tests used for model calibration.

2.4 Material Characterization Testing and Analyses

A wide variety of material characterization tests were performed to calibrate and validate the material constitutive and failure models. These include material tests such as standard tensile testing to assess the material stress-strain behavior and testing under various stress states (notched tensile or tensile-shear tests) to obtain the characteristics of the failure surface. Subsequent tests under more general loading conditions, such as the punch test configuration, are used to validate the models. The approach applied here is to perform detailed analyses of the material testing conditions to assess the accuracy and validity of the models. The comparisons for the different testing conditions are provided in the following sections of this report.

2.4.1 Tensile Tests and Analyses

Standard tensile test methods were employed in accordance with ASTM E8 (McKeighan, 2007a). The thick TC128B allowed fabrication of a round tensile specimen (diameter of 0.505-inch). For all other materials a flat specimen, as shown in Figure 33, was utilized. The specimen had a gage length of 2-inch. No machining was performed in the thickness direction, and it was tested as received.

Photographs of the TC128B round bar specimens that were tested are provided in Figure 34. An extensometer with a 2-inch gage length was mounted on the specimen during testing. In one case, the thickest TC128B condition, strain gages were also mounted (2 gages, oriented opposite of each other) on the specimen gage length. Due to the excellent agreement between the strain gage and extensometer results, strain gages were omitted in all subsequent testing.

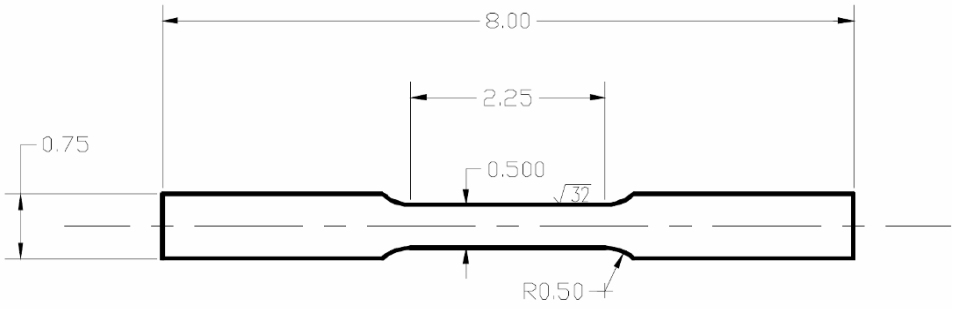

Figure 33. Dimensions of the specimen used in tensile testing.

Figure 34. Necking behavior observed in the TC128B round bar specimens.

All tests were performed in constant-rate displacement control. Two rates were used, either 0.035 or 0.050 inch/minute. Due to the large elongation observed in the steel materials, typical test times ranged from 15-30 minutes under the constant displacement testing. The data acquisition system was configured to record data at 3 Hz.

To confirm that the tensile test data reduction and material constitutive parameter extraction process was performed correctly, a model of the tensile specimen was generated, and the tensile test was simulated using the constitutive model. The load and displacements were extracted from the analysis using consistent methodologies to the test. A comparison of the measured and calculated engineering stress-strain behaviors for TC128B is shown in Figure 35. The comparison shows that the model accurately reproduces the stress-strain behavior and captures the initialization of the necking response.

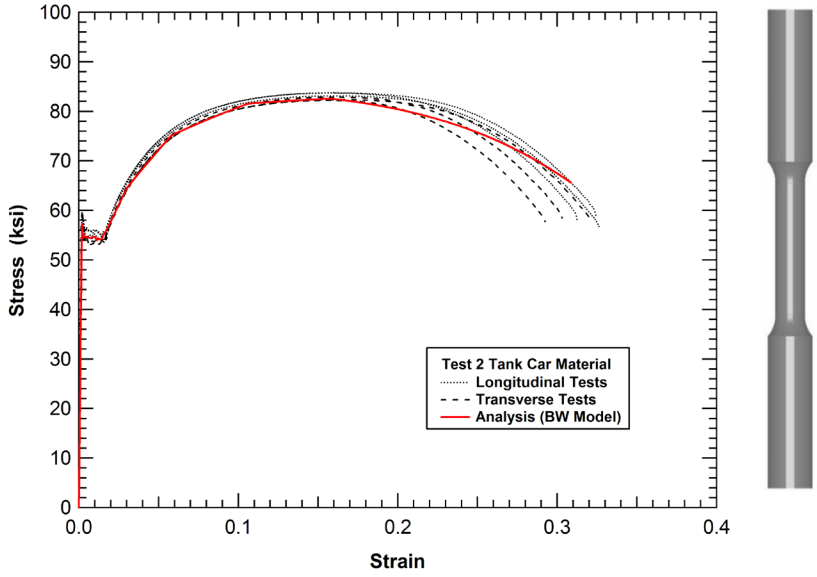

Figure 35. Validation of the tensile test behavior for TC128B.

2.4.2 Notched Round Bar Tensile Tests and Analyses

The notched round bar tensile tests were used to assess the performance of the BW failure model in the high stress triaxiality regime. The tests were performed using round bars with various notch radii (McKeighan, 2007b) to achieve different levels of confinement at the notch root and thus different stress triaxiality levels. Models were created for the different notched round bar specimens and the tests were simulated.

Material was provided from the two full-scale tank shell test articles (Tests 1 and 2) in the form of 12x12-inch plates. These plates were taken from near the impact site and were fabricated from normalized TC128B with a thickness of 0.777-inch. Specimens were extracted from these plates for mechanical testing. All specimens were oriented in the transverse orientation relative to the original plate rolling direction. The transverse orientation of the plate used to fabricate a tank car ring segment corresponds to the axial direction of the tank.

The notched tensile testing was performed similar to the procedures of the conventional tensile test standard, ASTM E8. The inner net diameter of the notched specimen is 0.25-inch, and the gross outer diameter is 0.5-inch. The three different notch geometries, with radii of 0.25, 0.10 and 0.05-inches, were all gripped in smooth clamping friction grips. A photograph of the test setup is shown in Figure 36.

A comparison of the calculated and measured stress-strain behavior across the notch for the three different radii specimens is shown in Figure 37. The comparison shows that the constitutive and damage model were capable of reproducing both the increase in stress level and reduction in ductility that occur as the notch radius is reduced. The BW failure parameters used provide a good correlation to the observed failures of the specimens.

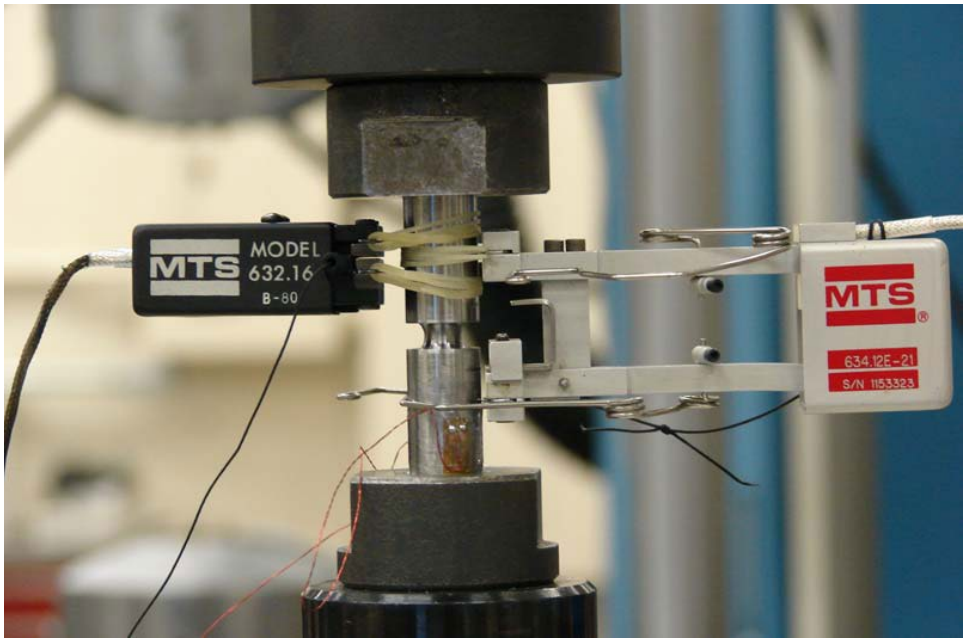

Figure 36. Test setup for the TC128B notched round bar specimens.

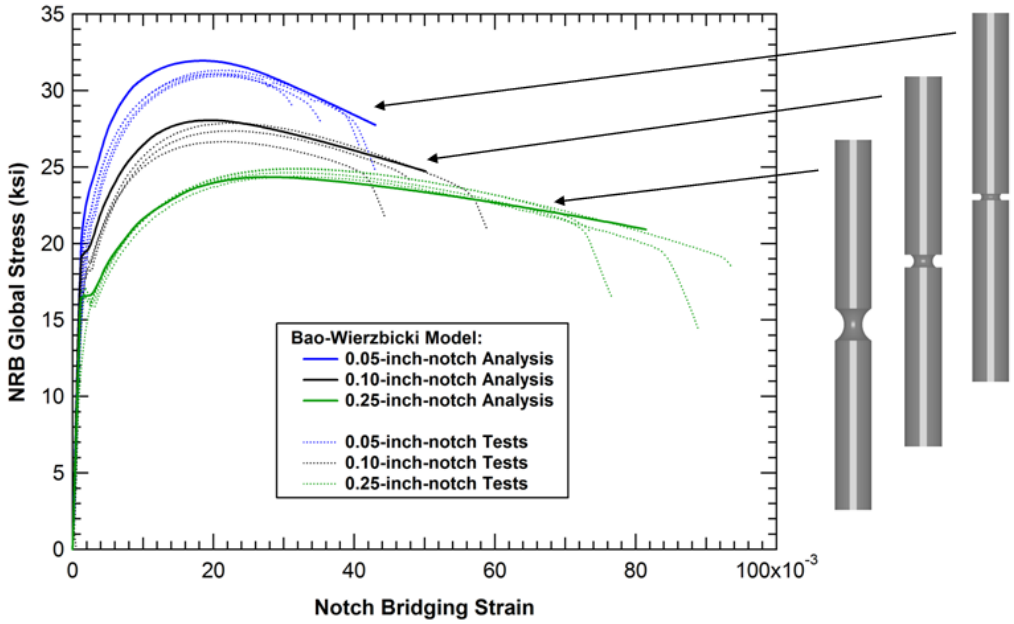

Figure 37. Validation of the notched round bar test behavior for TC128B.

2.4.3 Tensile-Shear Tests and Analyses

The combined tensile-shear tests were used to assess the performance of the BW failure model in the low stress triaxiality regime (stress triaxiality between 0 and 1/3). The tests were performed using a modified Arcan specimen (Arcan, Hashin, & Voloshin, 1978) to achieve different ratios of tensile and shear by rotating the orientation of the gauge section relative to the loading axis, as

shown in Figure 38. A photograph of the test setup is shown in Figure 39. Instrumentation includes clip gauges across both slots separating the upper and lower specimen sections, a string potentiometer to measure the displacement along the load path, the load ram LVDT, and the load cell. The tests were performed in a displacement control mode at a rate of 0.002 inch per second and data was collected at 5 Hz.

Simulations of the specimen geometry were initially performed to assess that a relatively uniform stress state could be achieved in the specimen gauge section, as shown in Figure 40. Models were then created for each of the specimens with different gauge section orientations and the tests were simulated. A comparison of the calculated and measured load-displacement behaviors is shown in Figure 41. The comparison shows again that the constitutive and damage model could reproduce both the decrease in load level and increase in displacement that occur as the orientation was rotated from pure tension to pure shear. The BW failure parameters used provide a good correlation to the observed failures of the specimens.

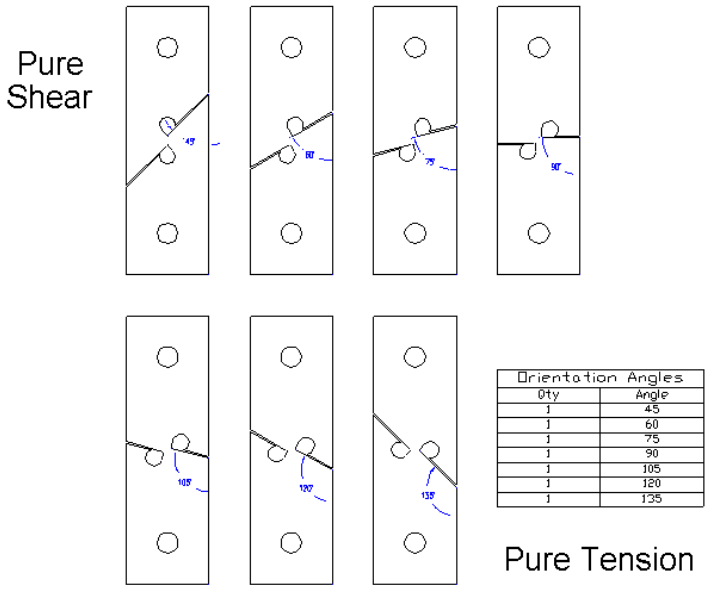

Figure 38. Specimen geometries for the combined tensile shear tests.

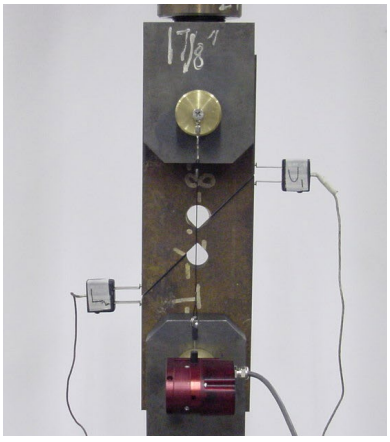

Figure 39. Photograph of the combined tensile shear test configuration.

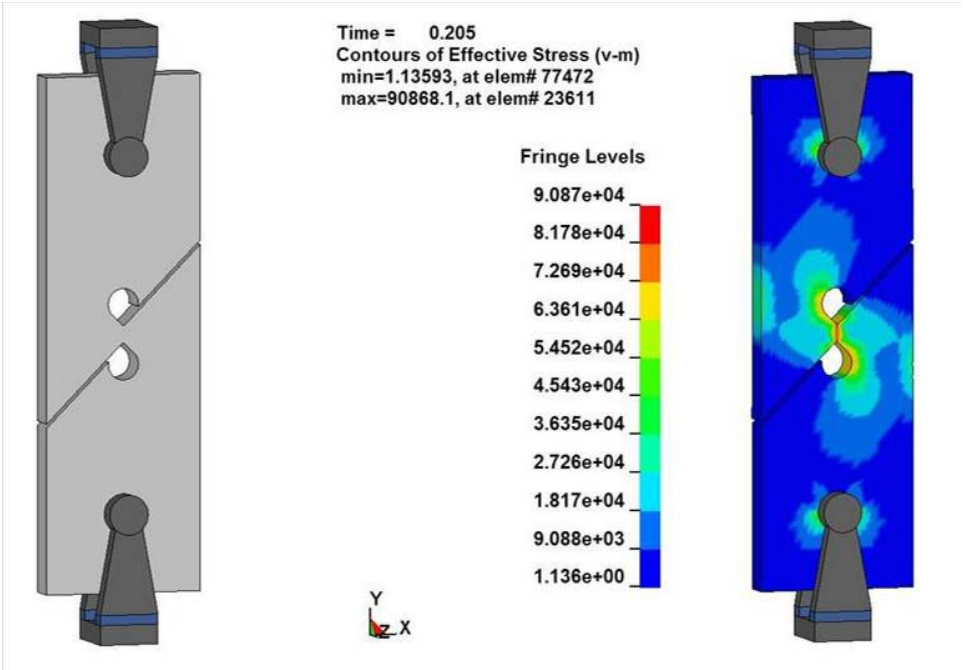

Figure 40. Analysis of the specimen behavior in the pure shear orientation.

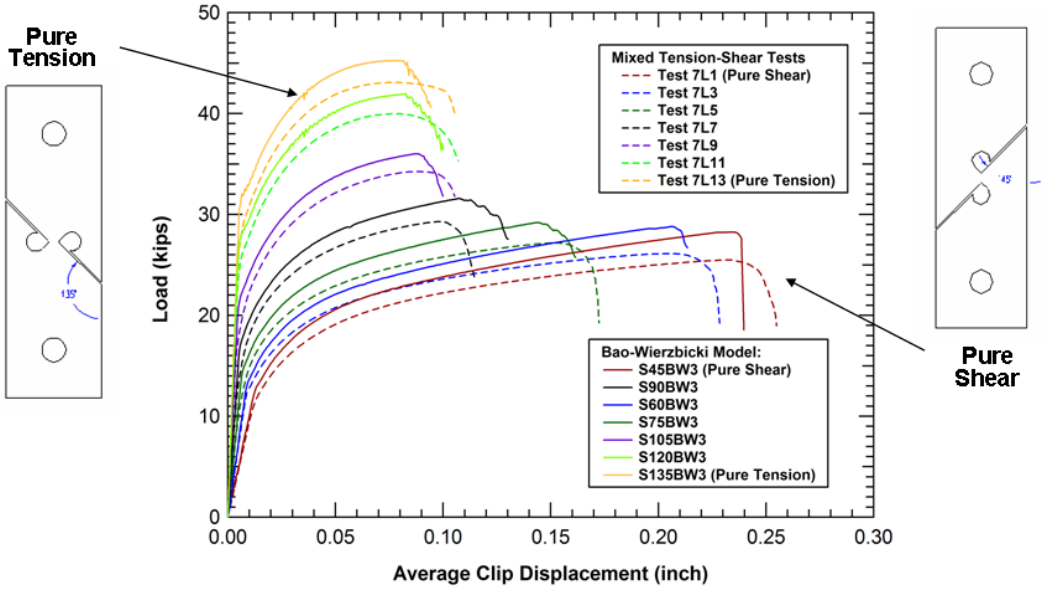

Figure 41. Validation of the combined tensile shear test behavior for TC128B.

2.4.4 Punch Tests and Analyses

The above notched round bar and tensile shear tests provide a good set of data to validate that the BW failure model can predict the damage development and failure of the TC128B material for a wide range of stress states. However, these tests were used to assess only the failure parameters *A* and *B* in Equation 7. Therefore, an independent punch test was developed and applied to

validate that the model could predict the failure of the material under a more general loading condition.

The specialized puncture fixture was developed for the NGRTC program at the SwRI Materials Test Lab and installed in a 220-kip test machine as shown in Figure 42. The punch test fixtures are shown with the 1.5-inch diameter punch and the 3-inch diameter receiving hole bore (so-called manhole cover). The fixture was designed so that different punch sizes and different manhole cover diameters can be used.

The punches were fabricated from hardened bar stock material. The punch contact face was flat with a 0.30-inch radius around the perimeter. Punches were fabricated with diameters of 1.0, 1.5, 2.0 and 3.0 inches. Manhole covers were fabricated with hole diameters of 2.0, 2.5, 3.0, 3.5, 4.5, and 5.5 inches. As a result, the punch test fixture was applicable for evaluating the behavior of multiple materials and structural components [(McKeighan, 2007d), (2008a), (2008b)].

Figure 42. Simulation of the punch test on the thin TC128B plate material.

During testing, the actuator (actually, the punch frame) displacement was measured with a remote LVDT mounted on the actuator. Three string pots were attached to the backside (opposite the punch) surface of the test specimen. These three string pots were all in a line with the middle location in the center of the punch and the two outer locations at the circumferential periphery of the punch. This provided additional measurements of the backside deformation opposite the punch on the front of the panel. Load was also measured from the load cell on the servo-hydraulic test frame. Tests were performed in displacement control at an applied rate of 1 inch/minute. The multiple data channels were recorded with a custom data acquisition system operating at 10 Hz. This typically provided total data files of anywhere from 500-2000 points.

The test series used for the validation of the TC128B constitutive and failure model was performed on 0.488-inch-thick plate specimens with various combinations of ram and manhole diameters (McKeighan, 2007d). The three tests performed used the 1.0, 1.5, and 2.0-inch diameter punches in combination with the 2.5, 3.0, and 3.5-inch diameter manhole covers, respectively. Photographs of the specimen failure behavior in these punch tests are shown in

Figure 43. In all cases, the punch test sheared out a plug of material with a diameter approximately equal to the punch diameter.

An example of a model and simulation of a punch test on a 0.488-inch-thick TC128B plate is shown in Figure 44. The corresponding comparison of measured and calculated punch force-displacement curves for a series of three different tests on the TC128B plate is provided in Figure 45. In addition to the force-deflection curve the final profile of the plate specimens after the punch tests were digitized and compared to the analyses. A representative profile comparison is shown in Figure 46.

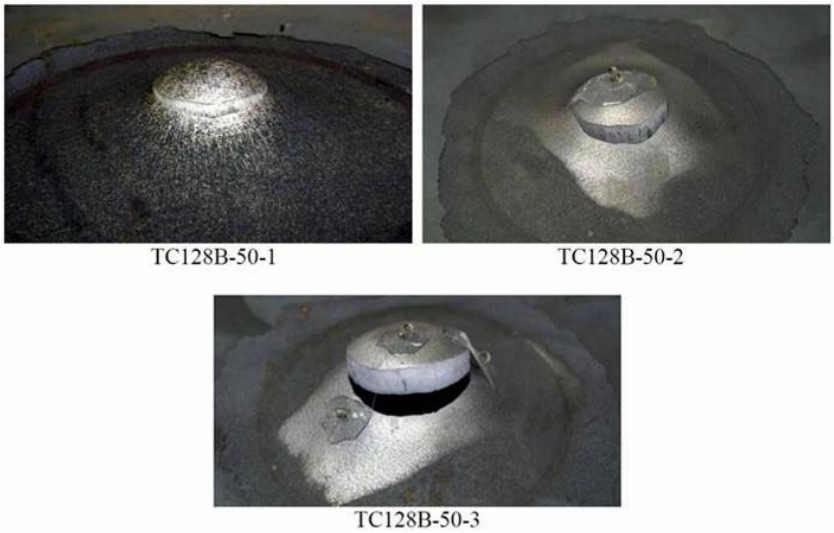

Figure 43. Punch test failure mode for the thin TC128B plate material.

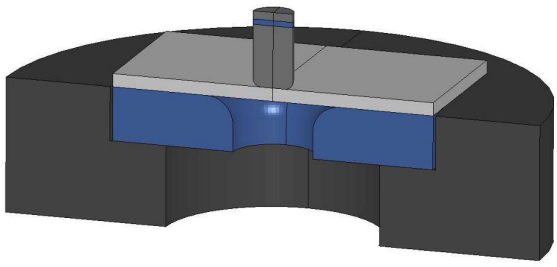

(a) Cross section of punch test geometry

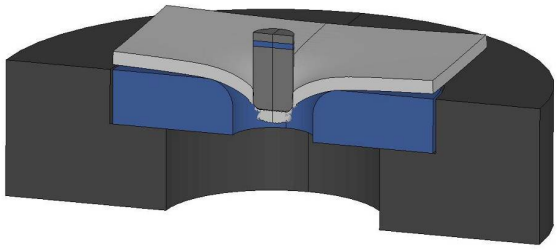

(b) Punch test response

Figure 44. Simulation of the punch test on the thin TC128B plate material.

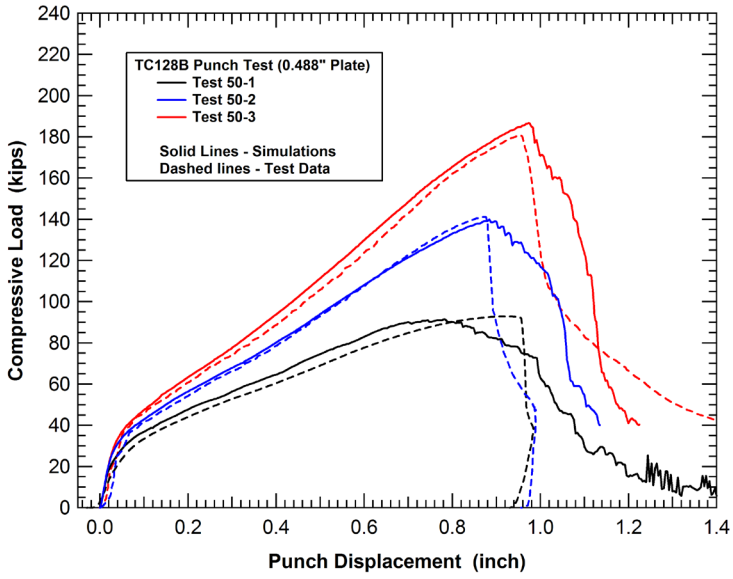

Figure 45. Force-deflection curves for three punch test configurations on TC128B.

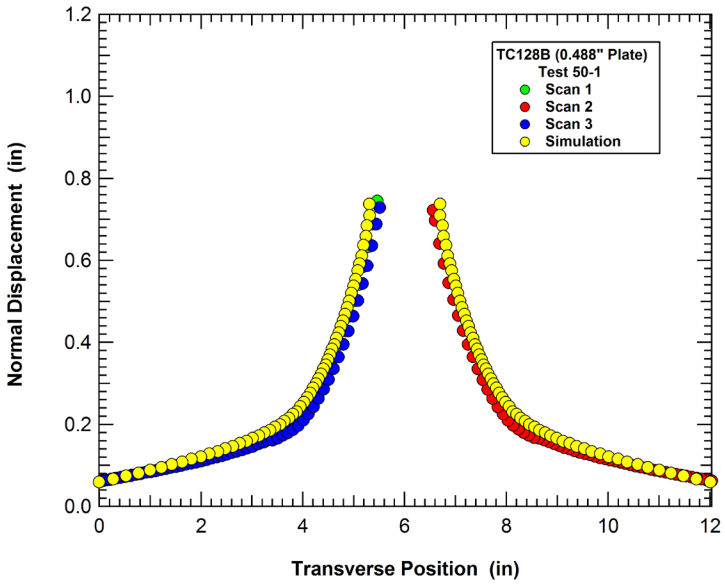

Figure 46. Comparison of the calculated and measured punch test plate profile.

The agreement of the measured and calculated behaviors for this punch test provides an additional validation that the BW failure model is appropriate for predicting puncture of the tank cars. The application of the failure model for assessing puncture energies for different tank geometries and impact conditions is provided in the following section of this report.

2.5 Cryogenic 304 Stainless Steel Material Properties

Assessing the puncture resistance of the DOT-113C120W9 tank car in LNG service requires the development of a constitutive model for the 304 stainless steel (SS) material at cryogenic LNG temperatures. A materials characterization testing program was previously performed for A240

304 SS at LNG temperatures (-260F, 110K) as part of the research supporting a Natural Gas Fuel Tender (NGFT) technical specification (Kirkpatrick, Wagner, & Northrup, 2019). This data is summarized here and applied to develop the constitutive model for 304 SS at LNG temperature required for the DOT-113C120W9 LNG tank car analyses.

Prior to performing the puncture assessment of the LNG tank car, the DOT-113C120W9 tank car puncture model was validated by analysis of the full-scale impact test on a DOT-113 tank car (Test 13) (FRA, 2022). This test was performed with liquid nitrogen as a surrogate lading at a colder cryogenic temperature (-321F, 77K). In preparation for this test, a corresponding series of material characterization tests was performed under FRA sponsorship at the colder liquid nitrogen cryogenic temperature (Wilson, Carolan, Trevithick, & Eshraghi, 2021). For analysis of the full-scale impact test, an additional material model was developed for the 304L stainless steel using this material data set.

As part of the characterization test program for A240 304 SS at LNG temperatures (-260F, 110K), tests of tensile and notched tensile behaviors were performed at quasistatic rates (0.0005/s) and tensile testing was performed at various elevated rates (0.01/s-10/s). Similarly, the test program on 304 SS at the colder Liquid Nitrogen cryogenic temperature (-321F, 77K) included tensile and notched tensile tests performed at quasistatic rates (0.0005/s) and at various elevated rates (0.05/s-16/s). Both sets of data showed a trend where there were significant effects of strain rate between the quasistatic test rate (0.0005/s) and a relatively low strain rate of 0.05-0.10/s. At higher rates there was much less strain rate sensitivity. As a result, three separate constitutive models were developed:

1. A model for A240 304 SS at LNG temperatures (-260F, 110K) and quasistatic rate (0.0005/s). The model was developed at this strain rate since it was the only consistent set of tests including the notched tensile test required to develop the BW failure model.
2. A model for A240 304 SS at LNG temperatures (-260F, 110K) and elevated rate (0.10/s). The model will be used in the evaluation of the puncture resistance for the DOT-113C120W9 tank car in LNG service.
3. A model for A240 304 SS at liquid nitrogen cryogenic temperatures (-321F, 77K) and elevated rate (0.50/s). The model will be used in the evaluation of the full-scale impact Test 13 used to validate the puncture model for the DOT-113C120W9 tank car.

2.5.1 Constitutive Model for A240 304 SS at LNG Temperature

A characterization test program was performed on A240 304 stainless steel at LNG cryogenic temperature. The testing found that the behavior was similar to those used from literature sources for cryogenic 304L stainless steel [(Kim, Kang, Kim, & Lee, 2012), (Blandford, Morton, Snow, & Rahl, 2007)]. Overall, the testing of the material produces strength and ductility properties that would result in a high puncture resistance for this material at cryogenic temperatures compared to other tank car steels.

The material characterization test program included longitudinal and transverse tensile tests, notched round bar tensile tests, and longitudinal tensile tests at elevated strain rates. The objective was to perform three repeat tests at each condition to assess repeatability of results. The tensile data for the A240 304 at -260F and various strain rates is shown in Figure 47. The

quasistatic testing has a strain rate of approximately 0.0005 (in/in)/s. The elevated rate testing was performed using strain rates of 0.01, 0.1, 1.0, and 10.0 (in/in)/s. The testing was performed to ASTM E8/E8M − 16a standard test methods for tension testing of metallic materials using the specimen geometries shown in Figure 48 (Wakulchik, 2017). The stress-strain behaviors show a yield strength on the order of 100 ksi and an ultimate of approximately 195 ksi for the A240 304 material at quasistatic rates.

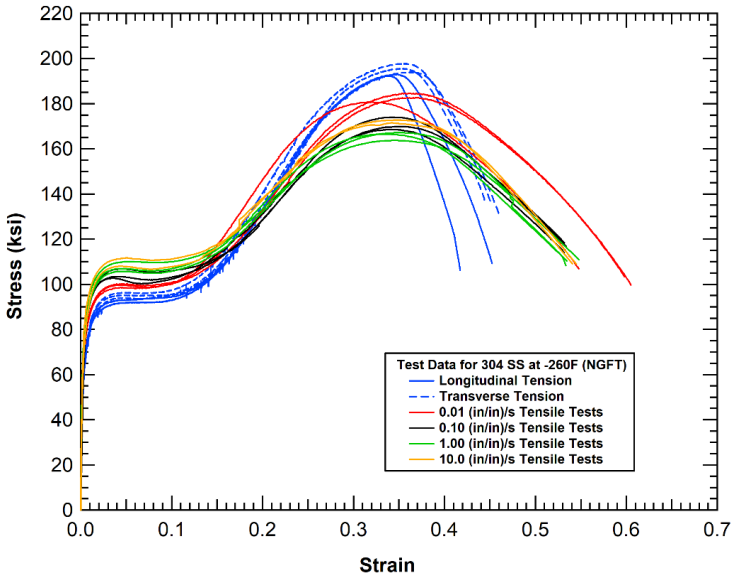

Figure 47. Comparison of the engineering tensile data for A240 304 SS at LNG temperature.

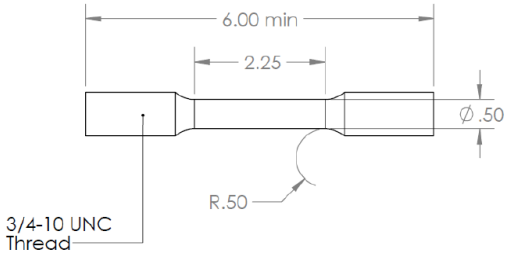

(a) ASTM E8 specimen geometry used in the quasistatic tensile testing

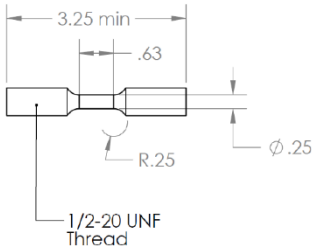

(b) Specimen geometry used in the elevated strain-rate testing

Figure 48. Specimen geometry used for the quasistatic and elevated strain-rate tensile tests.

Increasing the loading rates results in an increase in the yield strength and a reduction in the ultimate strength. The elongation at the ultimate strength is similar for all the strain rates. The additional elongation after the ultimate stress for the high-rate tests is most likely a result of the smaller 0.5-inch gauge length in the high-rate tests compared to the 2.0-inch gauge length in the quasistatic tests. As a result, the necking behavior would produce a greater engineering elongation for the shorter gauge length measurements. At or above a loading rate of 0.1 (in/in)/s the stress-strain response is reasonably consistent. As a result, the tensile data at this rate was used to develop the constitutive model for the DOT-113 tank puncture analyses.

Baseline Constitutive Model Development

The baseline constitutive model for the puncture performance assessment of the DOT-113 tank was developed based on testing of different samples of the A240 304 at -260F (110K) and a loading rate of 0.1 (in/in)/s. The model is developed by first converting the engineering stress-strain data to true stress and strain and then fitting these data with a piecewise linear curve, as shown in Figure 49. The procedure followed was previously described in Section 2.2. The resulting piecewise linear constitutive model was then applied to simulate the tensile test and compared back to the engineering data to confirm the material model properties. The model accurately reproduces the tensile behavior including necking and failure as shown in Figure 49.

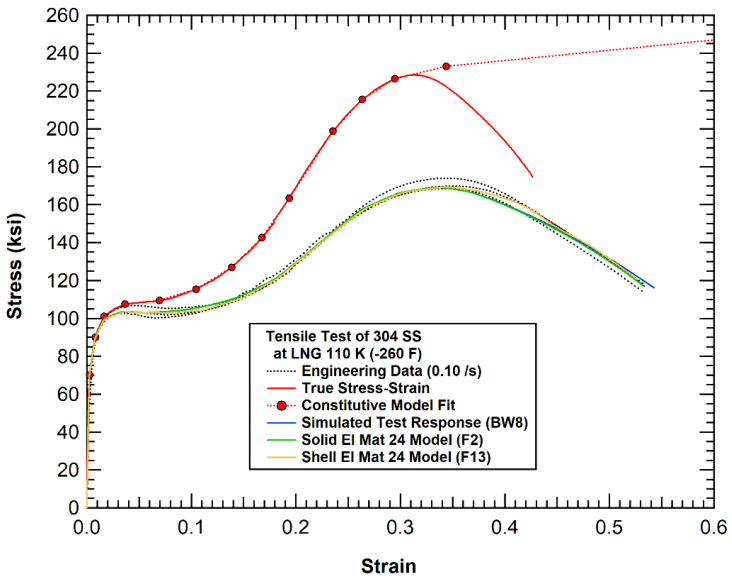

Figure 49. Constitutive model fit and tensile test validation for A240 304 SS at 110K (0.10/s).

The BW failure surface for the baseline model was adapted by using a previous BW failure surface for stainless steel and scaling the damage parameters proportionally to match the tensile test results. Normally, we would apply notched tensile tests to better define the shape of the BW failure surface. However, in this case, the notched tensile tests were performed on the material at the quasistatic loading rate instead of the elevated 0.1 (in/in)/s loading rate. To further investigate the potential effects of this assumed failure surface, a similar model was developed based on the quasistatic tensile data and applied to simulate the notched tensile test data.

Quasistatic Constitutive Model Development

The comparison of the quasistatic smooth tensile and notched tensile data for the A240 304 SS material at LNG cryogenic temperature is shown in Figure 50. The drawings of the specimen geometries used in the notched tensile testing are shown in Figure 51. Since the notch increases the stress triaxiality in the gauge section it results in an increase in the yield and ultimate strength, as expected. The testing used a 1.0-inch gauge length extensometer bridging the notch, but the deformation will not be uniform within this gauge section due to the presence of the notch. As a result, the overall engineering elongation for these tests are reduced compared to the smooth round bar tension tests. However, the measured elongations of approximately 25 percent are quite large for this type of testing on typical tank car steels.

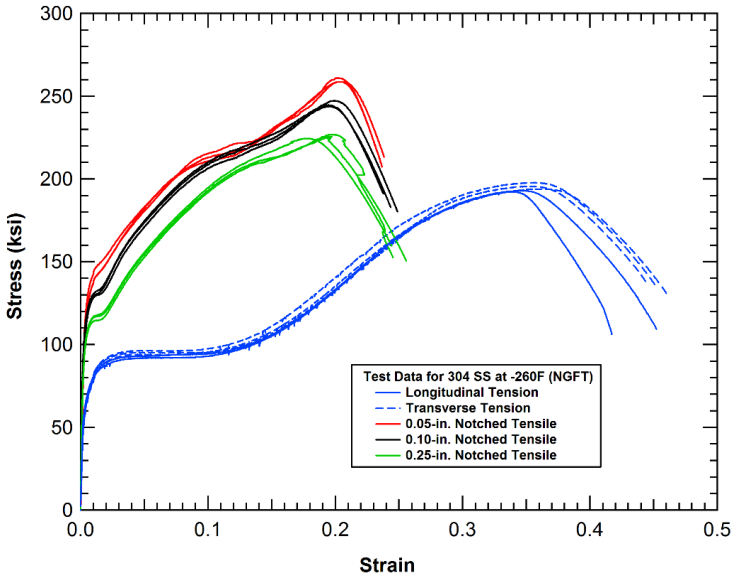

Figure 50. Summary of the 304 stainless quasistatic tensile test data at 110K (0.0005/s).

The constitutive model for the investigation of the stress triaxiality effects was developed based on testing of different samples of the A240 304 at -260F (110K) and the quasistatic loading rate of 0.0005 (in/in)/s. The piecewise linear true stress-strain curve for the quasistatic material constitutive model was developed and applied to simulate the tensile test using the same approach as in the baseline model. The model accurately reproduces the tensile behavior including necking and failure as shown in Figure 52.

The quasistatic constitutive model was then applied to investigate the performance of the model at various levels of confinement (stress triaxiality) by simulating the notched tensile tests. The comparison of the measured and simulated engineering stress-strain behaviors for the tensile and notched tensile tests are compared in Figure 53. The model is seen to match the shift in the stress-strain curves caused by the increase in stress-triaxiality but underpredict the failure loads and ductility of the notched tensile test. The comparison was considered to be acceptable since it would result in conservative estimates for failures in zones with elevated stress triaxiality. In addition, previous studies have shown that the punctures typically initiate at the inner surface of the tank with triaxialities that are similar to those in the tensile test.

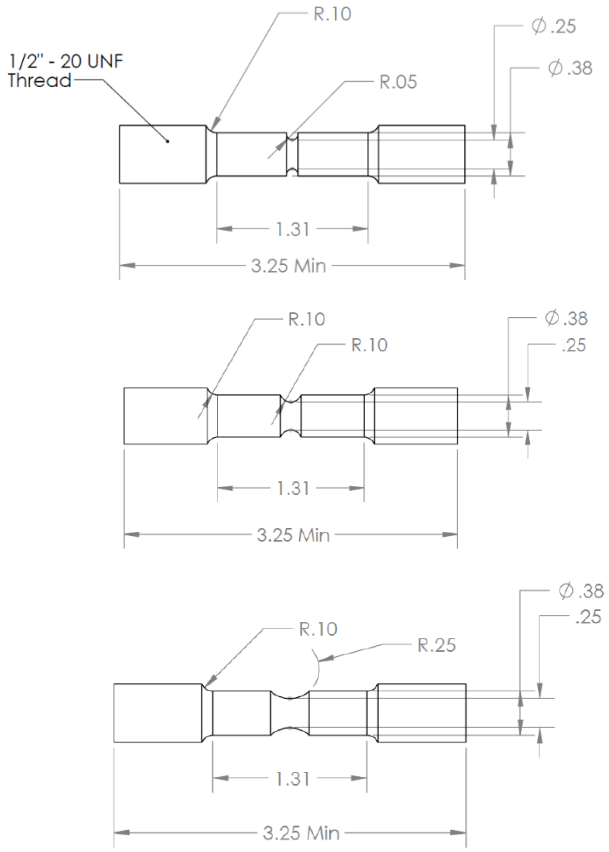

Figure 51. Notched specimen geometries used in cryogenic stainless-steel testing.

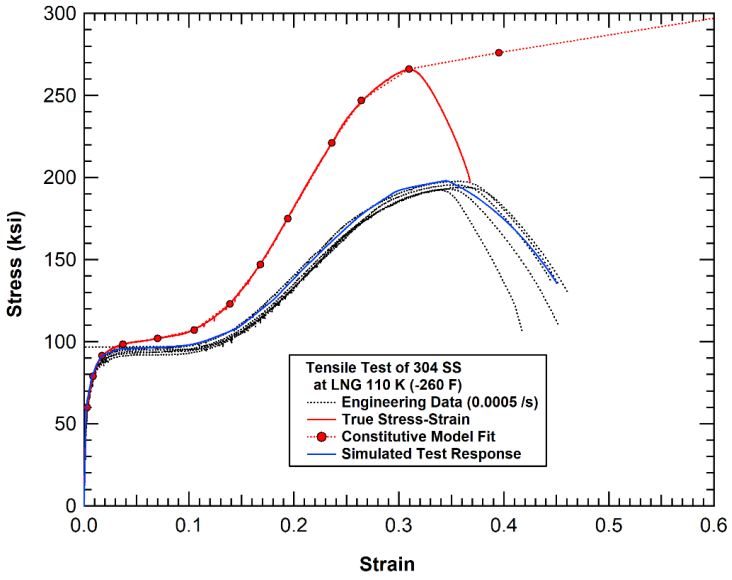

Figure 52. Constitutive model fit and quasistatic tensile test validation for T304 SS at 110K (0.0.005/s).

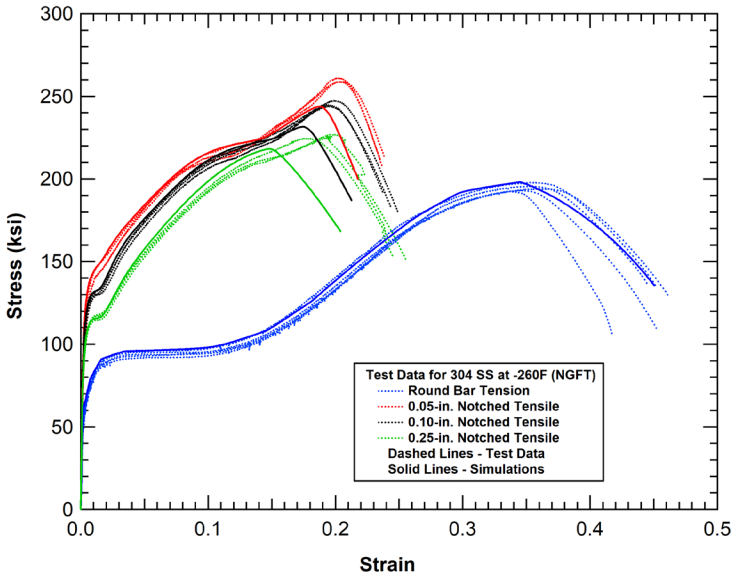

Figure 53. Constitutive model validation for quasistatic T304 SS at 110K (0.0005/s).

2.5.2 Constitutive Model for A240 304 SS at Liquid Nitrogen Temperature

The final constitutive model for A240 304 stainless steel was developed for the validation analysis of the full-scale impact test on a DOT-113 tank car (Test 13) (FRA, 2022) performed with liquid nitrogen as a surrogate lading at a colder cryogenic temperature (-321F, 77K). The material characterization tests were performed under FRA sponsorship at the colder liquid nitrogen cryogenic temperature (Wilson, Carolan, Trevithick, & Eshraghi, 2021). A comparison of the engineering stress-strain data for a range of strain rates is shown in Figure 54. The quasistatic loading rate was again 0.0005 (in/in)/s and the elevated rate testing was performed using strain rates of 0.05, 0.5, 5.0, and 16.0 (in/in)/s. As seen in the previous test series, increasing the loading rates results in an increase in the yield strength and for this test series a significant reduction in the ultimate strength.

At the highest strain rates in this test series, the strain response is not smooth and a significant reduction in the strain levels during strain hardening and failure was observed. However, the corresponding comparison of the force-displacement behaviors, shown in Figure 55, show no indication of this effect. Therefore, the likely cause of the reduced stains at high loading rates is slipping of the extensometer and should be neglected. Comparisons of the stress-strain and force-displacement behaviors for the elevated rate data between 0.05 and 16 (in/in)/s show a relatively consistent behavior and strengths. Based on the responses measured, the data at 0.50 (in/in)/s. was selected for the constitutive model development. At this loading rate, good quality engineering stress-strain data measurement were still recorded.

The constitutive model for the validation analyses of the full-scale Test 13 conditions was developed based on testing of different samples of the A240 304 at -321F (77K) and the loading rate of 0.50 (in/in)/s. The piecewise linear true stress-strain curve for the quasistatic material constitutive model was developed and applied to simulate the tensile test using the same

approach as in the baseline model. The model accurately reproduces the tensile behavior including necking and failure as shown in Figure 56.

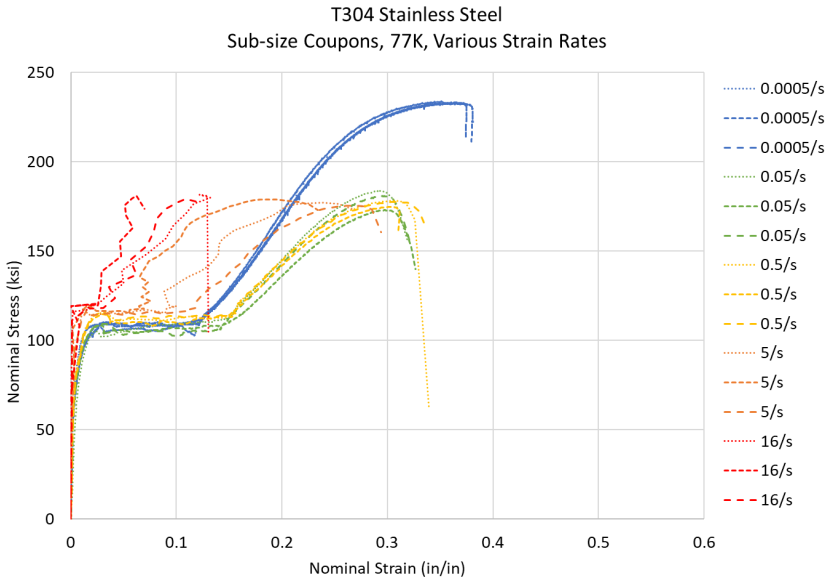

Figure 54. Engineering stress-strain data for T304 SS at 77K at different strain rates (Wilson, Carolan, Trevithick, & Eshraghi, 2021).

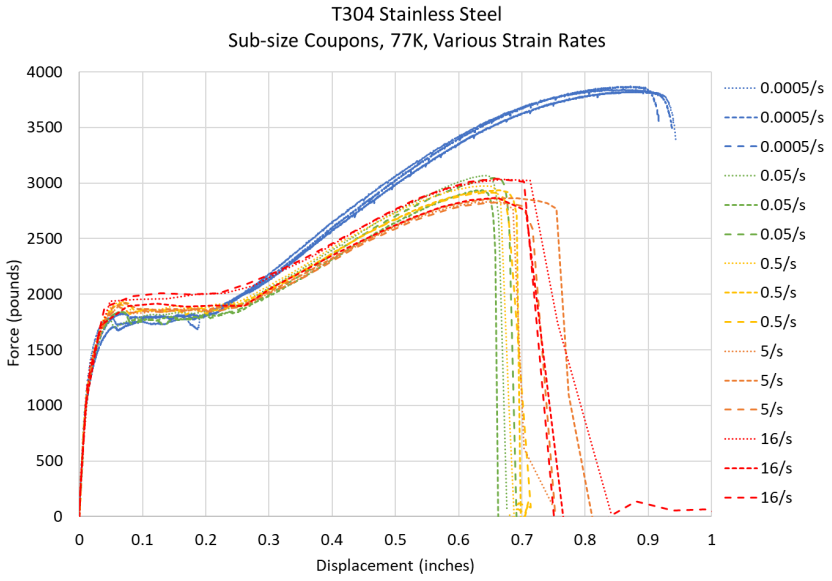

Figure 55. Force-displacement data for T304 SS at 77K at different loading rates (Wilson, Carolan, Trevithick, & Eshraghi, 2021).

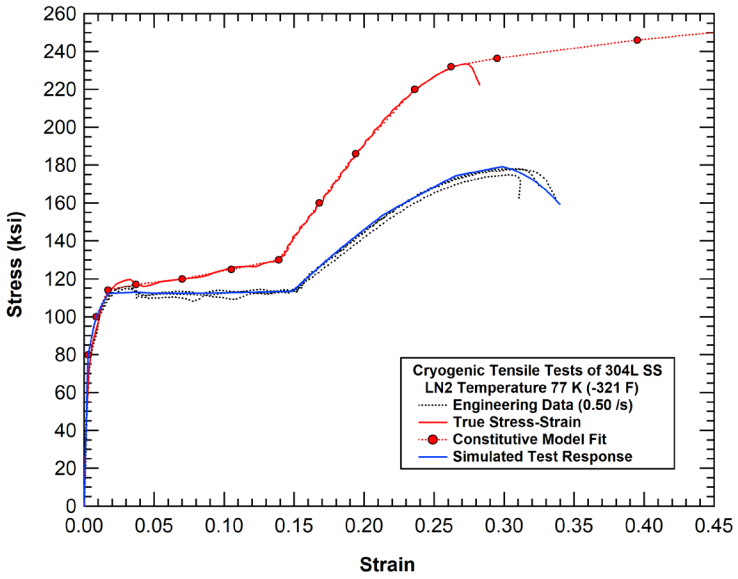

Figure 56. Constitutive model fit and tensile test validation for T304 SS at 77K (0.50/s).

3. Analysis of Different Size and Shape Impactors

3.1 Introduction and Background

In this section, the detailed BW failure model described in Section 2 is applied to assess various tank and head puncture conditions. The analyses in this section are focused on the two primary impact configurations studied in the NGRTC program of a normal side impact centered on the tank and an offset head impact with the impact point offset approximately 29 inches vertically downward from the center of the head. However, in this section we expand the range of impactors used in these scenarios to include a wide range of different sizes and shapes.

3.1.1 Puncture Analysis Methodologies

The baseline failure models use a fine mesh of solid brick elements in the impact zone with an element dimension of approximately 0.040 inch (1 mm). The mesh transitions to shell elements outside the impact zone with increasingly mesh coarseness. The model of the commodity tank and BW impact zone mesh used in the tank shell puncture analyses is shown in Figure 57. An algorithm in LS-DYNA is used to tie the edge of the shell elements to the solid elements around the edge of the impact zone.

As a result of the very fine mesh in the impact zone, the puncture models were significantly larger and have correspondingly longer run times. To allow for the evaluation of a wide range of impact conditions and tank geometries, some simplifications in the tank model were implemented.

The first simplification was the use of symmetry planes. For the majority of side impact analyses described in this section, two symmetry planes were used to reduce the model to one-quarter of the full tank (a half model was used for the offset head impacts). This had a small effect since some tank car structural details could not be included in the quarter model (e.g., manway and bolsters). The primary effect of this approximation was that a side impact centered on the tank may have a slightly reduced stiffness for large dent sizes since the manway and surrounding structures are stiffer than the bare commodity tank.

The head puncture modeling approach was identical to that of the tank side impact puncture analyses. The head impacts analyzed matched the NGRTC Test 1 impact condition (impact point offset below the tank head center). As a result, the problem had only 1 symmetry plane running vertically through the test specimen. This symmetry plane was used in most of the head impact simulations to reduce the model size by one half compared to the full head model. An example model of a tank head and BW impact zone mesh used in the head puncture analyses is shown in Figure 58.

Another simplification in the tank puncture model was in the modeling approach used for the fluid lading. In the preliminary analyses an explicit model was used for the lading. However, this explicit model required a significant increase in the model size and was not ideally compatible with a quarter symmetry model. An alternate modeling approach was to smear the weight of the lading uniformly into the commodity tank wall. A comparison of the full tank car impact response using the two different lading modeling methodologies is shown in Figure 59. The comparison shows that the simplification of the smeared lading approach did not have a large

influence on the impact behavior. As a result, this approximation was applied for most analyses in this study.

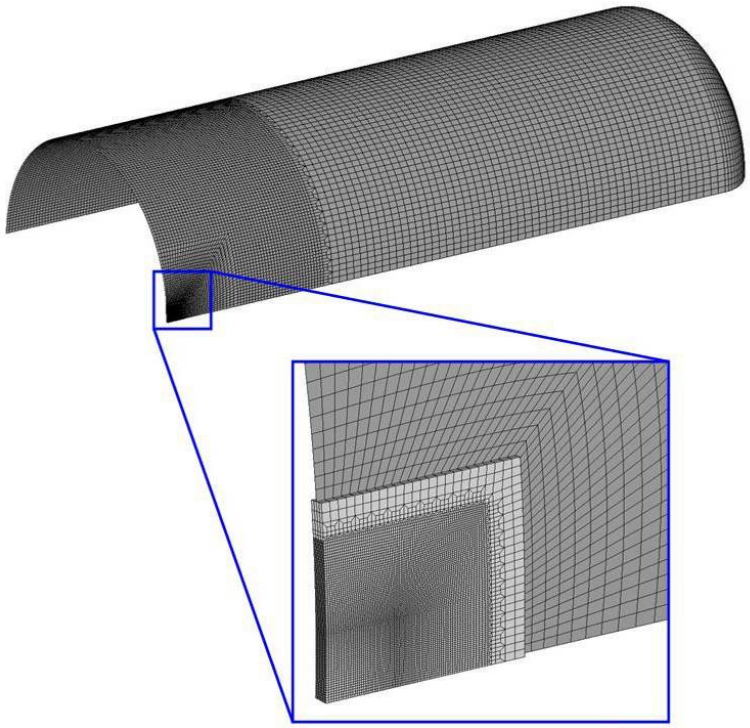

Figure 57. Tank model and impact zone mesh used for side impact puncture analyses.

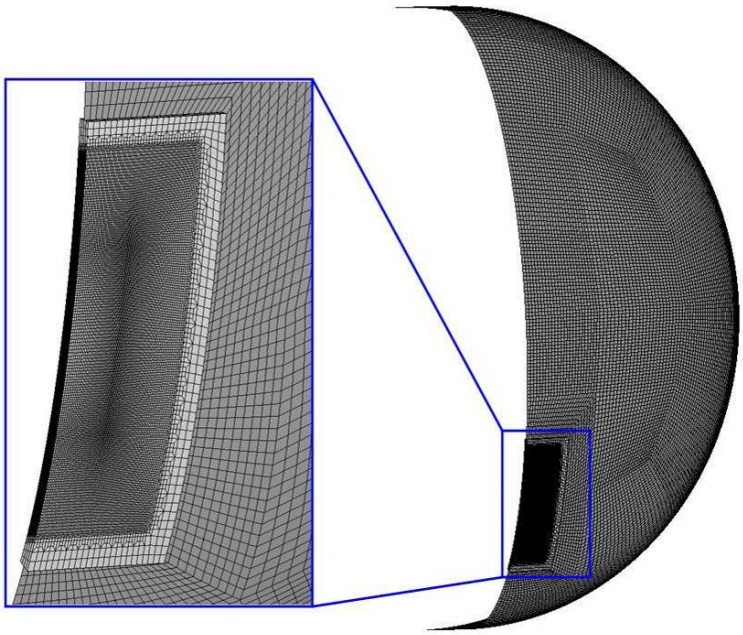

Figure 58. Tank head model and impact zone mesh used for the head puncture analyses.

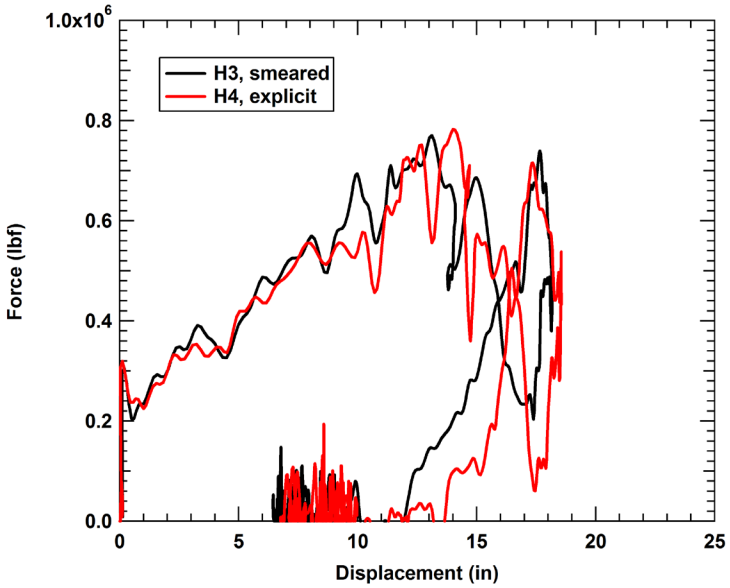

Figure 59. Calculated tank car impact behavior using two different lading models.

The final geometric simplification of the impact modeling was that the ram car was not used in the analyses. Instead, a rigid model of the ram head was used with the mass of the entire ram car. This was a reasonable simplification since the measurements of ram car acceleration at distributed measurement locations were all in good agreement.

Analysis of Tank Pressure Effects

The constant internal pressure modeling approximation used in the majority of the NGRTC analyses was found to introduce significant errors for larger impactor sizes. In the NGRTC chlorine tank car analyses the internal pressure was a constant 100 psi. However, with the formation of the dent in the tank during impact there will be an increasing hydrostatic internal pressure level. For the 6-inch impactor this increase in pressure was relatively small (10-15 percent). However, the larger dents produced by the larger impactor sizes would result in a larger internal pressure increase.

To demonstrate the influence of the variable internal pressure during the impact a series of analyses was performed. In these analyses, a control volume was established for the tank and the change in volume was used to calculate a corresponding change in pressure. The assumption in these analyses is that the tank has a 10.6 percent outage and the gas in the outage follows an ideal constant temperature compression behavior during impact. The resulting relationship between the relative volume and pressure in the tank is shown in Figure 60.

The force-deflection curves with both constant and variable internal pressure for the 500 lb Cl tanks and the three different impactor sizes are shown in Figure 61. For the updated analyses with the variable pressure, the impact velocities were also reduced by 5 mph to be closer to the expected puncture threshold velocity. Adding variable pressure to the model results in a stiffening of the later portions of the force-deflection curve and a reduction in the ram displacements prior to the tank puncture. The reductions are more significant for the larger ram sizes. This is expected since the larger rams have larger displacements prior to the puncture with

a larger associated pressure change inside the tank. The comparisons show that the variable internal pressure does not have a significant influence on the puncture forces but does reduce the puncture energies by approximately 25-30 percent in the analyses with the 9x9 and 12x12 inch impactors.

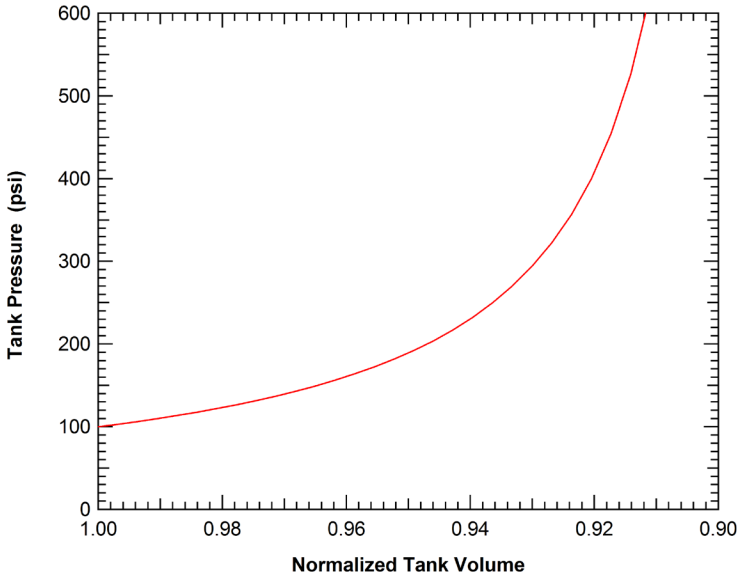

Figure 60. Pressure-volume relationship used for the tank control volume (10.6% outage).

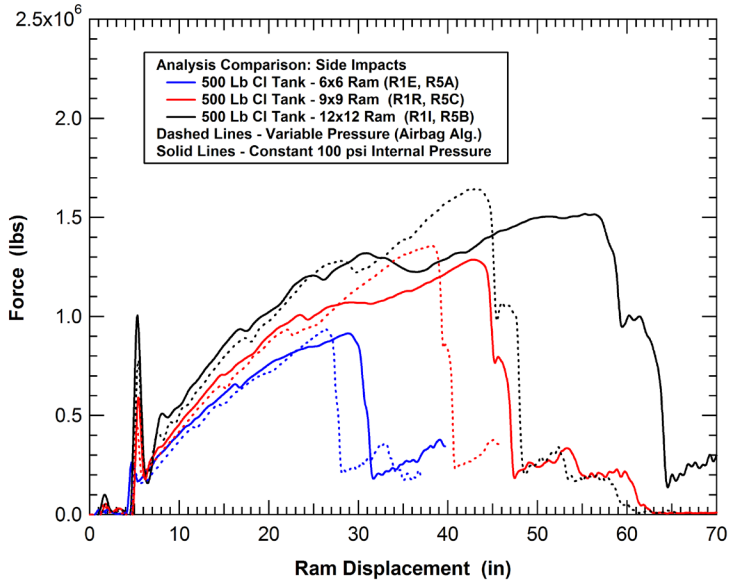

Figure 61. Effect of variable internal pressure on 500 lb tank impact response.

The control volume pressure histories for the three 500 lb Cl tank impact analyses are plotted as a function of the ram displacement in Figure 62. In the 6x6 inch impactor analysis the pressure change is less than 10 percent and the previous approximation of a constant 100 psi internal pressure is a reasonable simplification for the analyses. For the 9x9 and 12x12 inch impactors,

the internal pressures increase to approximately 120 psi and 140 psi, respectively, at the point of the puncture initiation. These pressure increases are becoming sufficiently large to influence the tank effective stiffness during the impact.

The simulation of the NGRTC Test 2 impact conditions using the tank puncture model and variable internal pressure is shown in Figure 63. The model shown was reflected vertically about the symmetry plane (seen as a line in the figure) for improved visualization of the impact behavior. The impactor in this analysis was a rigid 6x6 inch ram with a 0.5-inch radius around the edges and a total weight of 286,000 lbs. The small rectangular patch of elements under the impactor (already punctured in Figure 63) is the fracture zone where the BW failure model was applied. The remainder of the tank structure was again modeled with 4-node shell elements and a tied shell-to-solid constraint was used at the interface of the two model regions.

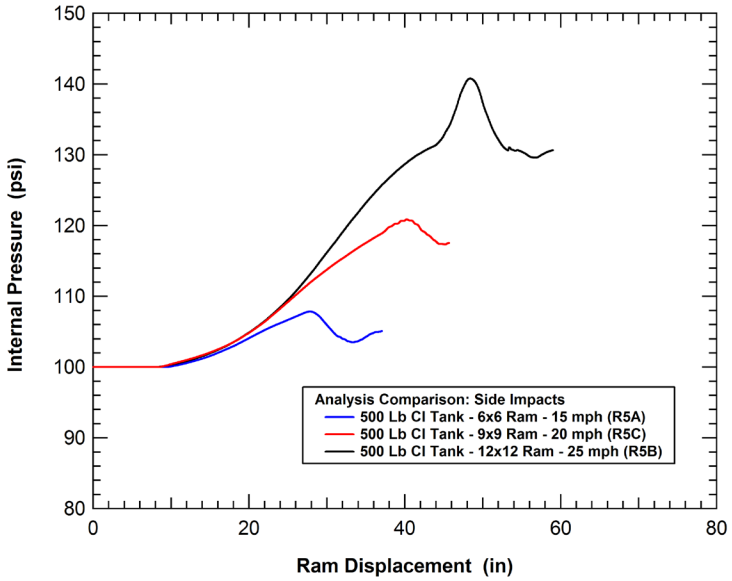

Figure 62. Calculated internal pressure variations in the 500 lb tank impact analyses.

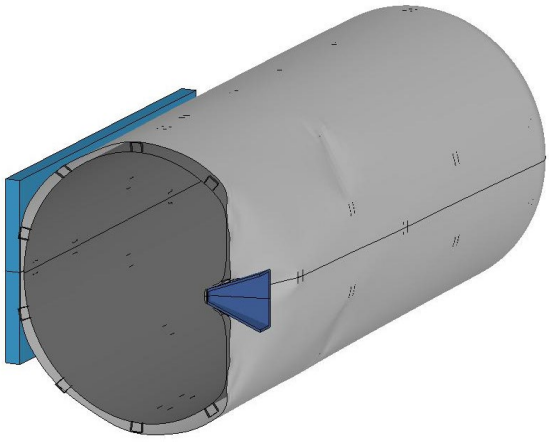

Figure 63. Simplified tank model analysis with Bao-Wierzbicki failure assessment.

The comparison of the measured and calculated force-deflection behavior for Test 2 with the tank puncture model is provided in Figure 64. The comparison shows overall good agreement between the calculation and test. The peak load at which the tank was punctured was very accurately captured by the model. The primary discrepancy of the test and model was a slightly more compliant behavior in the model at large displacements. This difference in compliance could primarily be attributed to the removal of the manway from the tank model.

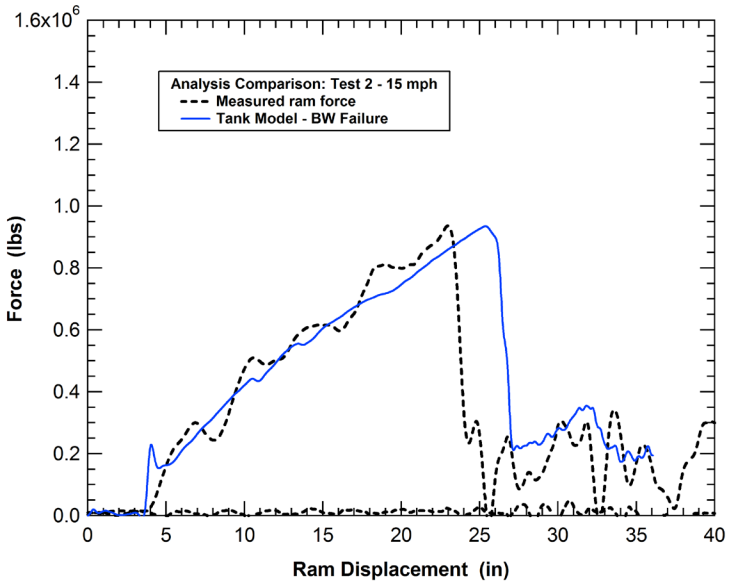

Figure 64. Comparison of the calculated and measured Test 2 impact and puncture behavior.

3.2 Side Impact Analysis of Different Size and Shape Impactors

The tank puncture model was used to assess the puncture energies for a wide range of impactor sizes and shapes. The tank design used in these analyses is the 105J600 chlorine tank car. The TC128B tank shell is 100 inches in diameter and 472 inches long with 2:1 ellipsoidal heads. The tank is covered by a 0.119-inch-thick A1011 jacket with a 4-inch standoff from the tank.

An example puncture response is shown in Figure 65. The analysis shown corresponds to the 600 lb Cl tank geometry (note: the 600 lb tank designation is used in the industry and refers to a tank with a 600-psi test pressure). The ram head model was updated in these analyses to include the tapered geometry used in the full-scale testing and an updated weight of 295,000 lbs. The tapered geometry included a 6x6 inch contact face but flared out to duplicate the ram geometry in the impact tests of the NGRTC program. Although the ram head was tapered in the analyses, the contact patch remained the 6x6 inch face until the protective layers and/or tank were punctured. As a result, the tapered geometry did not play a significant role in the prediction of the puncture energies reported in this report.

The progression of the fracture behavior in the BW failure patch is shown in Figure 66. The fracture initiated near the corners of the impactor and propagated initially along the side of the impactor face. The crack subsequently ran along the top and bottom of the ram face.

The energy balance for the 600 lb chlorine car impact is shown in Figure 67. The initial impact energy is approximately 4 million ft-lbs (all in the kinetic energy). As the impact progresses, the ram is decelerated, and the kinetic energy drops off. The energy transfer is from the kinetic energy of the ram to the internal energy of the tank (plastic deformations of the tank material) and the pressure-volume work caused by the indentation reducing the total tank volume. The internal energy of the tank at rupture is approximately one million ft-lbs and the pressure volume work is between 500,000 and 600,000 ft-lbs. The hourglass energy and sliding energy in the calculation are both negligible indicating that the calculation is stable and does not have any numerical energy losses.

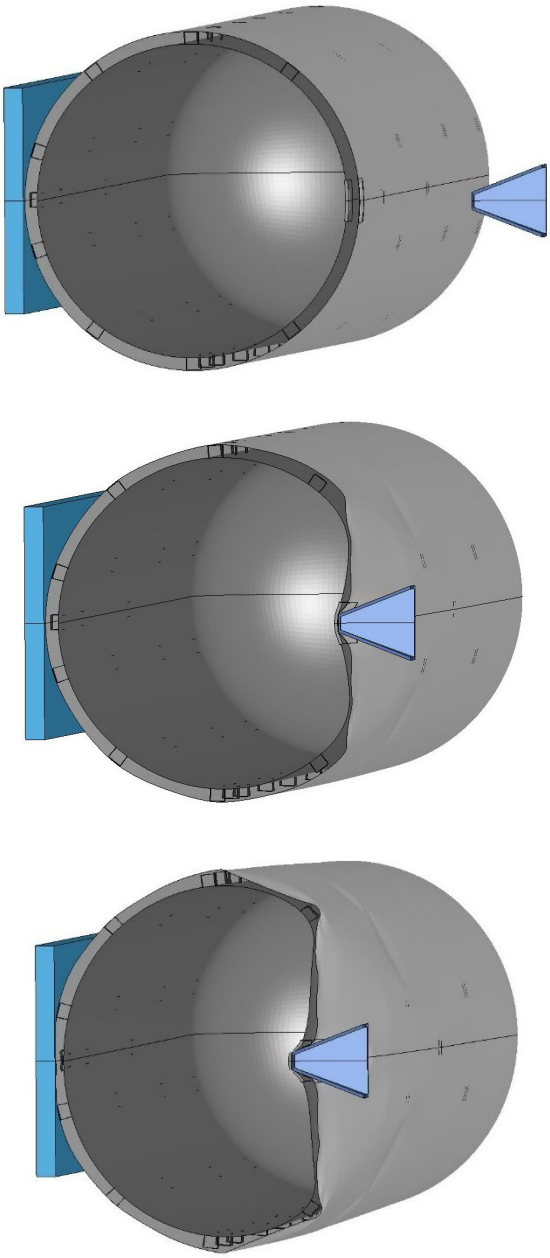

Figure 65. Detailed impact and puncture sequence for a 600 lb chlorine car.

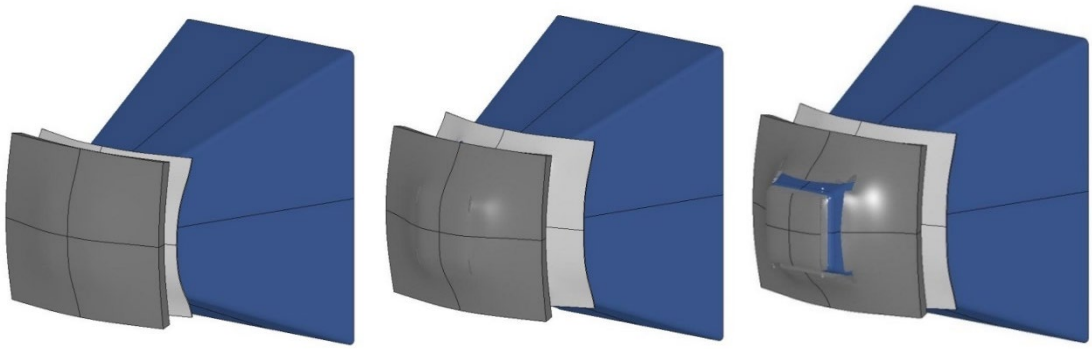

Figure 66. Calculated puncture initiation and fracture progression.

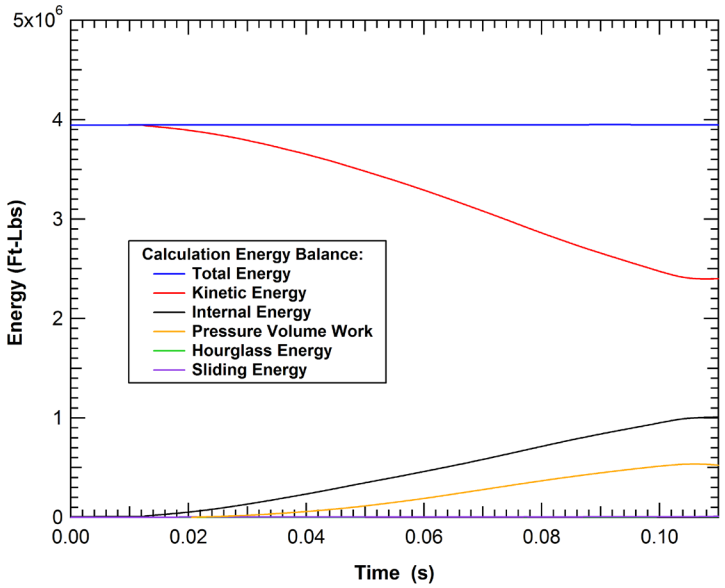

Figure 67. Calculated energy balance for the 600 lb chlorine tank car impact (R10F).

3.2.1 Effects of Impactor Size and Shape

A potential concern is that the selection of the 6x6 inch ram, as the primary threat used in the NGRTC program, will not identify the protection concept that provides the greatest benefit for impacts with a wide range of impactor types. To evaluate the effects of the ram impactor size and shape, analyses were performed on the 600 lb chlorine tank car being impacted by a range of impactors.

The first set of analyses used 3x3, 3x6, 6x6, 9x9, 12x12, 3x12, 12x3 rectangular impactors, all with a 0.50-inch radius around the edges. The models for the tank were similar but with changes in the BW impact zone to match the corresponding impactor face shape and size. The model of the commodity tank and BW impact zone mesh used in the 12x12 inch impactor analyses is shown in Figure 68. Again, the refined zone is maintained along the perimeter of the impactor face with a characteristic element dimension of approximately 0.040 inch (1 mm).

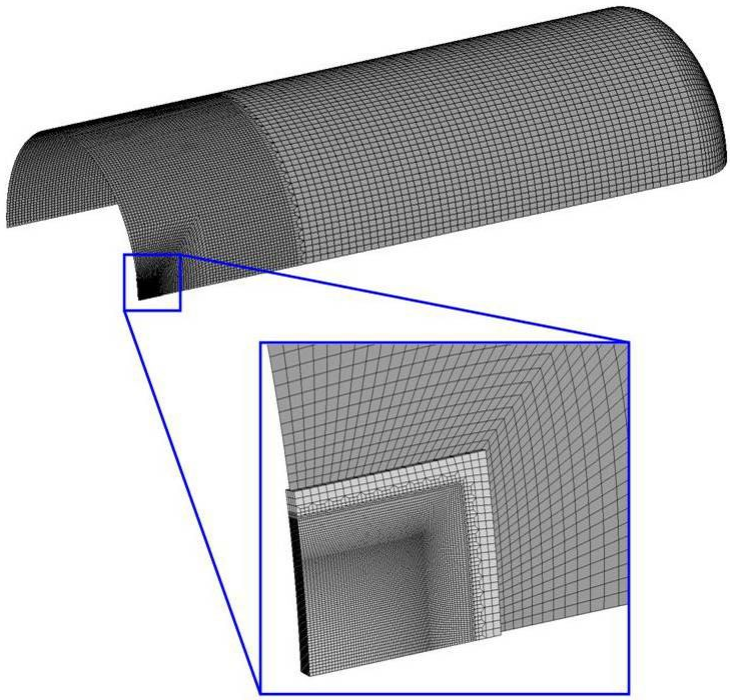

Figure 68. Tank model and impact zone mesh used for the 12x12 inch impactor.

The initial set of shell puncture analyses were performed with the square impactors. The models for the square impactors are shown in Figure 69. The comparison of the force-deflection behaviors and puncture energies with the 3x3-inch, 6x6-inch, 9x9-inch, and 12x12-inch square impactors is shown in Figure 70 (the puncture energy is obtained by integrating the force-deflection curve of the impact up to the point of the tank puncture). Note that higher impact speeds are used in the calculations as the impactor size is increased to achieve the higher puncture energies required. Since the impact behavior is relatively insensitive to impact speed (within a limited range), the impact velocities were not considered to be a significant factor in the comparison.

The calculated puncture behaviors in Figure 70 show progressively increasing puncture forces and puncture energies with increasing impactor size. Figure 71 shows a plot the puncture force for all the square impactor analyses correlated to the impactor perimeter length. The puncture forces show a nearly linear correlation with the ram perimeter length which is consistent with the punch shear failure mechanisms described in Section 1.3. The failure behavior can also be seen by the puncture of the ram through the tank shell BW impact zone as shown for the 3x3 and 12x12 inch impactors in Figure 72. Similar failure behaviors were seen for the 6x6 and 9x9 inch impactors. All the impactors punch out a section of the tank wall approximately equal in size and shape to the impactor face.

The second set of tank impact analyses performed used rectangular impactor face profiles to investigate the effects of the impactor aspect ratio. The additional impactors used were a 3x6, 3x12, and 12x3 impactors as shown in Figure 73. The results from these impact analyses are added to the puncture force versus ram perimeter length graph reproduced in Figure 74. The 3x6 impactor agrees well with the original linear correlation for the square impactors. However, the

3x12 and 12x3 impactors both puncture at a force level that is 100-200 kips below the linear correlation.

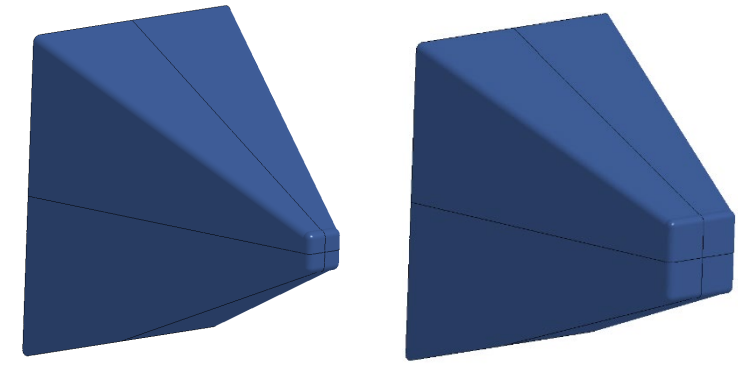

(a) 3x3 impactor **(b) 6x6 impactor**

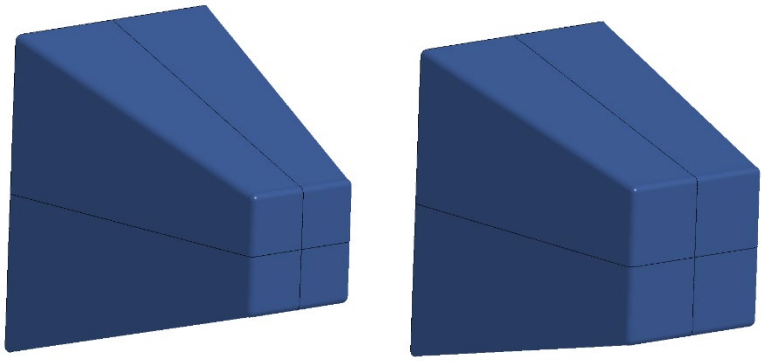

(c) 9x9 impactor **(d) 12x12 impactor**

Figure 69. Models of the different size square impactors.

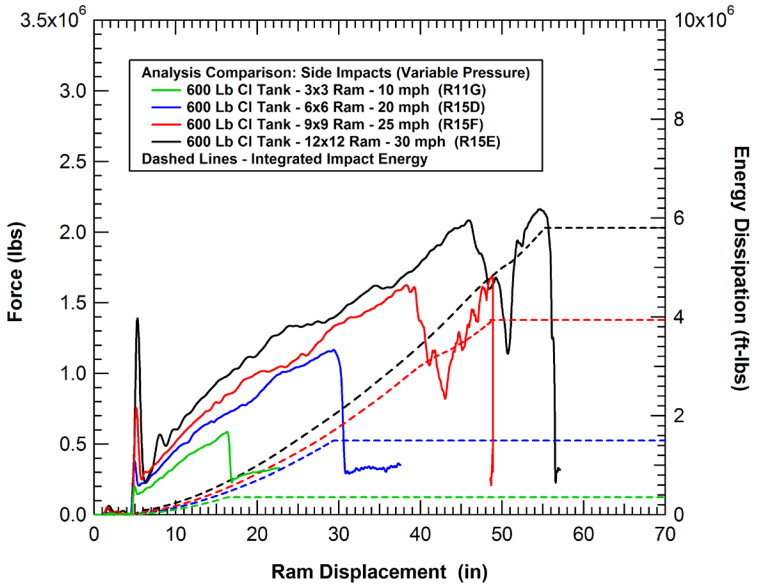

Figure 70. Updated 600 lb tank impact analysis with different size impactors.

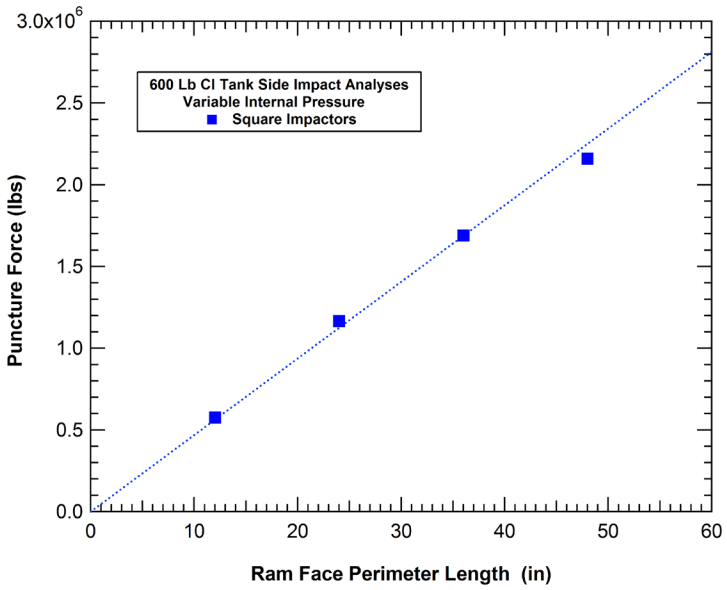

Figure 71. Puncture forces for the 600 lb tank impacts with different size impactors.

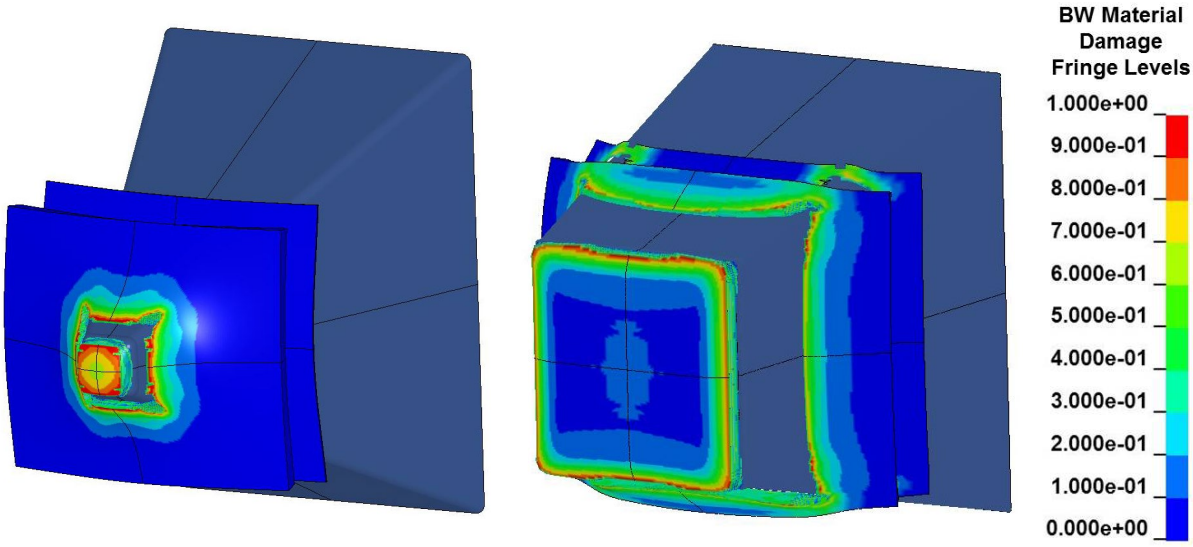

Figure 72. Calculated puncture behaviors (3x3 and 12x12 inch Impactors).

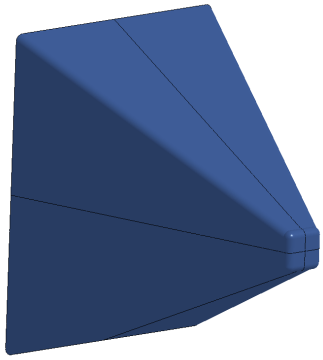

(a) 3x3 impactor

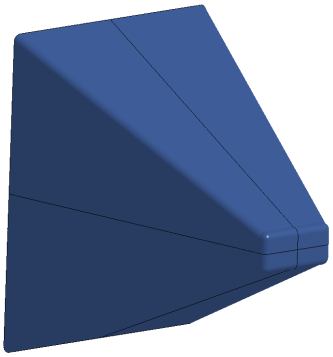

(b) 3x6 impactor

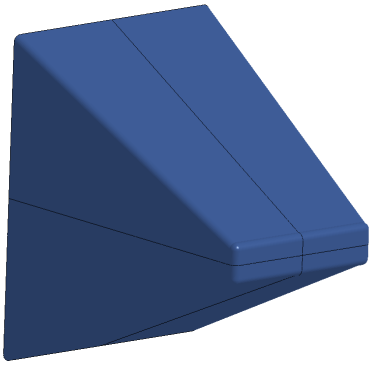

(c) 3x12 impactor

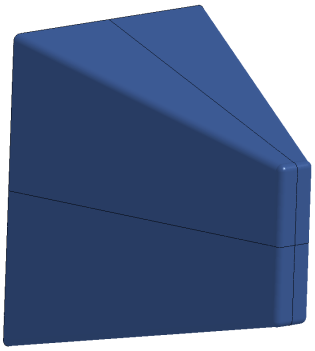

(d) 12x3 impactor

Figure 73. Models of the different size rectangular impactors.

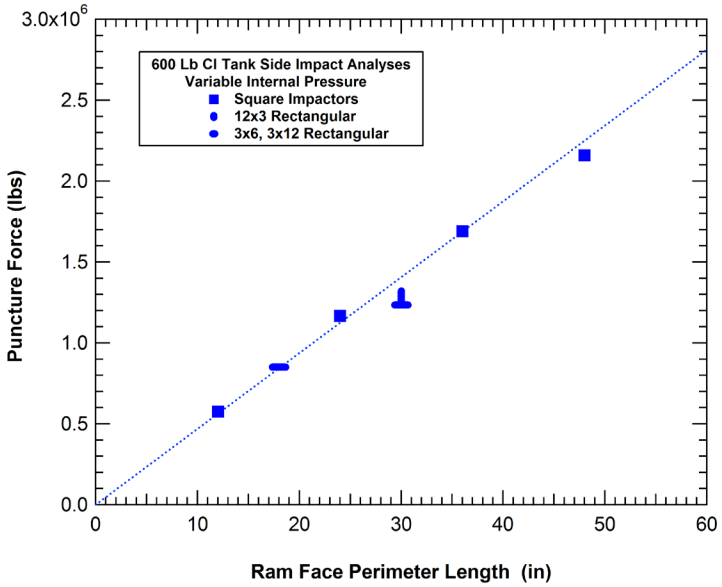

Figure 74. Puncture forces for the 600 lb tank impacts with different size impactors.

The calculated damage development in the tank wall prior to puncture is shown for the 3x3, 3x6, 3x12, and 12x3 inch impactors in Figure 75. An examination of the damage profiles explains the

reduction of the puncture force levels for the 12x3 and 3x12 impactors relative to the linear correlation. All the analyses develop stress concentrations and increased damage at the corners. However, for the larger aspect ratio impactors, the discrepancy is much larger between the maximum loading and damage at the corners and at the minimum locations along the middle of the long edges of the impact face. Thus, the long edges of the impactor do not effectively contribute to the puncture force resistance and the high aspect ratio impactors behave as if they were effectively smaller.

The third set of tank impact analyses performed used round impactor face profiles to investigate the effects of the impactor shape. The additional impactors used were a 5.73-, 7.64-, 9.55-, 11.46-, and 13.37-inch diameter impactors (ram face perimeter lengths of 18, 24, 30, 36, and 42 inch, respectively), as shown in Figure 76. The results from these impact analyses are added to the puncture force versus ram perimeter length graph reproduced in Figure 77. All the round impactor analyses predict puncture at a force level that is approximately 200 kips above the linear correlation.

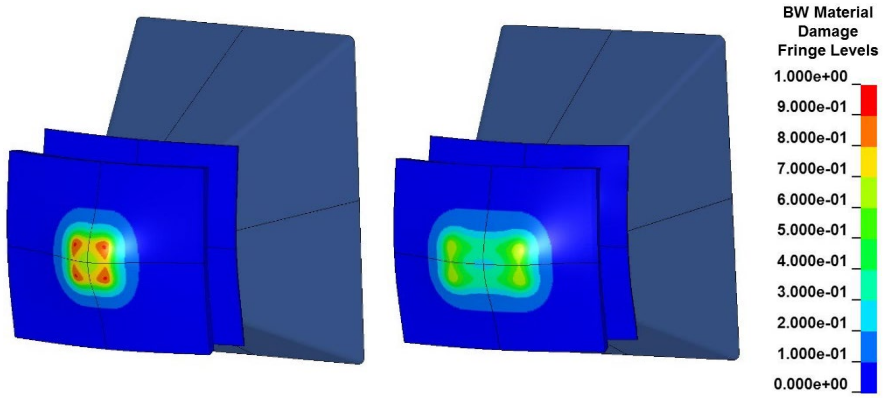

(a) 3x3 impactor **(b) 3x6 impactor**

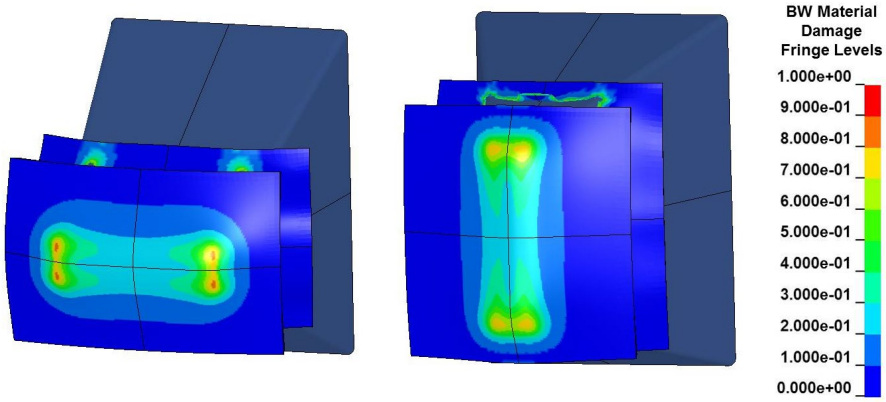

(c) 3x12 impactor **(d) 12x3 impactor**

Figure 75. Calculated puncture behaviors (3x3 and 12x12 inch Impactors).

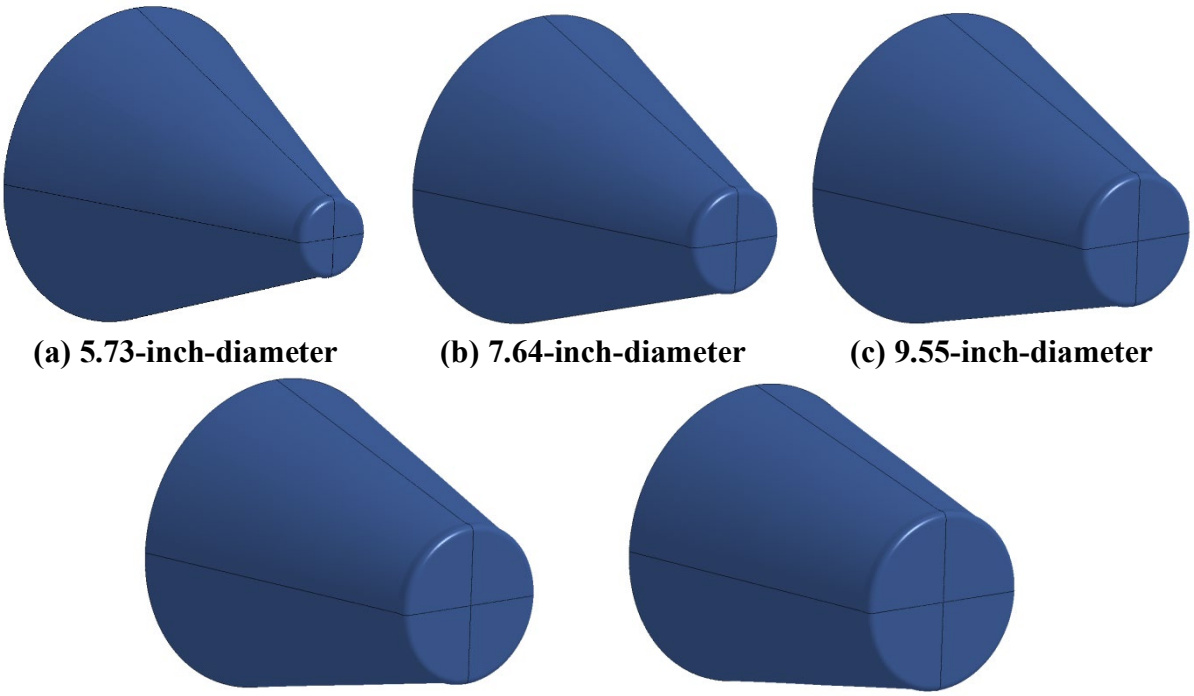

(a) 5.73-inch-diameter (b) 7.64-inch-diameter (c) 9.55-inch-diameter

(d) 11.46-inch-diameter impactor (e) 13.37-inch-diameter impactor

Figure 76. Models of the different size round impactors.

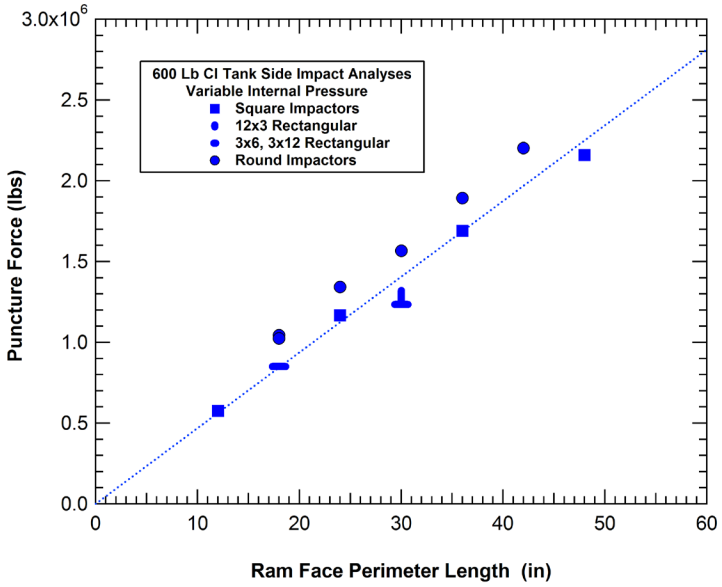

Figure 77. Puncture forces for the 600 lb tank impact analyses with different size and shape impactors.

The calculated damage development in the tank wall prior to puncture is shown for the 5.73- and 13.37-inch diameter impactors in Figure 78. An examination of the damage profiles explains the increase for the puncture force levels for the round impactors relative to the linear correlation. The round impactor analyses have very uniform loads and damage development around the

impact face perimeter with no significant stress concentrations. Thus, the round shape of the impactors maximizes the contribution of the entire perimeter to the puncture force resistance.

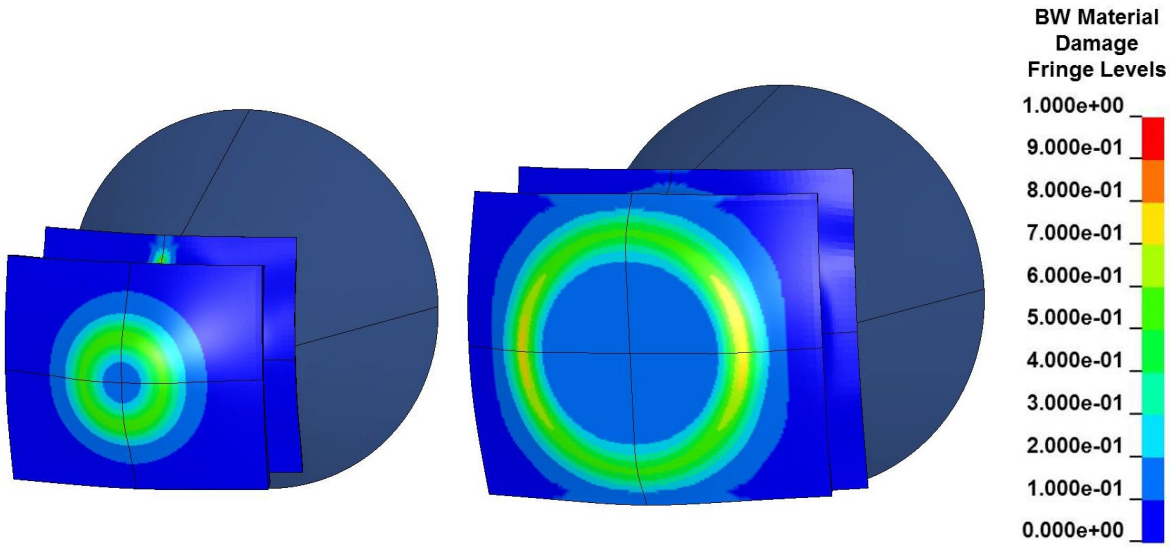

(a) 5.73-inch-diameter impactor (b) 13.37-inch-diameter impactor

Figure 78. Calculated puncture behaviors for different size round impactors.

3.2.2 Definition of the Impactor Characteristic Size

A summary of the above analyses of side impact puncture behaviors for various size and shape impactors is provided in Table 2. The analyses show that the puncture force is strongly tied to the size of the impactor but also has a secondary influence of the impactor shape. The round impactors avoid any stress and strain concentrations that might occur at the corners of the rectangular impactors and therefore require a higher force to puncture the wall for an equivalent impactor face perimeter length. Similarly, the higher aspect ratio rectangular impactors accentuate the stress concentration effects and further reduce the puncture force compared to the square impactors.

These secondary effects of the impactor shape suggest that there is potentially an improved measure of the impactor effective size that might better capture these secondary shape effects. The parameter developed that best captured these effects was to define the impactor "characteristic size" as the square root of the area of the impactor face. For a square impactor the characteristic size is equal to the length along the edge of the impact face (i.e., the 6x6 inch impactor has a 6-inch characteristic size). For round impactors, the characteristic size is approximately 11 percent smaller than the diameter. For high aspect ratio impactors, the characteristic size is smaller than the average length of the perimeter sides. For example, the 3x12 impactor has a perimeter length that is 25 percent larger than that for the 6x6 inch impactor. However, the 6x6 inch impactor and the 3x12 impactor both have the same characteristic size of 6 inches.

Table 2. Summary of the baseline side impact analyses for the 105J600 tank car

Calculation	Tank Type	Tank Shell	Shell Jacket	Impact Conditions	Internal Pressure (psi)	Puncture Force (lbs)	Puncture Energy (ft-lbs)
R15D	600 lb Cl	0.981 in TC128B	0.119 in A1011	15 mph 6”x6” ram	100 psi	1.167E+06	1.500E+06
R15E	600 lb Cl	0.981 in TC128B	0.119 in A1011	25 mph 12”x12” ram	100 psi	2.160E+06	5.800E+06
R15F	600 lb Cl	0.981 in TC128B	0.119 in A1011	20 mph 9”x9” ram	100 psi	1.690E+06	3.940E+06
R11G	600 lb Cl	0.981 in TC128B	0.119 in A1011	10 mph 3”x3” ram	100 psi	5.760E+05	4.050E+05
R11H	600 lb Cl	0.981 in TC128B	0.119 in A1011	25 mph 3”x12” ram	100 psi	1.235E+06	1.950E+06
R11I	600 lb Cl	0.981 in TC128B	0.119 in A1011	25 mph 12”x3” ram	100 psi	1.280E+06	2.360E+06
R11M	600 lb Cl	0.981 in TC128B	0.119 in A1011	25 mph 5.73 in. dia.	100 psi	1.044E+06	1.000E+06
R11N	600 lb Cl	0.981 in TC128B	0.119 in A1011	25 mph 13.37 in. dia.	100 psi	2.203E+06	6.040E+06
R11O	600 lb Cl	0.981 in TC128B	0.119 in A1011	25 mph 9.55 in. dia.	100 psi	1.567E+06	3.000E+06
R11Q	600 lb Cl	0.981 in TC128B	0.119 in A1011	15 mph 5.73 in. dia.	100 psi	1.025E+06	1.300E+06
R11T	600 lb Cl	0.981 in TC128B	0.119 in A1011	15 mph 3”x6” ram	100 psi	8.505E+05	8.350E+05
R11U	600 lb Cl	0.981 in TC128B	0.119 in A1011	20 mph 7.64 in. dia.	100 psi	1.343E+06	2.180E+06
R11V	600 lb Cl	0.981 in TC128B	0.119 in A1011	25 mph 11.46 in. dia.	100 psi	1.894E+06	3.950E+06

The summary of the puncture forces for the various impactors, shown in Figure 78, is regenerated using the impactor characteristic size in Figure 79. The figure shows that the impactor characteristic size parameter provides a much closer correlation for all the impactor sizes and shapes analyzed. Overall, there is a strong linear correlation of the puncture force with the characteristic size of the impactor.

A similar summary of the puncture energies for the various impactors is shown in Figure 80. The figure shows that the impactor characteristic size parameter also correlates well to the puncture energies. There is more scatter in the correlation of the puncture energies but that is expected since various factors such as the impact speed and BCs have been shown to introduce variations in the calculated impact energy. The impact energies in Figure 80 show that the correlation is roughly with the square of the characteristic size of the impactor. This is a result of the linear increase in the puncture force combined with a similar increase in the displacements required to reach the impact force.

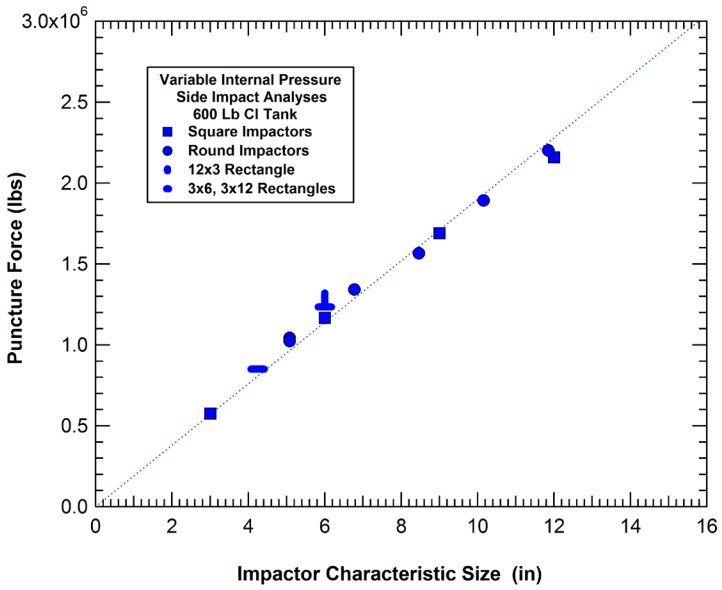

Figure 79. Correlation of the puncture forces with ram characteristic size.

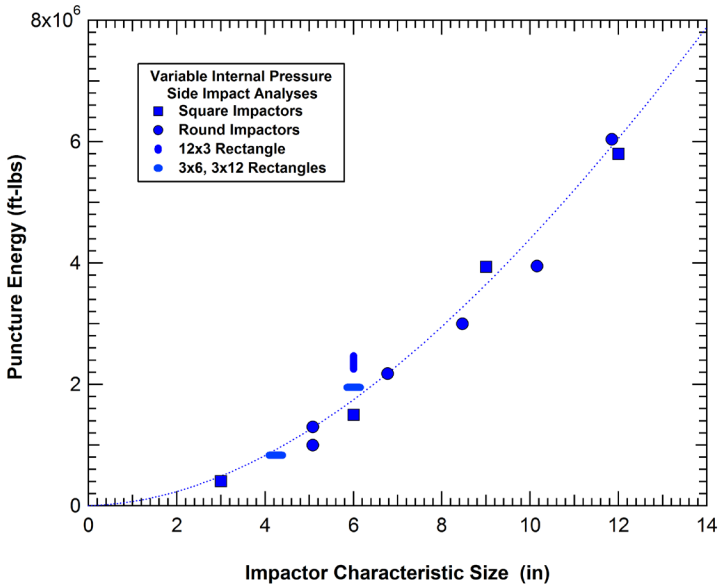

Figure 80. Correlation of the puncture energies with ram characteristic size.

3.2.3 Analysis of Impactor Edge Sharpness

The impactor models used in the above analyses all had a 0.5-inch-radius edge around the face of the impactor. This value was originally selected to match the edge conditions on the 6x6 inch impactor used in the NGRTC testing and analyses (Kirkpatrick, 2009a). The edge radius was a simplification that would eliminate effects such as the edge deformation and wear for repeated use of the impactor in testing and was expected to produce more repeatable impact behaviors. In this section, the effect of the edge radius was analyzed to quantify the importance of the impactor edge sharpness.

The analyses performed used the 3x3, 3x12, and 12x12 inch impactors. These were selected to include the smallest, largest and highest aspect ratio of the impactors studied with the assumption that these would be the cases where the edge radius might be the most significant. The analyses were performed for all three impactors with the original 0.5-inch edge radius as well as a much sharper 0.1-inch edge radius. In addition, an analysis using the 12x12 inch impactor with a large 1.0-inch edge radius was also performed.

A summary of the results for these side impact analyses with different impactor face edge radii is listed in Table 3. The corresponding force deflection curves for all the analyses are shown in Figure 81. The comparisons show that the edge radius has a small effect on the overall response and calculated puncture forces and energies. The largest discrepancy was for the puncture energies with the 3x12 impactor where the 0.1-inch edge radius resulted in a 10 percent reduction in the puncture energy compared to the baseline 0.5-inch radius. However, this difference was probably influenced by the fact that the puncture occurred in a very flat region of the force-deflection response for this impact scenario. The comparison of the corresponding puncture forces for these two 3x12 impactor analyses show that they agree to within approximately 1 percent.

Table 3. Summary of the analyses to assess the impactor face edge radius.

Impact Calc.	Tank Type	Tank Shell	Tank Jacket	Impact Conditions	Impactor Edge Radius	Internal Pressure (psi)	Puncture Force (lbs)	Puncture Energy (ft-lbs)
R11G	600 lb Cl	0.981 in TC128B	0.119 in A1011	10 mph 3”x3” ram	0.50 inch	100 psi	576,000	405,000
R11J	600 lb Cl	0.981 in TC128B	0.119 in A1011	10 mph 3”x3” ram	0.10 inch	100 psi	590,000	375,000
R11H	600 lb Cl	0.981 in TC128B	0.119 in A1011	25 mph 3”x12” ram	0.50 inch	100 psi	1,235,000	1,950,000
R11K	600 lb Cl	0.981 in TC128B	0.119 in A1011	25 mph 3”x12” ram	0.10 inch	100 psi	1,227,000	1,750,000
R15E	600 lb Cl	0.981 in TC128B	0.119 in A1011	35 mph 12”x12” ram	0.50 inch	100 psi	2,160,000	5,800,000
R11P	600 lb Cl	0.981 in TC128B	0.119 in A1011	35 mph 12”x12” ram	0.10 inch	100 psi	2,006,000	5,700,000
R12V	600 lb Cl	0.981 in TC128B	0.119 in A1011	35 mph 12”x12” ram	1.00 inch	100 psi	2,206,000	5,780,000

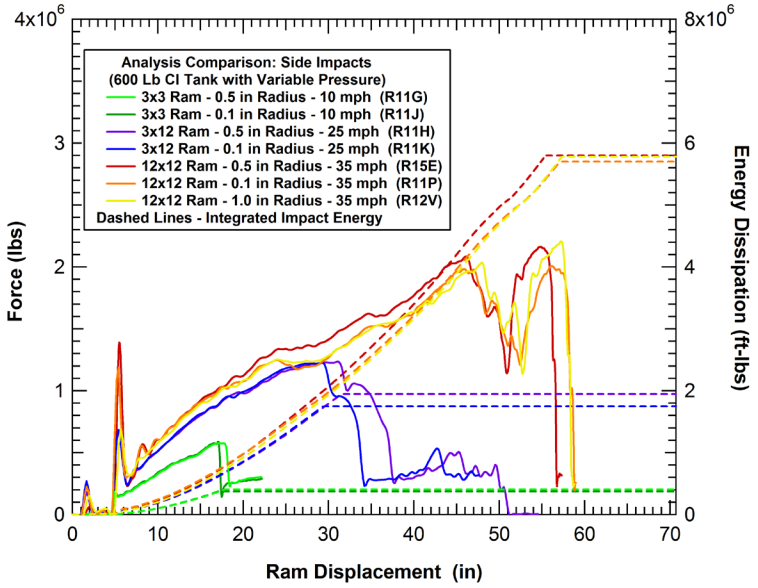

Figure 81. Calculated force-deflection behaviors for the impactor edge radii evaluations.

The calculated puncture response for the two analyses with the 3x12 inch impactors is shown in Figure 82. The calculated response is shown at times of 80 and 100 ms after impact corresponding to points after the fracture initiation and full penetration of the impactor through the tank wall. The comparison shows that the 0.1-inch impactor puncture development is further along at a time of 80 ms and results in a slightly cleaner fracture surface around the final plug formation at 100 ms. However, these differences were minor, and the dominating punch-shear failure mechanism is seen for all the analyses. As a result, the edge radius is considered to be a secondary effect for the puncture of the pressure tank cars.

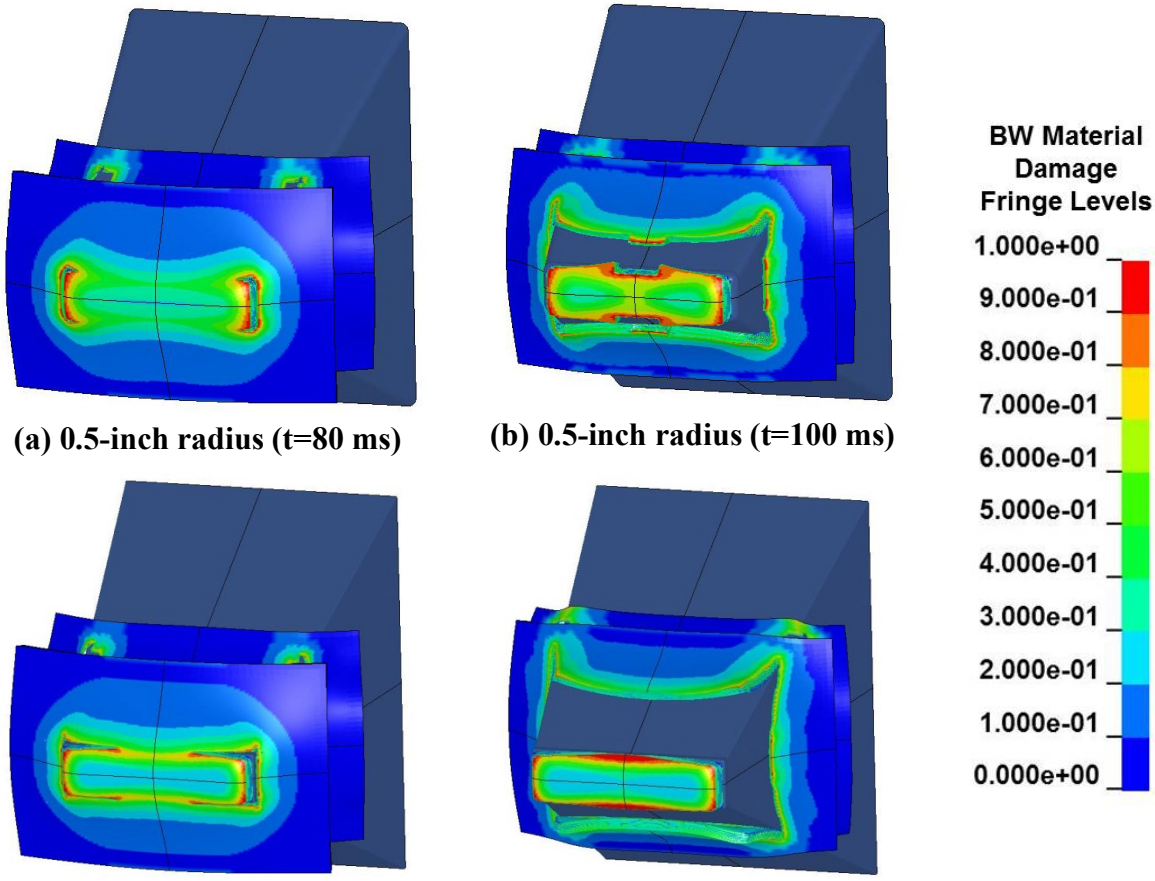

(a) 0.5-inch radius (t=80 ms)

(b) 0.5-inch radius (t=100 ms)

(c) 0.1-inch radius (t=80 ms)

(d) 0.1-inch radius (t=100 ms)

Figure 82. Calculated puncture behavior for the 3x12impactor with 0.5- and 0.1-inch edge radii.

3.2.4 Analysis of Complex Impactor Shapes

The above analyses of the effects of impactor sizes and shapes considered only idealized rectangular and round impactors. However, in more general derailment and impact conditions, the impactors may have a much more complex geometry or impact condition. In this section, we analyze the impact behavior for some of these complex impactor scenarios.

Rail Section Impactor

One significant impactor threat that has been observed in derailments is a section of broken or displaced rail. To evaluate this threat, a rail section impactor was created and used to calculate the puncture behavior. The impactor model created is shown in Figure 83. The impactor is a section of 141-pound rail with a flat end impactor face. The geometry used to generate the rail section impactor is shown in Figure 84.

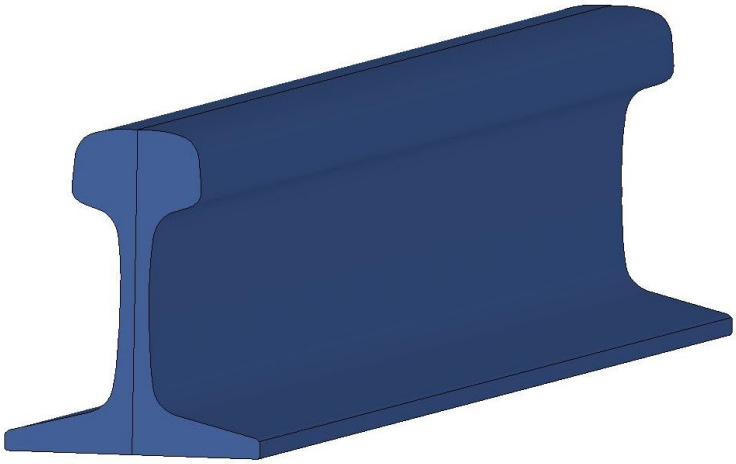

Figure 83. Model for the rail section impactor.

To compare the puncture behavior to other impactor shapes, we need to evaluate the characteristic size of the rail section impactor. However, for this impactor with a mix of concave and convex curves around the perimeter of the impact face the impactor area can be defined by different methodologies. The first is to use the cross-sectional area of the rail as shown in Figure 84(a). This cross-sectional area is 13.8 square inches which corresponds to an impactor characteristic size of 3.7 inches. The second methodology would be to use the bounding impact area defined in Figure 84(b). This bounding impact area is 33.4 square inches and corresponds to an impactor characteristic size of 5.8 inches.

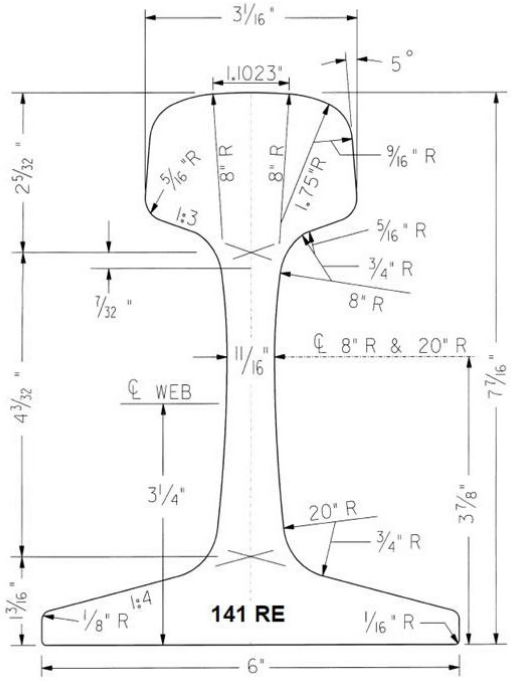

(a) Cross section geometry

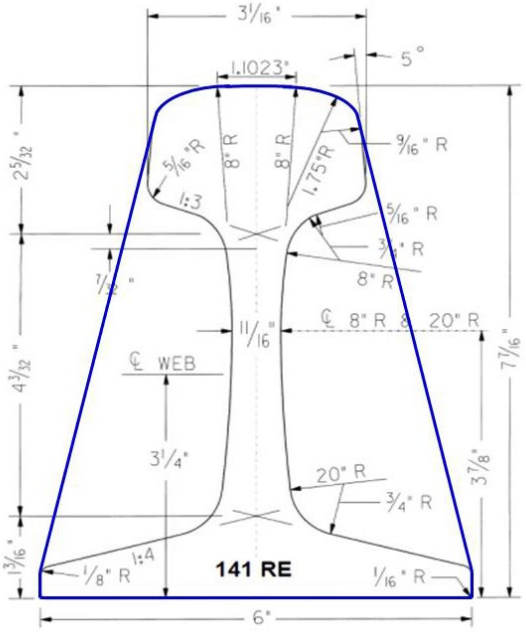

(b) Cross section and bounding area definition

Figure 84. Geometry for the rail section impactor.

The calculated side impact puncture behavior for the rail section impactor is shown in Figure 85. The damage is greatest at the stress concentrations at the corners of the head and base of the rail and the puncture initiates at these sites. The puncture then progresses to the point that a rail shaped plug of material is removed from the tank wall.

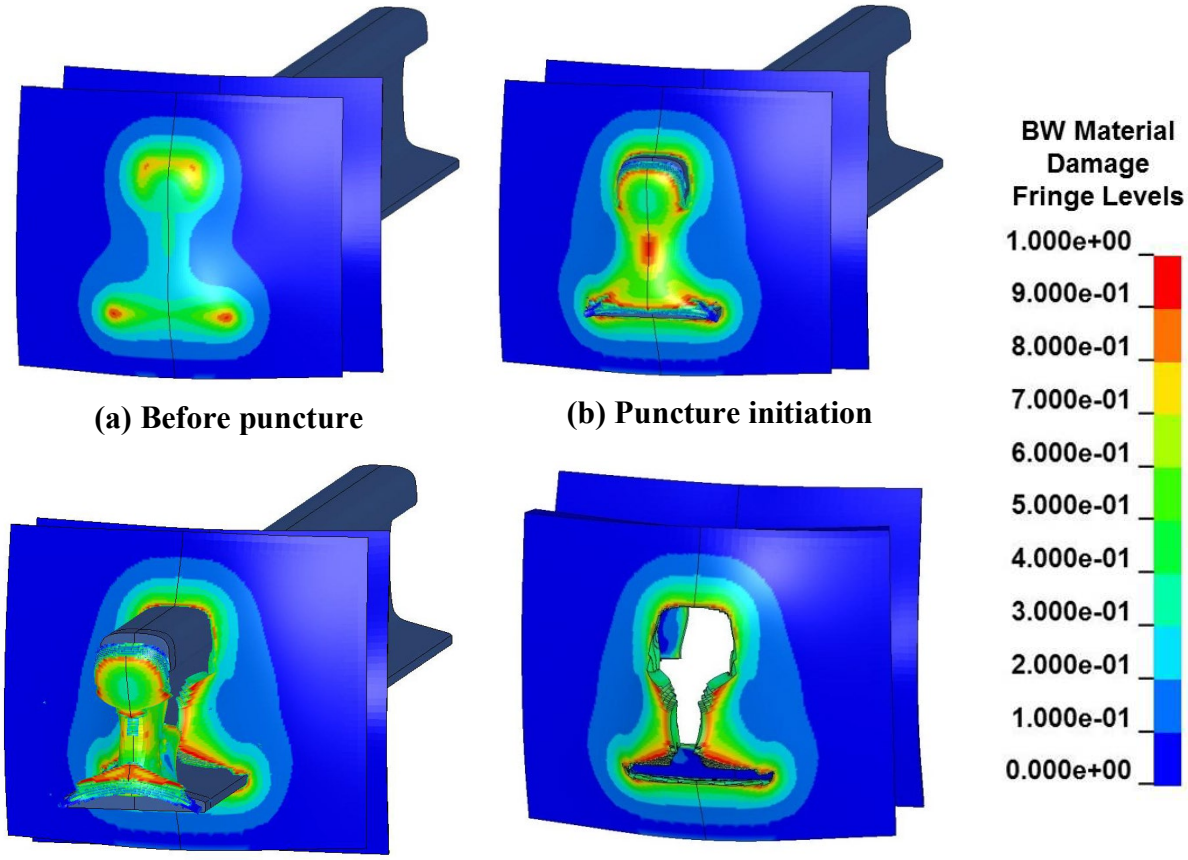

Figure 85. Calculated side impact puncture behavior for the rail section impactor.

The calculated side impact puncture force for the rail impactor is compared to the other impactors in Figure 86. The rail puncture force is shown using both the 3.7- and 5.8-inch initial estimates for the impactor characteristic size. The comparison in Figure 86 shows that these estimates for the characteristic size bound the correlation for the other simple impactor geometries. If we use the fit from the previous analyses, the rail impactor puncture force corresponds to an impactor with a 5-inch characteristic size.

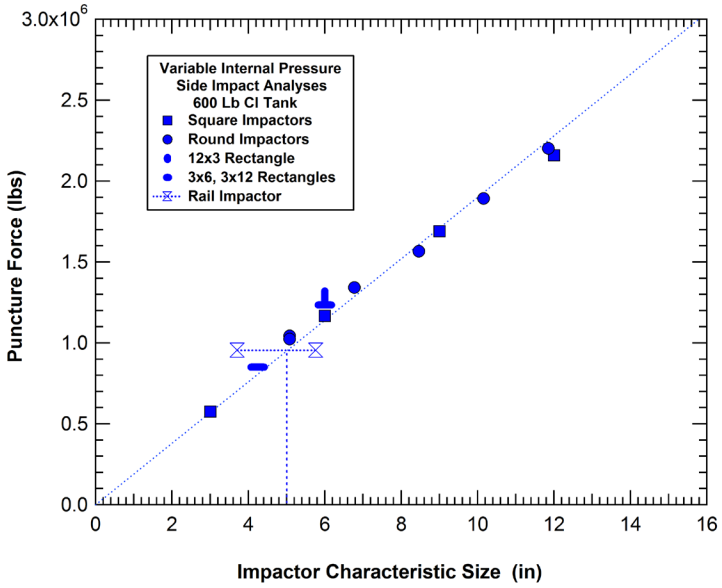

Figure 86. Puncture forces for the 600 lb tank impact analyses with the rail impactor.

Coupler Impactor

A second significant impactor threat that has been observed in derailments is a coupler. To evaluate this threat, a coupler impactor model was created and used to calculate the puncture behavior. The impactor model created is shown in Figure 87. It is a rigid model of the coupler head and shank with the complex impactor face geometry.

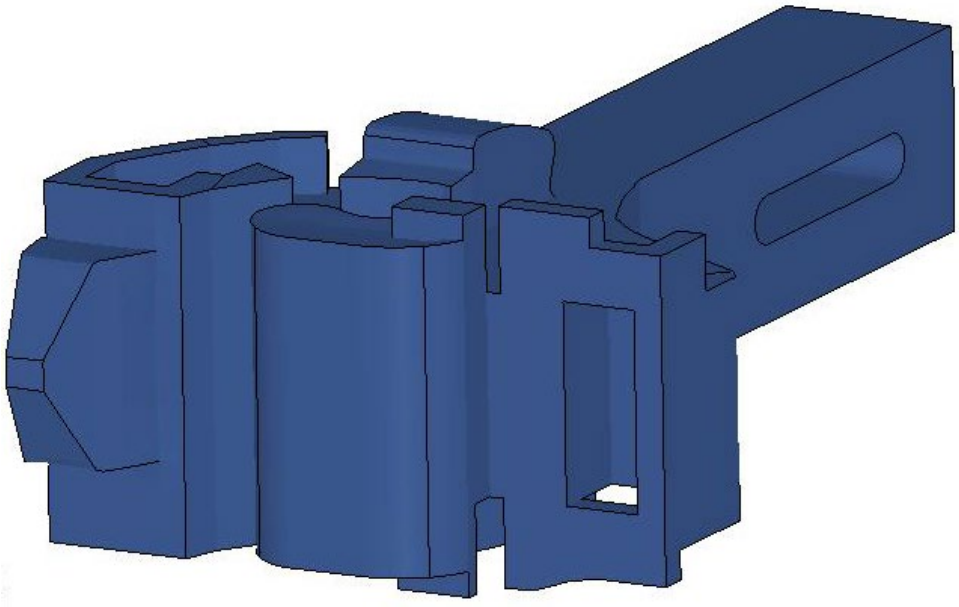

Figure 87. Model for the coupler head impactor.

As a result of the complex impactor face profile of the coupler, it was not possible to estimate the characteristic size in advance. As a result, the impact and puncture analyses were performed, and the calculated puncture behaviors were used to back calculate the equivalent characteristic size of the impactor.

The initial coupler impact analysis was performed using a normal side impact scenario with an initial impact velocity of 25 mph and an impactor weight of 295,000 lbs. The calculated coupler impact damage development and puncture behavior is shown in Figure 88. The calculated damage profile shows that the damage development is nonuniform over the impact face of the coupler with the largest concentration of damage around the protruding interlocking lug on the wing with secondary concentrations around the knuckle. These load concentrations are significant since the damage under the interlocking lug initiates a crack through the tank shell significantly earlier than the load at which the entire coupler head punctures the tank.

The calculated force-deflection behavior for the coupler normal side impact is compared to that of the 12x12 impactor in Figure 89. The comparison shows that the force deflection behaviors for the complete puncture are very similar with a peak force of approximately 3 million pounds and a maximum ram displacement of 55-60 inches. However, the fracture initiation under the interlocking lug occurs at a load of approximately 1.7 million pounds and a ram displacement of 40 inches. Thus, the point at which the commodity release would occur is significantly earlier for the coupler normal impact than for the 12x12 inch impactor.

The nonuniformity of the loading and damage suggests that the coupler impact and puncture behavior could be very sensitive to the orientation of the coupler head relative to the tank wall. To investigate this effect, two additional calculations were performed where the coupler head orientation was rotated laterally in each direction by 15 degrees. The motion of the rotated impactors is still in a direction normal to the tank wall.

The calculated impact damage and force deflection for the first rotated coupler impact are shown in Figure 90 and Figure 91, respectively. The rotation for this case results in a more concentrated load on the coupler interlocking lug and the tank wall in initially breached at a force of approximately 1 million pounds and an impact energy of 800,000 ft-lbs.

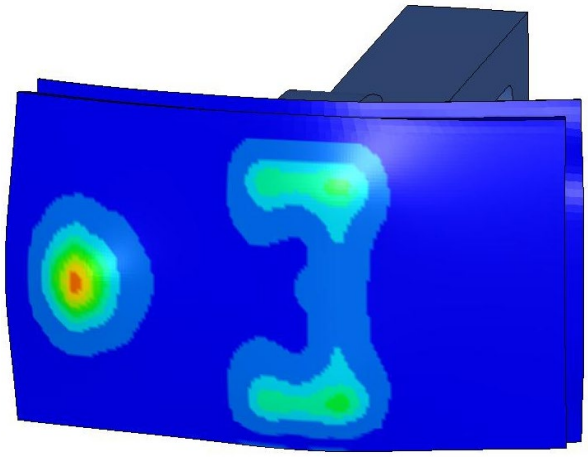

(a) Before puncture (t=60 ms)

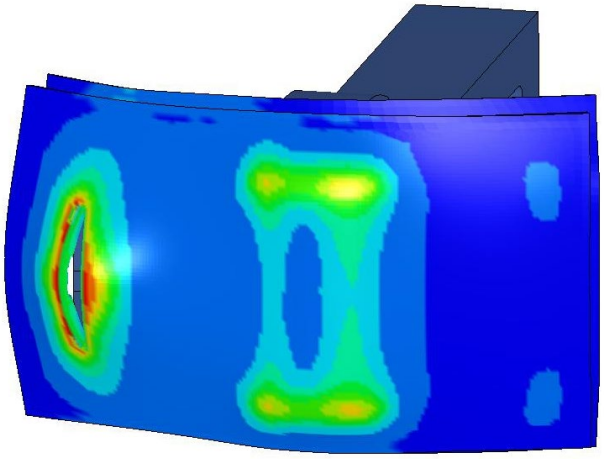

(b) Puncture initiation (t=120 ms)

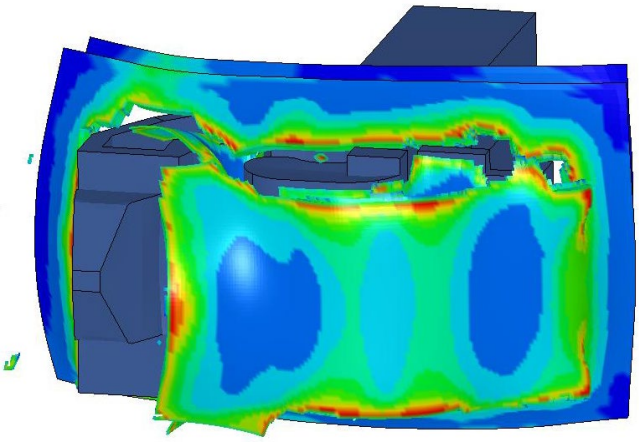

(c) Complete puncture (t=220 ms)

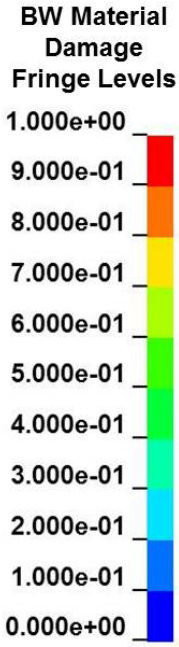

Figure 88. Calculated puncture behavior for the coupler head normal impact.

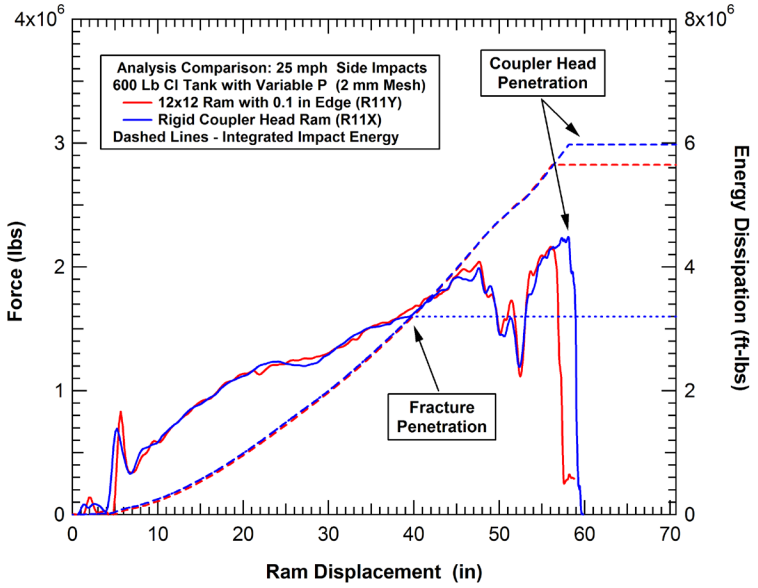

Figure 89. Calculated force-deflection behavior for the coupler head normal impact.

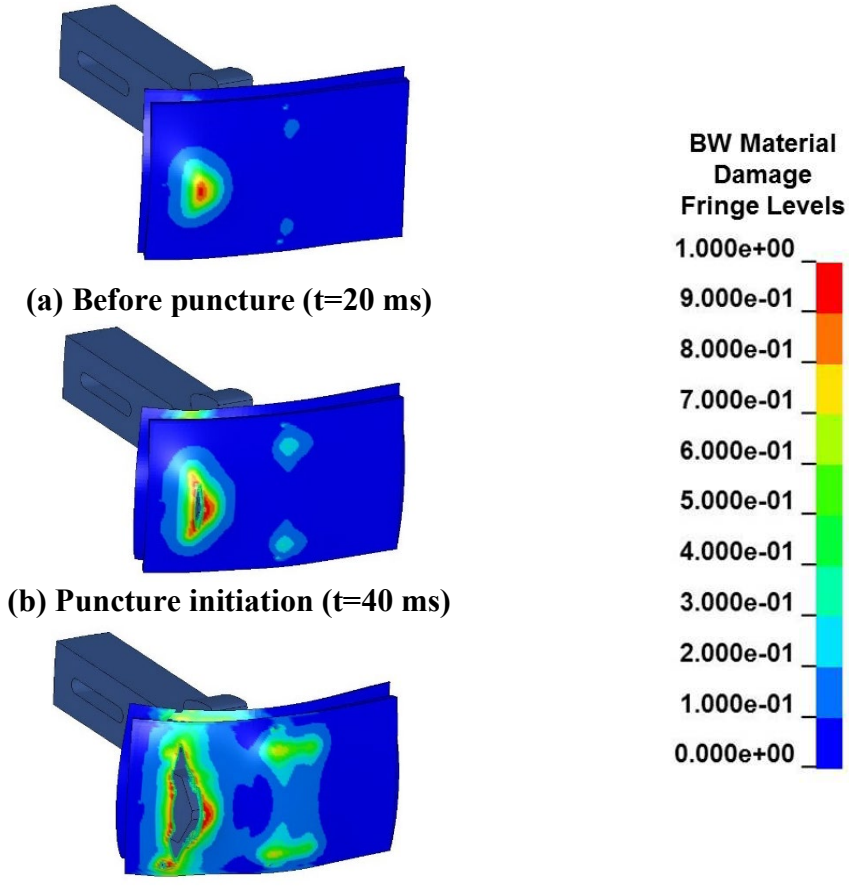

(a) Before puncture (t=20 ms)

(b) Puncture initiation (t=40 ms)

(c) Puncture growth (t=100 ms)

Figure 90. Calculated puncture behavior for the coupler head 15-degree rotation impact.

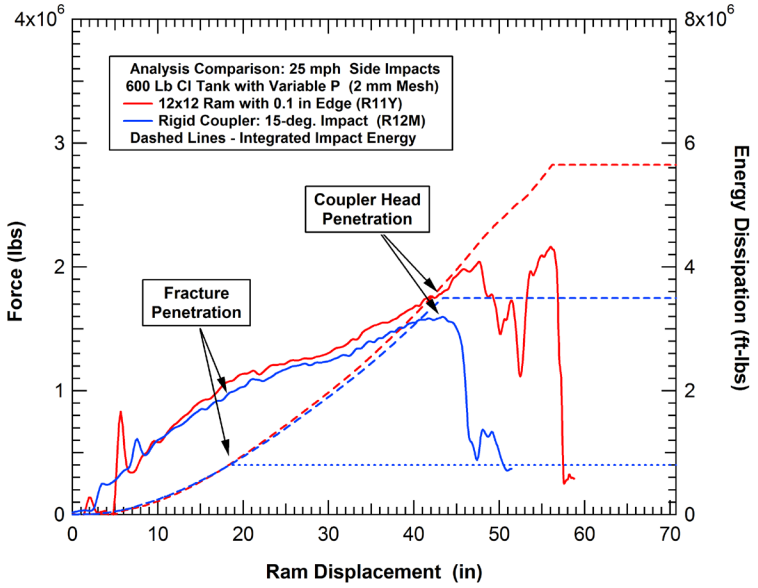

Figure 91. Calculated force-deflection behavior for the coupler 15-degree rotation impact.

The calculated impact damage and force deflection for the second rotated coupler impact configuration are shown in Figure 92 and Figure 93, respectively. The rotation for this case produces a more distributed load across the coupler face. The tank wall is not breached until reaching a force of approximately 2.3 million pounds and an impact energy of 5.7 million ft-lbs.

The forces for which the tank wall is breached in the three coupler impact scenarios are added as the horizontal dashed lines in Figure 94. Using the correlation between puncture force and impactor characteristic size developed in the previous analyses with the idealized impactors, we can calculate the effective size of the coupler in these three impact analyses. This methodology shows that in the unfavorable orientation the coupler head has the puncture potential of a 5-inch characteristic size impactor (e.g., a 5x5 inch impactor). However, at a more favorable orientation, the coupler head has a similar puncture potential to the 12x12 inch impactor (12-inch characteristic size).

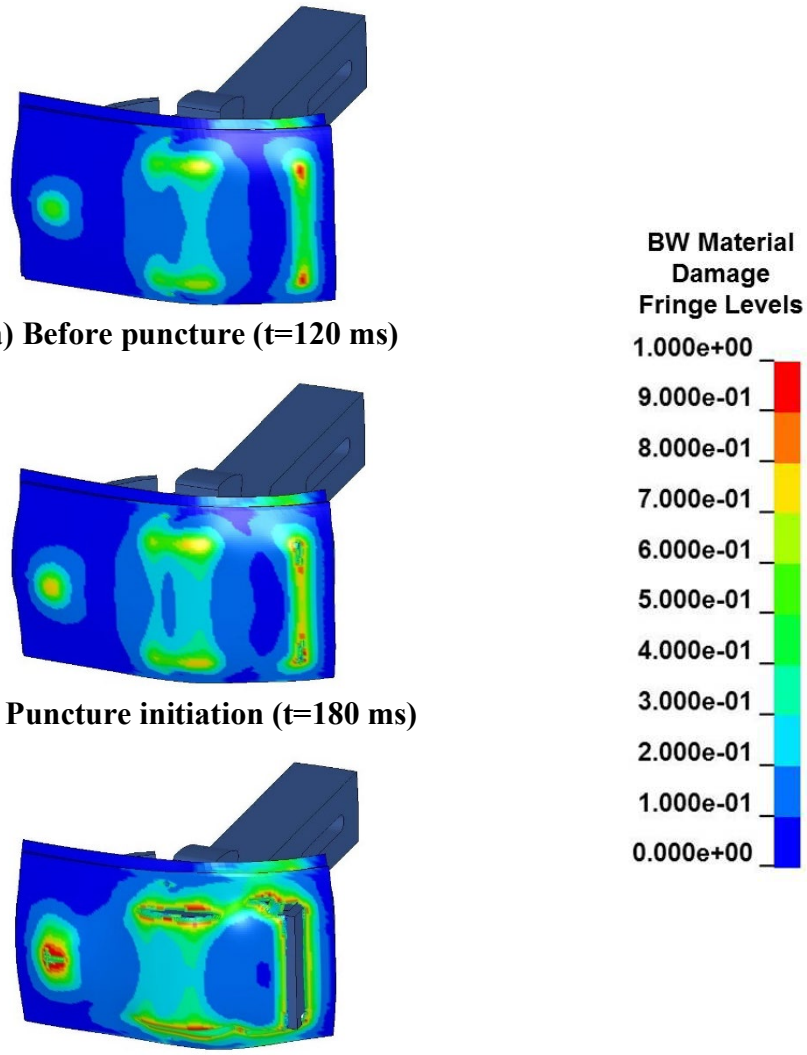

(a) Before puncture (t=120 ms)

(b) Puncture initiation (t=180 ms)

(c) Puncture growth (t=200 ms)

Figure 92. Calculated puncture behavior for the coupler -15-degree rotation impact.

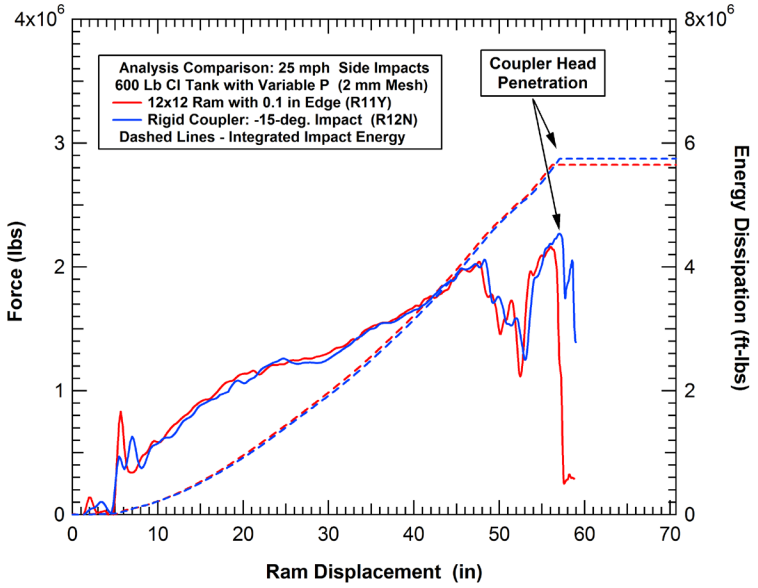

Figure 93. Calculated force-deflection behavior for the coupler -15-degree rotation impact.

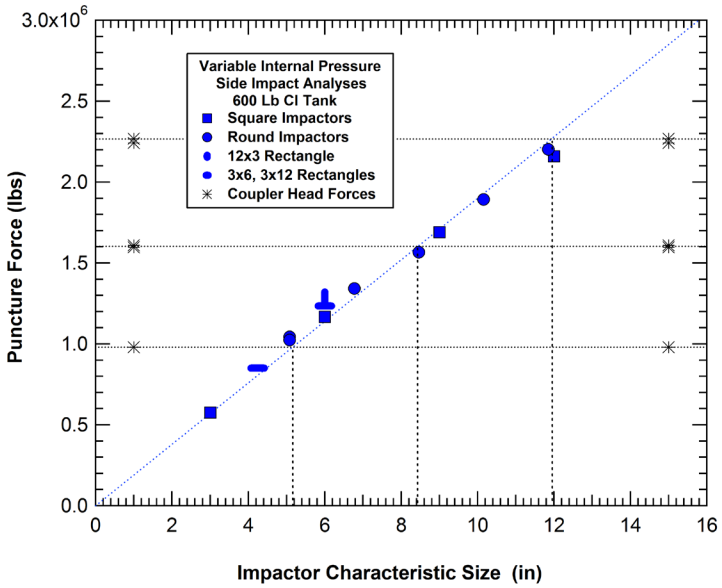

Figure 94. Puncture forces for the 600 lb tank impact analyses with the coupler head impactor.

3.2.5 Analysis of Impactor Orientation Effects

The above analysis of the coupler head impacts at various orientations show that the orientation of an impactor can play a significant role on the puncture response. To quantify this effect, the 12x12 inch impactor with a 0.1-inch edge radius was used in a series of analyses where the orientation was varied. The orientation included various combinations of yaw and pitch rotation of the impactor head. Examples of the impact scenarios for various impactor yaw rotation are

shown in Figure 95. The impact condition for all the analyses was still a normal velocity trajectory with a 25-mph impact speed and a total impactor weight of 295,000 lbs.

The calculated force-displacement curves and integrated puncture energies for the analyses with various levels of yaw rotation are shown in Figure 96. The figure shows that all the analyses are following along a roughly equivalent characteristic force-deflection curve for the tank and impact conditions. However, as the yaw rotation increases, the concentration of impact load and damage along the leading edge of the impactor increases and the point at which the impactor punctures the tank is earlier (lower force levels).

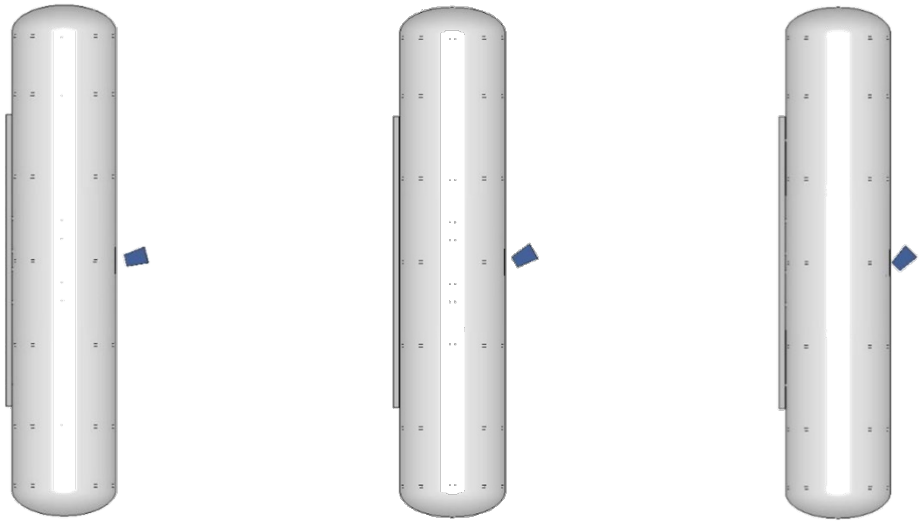

(a) 15-degree yaw rotation (b) 30-degree yaw rotation (c) 45-degree yaw rotation

Figure 95. Example impactor orientation analyses performed for side impacts.

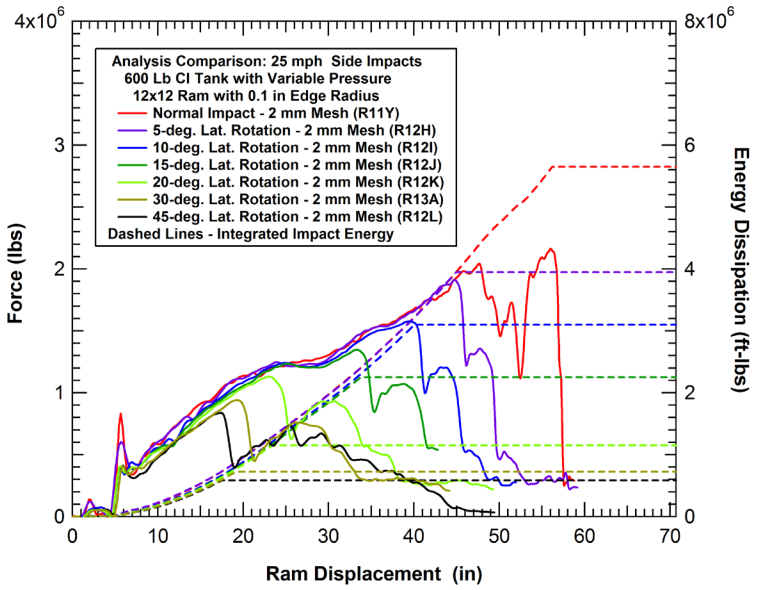

Figure 96. Calculated force-deflection behaviors for the 12x12 inch impactor and various levels of yaw rotations.

A summary of all the analyses performed to quantify the impactor orientation effects is provided in Table 4. Similarly, the puncture forces for all the analyses are plotted against the impactor rotation angles in Figure 97. The effects for the pitch rotation are similar to those for the yaw rotation, but with a slight increase in the puncture forces resulting from the relative stiffness of the tank for bending in the longitudinal and radial directions in the impact zone. The analyses where the yaw rotation was maintained at 45 degrees then various levels of pitch rotation were added further concentrates the load and damage at the corner of the impactor. The damage profiles for the edge and corner impacts produced by the extreme rotation combinations analyzed are shown in Figure 98.

Table 4. Summary of the analyses to assess the impactor orientation effects.

Side Impact Calculation	Tank Type	Tank Shell	Tank Jacket	Impact Conditions	Ram Yaw Angle (deg.)	Ram Pitch Angle (deg.)	Puncture Force (lbs)	Puncture Energy (ft-lbs)
R11P	600 lb Cl	0.981 in TC128B	0.119 in A1011	25 mph 12”x12” ram	0.0	0.0	2.154E+06	5.650E+06
R12H	600 lb Cl	0.981 in TC128B	0.119 in A1011	25 mph 12”x12” ram	5.0	0.0	1.910E+06	3.950E+06
R12I	600 lb Cl	0.981 in TC128B	0.119 in A1011	25 mph 12”x12” ram	10.0	0.0	1.576E+06	3.100E+06
R12J	600 lb Cl	0.981 in TC128B	0.119 in A1011	25 mph 12”x12” ram	15.0	0.0	1.348E+06	2.250E+06
R12K	600 lb Cl	0.981 in TC128B	0.119 in A1011	25 mph 12”x12” ram	20.0	0.0	1.130E+06	1.150E+06
R12L	600 lb Cl	0.981 in TC128B	0.119 in A1011	25 mph 12”x12” ram	45.0	0.0	8.380E+05	5.850E+05
R12O	600 lb Cl	0.981 in TC128B	0.119 in A1011	25 mph 12”x12” ram	45.0	5.0	8.160E+05	5.400E+05
R12P	600 lb Cl	0.981 in TC128B	0.119 in A1011	25 mph 12”x12” ram	45.0	10.0	7.850E+05	4.800E+05
R12Q	600 lb Cl	0.981 in TC128B	0.119 in A1011	25 mph 12”x12” ram	45.0	15.0	7.400E+05	4.250E+05
R12R	600 lb Cl	0.981 in TC128B	0.119 in A1011	25 mph 12”x12” ram	45.0	20.0	6.510E+05	3.300E+05
R12S	600 lb Cl	0.981 in TC128B	0.119 in A1011	25 mph 12”x12” ram	45.0	45.0	9.096E+05	7.000E+05
R13C	600 lb Cl	0.981 in TC128B	0.119 in A1011	25 mph 12”x12” ram	0.0	5.0	2.020E+06	5.400E+06
R13D	600 lb Cl	0.981 in TC128B	0.119 in A1011	25 mph 12”x12” ram	0.0	10.0	1.830E+06	3.900E+06
R13E	600 lb Cl	0.981 in TC128B	0.119 in A1011	25 mph 12”x12” ram	0.0	15.0	1.613E+06	3.400E+06
R13F	600 lb Cl	0.981 in TC128B	0.119 in A1011	25 mph 12”x12” ram	0.0	20.0	1.423E+06	2.900E+06
R13G	600 lb Cl	0.981 in TC128B	0.119 in A1011	25 mph 12”x12” ram	0.0	45.0	1.090E+06	1.150E+06

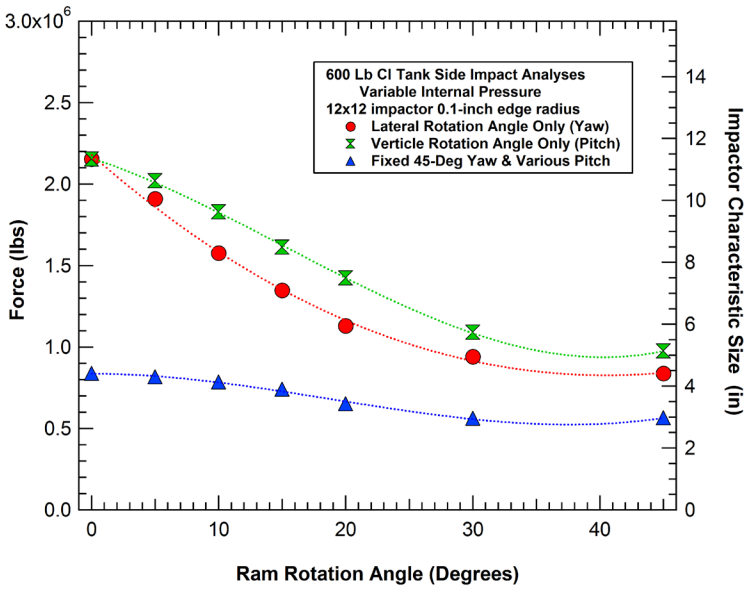

Figure 97. Puncture forces for the 12x12 inch impactor at various orientations.

For comparison, the puncture forces calculated for the rotated 12x12 inch impactor were converted to obtain the impactor characteristic size which is shown on the right axis of Figure 97. The plot shows that the characteristic size of the impactor decreases rapidly as the rotation increases from 0 to approximately 30 degrees then levels out beyond that point where the contact is primarily with only the edge or corner of the impactor. The characteristic size of the 12x12 impactor drops from 12 inches in the normal impact to approximately 4.5-5 inches in an edge impact. The characteristic size is further reduced to approximately 3 inches for the corner impact. These results show that impacting objects with corners and edges can have the penetration potential of a much smaller object if the orientation of the impactor concentrates the loading to the edge or corner.

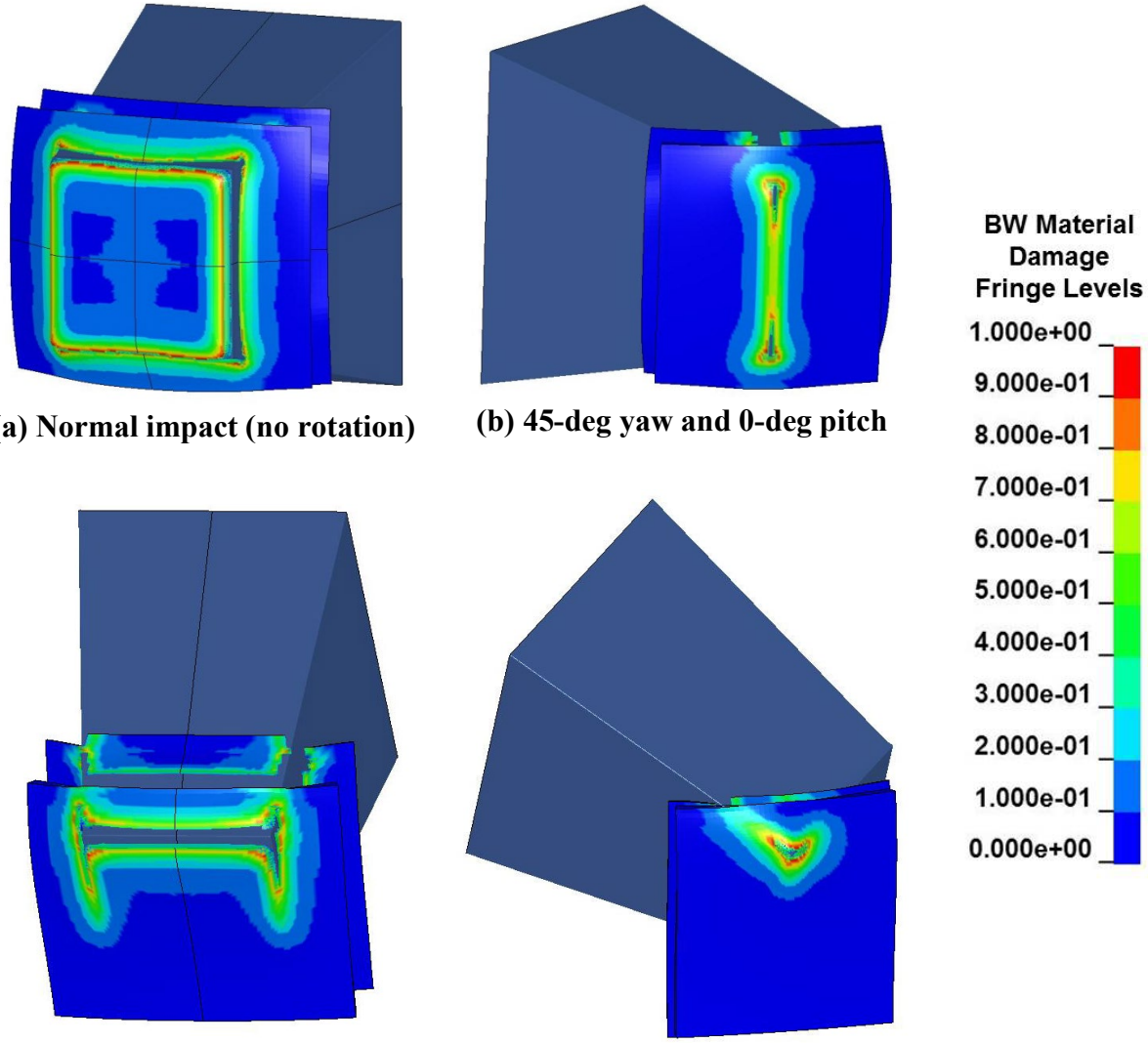

(a) Normal impact (no rotation) **(b) 45-deg yaw and 0-deg pitch**

(c) 0-deg yaw and 45-deg pitch **(d) 45-deg yaw and 45-deg pitch**

Figure 98. Puncture behavior for the 12x12 inch impactor with face, edge, and corner impacts.

3.3 Head Impact Analysis of Different Size and Shape Impactors

The above sections describe the effects of different size and shape impactors on the side impact behavior and puncture response. A similar set of analyses were performed for the head impact on the 600 lb tank car. The head impact analyses were performed using a configuration similar to the head impact tests in the NGRTC program (Kirkpatrick, 2009a). The head and a short length of the tank shell are used, and the boundary condition is a rigid restraint at the trailing edge of the shell. This boundary condition is representative of the head impact test frame used in the NGRTC program.

The heads were impacted by various size impactors. In the analyses, the impactor is given an initial velocity and constrained to move in the longitudinal direction only. The target impact point was offset approximately 29 inches vertically downward from the center of the head. The weight of the impactor is 295,000 lbs which matches the final impactor test sled weight used in the NGRTC tests. The primary difference from the NGRTC head test series is that the heads were pressurized to 100 psi in the analyses performed in this section. For these preliminary analyses a constant internal pressure level is used. The constant pressure assumption is more appropriate for the head impacts where the structural stiffness of the head geometry is larger (thus pressure effects play a smaller role). In addition, the dent shape for head impacts is a smaller fraction of the tank volume than the side impact dent shape and the pressure change is smaller.

3.3.1 Effects of Impactor Size and Shape

An example of the calculated impact and puncture behavior for the 600 lb tank head is shown in Figure 99. The specific example shown is for the 11-mph impact with the 6x6 inch impactor. The response mechanisms include a dent formation under the impactor for both the tank head and head shield, buckling of the jacket supporting the head shield, and eventually the puncture of the head and shield. The puncture initiates at the top edge of the impactor and opens a flap of material under the impact face.

A summary of results from the baseline head impact analyses is provided in Table 5. All the analyses in the table are for the 600 lb tank geometry with a 0.5-inch-thick A572-50 head shield and 100 psi internal pressure. The impactors all have the baseline 0.5-inch edge radius. The calculated force-deflection behaviors and puncture energies for the 3x3, 6x6, 9x9, and 12x12 inch impactors are shown in Figure 100. The highly constrained head structures result in a behavior where the impact force is roughly linearly proportional to the impactor displacement (dent depth).

The calculated head impact puncture forces are plotted against the impactor characteristic size in Figure 101. The puncture forces again show a trend of a linear correlation with the impactor characteristic size, with slightly more scatter in the correlation. It is believed that this is a result of the offset impact condition that produces uneven loading at the upper and lower edges of the impactor. As a result, the results are more sensitive to the shape of the impactor.

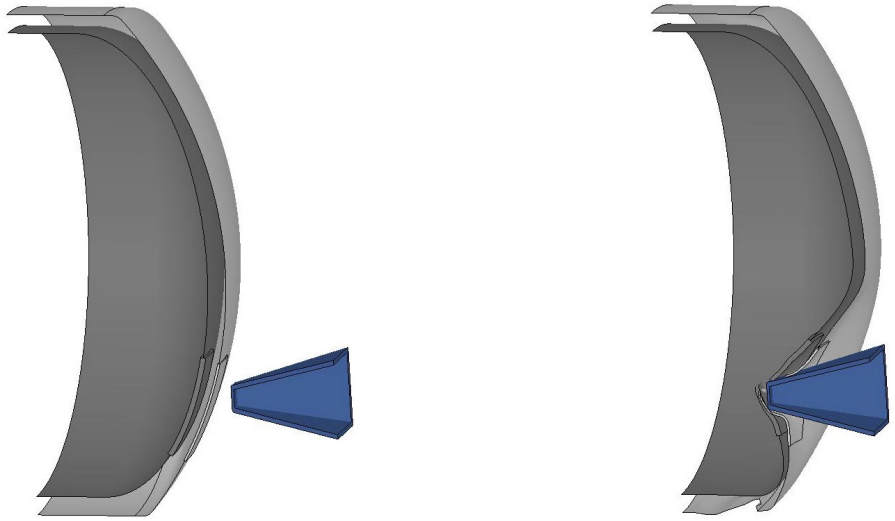

(a) Impact configuration **(b) Puncture behavior**

Figure 99. Analysis of the tank head puncture behavior for the 6x6 inch impactor.

Table 5. Summary of the baseline head impact analyses.

Head Impact Calculation	Tank Type	Tank Head	Jacket or Head Shield	Impact Conditions	Impactor Edge Radius	Internal Pressure (psi)	Puncture Force (lbs)	Puncture Energy (ft-lbs)
R10K	600 lb Cl	1.1360 A516-70	0.500" A572-50	14 mph 6"x6" ram	0.50 inch	100 psi	1,206,000	1,121,000
R10N	600 lb Cl	1.1360 A516-70	0.500" A572-50	11 mph 6"x6" ram	0.50 inch	100 psi	1,229,000	1,110,000
R10V	600 lb Cl	1.1360 A516-70	0.500" A572-50	20 mph 9"x9" ram	0.50 inch	100 psi	1,868,000	2,450,000
R11F	600 lb Cl	1.1360 TC128B	0.500" A572-50	25 mph 12"x12" ram	0.50 inch	100 psi	2,334,000	3,672,000
R11L	600 lb Cl	1.1360 TC128B	0.500" A572-50	10 mph 3"x3" ram	0.50 inch	100 psi	774,000	400,000
R11M	600 lb Cl	1.1360 TC128B	0.500" A572-50	18 mph 3"x12" ram	0.50 inch	100 psi	1,298,000	1,035,000
R11N	600 lb Cl	1.1360 TC128B	0.500" A572-50	18 mph 12"x3" ram	0.50 inch	100 psi	1,660,000	1,830,000
R11O	600 lb Cl	1.1360 TC128B	0.500" A572-50	12 mph 5.73" Dia.	0.50 inch	100 psi	1,176,000	915,000
R11P	600 lb Cl	1.1360 TC128B	0.500" A572-50	18 mph 9.55" Dia.	0.50 inch	100 psi	1,753,000	2,000,000
R11R	600 lb Cl	1.1360 TC128B	0.500" A572-50	15 mph 7.64" Dia.	0.50 inch	100 psi	1,562,000	1,520,000
R11S	600 lb Cl	1.1360 TC128B	0.500" A572-50	21 mph 11.46" Dia.	0.50 inch	100 psi	2,236,000	3,500,000

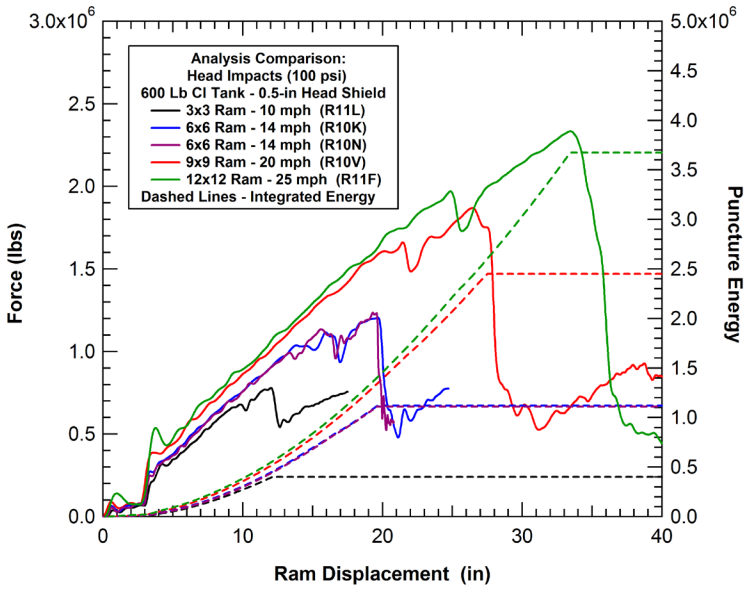

Figure 100. Calculated head impact force-deflection behaviors for the square impactors.

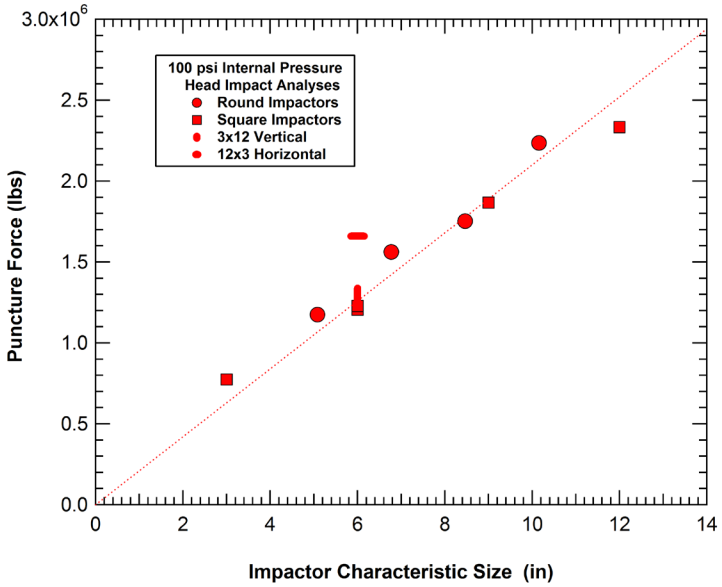

Figure 101. Calculated head impact puncture forces for various impactors.

The largest discrepancy from the linear puncture force correlation was for the 12x3 inch impactor that has a puncture force significantly larger than the fit to the data. The damage development and puncture behavior for the 12x3 and 3x12 inch impactors are shown in Figure 102. The comparison shows that the load is distributed over a much wider region for the 12x3 impactor and as a result it acts like a larger impactor compared to the 3x12 impactor for this scenario. Therefore, the 12x3 impactor orientation had a small sensitivity to the offset impact effects and the 3x12 impactor had a large sensitivity to the offset impact geometry.

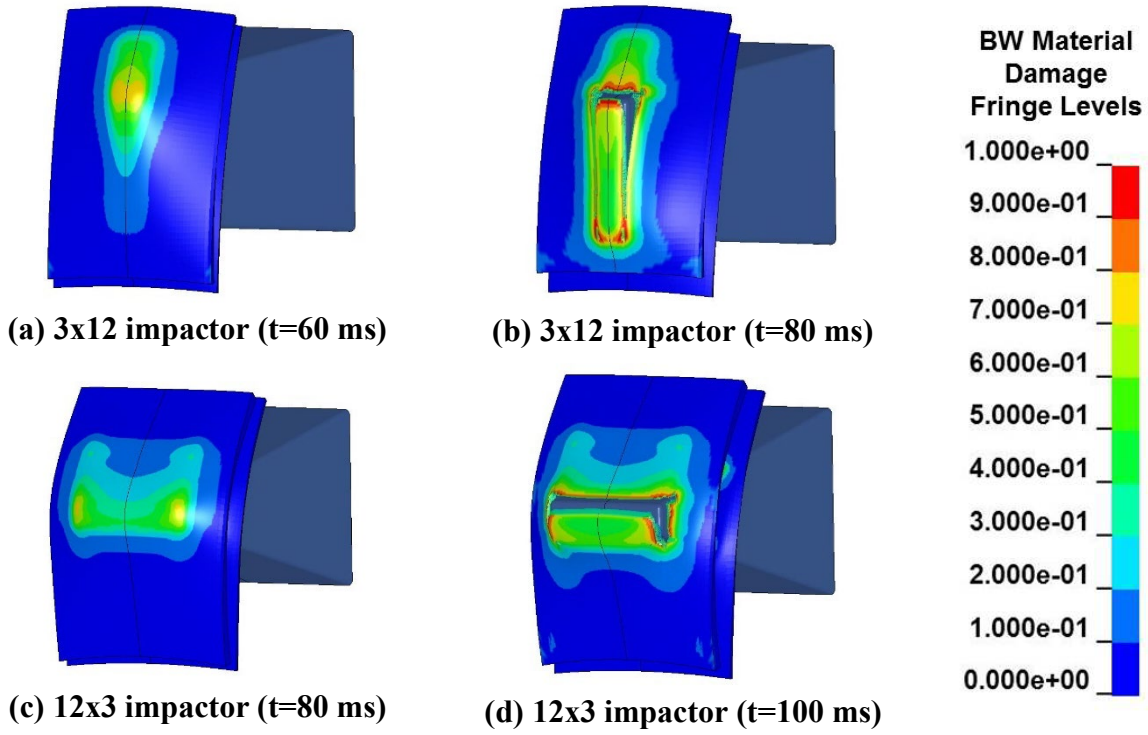

(a) 3x12 impactor (t=60 ms) **(b) 3x12 impactor (t=80 ms)**

(c) 12x3 impactor (t=80 ms) **(d) 12x3 impactor (t=100 ms)**

Figure 102. Calculated head puncture behaviors for the 3x12 and 12x3 impactors.

The calculated head impact puncture forces and energies are compared to the corresponding side impact values in Figure 103 and Figure 104, respectively. The head puncture forces are on average approximately 10 percent greater than the side impact puncture forces. The difference is a combination of two competing factors. First the combined head and head shield thickness is almost 50 percent thicker than the combined thickness of the tank shell and jacket. However, this thickness increase is partially negated by the offset head impact scenario producing larger stress and strain concentrations at the top edge of the impactor that reduce the puncture forces.

The comparison of the side and head puncture energies in Figure 104 show that again the head impacts have a similar fit to the square of the ram characteristic size, but the puncture energies are 30 to 35 percent lower for the head than for the shell. The difference is primarily that the head and rigidly constrained impact scenario are much stiffer than for the shell side impacts. As a result, the puncture forces are reached at significantly lower ram displacements resulting in the reduction of puncture energies.

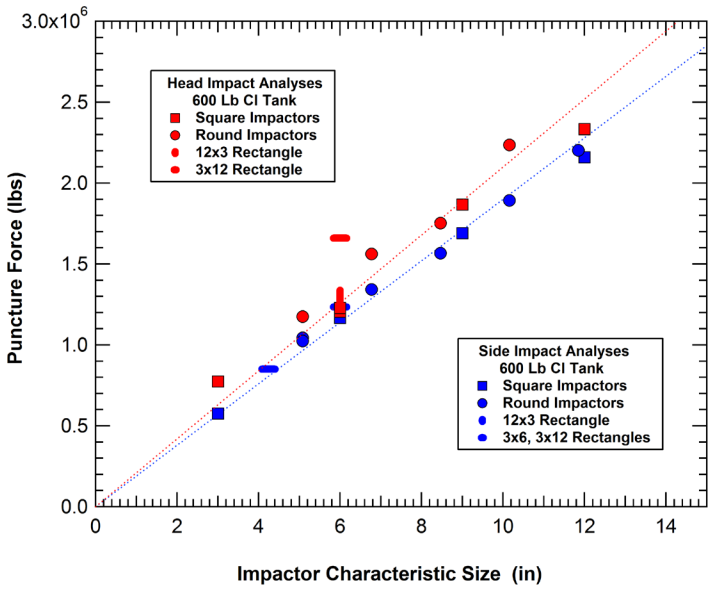

Figure 103. Comparison of the calculated head and side impact puncture forces.

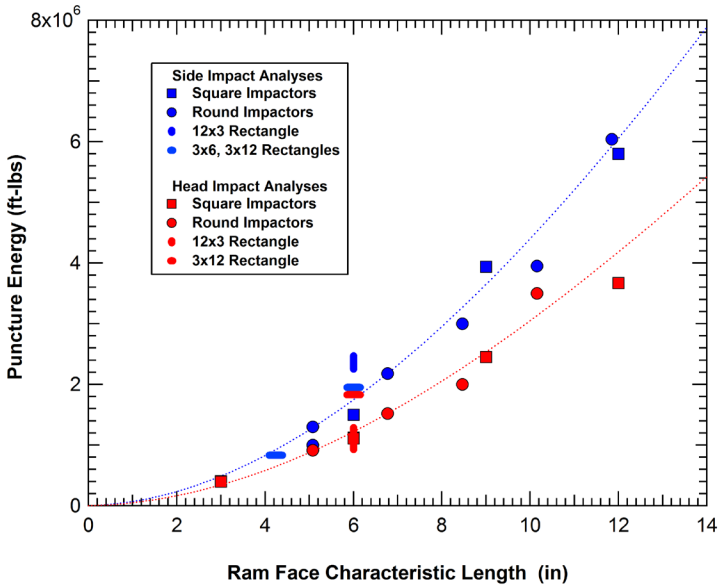

Figure 104. Comparison of the calculated head and side impact puncture energies.

3.3.2 Analysis of Complex Impactor Shapes

The above analyses of the effects of impactor sizes and shapes considered only idealized rectangular and round impactors. However, in more general derailment and impact conditions, the impactors may have a much more complex geometry or impact condition. In this section, we analyze the head impact behavior for complex impactor scenarios.

Rail Impactor

The calculated head deformations for an 11-mph impact with the rail section impactor are shown in Figure 105. The impactor forms a dent in the head shield and head at the impact location and the rail punctures the head. The section of the 11-gauge jacket supporting the head shield buckles as a result of the offset impact loads. The corresponding puncture behavior in the detailed impact patch for the rail section impactor is shown in Figure 106. As a result of the offset impact the damage is greatest at the stress concentrations at the corners of the rail head and the puncture initiates at these sites. The puncture then progresses to the point that a rail shaped flap of material is punched in the tank head.

The calculated force-deflection behavior for the rail section impact analyses is compared to those of the 3x3 and 6x6 inch impactors in Figure 107. The comparison shows that the rail impact more closely corresponds to the behavior of a 6-inch impactor. We can evaluate the characteristic size of the rail impactor by comparing the calculated head impact puncture force to the other impactors, as shown in Figure 108. The rail puncture force is shown using both the 3.7- and 5.8-inch initial estimates for the rail impactor characteristic size (defined previously in Section 3.2.4). The comparison in Figure 108 indicates that the upper range 5.8-inch characteristic size estimate correlates best with the linear fit generated from the other simple impactor geometries.

An additional head impact analyses was performed using the rail impactor in an upside-down orientation. In this impact scenario, the wider bottom flange of the rail is the primary contact zone against the head. The calculated puncture behavior in the impact zone for the upside-down rail impactor is shown in Figure 109. A comparison of the corresponding force-deflection curves for the rail impactor in the two orientations is shown in Figure 110. The comparison shows that the orientation does not have a big effect on the puncture force. The puncture energy is increased by approximately 20 percent for the upside-down orientation impact.

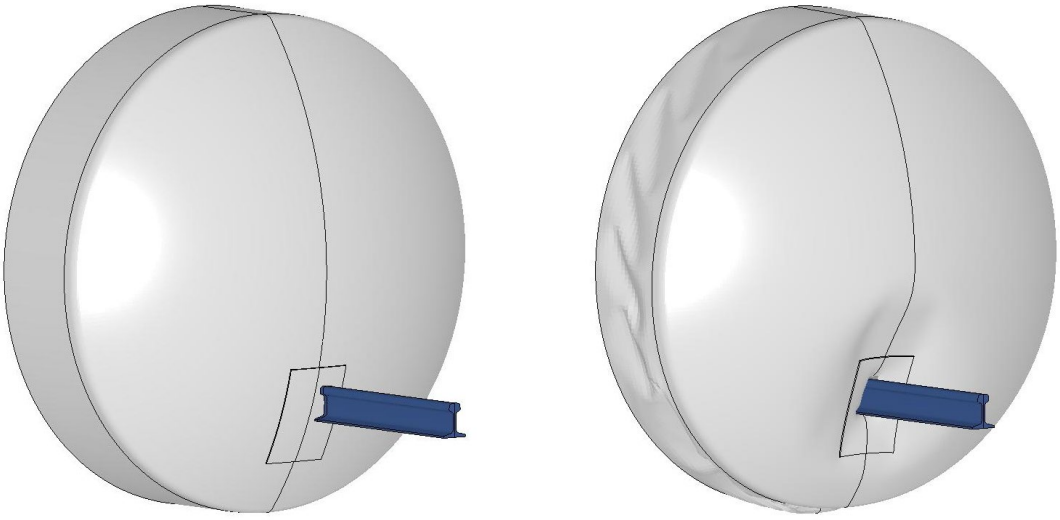

(a) Impact configuration **(b) Impact behavior**

Figure 105. Analysis of the 11-mph rail section impact behavior on the constrained head.

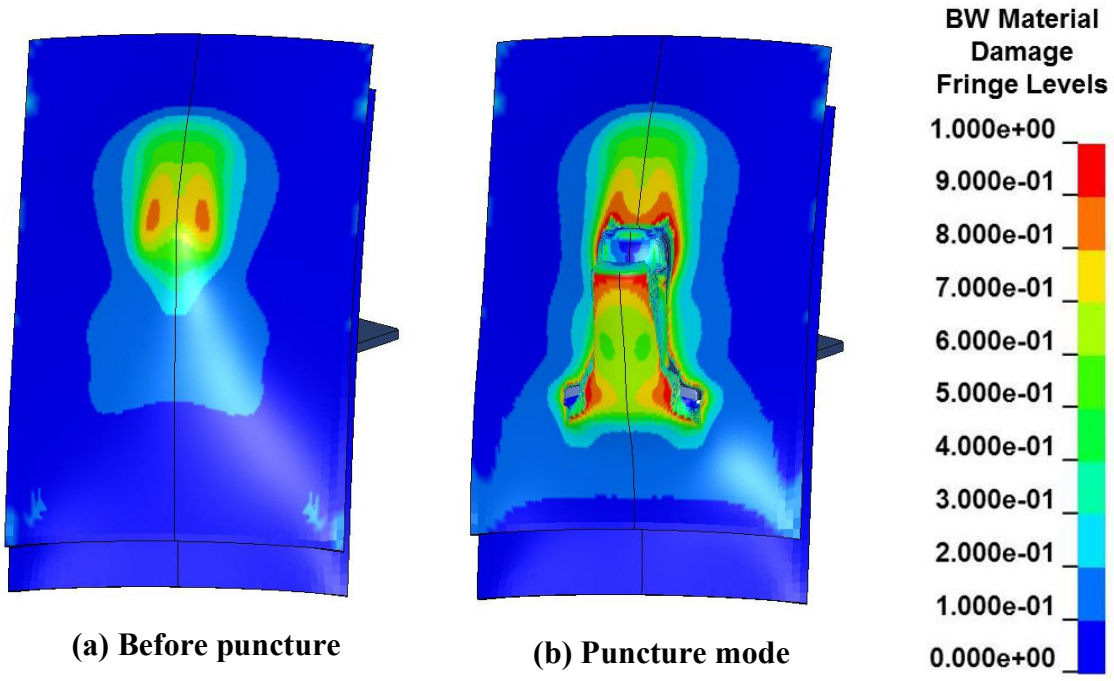

Figure 106. Calculated head impact puncture behavior for the rail section impactor.

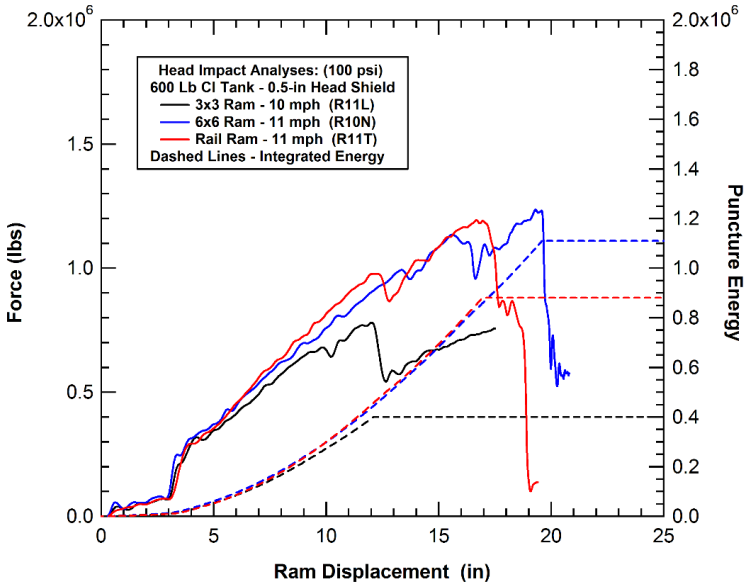

Figure 107. Calculated head puncture impact response for the rail section impactor.

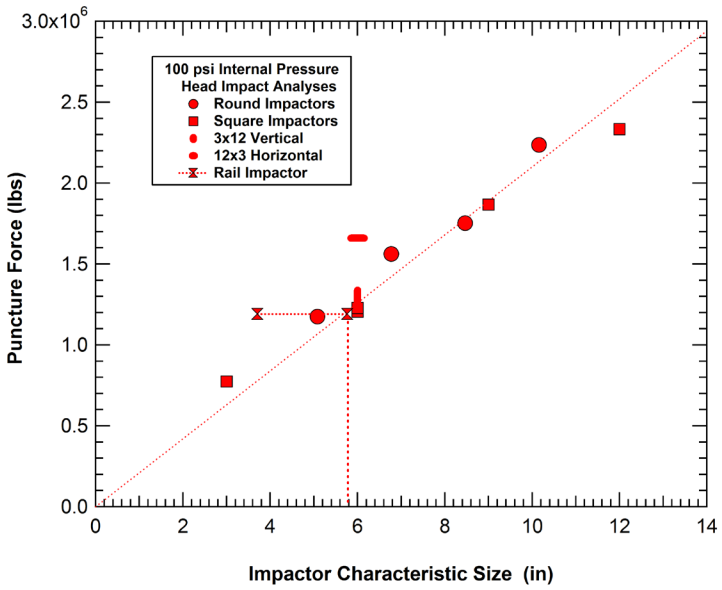

Figure 108. Calculated head impact puncture forces for various impactors.

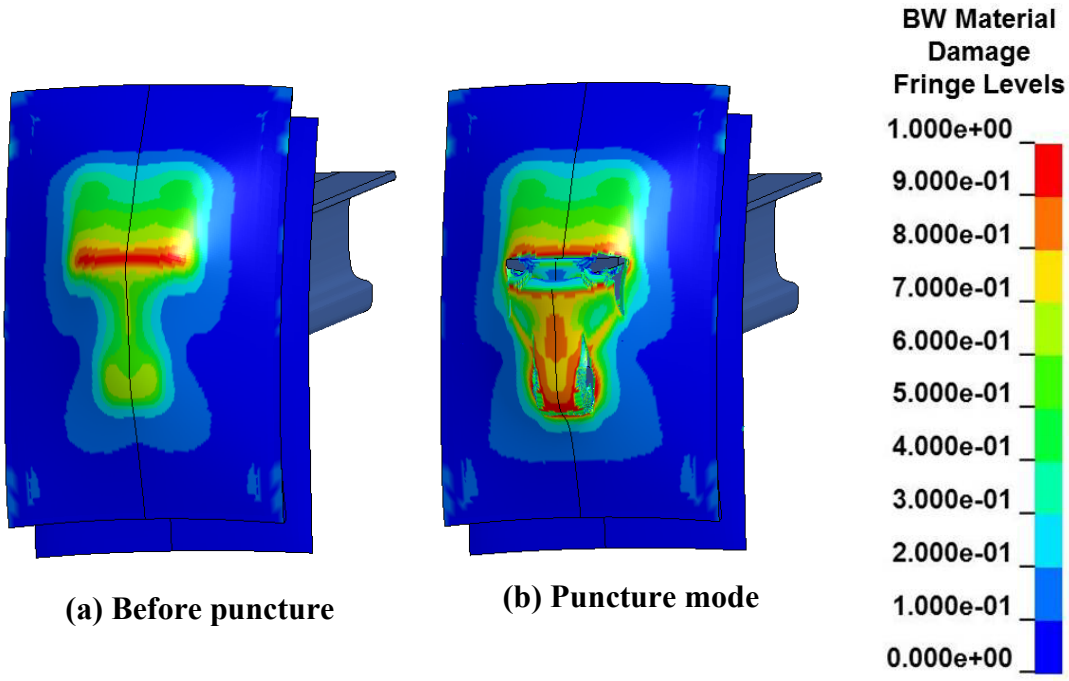

(a) Before puncture **(b) Puncture mode**

Figure 109. Calculated head puncture behavior for the upside-down rail impactor.

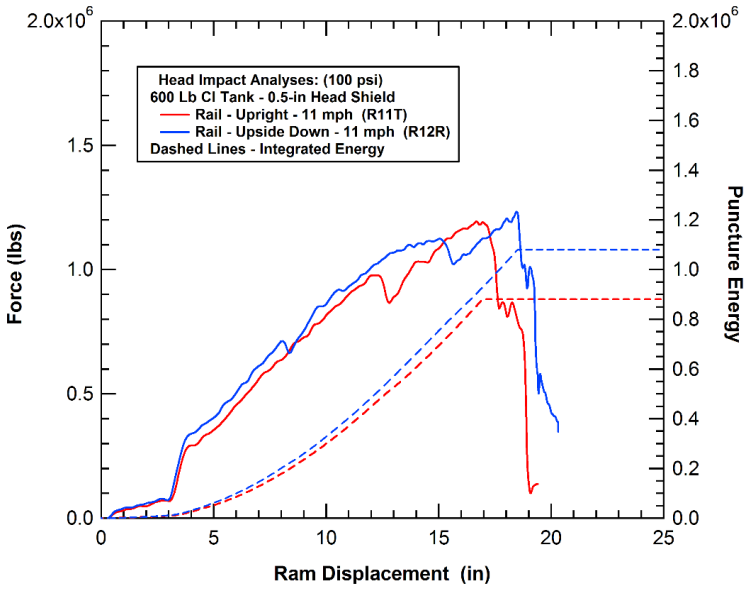

Figure 110. Calculated head impact response for the rail section impactors.

Coupler Impactor

A significant impactor threat for the tank head is a coupler. To evaluate this threat, the coupler impactor model, shown previously in Figure 87, was used to calculate the head impact puncture behavior. The initial impact analysis was performed with the constrained tank head impact configuration and an impact speed of 18 mph. The calculated head deformations for the 18-mph coupler impact are shown in Figure 111. The coupler impact forms a dent in the head shield and head at the impact location. The section of the 11-gauge jacket supporting the head shield buckles as a result of the offset impact loads.

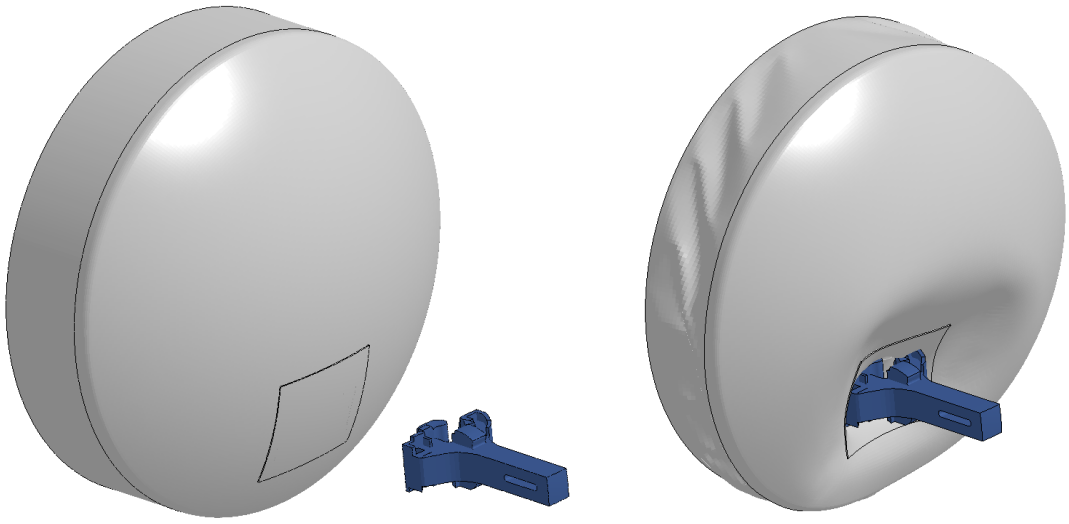

(a) Impact configuration **(b) Impact behavior**

Figure 111. Analysis of the 18-mph coupler impact behavior on the constrained head.

The corresponding damage on the inside surface of the tank head is shown in Figure 112. This damage profile shown in Figure 112 corresponds to the end of the analysis where the ram has rebounded and the contact force between the tank head and coupler are zero. The coupler impact was not sufficient to fully penetrate the tank head but the damage under the location of the greatest load concentration formed an incipient through crack in the head that would result in a release. The crack develops at a time close to the maximum ram displacement of approximately 31 inches.

A second coupler head impact analysis was performed where the impact speed was increased from 18 to 25 mph. At this impact speed, the coupler has sufficient impact energy to fully penetrate the tank head for this scenario. The puncture response is shown in Figure 113. The damage is shown at two times corresponding to a 32-inch ram displacement where a through crack in the head is fully developed and after the coupler has fully penetrated the tank head and the impact loads have significantly dropped (approximately 46 inches of ram displacement).

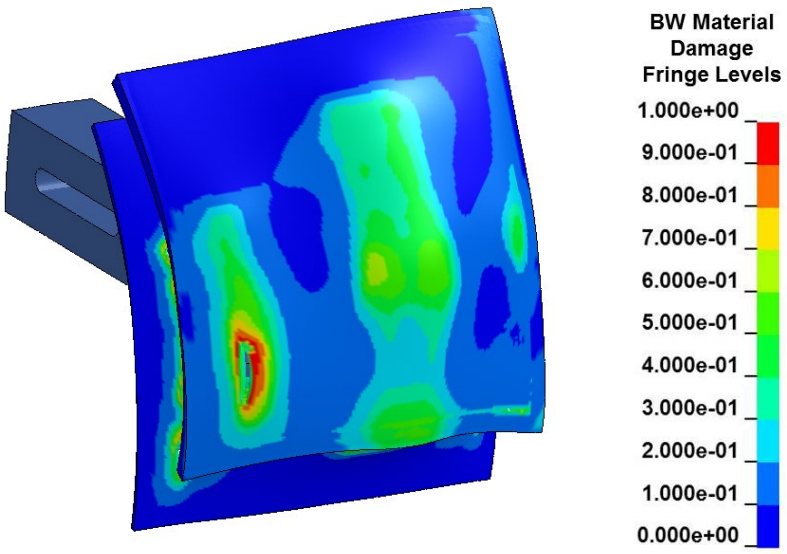

Figure 112. Calculated damage for the 18-mph coupler impact on the constrained head.

The calculated force-deflection behaviors for the two coupler impact analyses are compared to those of the 9x9 and 12x12 inch impactors in Figure 114. The force-deflection behaviors were very similar for the two coupler impact analyses up to the maximum displacement of the 18-mph impact. At the higher impact speed, the forces continue to rise until the coupler fully punctures and penetrates the tank head. The comparison to the idealized impactors in Figure 114 shows that the coupler impact more closely corresponds to the behavior of the 12-inch impactor. However, the point at which a through crack penetrates the tank head corresponds to a puncture energy of 3.15 million ft-lbs which is between that of the 9-inch and 12-inch impactors.

We can evaluate the characteristic size of the coupler impactor by comparing the calculated head impact puncture force to the other impactors, as shown in Figure 115. The coupler puncture force shown in Figure 115 is the force at which the through crack is formed in the tank head (at approximately 32 inches of ram displacement). The comparison in Figure 115 indicates that the

coupler impactor has a characteristic size of approximately 10.8 inches based on the linear fit generated from the other simple impactor geometries.

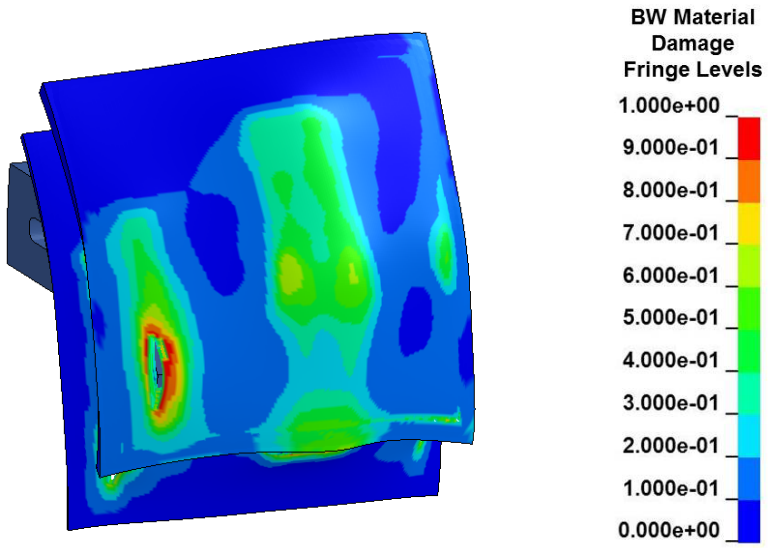

(a) Initial head puncture (32-inches ram displacement)

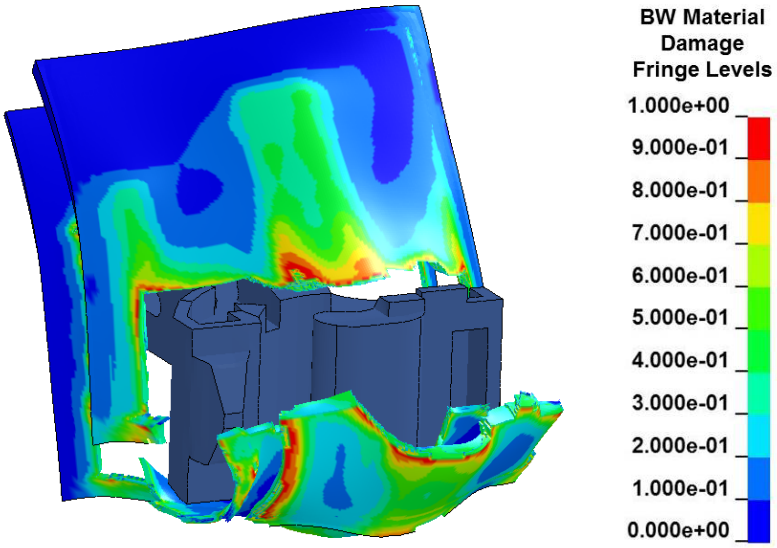

(a) Full head penetration (46-inches ram displacement)

Figure 113. Calculated damage for the 25-mph coupler impact on the constrained head.

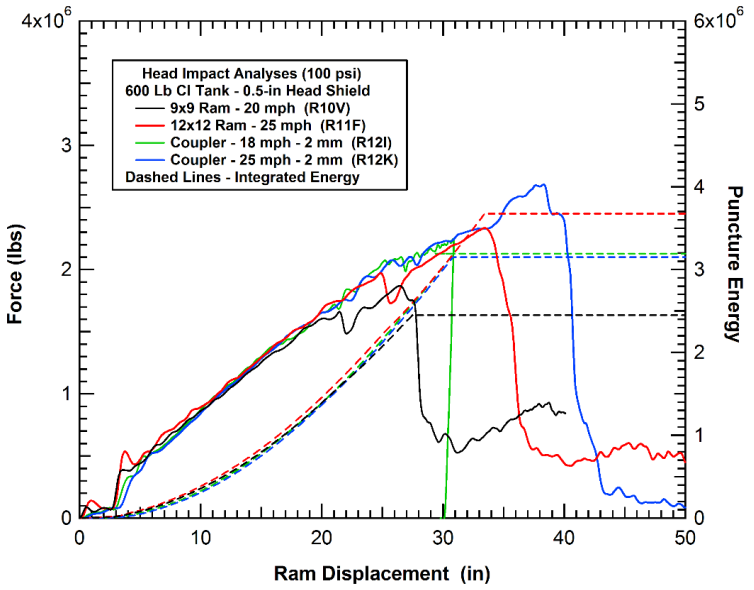

Figure 114. Calculated head puncture impact response for the rigid coupler impactor.

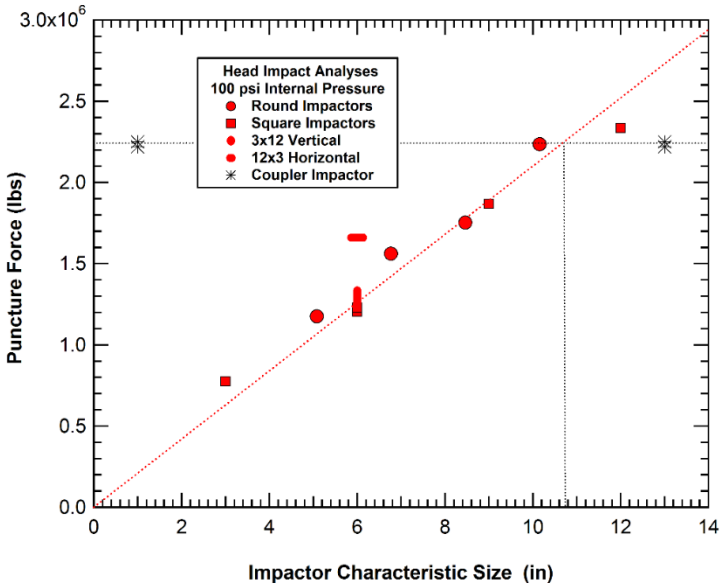

Figure 115. Calculated head impact puncture forces for various impactors.

3.3.3 Analysis of Offset Head Impact Location Effects

The above analyses all used the baseline offset head impact configuration. A parameter of interest is the impact location on the head. In this idealized impact scenario, the sill is not modeled so the distance from the tank head center should be similar in any direction. As a result, a set of analyses was performed using the half head model with one symmetry plane and different offset distances for the impact point. The offsets used are 0.0-inches (center impact), 15.0-inches, 28.5-inches, and 40.0-inches. The head impact models for the offset impact scenarios are shown in Figure 116.

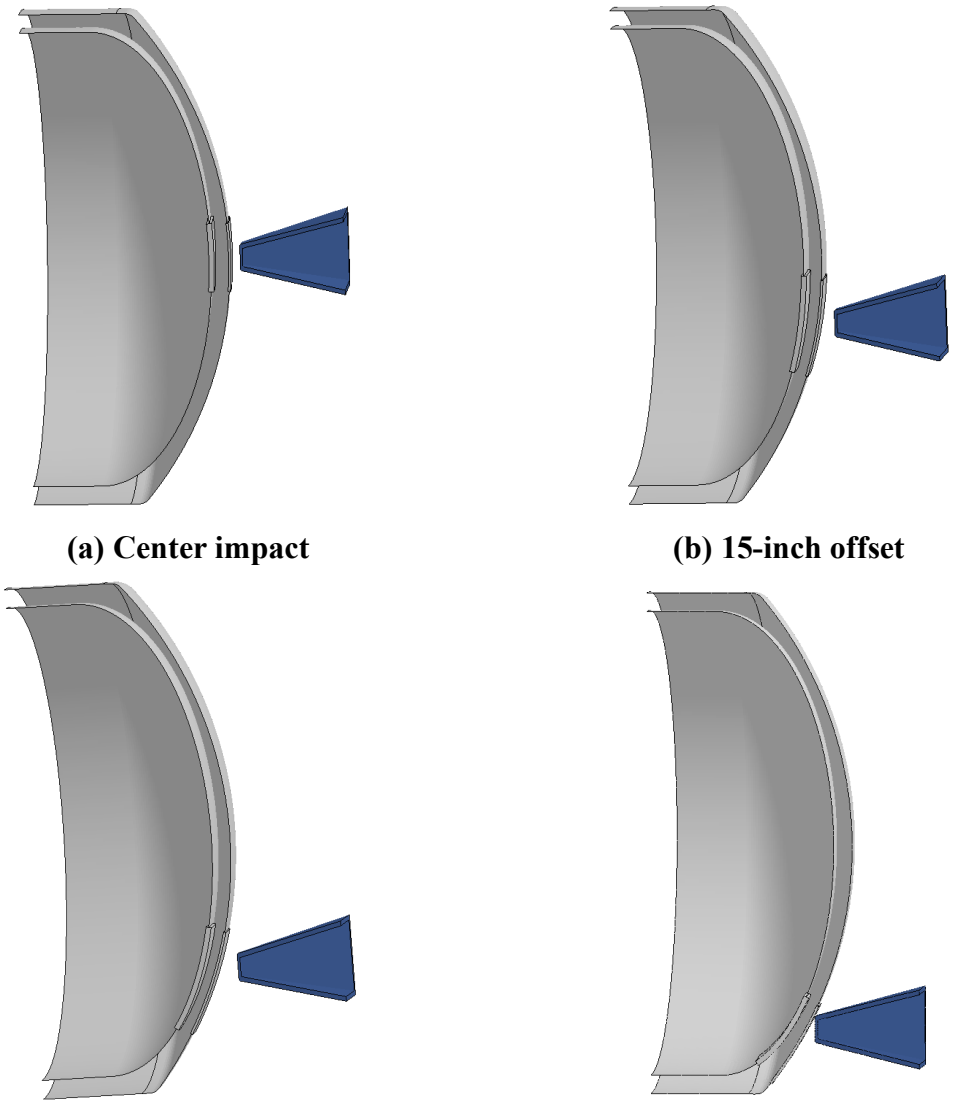

(a) Center impact **(b) 15-inch offset**

(c) 28.5-inch offset **(d) 40-inch offset**

Figure 116. Impact scenarios used in the vertical offset impact analyses.

A comparison of the calculated force-deflection curves for the four different offset head impacts are shown in Figure 117. As expected, the center head impact has the highest puncture force and puncture energy. At the center impact location, the behavior is nearly axisymmetric and the load around the perimeter of the impactor is more uniform, resulting in a higher puncture force. As the impact location moves further from the head, the angle between the normal vectors of tank head impact position and the impactor face becomes greater and the corresponding puncture force drops.

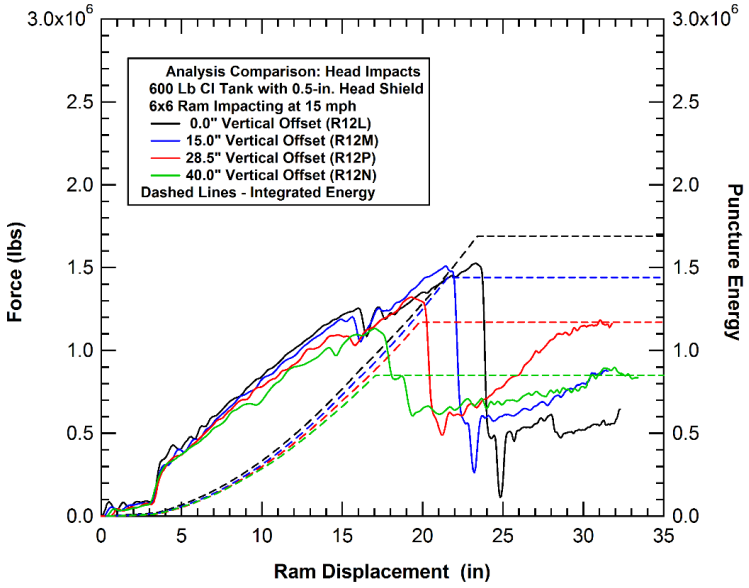

Figure 117. Calculated force-deflection behaviors for variable offset head impacts.

3.4 Analysis of Impact Speed Effects

For the analyses described in this report, the selection of the impact speed is primarily based on engineering judgment with the objective of picking an impact speed that will have a high probability of puncturing the tank but not have too large of a residual kinetic energy. The assumption is that the puncture energy for this impact speed is a good approximation to the threshold puncture energy for the tank. This methodology was used previously in the NGRTC program (Kirkpatrick, 2009a). In that study, some analyses were performed at different impact speeds to investigate the magnitude of the effects. In this section we revisit the impactor speed effects for the 600 lb chlorine tank car design and the updated impact analysis methodologies used in this study.

3.4.1 Analysis of Impact Speed for Side Impacts

For this side impact comparison, a set of the normal side impacts summarized in Table 2 were repeated at higher impact velocities. The comparison of the original force-deflection curves for the 3-inch, 6-inch, 9-inch, and 12-inch square impactors and the corresponding behavior for the higher speed impacts is provided in Figure 118. In this comparison, the impact speed was increased by 5 mph for each of the impact scenarios. For many impacts the effects of the impact are relatively small with slightly higher forces produced by increased inertial resistance and corresponding small reductions in the ram displacement required to puncture the tank.

For the larger impactors, the impact speed has a slightly larger effect on the impact behavior. For the 9-inch and 12-inch impactors the higher speed impact results in a puncture near the end stage of the initial loading response of the force-deflection curve. By increasing the impact speed, some of the late time tank impact kinematics and interaction with the reaction wall are eliminated (some of these boundary condition effects are discussed below as well as in Section 4.3.1 of this report). As a result, the calculated puncture energy will be reduced at the higher impact velocity.

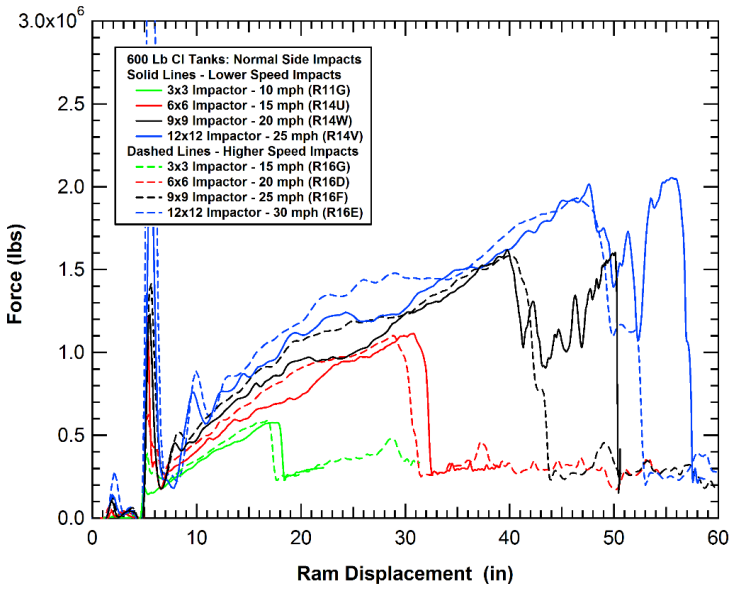

Figure 118. Comparison of side impact behaviors at different impact speeds.

The comparison of the puncture forces and puncture energies for the baseline and higher speed impacts are provided in Figure 119 and Figure 120, respectively. Overall, there is little difference in the puncture forces with a 4 percent reduction in the slope of the linear fit to the higher speed impacts. The effect of the impact speed on the puncture energies is slightly larger than on the puncture forces but still relatively small with on average an approximately 9 percent reduction in the puncture energies for the cases analyzed.

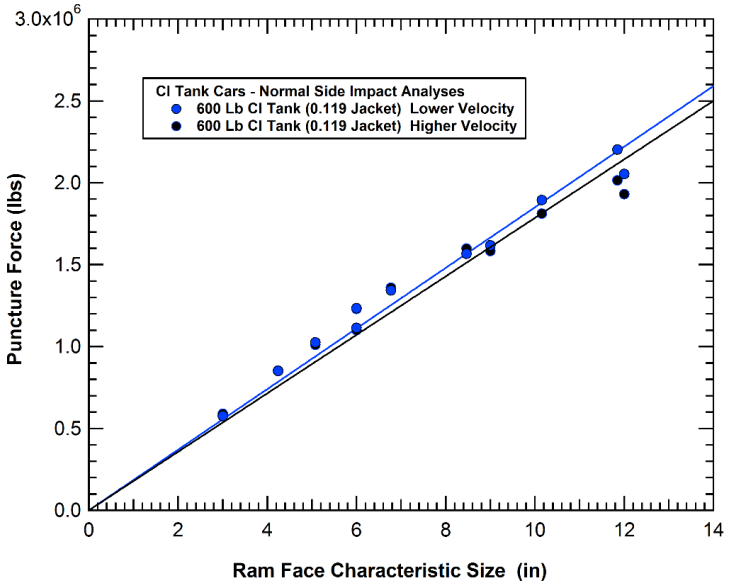

Figure 119. Comparison of side impact puncture forces at different impact speeds.

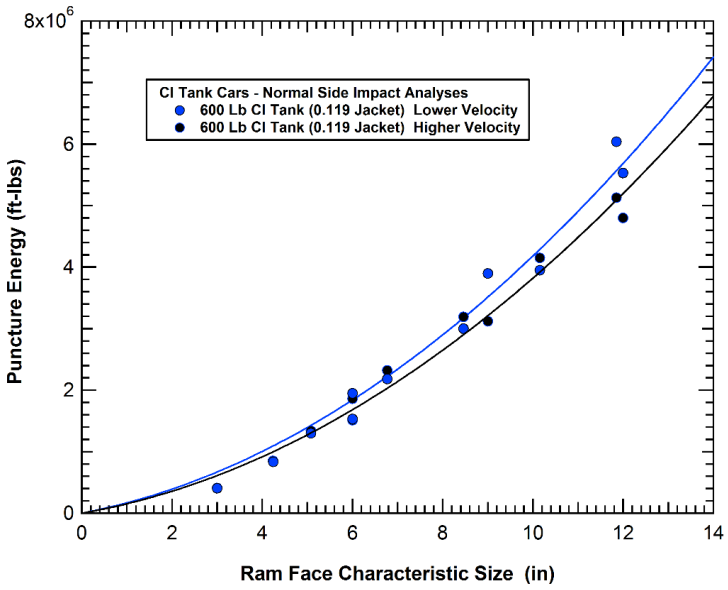

Figure 120. Comparison of side impact puncture energies at different impact speeds.

An alternative evaluation of the speed effects was performed by running the 9.55-inch-diameter impactor at impact speeds of 10, 15, 20, and 25 mph. A comparison of the force-deflection behaviors is shown in Figure 121. All the curves have similar behaviors in the initial phase of the impact loading. However, the effects of the unloading and interaction with the wall appear much earlier in the force-deflection behavior for the lower speed impacts. Note that the 20 and 25 mph impacts puncture the tank, but the 15 and 10 mph impacts are below the puncture threshold for this tank and impactor.

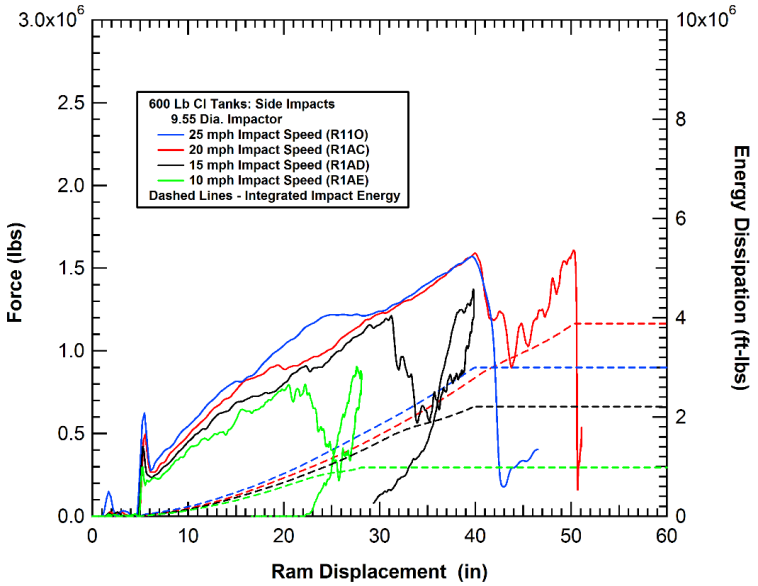

Figure 121. Comparison of the tank side loading response at different speeds.

An alternative comparison for the different speed impacts, shown in Figure 121, is to plot the force-time histories, as shown in Figure 122. In this comparison we see that the timing for the initial unloading is similar and initiates at around 150 ms. However, the point at which the wall

interaction and reloading of the tank occurs is earlier for the higher speed impacts. This is a result of both the ram and tank moving at a higher speed in the unloading for the higher speed impact scenarios.

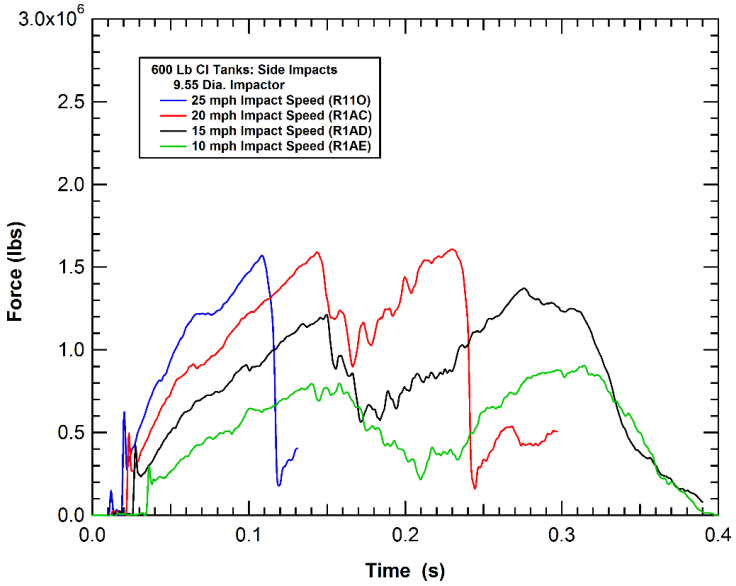

Figure 122. Comparison of the tank side loading response at different speeds.

The lower bound of side impact speeds was analyzed for the 9.55-inch-diameter round impactor. An analysis was performed using a steady rate displacement control boundary condition at a loading rate sufficiently slow to minimize dynamic impact effects (quasistatic). The calculated force-deflection behavior for this analysis is compared to the 25-mph impact in Figure 123.

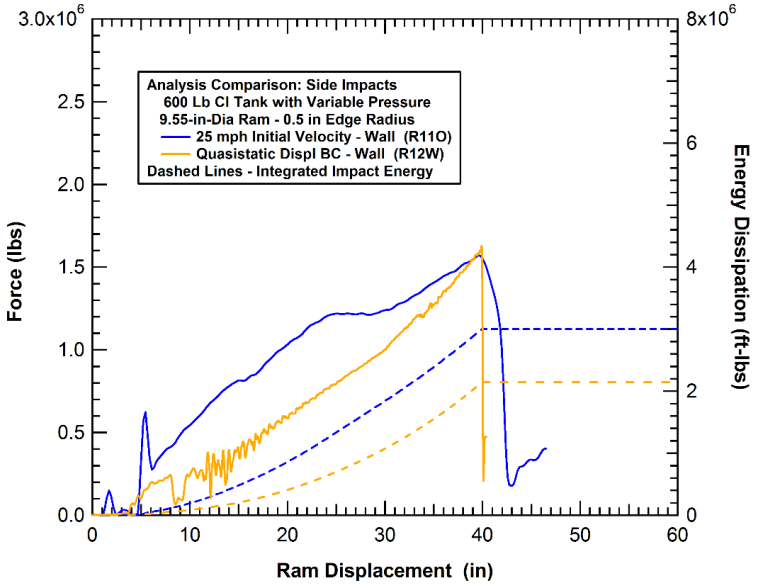

Figure 123. Comparison of the tank side loading response at different speeds.

The comparison shows that the puncture forces again are similar, but the loading rate can significantly change the force-deflection behavior for this side loading scenario. These effects, and their interaction with different tank BCs, will be explored further in Section 4.

3.4.2 Analysis of Impact Speed for Head Impacts

A set of analyses were performed to evaluate the effects of the impact speed for the baseline constrained tank head impact condition. The head was pressurized to 100 psi and the 6x6 inch square impactor was used. Impact analyses were performed at 11 and 14 mph. In addition, a quasistatic loading was applied where the ram was given a steady rate displacement control boundary condition at a rate sufficiently slow to minimize dynamic impact effects.

The calculated head force-deflection characteristics for the three loading rates are compared in Figure 124. The comparison shows that there is little difference in the calculated deformation or puncture behavior. Thus, the behavior of the constrained tank head is mostly independent of the impact speed. The corresponding effects for a head impact on an unconstrained tank will be explored further in Section 4.

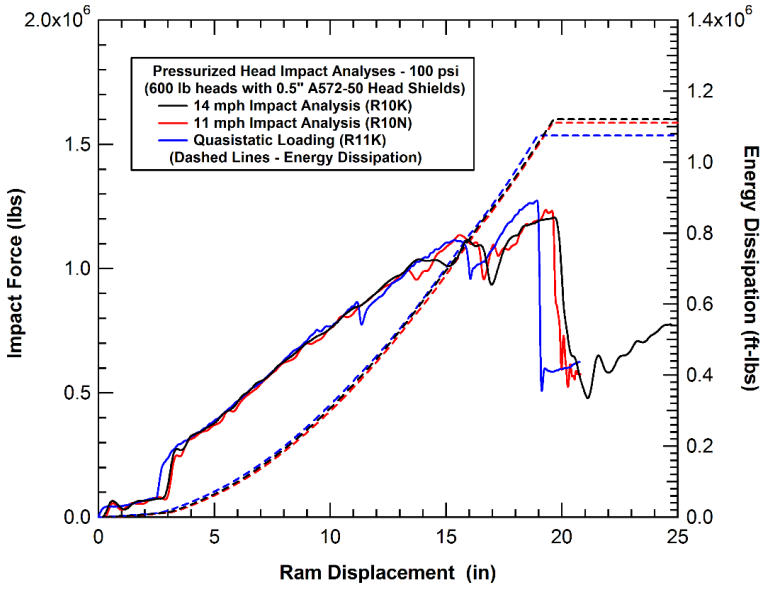

Figure 124. Comparison of Head impact behaviors at different impact speeds.

3.5 Analysis of Tank and Lading Temperature Effects

An important assumption used in the above impact analyses are that the tank and lading are at a nominal temperature of approximately 78° F. From the chart of chlorine physical properties in Figure 125, this temperature produces an internal vapor pressure for the tank of 100 psi. The corresponding outage volume for a tank loaded to the specified limit would be 10.6 percent. In this section, we investigate the effects that the lading will have on the impact and puncture response if the temperature is significantly different.

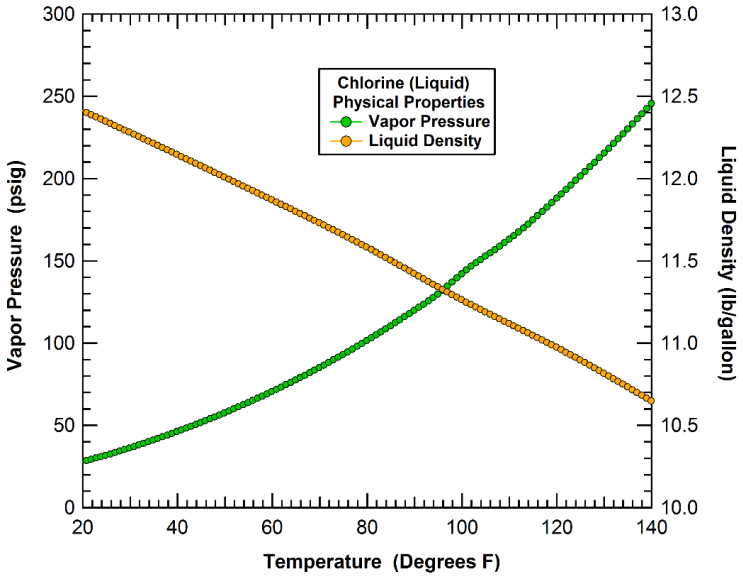

Figure 125. Physical properties of chlorine as a function of temperature.

From the physical properties shown in Figure 125, we see that the vapor pressure increases, and the liquid density decreases as the temperature rises. A decrease in the liquid density will produce an increase in the liquid volume with a corresponding reduction in the outage volume. Both increasing the pressure and reducing the outage can reduce the puncture resistance of a tank car. As a result, a higher temperature for the tank and lading are expected to lower the tank puncture energies in impacts.

The condition analyzed in this section is a 105J600W chlorine tank car at an equilibrium temperature of 105° F. This temperature increases the internal vapor pressure for the tank to 155 psi and lowers the corresponding outage volume for a tank loaded to the specified limit to 7.5 percent. The resulting pressure-volume relationships for the chlorine tank at 78° and 105° F are compared in Figure 126. The comparison shows that the higher temperature results in significantly higher pressures at the initial condition and the pressures rise more rapidly as a result of volume changes produced by dent formations.

The calculated puncture forces and energies in normal side impacts for the chlorine tank car at the two temperature conditions are compared in Figure 127 and Figure 128. The comparison shows that the temperature has little effect on the puncture forces. This result was expected since the puncture force for a given impact geometry is primarily a function of tank shell thickness and strength which are unchanged in these scenarios. However, the corresponding puncture energies are reduced on average approximately 25 percent.

In addition to the normal side impacts, a set of 45-degree oblique impacts were also performed for the 105J600W chlorine tank car at an equilibrium temperature of 105° F. A summary of results for all the normal and oblique impacts for the tank at higher temperature is given in Figure 129. In the figure, the calculated puncture energies at 105 F are normalized by the puncture energies at 78° F for the corresponding impact conditions. In addition, an average value line is added to the graph. We see that on average, the increase in temperature dropped the puncture energies by 20 percent. However, the puncture energies for smaller impactor sizes are

more similar at the two temperatures. This is because the impact response for small impactors is dominated more by the structural stiffness. The internal pressure (and pressure increase) plays a smaller roll for the small dent sizes prior to puncture with the small impactor sizes.

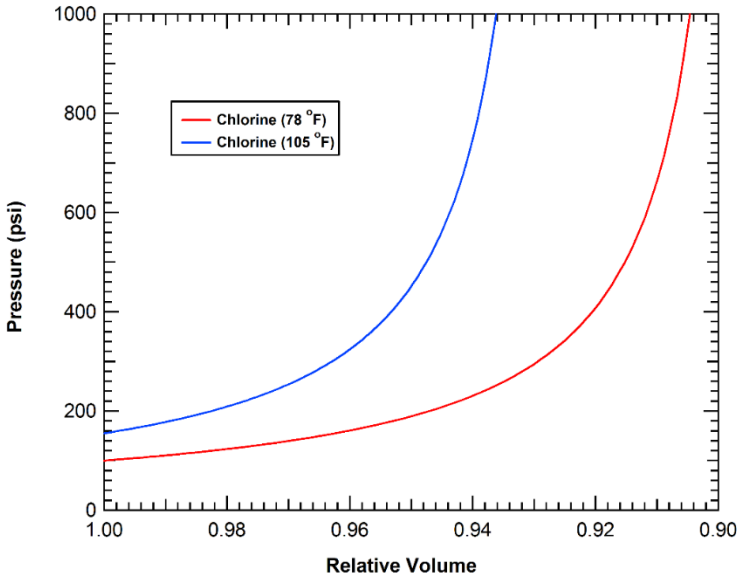

Figure 126. Pressure-volume relationships for the chlorine tank car at 78º and 105º F.

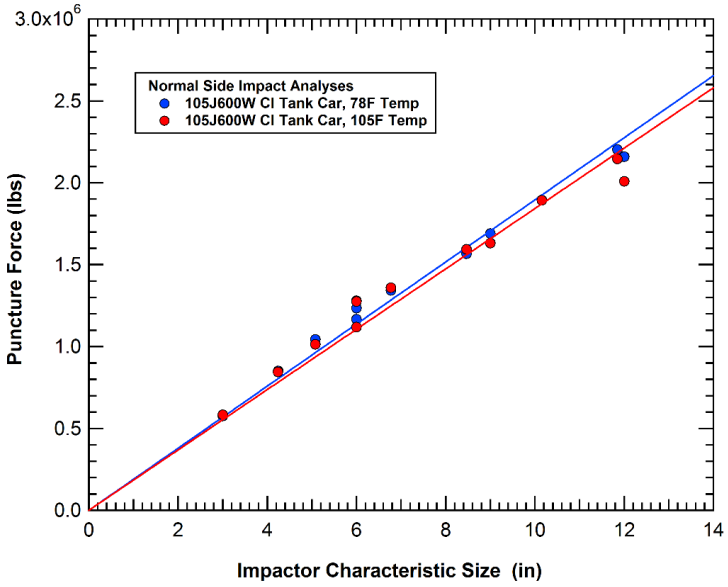

Figure 127. Comparison of side impact puncture forces at 78º and 105º F.

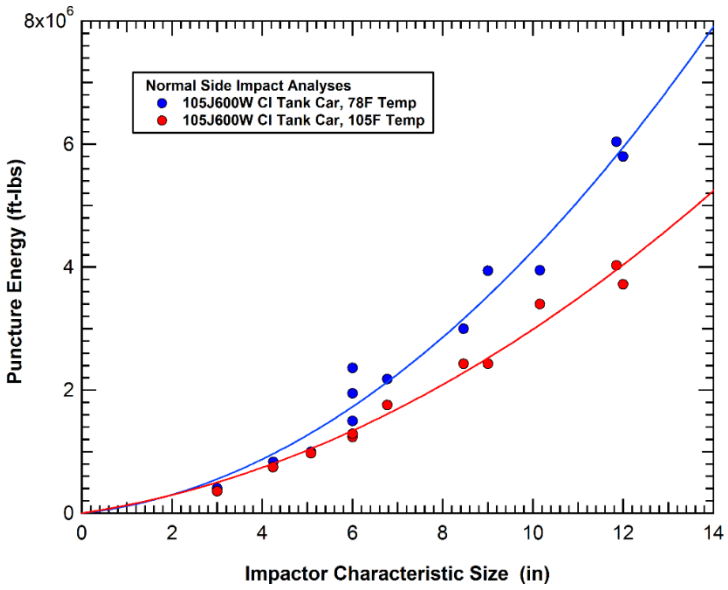

Figure 128. Comparison of the side impact puncture energies at 78° and 105° F.

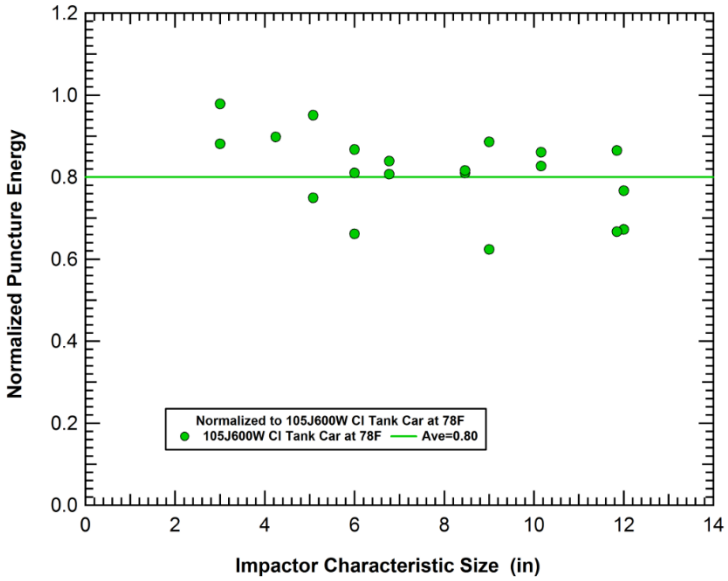

Figure 129. Normalized side impact puncture energies at 105° F.

4. Analysis of General Impact Conditions

4.1 Introduction

In this section, the detailed BW failure model described in Section 2 is applied to assess various tank and head puncture conditions. The analyses in this section are focused on expanding the impact scenarios to understand the tank response when exposed to more general impact conditions.

4.2 Oblique Impacts

An initial set of oblique impact analyses was performed using the 12x12 inch square impactor at an impact speed of 25 mph. The obliquity angles were 15, 30, and 45 degrees as shown in Figure 130. These oblique impact analyses are significantly different than the rotated impactor analyses, previously described in Section 3.2.4, because the impactor trajectory is now rotated relative to the tank axis. In the rotated impactor analyses the orientation of the impactor was rotated but the impact trajectory was still normal to the tank. The force deflection curves for these oblique impacts are compared to each other and to the normal impact in Figure 131.

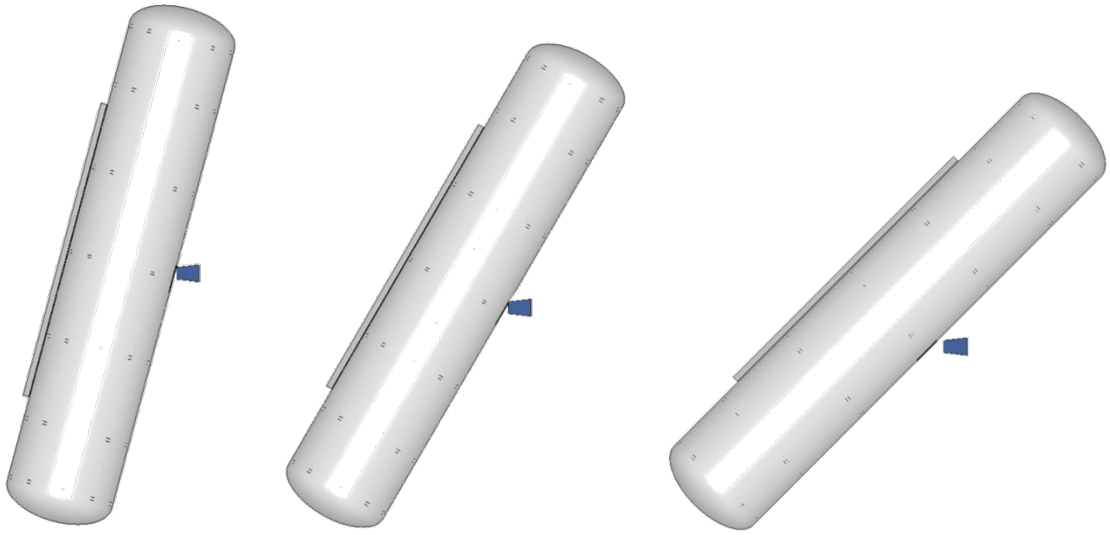

(a) 15-degree obliquity (b) 30-degree obliquity (c) 45-degree obliquity

Figure 130. Various oblique impact conditions investigated for side impacts.

The force deflection characteristics for the oblique impacts show a few specific trends. First, the force level at which the tank punctures is reduced for higher obliquity angles. This trend is expected since the impact face is now rotated relative to the tank wall producing stress concentrations at the edges and corners of the impact face (as seen in the rotated impactor analyses described in Section 3.2.4).

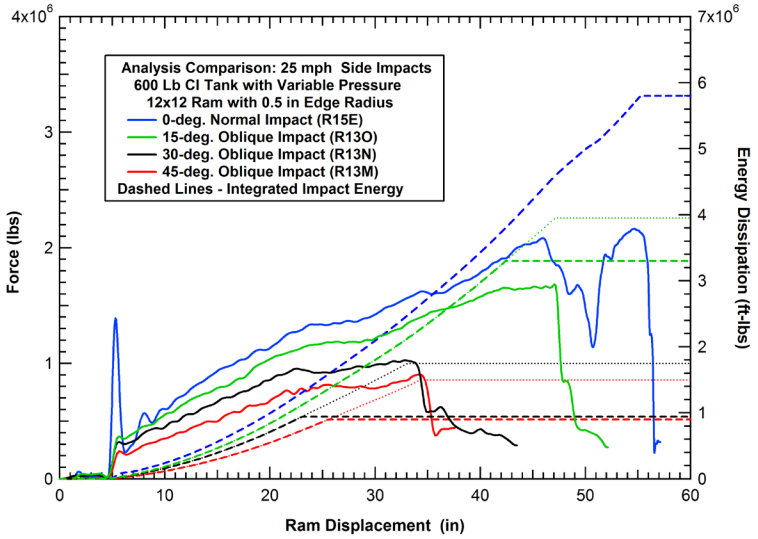

Figure 131. The effects of impact obliquity on the tank impact and puncture response.

One significant difference seen in the oblique impacts compared to the normal impact with a rotated impactor is the puncture initiation behavior. A sequence of the impact damage and failure of the tank wall for the 45-degree oblique impact is shown in Figure 132. The sliding contact with the oblique impact results in large concentrations of damage at the corners of the impactor. These concentrations result in cracks that penetrate the tank wall significantly earlier than the time at which the entire impact face punctures the tank wall. Thus, with this type of oblique impact scenario, it is possible to have conditions that produce small cracks through the tank wall but do not produce a large puncture hole.

A second unique feature of the force-deflection curves in Figure 131 is that the slope of the force-displacement curve is reduced as the impact obliquity increases. However, this can be attributed to the reference displacement in the plot being the ram displacement which is no longer normal to the tank axis. If we modify the plot to use only the component of displacements normal to the tank axis, the slopes of the curves are much more consistent, as seen in Figure 133. This suggests that the force buildup is a function of the component of the ram displacement normal to the tank axis.

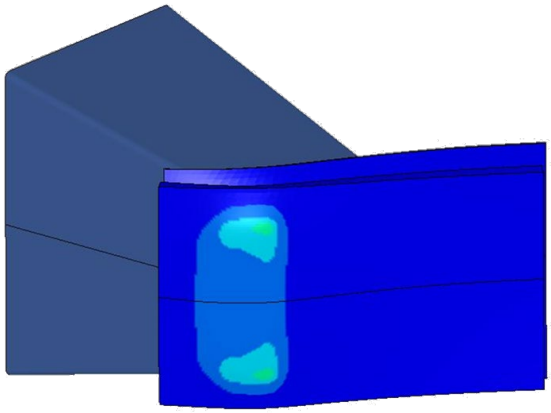

(a) Initial impact

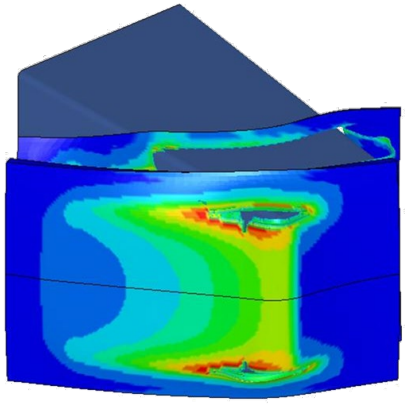

(b) Fracture at impactor corners

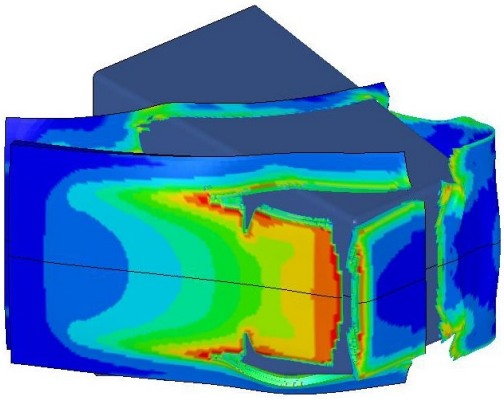

(c) Full tank puncture

Figure 132. Oblique impact damage development and puncture behavior for side impacts.

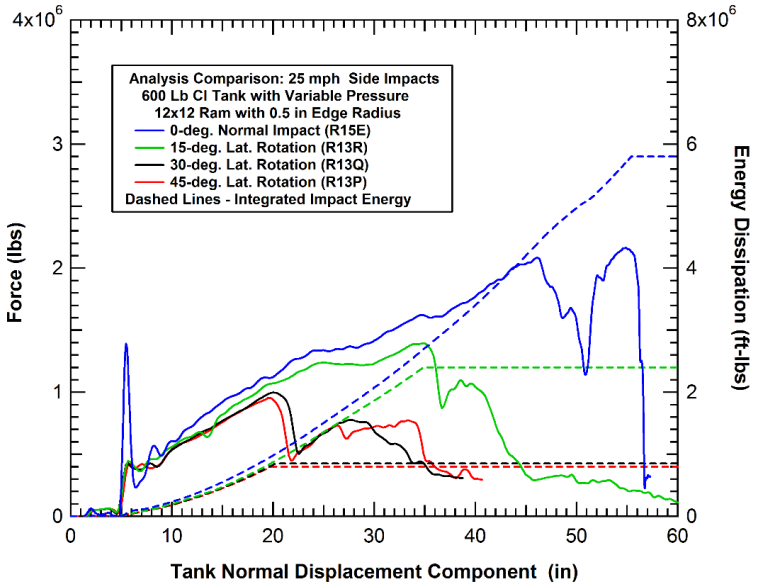

Figure 133. The effects of impact obliquity on the tank impact response and puncture.

Further insight into the oblique impact behavior can be obtained by comparing the oblique impact with the normal impact where the impactor face is rotated by the same angle. Here we will compare the 45-degree rotated impactor and 45-degree oblique impact configurations shown in Figure 134. The comparison of the corresponding force-displacement curves for these two impact scenarios is shown in Figure 135 (using the tank normal displacement). By correcting for the tank normal displacement, the two curves have a similar slope. In addition, by using the rotated impactor, the puncture forces and puncture energies are relatively similar.

In addition to the above oblique analyses with the 12x12 inch square impactor, a full set of analyses was performed with the full range of impactor sizes and shapes at a 15, 30, and 45-degree oblique impact angle. Comparisons of the normal and oblique impact puncture forces and energies are provided in Figure 136 and Figure 137, respectively. The puncture forces are reduced with increasing obliquity angles and at the 45-degree oblique impacts the puncture forces are more than 50 percent lower than the normal impacts for the largest impactor. However, as the impactor size is reduced the differences in puncture force are also reduced. At a 6-inch characteristic size the 45-degree oblique impact puncture force is only reduced by 40 percent compared the normal impact. Finally, for the 3x3 inch impactor there is very little difference between the normal and oblique impact puncture forces. As a result, a linear fit to the oblique puncture force data would not intercept the origin of the graph as used in the normal impact data. The fits shown for the oblique impacts correlate the puncture forces to the square root of the impactor characteristic size.

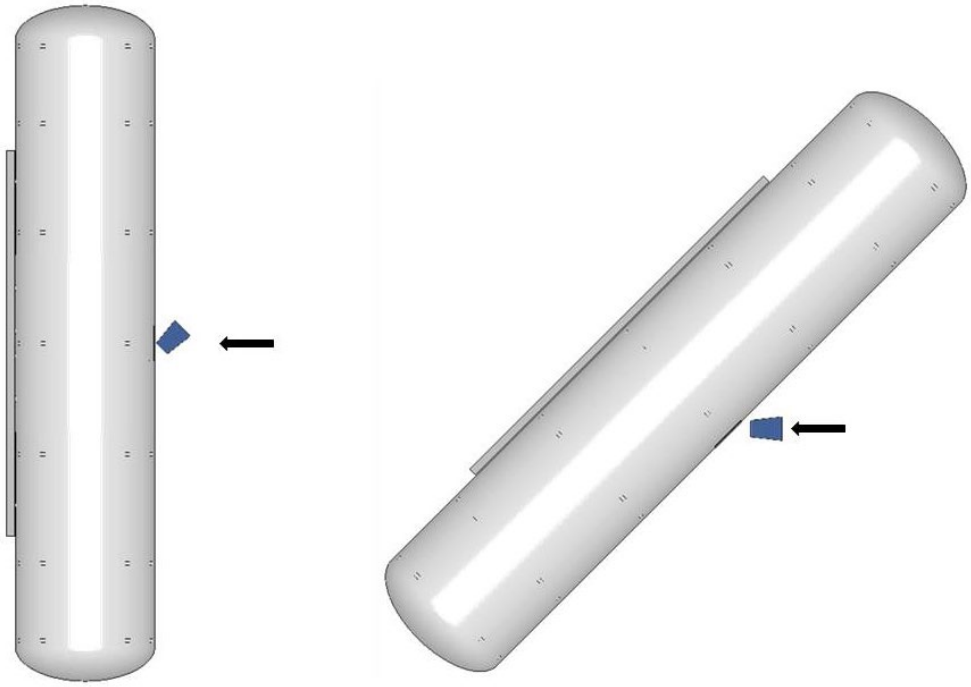

(a) 45-degree impactor Rotation (b) 45-degree oblique impact

Figure 134. Effect of impactor angle on oblique impact response for side impacts.

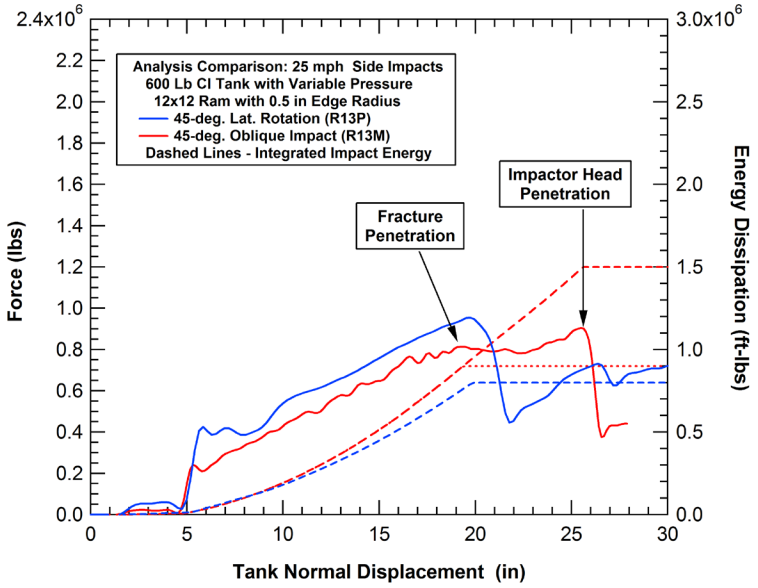

Figure 135. The effects of impact obliquity on the tank impact response and puncture.

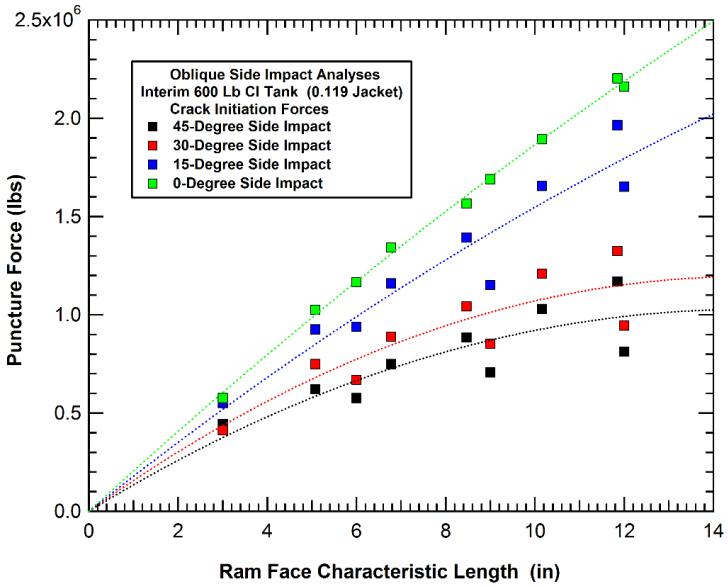

Figure 136. Comparison of puncture forces for normal and oblique impacts.

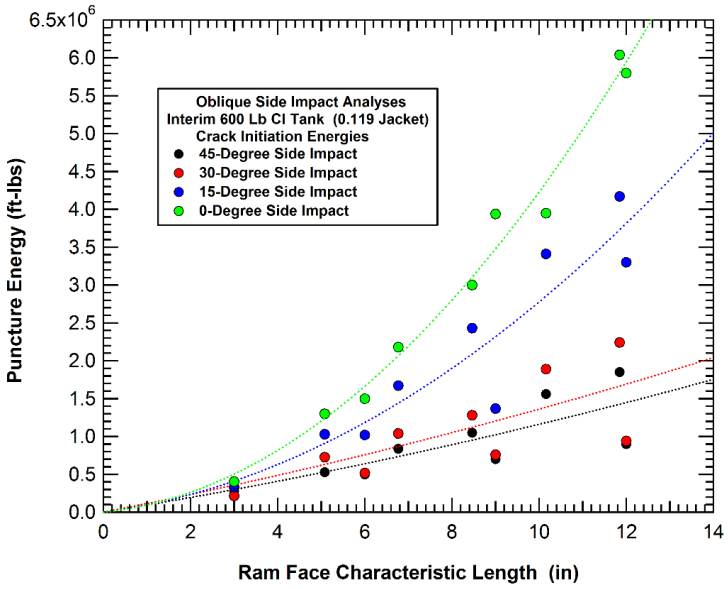

Figure 137. Comparison of puncture energies for normal and oblique impacts.

The puncture energies for the oblique impact show similar trends to the puncture forces. The puncture energies for the largest impactors are reduced by roughly 70 percent. Again, as the impactor size is reduced the differences in puncture energies are also reduced. At a 6-inch characteristic size the oblique impact puncture energy is only reduced by 50 percent compared the normal impact. Finally, for the 3x3 inch impactor there is very little difference between the normal and oblique impact puncture energies. For the oblique impact puncture energies, a linear fit of the data was used.

4.3 Impact Boundary Condition Effects

4.3.1 Side Impact Constraint Effects

A series of analyses were performed to investigate the effects of the constraint level on the tank response. The initial analyses are for the side impact of the 600 lb chlorine tank car. The impactor selected for these analyses was the 9.55-inch-diameter round impactor. Three different levels of constraint were considered as shown in Figure 138. The highly constrained boundary condition is the tank shown in Figure 138(a) backed by the rigid impact wall that has been used for the majority of the side impact analyses in this report, as well as the previous NGRTC analyses (Kirkpatrick, 2009a). The unconstrained boundary condition is a single tank that is free to translate, shown in Figure 138(b). The moderately constrained boundary condition is two deformable tanks sitting side-by-side, shown in Figure 138(c).

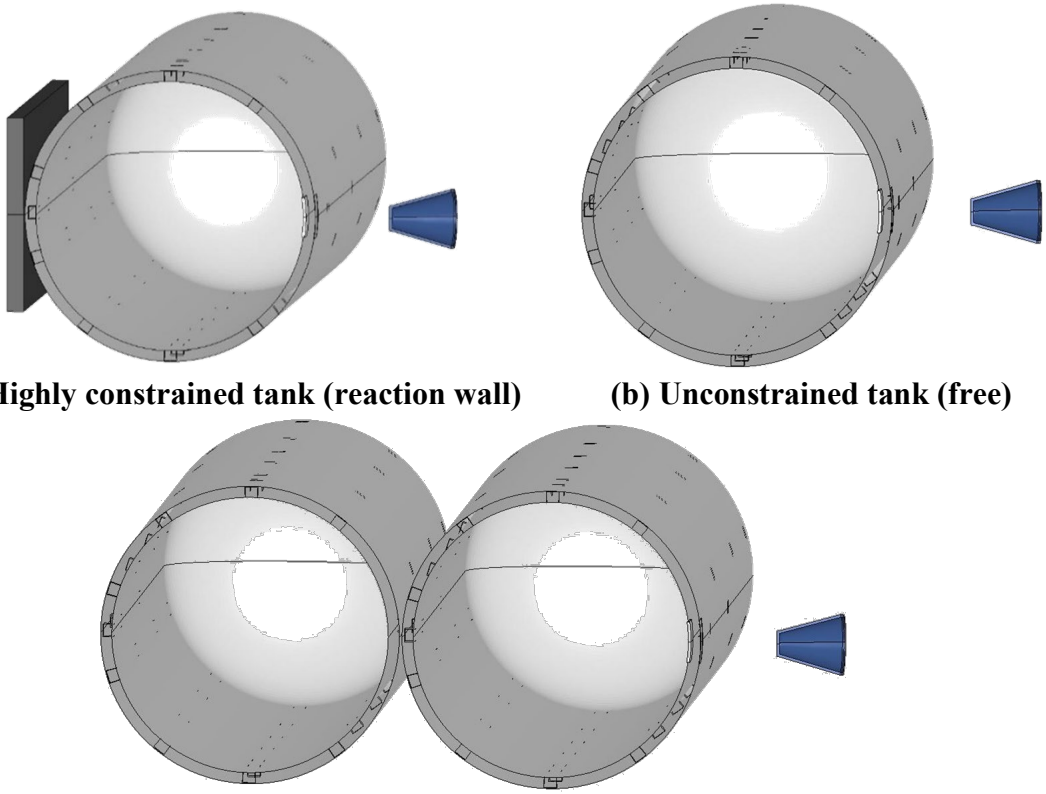

(a) Highly constrained tank (reaction wall) **(b) Unconstrained tank (free)**

(c) Moderately constrained tank (side-by-side tanks)

Figure 138. Various tank motion constraint BCs for side impacts.

One of the issues in evaluating the effects of the BCs is that for many impact conditions the constraint on the back of the tank is not significant. If the impact speed is sufficiently high for a given size impactor, the tank will be punctured before there is sufficient time for the tank to move. For example, the force-deflection curves for the 25-mph impact of the 9.55-in-diameter impactor for the 600 lb chlorine tank car with the impact wall and free BCs are compared with the red and blue curves in Figure 139. The comparison shows that the curves are nearly identical and the constraint conditions behind the tank are not significant for this impact scenario. With a fully loaded tank and relatively fast impact speed, the inertial constraint of the tank is the dominant factor. This example demonstrates that the scenario selected for the assessment of the

BCs is important. It must have a sufficiently large impactor moving sufficiently slowly to allow for the constraint conditions behind the tank to be significant.

To further demonstrate the importance of the inertial constraint on this impact scenario, the two 25 mph impacts using the 9.55-in-diameter impactor (wall and free) were repeated but the target tank models were modified to have the weight of an "empty" tank (the lading pressure effects were maintained). The comparison of the behaviors for the baseline and lighter "empty" tanks is shown with the black and green curves in Figure 139. The comparison shows that the lighter tanks develop forces more slowly since the ram motion does not need to accelerate as much mass. Similarly, the effects of the tank dynamic response and BCs are seen much earlier since the lighter tank has higher natural response frequencies. For these analyses the boundary constraint plays a large role. The tank constrained by the impact wall provides a reaction force where the impactor loads recover and eventually puncture the tank. The free tank is pushed away from the impactor and is not punctured.

To investigate the boundary constraint effects, a modification was made to the impactor BCs. In the majority of analyses performed in this study, the impactor was designed to represent the ram car from the NGRTC program (Kirkpatrick, 2009a). As such, the impactor model was given a 295,000 lb weight with an initial impact velocity and was constrained to 1D motion along the initial trajectory. The impactor was free to decelerate and even reverse direction as it interacted with the target tank.

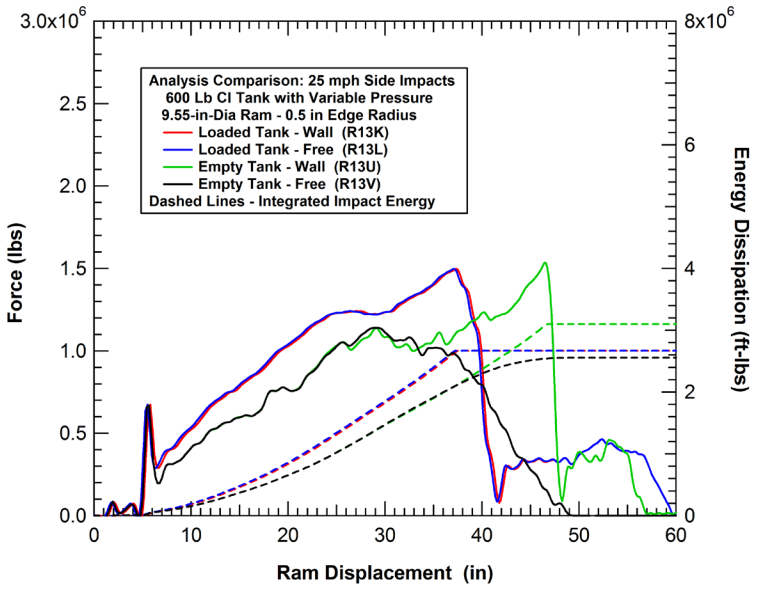

Figure 139. The effects of constraint conditions for a 25-mph impact and 9.55-inch-diameter impactor, with differing tank weights.

For many of the analyses in this section, the impactor was prescribed to have a constant velocity impact condition. This is more representative of the loading for an impactor that is attached to a longer section of train in a derailment where the very large mass results in small changes in impactor velocity over the duration of any individual impact event. A comparison of the force-deflection characteristics for the side impact response with the three different constraint conditions (wall, tank, free) is shown in Figure 140. For reference, a corresponding force-

deflection curve for the impact scenario of a 25-mph impact with the 295,000 lb impactor is also shown on the graph.

The comparison shows that the initial portion of the force-deflection curves for all three 15 mph impacts are identical (up to approximately 30 inches ram displacement). All three impacts reach an initial peak force that was very close to the failure level before the dynamic response of the tank results in a temporary drop in the impact force (at approximately 40 inches displacement). Beyond this time, the tank constraint BCs begin to play a large role in the behavior. With the highly constrained impact wall scenario the impact force quickly recovers, and the tank is punctured at approximately 48 inches of ram displacement. With the moderately constrained side-by-side tank scenario the impact force more slowly recovers, and the tank is punctured at approximately 56 inches of ram displacement. Finally, with the unrestrained tank the impact force never fully recovers to the puncture force level and the tank does not puncture.

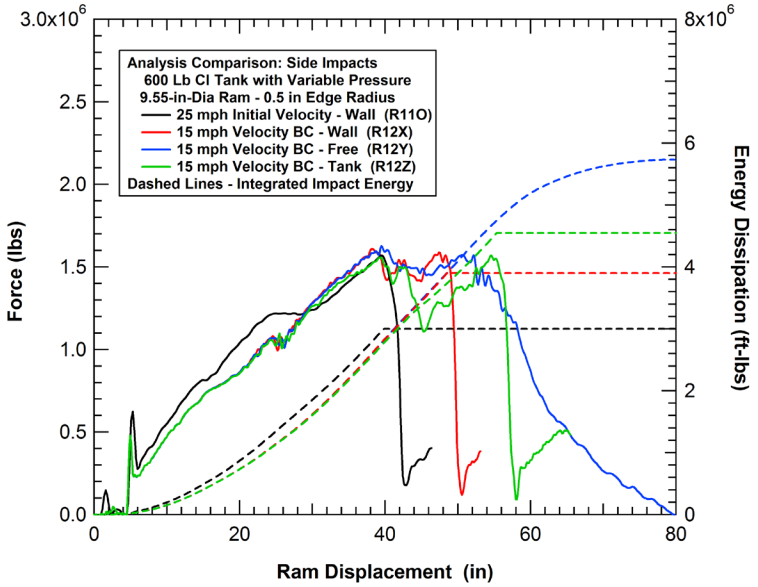

Figure 140. The effects of constraint conditions for the 15 mph constant velocity impacts.

To further remove the effects of the tank dynamics from the impact behavior, an additional analysis was performed using a constant velocity of the ram of approximately 0.5 mph. This slow impact speed eliminates most of the tank dynamic effects and approximates a quasistatic loading of the tank between the ram and the wall. The force deflection for this quasistatic analysis is compared to those of the 25-mph initial velocity and 15 mph constant velocity impacts in Figure 141. Without the dynamic effects, the initial portion of the force-deflection curve is lower for the quasistatic analysis. However, as the tank is compressed and the internal pressure increases, the slope of the force-deflection curve rises and the tank punctures at approximately 40-inches of displacement. The internal pressure rises from 100 psi initially to over 130 psi at the point of puncture for this analysis.

The wall provides a relatively high level of constraint against the tank translation in side impacts. However, it still allows for motion of the tank center of gravity (CG) away from the direction of impact. An idealized impact scenario that does not allow for any translation of the tank CG is to add the third symmetry plane to the tank normal to the direction of the impact. This is equivalent to a tank being impacted symmetrically between impactors on either side of the tank. An

example of the model and impact response for this symmetric impact condition is shown in Figure 142.

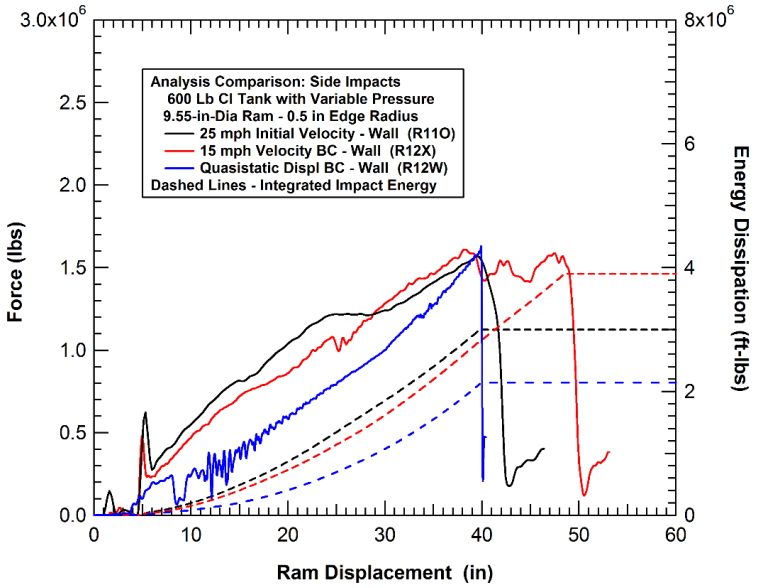

Figure 141. The effects of impact speed on the highly constrained side impacts.

Two analyses were performed for the symmetric impact condition with the 105J600 chlorine tank car. Both analyses used the 9.55-in-diameter impactor. The difference is that the first analysis used a constant velocity 15 mph impact speed, and the second analysis was performed at a much slower quasistatic loading condition. The calculated force deflection behaviors for these two analyses are shown in Figure 143. For comparison, the force deflection curve for the quasistatic loading of the tank against the wall is included in the figure.

The comparison of the behaviors using the symmetric BC helps to develop an improved understanding of the tank response. The first observation is that the gross behaviors of the quasistatic and 15 mph analyses are similar, and both fail at nearly identical displacements and forces. The primary difference is that the 15-mph impact behavior has some effects of the tank dynamic vibrations superimposed on the quasistatic force deflection path.

The other interesting comparison is between the quasistatic loading for the symmetric BC and the quasistatic loading against the wall. Both cases have relatively linear force deflection curves, and both fail at roughly equivalent puncture forces. However, the symmetric loading fails at a ram displacement of approximately 30 inches and the loading against the wall fails at a ram displacement of approximately 40 inches. However, the symmetric condition assumes that the tank is between two moving rams. Thus, the total compaction of the tank between the two ram faces is approximately 60 inches.

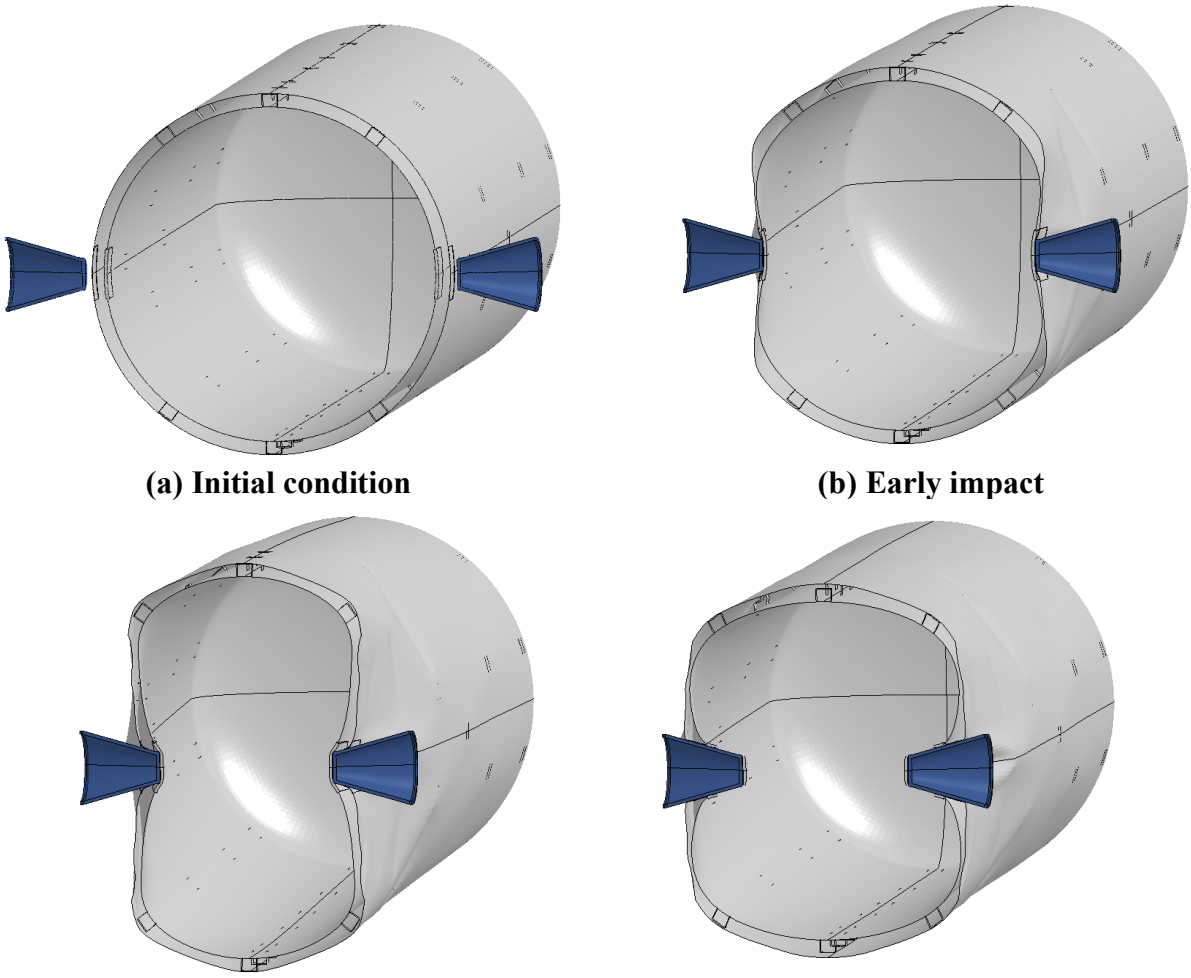

(a) Initial condition **(b) Early impact**

(c) Before tank puncture **(d) After tank puncture**

Figure 142. Calculated response for the symmetric tank side impact scenario.

The comparison can be further used to estimate the stiffness of the tank compressed against the wall. If we use the symmetric analyses to determine that the dent depth around the impactor is 30 inches at the time of puncture, then the compression of the far side of the tank against the wall has a 10-inch depth. We would expect this depth to be much smaller than the ram dent depth since the loaded area is very large, but the total wall reaction force is equal to that on the ram face. To investigate the wall reaction stiffness, an additional analysis was performed where the tank was quasistatically compressed between two reaction walls (symmetric analysis with a moving wall). The calculated force-deflection for the symmetric wall loading is compared to the to the other quasistatic load cases in Figure 144. The comparison shows that the 1.5 million lb reaction load develops over a displacement of approximately 10 inches (after the initial 4-inch standoff distance of the jacket from the tank is crushed).

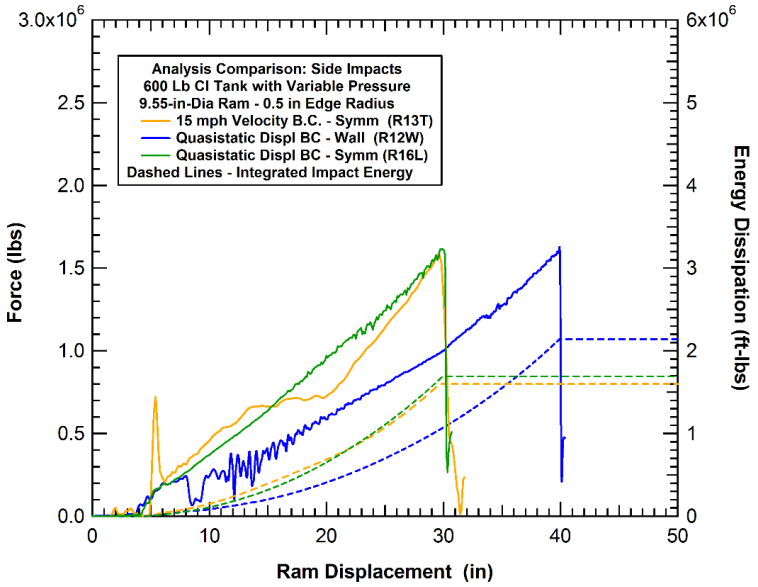

Figure 143. The effects of constraint BCs on the side impact response.

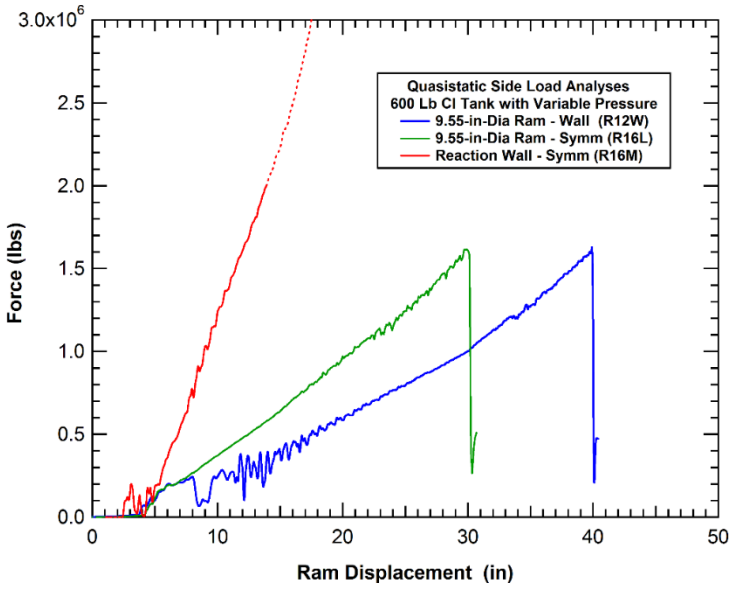

Figure 144. The effects of constraint BCs on the side impact response.

1.1.1 Head Impact Constraint Effects

A similar set of analyses were performed to investigate the effects of the constraint BCs on the head impact response. The baseline head impact conditions, adapted from the NGRTC program, were for a highly constrained tank head mounted on a test frame that does not allow for any motion at the specimen support. The head impact specimen included the tank head and head shield, supported by a short length of the tank shell and jacket, which were welded to a rigid test frame. A model for these highly constrained head impact conditions is shown in Figure 145(a). In the model, the nodes at the back of the shell and jacket section are fixed and do not allow for any displacement or rotations.

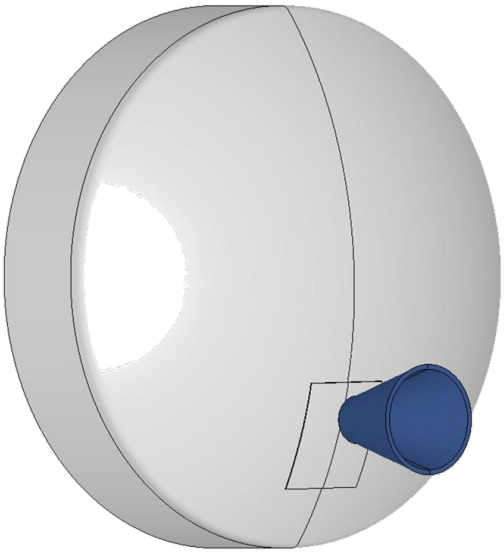

(a) Highly constrained head motion (fixed BC)

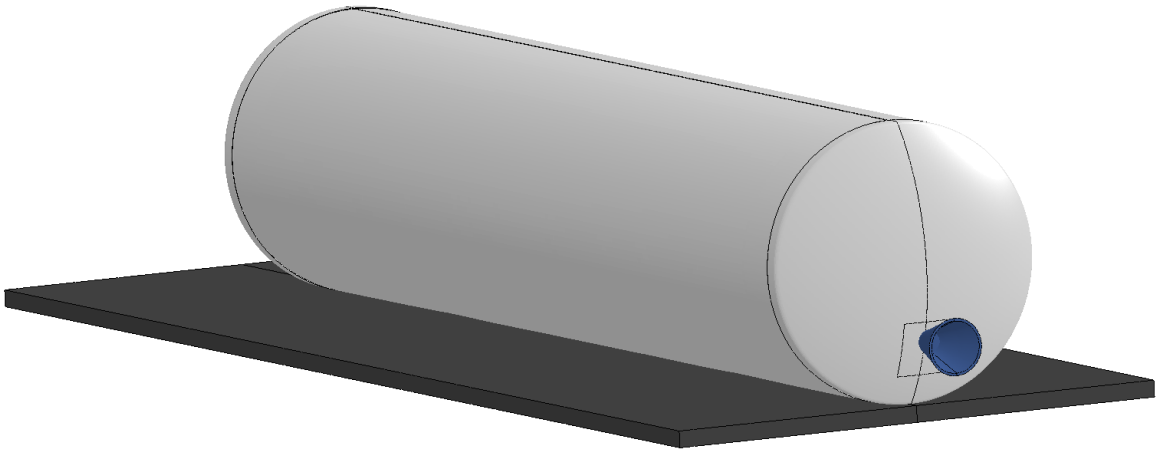

(b) Unconstrained tank motion (head impact)

Figure 145. Various tank motion constraint BCs for side impacts.

To investigate the constraint effects in head impacts an unconstrained tank model was developed as shown in Figure 145(b). The model includes the entire tank which is free to translate. Gravity was included in the analyses to develop appropriate vertical forces and motions in the offset impact scenario. Without the test frame support, a model of the ground was needed to resist the gravitational free-fall motions of the tank. The tank is free to slide along the ground as a result of the impact.

One factor of the head impact response that was unknown is how the lading couples to the tank motions. To determine the bounds on the effect an initial pair of analyses was performed where, in the first analyses, none of the weight of the lading was added to the tank, and in the second analysis, all the lading mass was smeared into the tank. The force deflection curves for these two analyses are compared to that of the fully constrained tank head impact analysis in Figure 146. The analyses are for an 18-mph impact of the 9.55-inch-diameter round impactor at 18 mph.

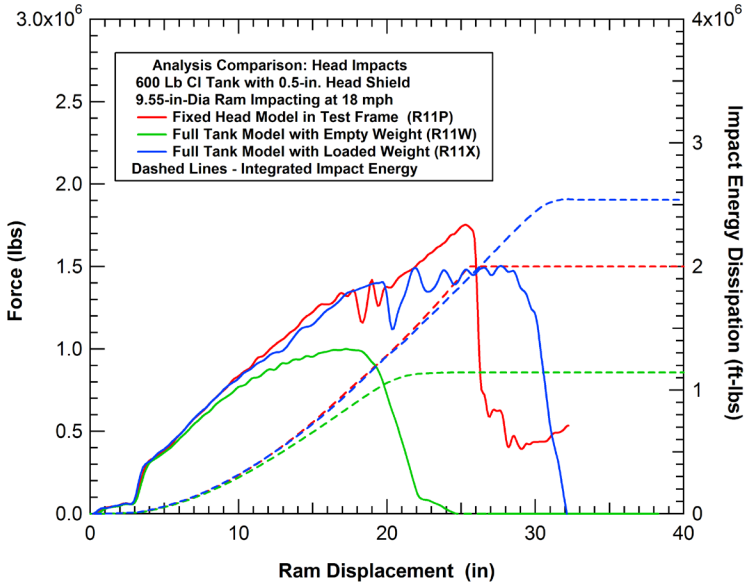

Figure 146. The effects of BC restraint on head impact response (18 mph impacts).

The force-deflection curve for the highly constrained tank head has a roughly linear relationship between the ram displacement and impactor force up to a puncture force of approximately 1.8 million lbs at a ram displacement of approximately 25 inches. The force-displacement curves for the two unconstrained tank models start along the same force deflection curve. However, the force curves for both begin to fall below that of the constrained head force curve. The rate at which to force curve diverges is much more rapid for the light tank than the heavy tank. This is because the impact forces can push the light tank away from the impactor more rapidly than the heavy tank.

A similar set of analyses was performed on the tank and tank head using the coupler impactor model and an impact speed of 25 mph. The analyses again included the bounds of the empty and fully laded tank weights. The force deflection curves for these two analyses are compared to that of the fully constrained tank head impact analysis in Figure 147. The trends are very similar to those of the 18-mph impact. These results will be discussed further in the development of a simplified head impact analysis algorithm, described in Section 6.2 of this report.

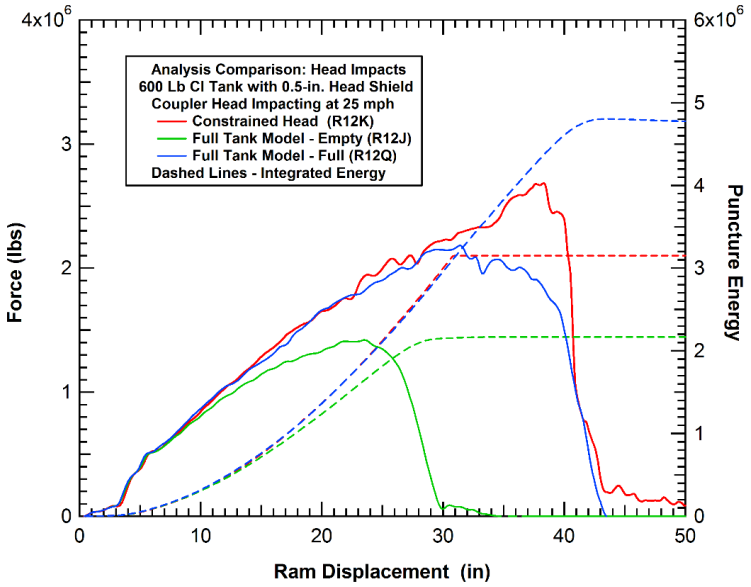

Figure 147. The effects of BC restraint on head impact response (25 mph coupler impacts).

4.4 Lading Response Effects

4.4.1 Lading Effects for Side Impacts

A set of preliminary analyses were used to assess the effects of the lading in the side impact response during the NGRTC program (Kirkpatrick, 2009a). The impact conditions for this analysis were the Test 1 side impact conditions from the NGRTC project on April 26, 2007, at the Transportation Technology Center, Inc. (TTCI) in Pueblo, Colorado (Witte & Anankitpaiboon, 2007). This test involved a side impact of a 23x17 inch impactor with 1-inch-radius edges and corners into the side of a 105J500 chlorine tank car backed by a rigid impact wall. The ram car impact speed was measured optically at 13.9 mph using speed trap reflectors placed within 6 feet of the impact point.

Additional parameters for Test 1 were as follows:

- Tank Car Weight (estimated) 265,000 pounds
- Tank Shell: 0.777-inch-thick normalized TC128B
- Jacket: 11-gauge A1011 steel at 4-inch standoff distance
- Slurry Density 11.6 lb/gallon
- Outage 10.4 percent
- Capacity 17,391 gallons
- Internal Pressure 100 psi
- Ram Car Weight: 285,600 pounds
- Ram Car Energy (derived): 1.86 million foot-pounds

A tank car model was developed and used to predict the Test 1 impact response. The model of the 105J500 chlorine tank car is shown in Figure 148. The model includes the commodity tank, jacket and jacket standoffs, sill and bolsters, trucks, and outriggers attached to the draft gear to prevent a post-test rollover of the target tank caused by the rebound off the reaction wall.

There are many different modeling approaches that can be used to include the dynamic effects of the fluid lading. The different modeling methodologies have tradeoffs on accuracy, efficiency, and utility. Some of these methodologies have been investigated in studies for side impacts of tank cars [e.g., (Kirkpatrick, 2009a), (Jeong, et al., 2009), (Tang Y. H., et al., 2007), (Tang Y. H., Yu, Gordon, Jeong, & Perlman, 2008)]. An example is the simplified explicit model of the lading included in the tank car model in the NGRTC program, shown in Figure 149 (Kirkpatrick, 2009a). The lading model consisted of a low strength viscoelastic material that fills the same volume as the slurry added to the test tank. The sloshing of the lading model can be seen in the cutaway view of the predicted impact response. This lading modeling approach was established to capture some of the momentum transfer of the coupled fluid-structure response but to minimize effects such as sloshing at the fluid free surface that can cause numerical stability problems.

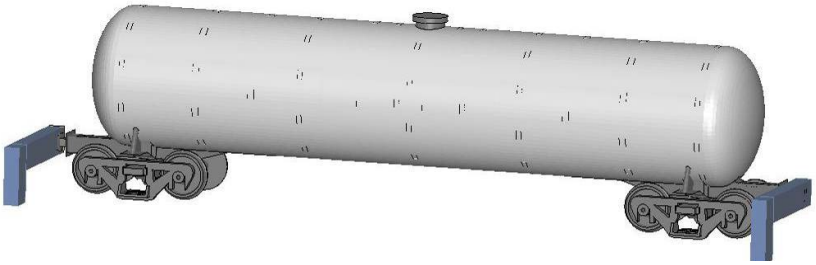

(a) Complete tank car model

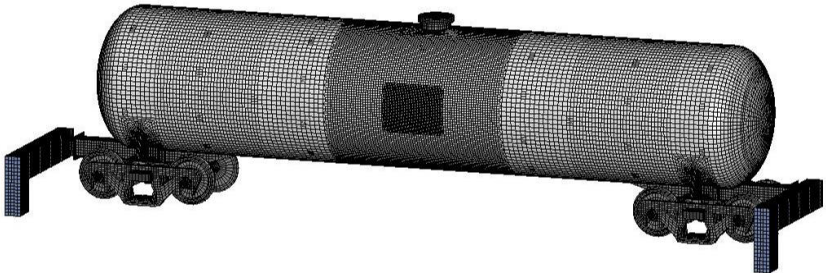

(b) Tank car mesh

Figure 148. Updated model generated for a 105J500W pressure tank car.

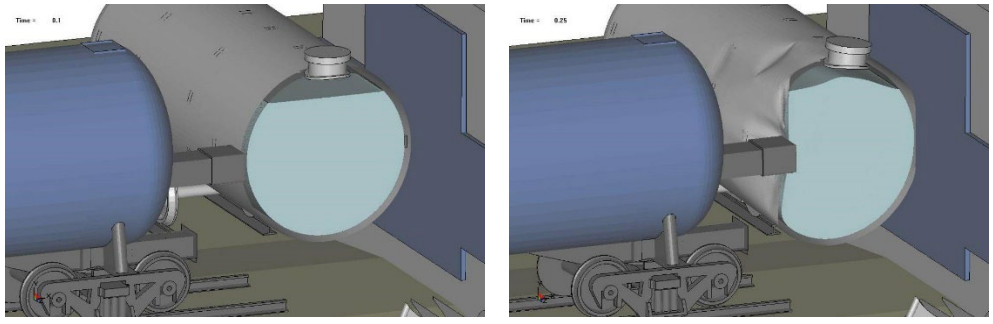

(a) Before impact (t=0.1 s) **(b) Near max. displacement (t=0.25 s)**

Figure 149. Calculated Test 1 impact response with cutaway showing lading.

The comparison of the predicted and measured force-deflection curves is shown in Figure 150. The comparison of the force-deflection behaviors shows good agreement between the calculation and the test. The comparison of the pretest prediction and impact test serves as a validation of the model for the tank collision dynamics and impact deformation behavior. The responses include the initial impact, the reaction of the impact loads against the wall, and the post-impact rebound from the wall. Additional details of the impact behavior captured in the model included the target tank roll motion and lifting forces on the ram car caused by the lateral support of the target tank truck on the stub rail sections and the action of the outriggers resisting a post-test rollover behavior.

In this study, an additional series of calculations was performed for this impact condition to evaluate the effects of various approximations to the lading models and BCs used in the analyses of side impacts. The three different BCs analyzed are shown in Figure 151. The first boundary condition, shown in Figure 151(a), is the idealized case where the tank is assumed to have vertical symmetry and no vertical gravitational loads are imposed. This is the simplest approximation and was used for the majority of analyses in this study. However, with symmetry and without gravity, this model is not suitable for explicit modeling of the effects of the lading sloshing behavior. The second boundary condition, shown in Figure 151(b), adds the effects of vertical gravitational loads and a rigid flat model of the ground to resist the vertical tank motions. The third boundary condition, shown in Figure 151(c), adds the effects of vertical gravitational loads and models of the bolsters and trucks to support the tank and resist vertical tank motions. As a simplification of this condition the motions of the wheels were fixed.

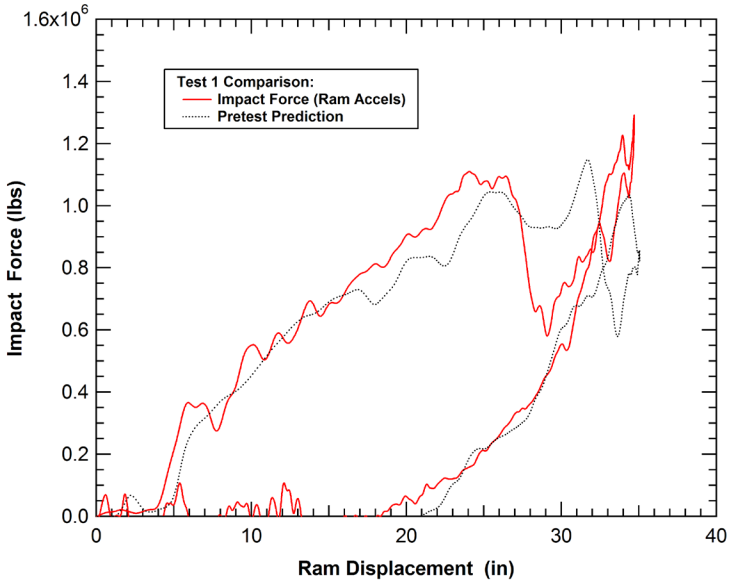

Figure 150. Comparison of the measured and predicted Test 1 force-deflection curves.

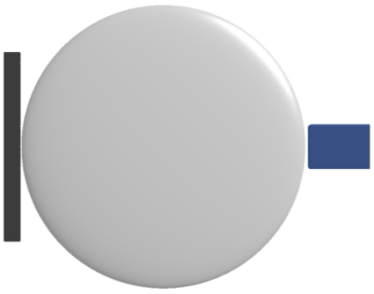

(a) Tank model with vertical symmetry

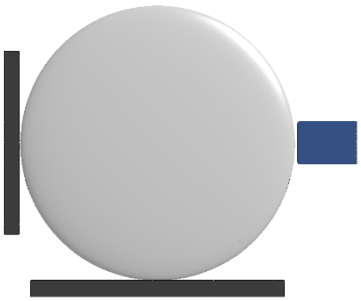

(b) Tank supported on ground

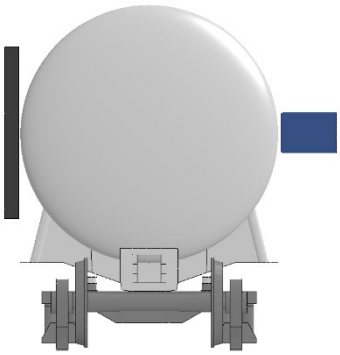

(c) Tank supported on trucks

Figure 151. Various model support BCs for a 105J500W pressure tank car.

The calculated tank impact force histories with the smeared lading model and the three different support BCs are compared to the measured impact force history in Figure 152. The response for the models with the vertical symmetry and the tank supported on the ground are very similar to each other and agree well with the peak force levels for both the initial loading and secondary loading to the maximum force for this test. The model supported on the trucks also agrees well with the initial loading and first force peak. However, the model with trucks unloads more slowly and does not accurately capture the reloading to the secondary peak force level. The reason for this discrepancy was not determined. However, it is possible that approximations such as the constrained motions of the wheels and the constrained vertical motion of the impactor resist the rotational movement of the tank for this scenario and modify the impact dynamics.

A second analysis was performed on the model with the truck support BCs to reassess the effects of the modeling approximations for the lading. In the analysis, an alternative mesh-free Smoothed Particle Hydrodynamics (SPH) approach is used to model the lading. This has the advantage of being able to capture the fluid sloshing without mesh distortion effects and possible numerical instability of classical Lagrangian analyses. The SPH methodology is also compatible with the traditional Lagrangian analysis methodologies being used to evaluate the tank response. As a result, it is more computationally efficient than the Arbitrary Lagrangian Eulerian (ALE) methodologies that have been used for the fluid-structure interaction in tank car impacts cars [(Jeong, et al., 2009), (Tang Y. H., et al., 2007), (Tang Y. H., Yu, Gordon, Jeong, & Perlman, 2008)].

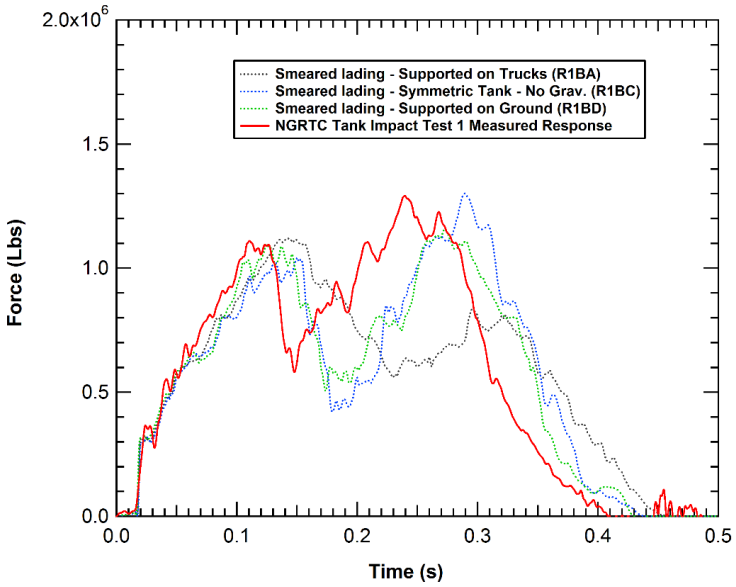

Figure 152. Calculated tank car impact behavior using three different support BCs.

The calculated Test 1 side impact tank and lading deformations at various times during the impact are shown in Figure 153. The corresponding force-time histories for the analyses with the smeared and SPH lading models are compared to the measured behavior in Figure 154. With the SPH lading model, the initial unloading occurs earlier and the reloading to a second peak force is more accurately reproduced. The timing of the initial and secondary force peaks is in good agreement with the experiment. The primary differences from the measured behavior are that the drop in load after the initial force peak is not as rapid or as large as measured, and some of the higher frequency response characteristics are dampened by the SPH lading model.

The above analyses of the Test 1 impact conditions with different lading models and tank BCs illustrate the complexities of this test configuration. The late time response will be influenced to varying degrees by the constraints on the lateral, vertical, and rotational motions as well as the modeling of the lading. However, all the modeling approximations agree well with the initial loading response which is the most important portion of the impact response (punctures often occur during this initial loading). In addition, the various modeling methodologies all give reasonable estimates for the duration and amplitude of the impact force pulse.

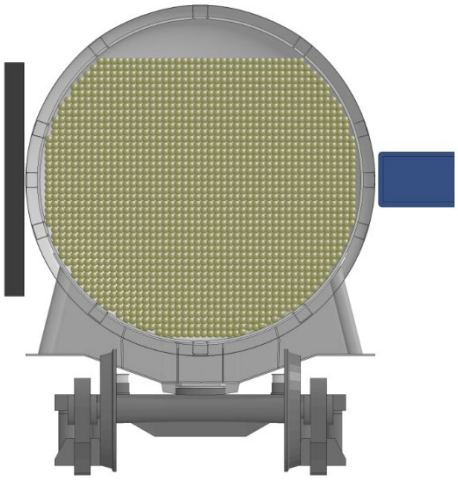

(a) Before impact (time=0.0 s)

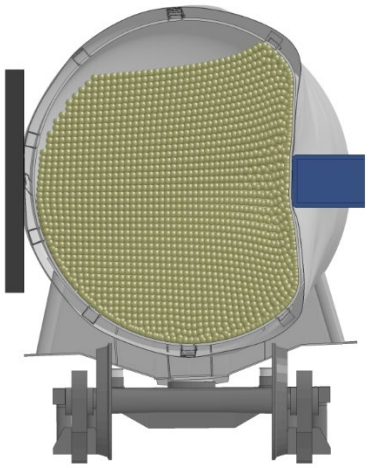

(b) Near first load peak (time=0.10 s)

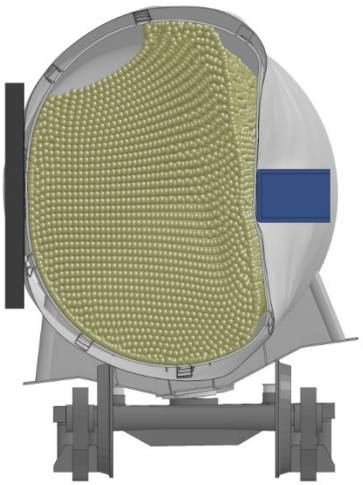

(c) Near second load peak (time=0.25 s)

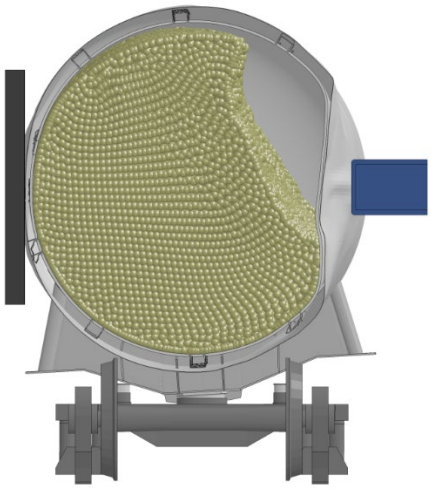

(d) After unloading (time=0.50 s)

Figure 153. Calculated side impact response with SPH lading model.

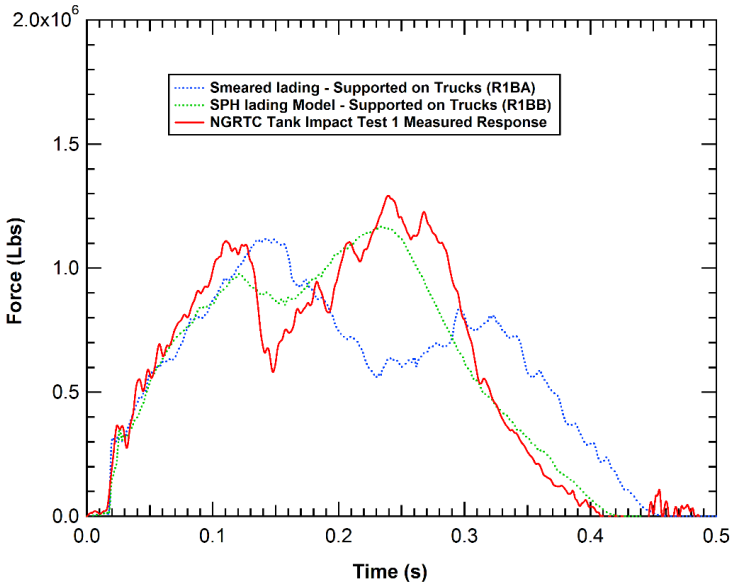

Figure 154. Calculated tank car impact behavior using two different lading models.

4.4.2 Lading Effects for Head Impacts

A similar head impact analysis in an unconstrained tank was performed using an 18-mph impact with the 9.55-inch-diameter impactor. Again, the impact was analyzed with the SPH lading model. The calculated tank and lading deformations at various times during the impact are shown in Figure 155. The corresponding force-displacement curve is compared with the analyses with the similar impact condition for the empty and loaded weight models in Figure 156. The comparison shows that the force-deflection curve for the SPH model is closer to that of the empty tank weight than the smeared mass model of the fully loaded tank. This suggests that only a fraction of the lading mass couples to the motions of the unconstrained tank in head impacts. This effect is confirmed by including fringes of longitudinal velocity in the lading as shown in Figure 157. The time shown is well past peak load halfway through unloading. However, the bulk of the lading is still stationary (blue fringes in the figure). Only the regions of the fluid very near to the tank wall or directly behind the impacted tank head are moving.

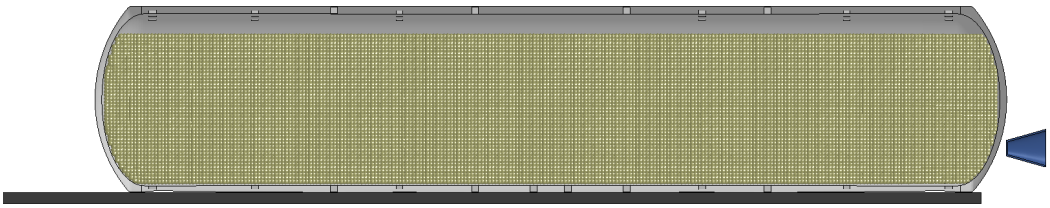

(a) Before impact (time=0.1 s)

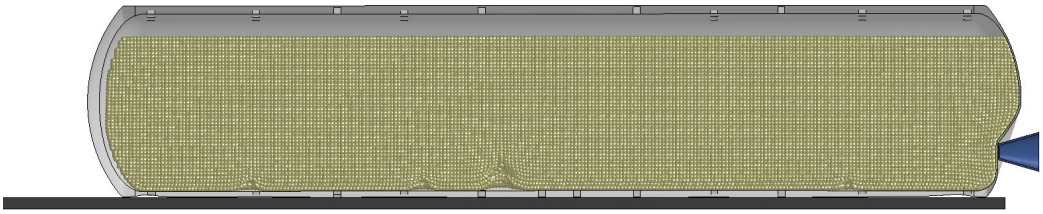

(b) Near load peak (time=0.16 s)

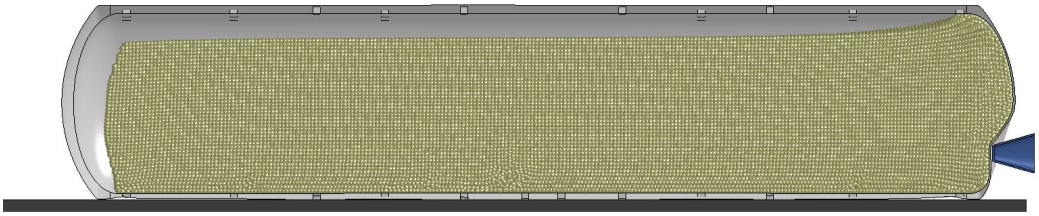

(c) After unloading (time=0.22 s)

Figure 155. Calculated head impact response with SPH lading model.

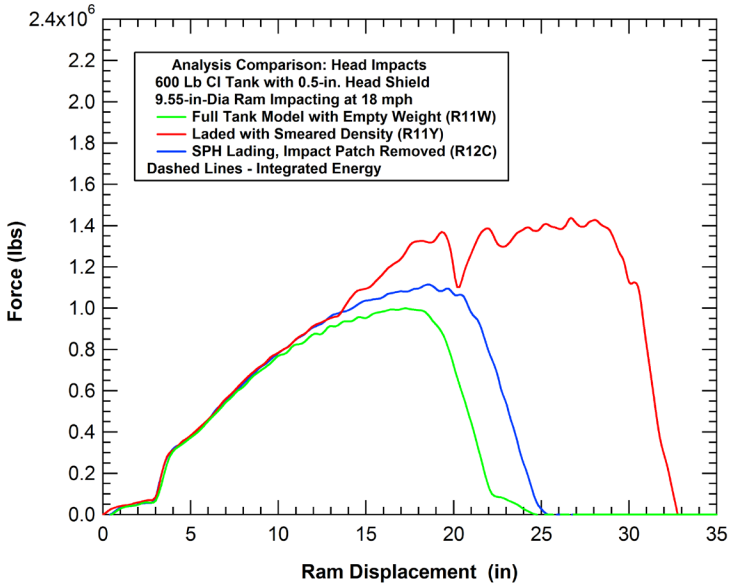

Figure 156. Calculated tank car head impact behavior using different lading models.

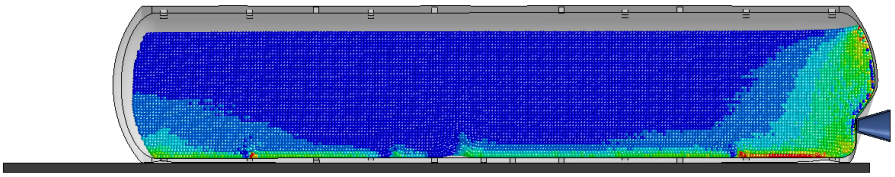

(a) Full tank profile (time=0.18 s)

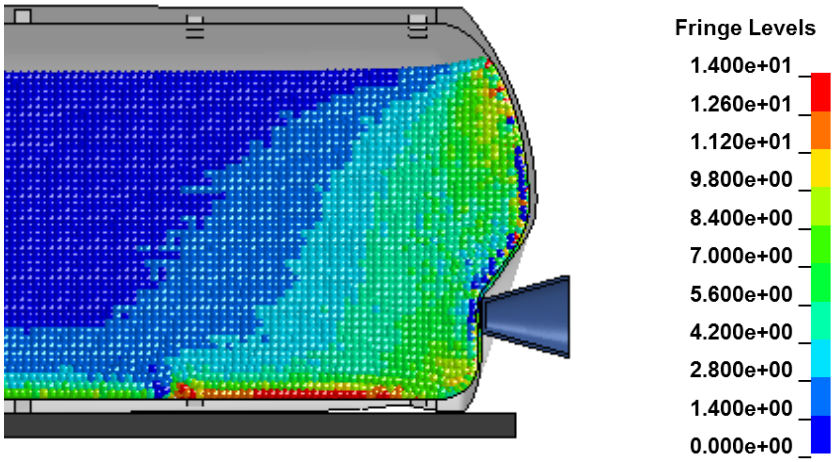

(b) Impact zone (time=0.18 s)

Figure 157. Calculated longitudinal velocity distribution in the SPH lading.

To investigate the effective weight of the fluid lading contributing to the motion in the head impact, we applied the impact response algorithm, described in Section 6.2.1, to run analyses at different tank weights and iterate on an approximate equivalent weight of the tank. The value that matched the analysis best was a tank weight of 130 percent of the empty weight. To confirm this result, we performed an additional finite element impact scenario where the weight of the tank was equal to 130 percent of the empty weight using a smeared mass approach (increasing the density of the commodity tank material). The comparison of this analysis with the 130 percent tank weight with the empty tank model, the full weight model (smeared mass) and full model with SPH lading is shown in Figure 158. The agreement of the SPH model with the 130 percent tank weight model is quite good. Note that the 130 percent weight model increases the tank from an empty weight of 61,300 lbs to a weight of 79,690 lbs. The full weight of the tank is 263,000 lbs which is the empty tank plus approximately 200,000 lbs for the lading. As a result, these analyses show that less than 10 percent of the lading is coupled to the motion of the tank for this head impact scenario.

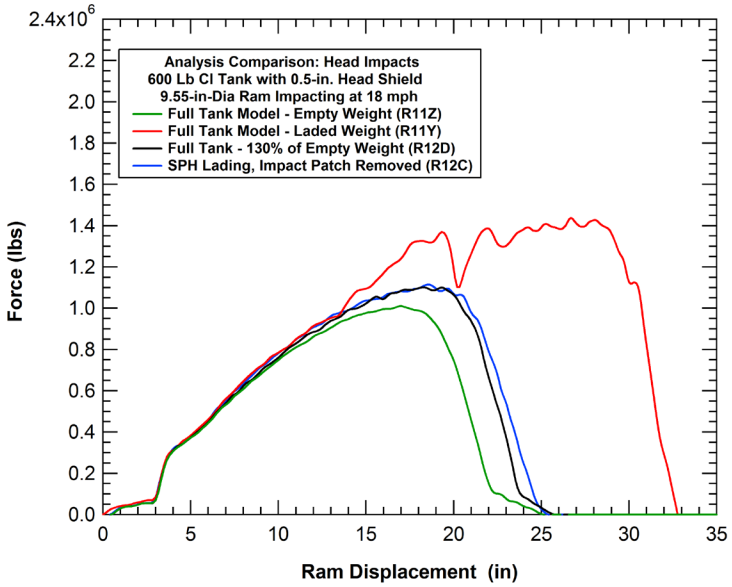

Figure 158. Calculated tank car head impact behavior using different lading models.

4.5 Head Impact Test Configuration

One of the important tank head protection requirements is to provide for the puncture resistance of a coupler impact at a relative impact speed of 18 mph. This head impact condition is designed to verify the integrity of new or untried tank head puncture protection systems and to test for system survivability after coupler-to-tank-head impacts. We have already analyzed many aspects of this head impact scenario including the effects of a coupler impacting the constrained tank head in Section 3.3.2, the effects of the BC constraints in Section 1.1.1, and the effects of the BC constraints in Section 4.3.2. In this section we extend these analyses to further analyze the head impact test configuration. The details of the head impact testing requirements are provided in Appendix A of this report.

The head impact condition uses a rigid 263,000-pound ram car equipped with a coupler, and a draft sill including the draft yoke and draft gear. The coupler protrudes from the end of the ram car so that it is the leading location of perpendicular contact with the impacted test car. The impacted test car is loaded and pressurized to 100 psi. In addition, the target tank car is coupled to a 200,000-pound rigid backup car (trailing mass) for a combined target total weight of 486,000 pounds. The overall model configuration for a head impact analysis is shown in Figure 159. The analysis was conducted with the coupler impacting on the lateral centerline of the tank car at a height of 21 inches above the top of the sill.

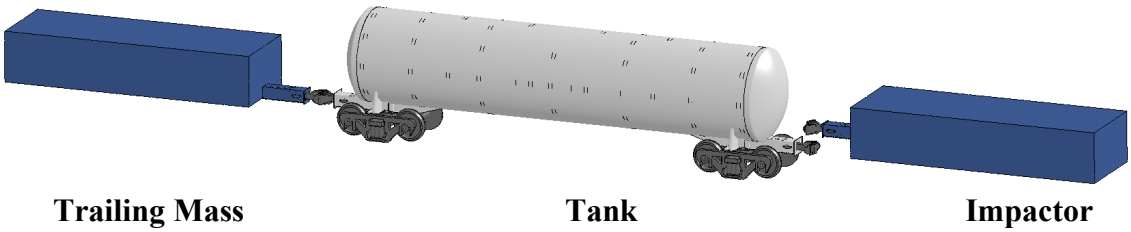

Figure 159. Tank head impact analysis model geometry.

1.1.2 Draft Gear Effects for the Impactor

There are several features of this head impact test configuration that add complexity. The first is the complex geometry of the impactor face with a coupler head impactor. This has already been analyzed for both side and head impacts and is discussed in Sections 3.2.4 and 3.3.2. The regulations of the testing configuration (49 CFR § 179.16) do not specify the specific coupler type or manufacturer. As a result, variations may exist in the impact face geometry that could influence the puncture potential.

A second effect that complicates this test configuration is the use of the coupler impactor "sled" with a sill and draft gear. To investigate this effect, a model of a coupler impact sled was developed and used in an impact analysis. The model for the coupler impactor sled is shown in Figure 160. It consists of a large rigid sled with a mass of 263,000 lbs. This value was selected to conform to the regulatory coupler head impact test specification. A rigid sill was attached to the mass and a model of the coupler and draft gear was included in the sill. The model of the draft gear is shown in Figure 160(b). It includes an energy absorbing draft gear model, a realistic geometry of a draft gear yoke, and a draft gear design that applies a retaining key to holds the assembly together. Identical draft gear models were used in both the tank car and the rigid impactor block. The energy absorbing draft block allows for 3.2 inches of travel before the draft gear follower plate seats against the friction draft gear case and the gear creates a direct load path from the coupler to the lugs.

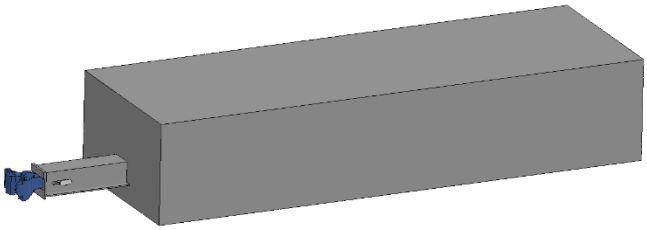

(a) Full coupler impact sled model

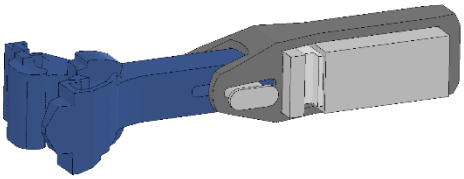

(b) Coupler and draft gear model

Figure 160. Model of the 263,000 lb coupler impactor sled.

The force-deflection characteristics of the draft gear were obtained using a nonlinear spring with the specified properties shown in Figure 161. The draft gear develops a force of approximately 500,000 lbs after one half inch of displacement that steadily increases to approximately 900,000 lbs at approximately 3 inches of displacement. After the three inches of travel the loads increase rapidly. During unloading the force deflection behavior follows the same curve and there is no hysteresis to dissipate energy in the draft gear. This is a conservative assumption in that the draft gear loads will remain at elevated levels and more of the energy dissipation will occur in the tank head deformations.

A comparison of the 25 mph impact behaviors of the restrained tank head using the initial rigid coupler impactor model and the new coupler impact sled model are shown in Figure 162. The

higher 25-mph impact speed was used in these analyses to increase the impact severity to a condition that would puncture the tank head. Overall, the force deflection characteristics of the two impact analyses are similar. The slight reductions in impact force are probably a result of the compaction of the draft gear allowing for a slight increase in the sled displacement compared to that of the coupler face. The larger discrepancy is in the point of failure initiation through the tank head. The impactor sled allows for small rotations of the coupler within the sill and this effect could allow for some redistribution of the contact loads across the coupler face. With the sled, the puncture force is increased by approximately 8 percent. However, with the additional compliance of the draft gear and the slope of the force-deflection curves, this results in a 27 percent increase in the puncture energy.

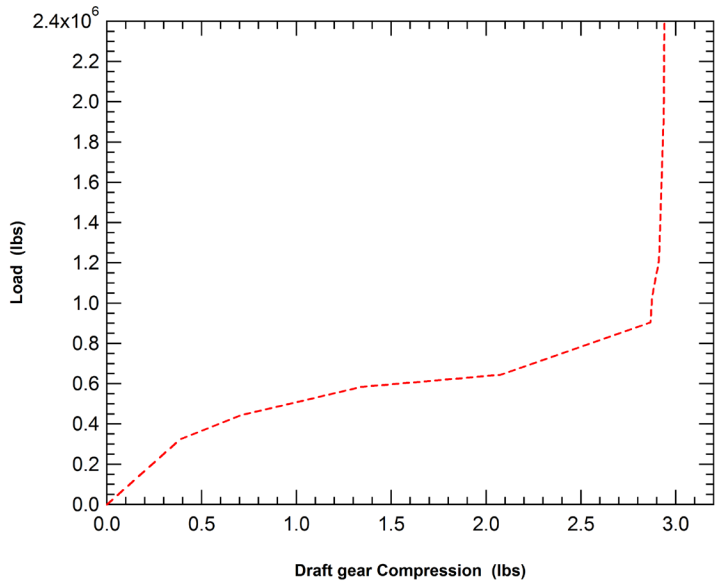

Figure 161. Force-deflection characteristics used for the energy absorbing raft gear.

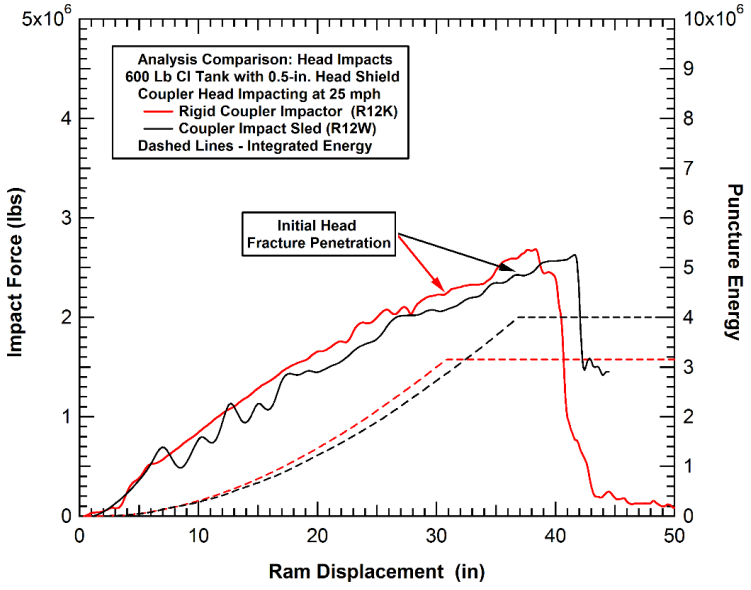

Figure 162. Comparison of 25 mph coupler impact and puncture behaviors.

4.5.1 Trailing Mass Effects for the Impactor

The head impact tests conditions specify that the impacted test car must be coupled to one or more “backup” cars to achieve a total weight of 217,724 kg (480,000 pounds) with hand brakes applied on the last “backup” car. To investigate the effects of the reaction forces from the backup car, a model for a 200,000 lb rigid trailing mass was generated and coupled to the test tank car. In the initial analyses, the tank was modeled at 130 percent of the empty tank weight using the smeared lading model approximation (1.3X). This provides the approximate inertial effects of the liquid lading in a head impact as shown in Section 4.3.2.

The transfer of momentum in the impact analysis is shown in Figure 163. In the figure blue is stationery and red is the initial velocity of the impactor mass of 18 mph. The times shown are before impact and at 40 ms intervals after impact. The corresponding velocity histories for the impact mass, the trailing mass, and the commodity tank are shown in Figure 164. The impact mass decelerates from the 18-mph initial velocity to less than 6 mph after impact. Similarly, the tank and trailing mass is accelerated to a velocity of greater than 10 mph after the impact.

The corresponding impact forces for the tank and the transmitted forces to the trailing mass are shown in Figure 165. For comparison, an identical impact analysis was performed without the trailing mass coupled to the tank. The comparison shows that the trailing mass has only a modest influence on the peak impact force (approximately a 20 percent increase in the peak force). This modest increase in impact severity does not justify the significant increase in the complexity of the test conditions and collision dynamics.

One of the modeling approximations used in this analysis of the head impact test condition is the 1.3X lading model. As described in Section 4.3.2, this model couples less than 10 percent of the lading to the motion of the tank for this head impact scenario. This is probably appropriate for the early time motion of the tank including the peak impact force. However, at some later time the lading inertial effects will interact with the tank motions. To evaluate the bounds of the effects, an additional set of analyses was performed using the modeling approximation where all the lading mass was smeared into the tank model.

The calculated velocity histories for the impact mass, the trailing mass, and the commodity tank for the smeared full lading model are shown in Figure 166. The impact mass decelerates from the 18-mph initial velocity to approximately 4 mph after impact. Similarly, the tank and trailing mass is accelerated to an average velocity of approximately 8 mph after the impact.

The corresponding impact forces for the tank and the transmitted forces to the trailing mass are compared to those of the 1.3X model in Figure 167. The comparison shows that the lading inertial approximation has a much larger effect than that of the trailing mass. In addition, with the smeared full lading model, the trailing mass has only a small influence on the peak impact force (approximately a 10 percent increase in the peak force).

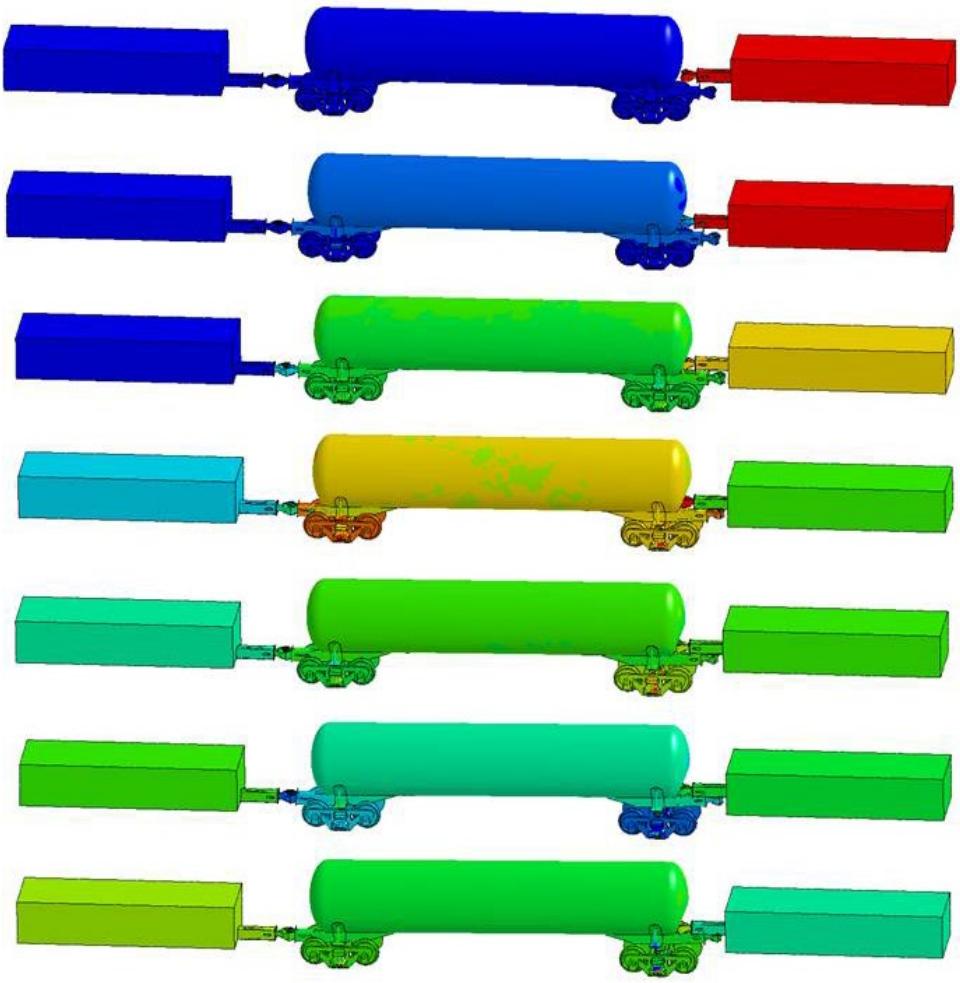

Figure 163. Momentum transfer for the tank car head impact analysis.

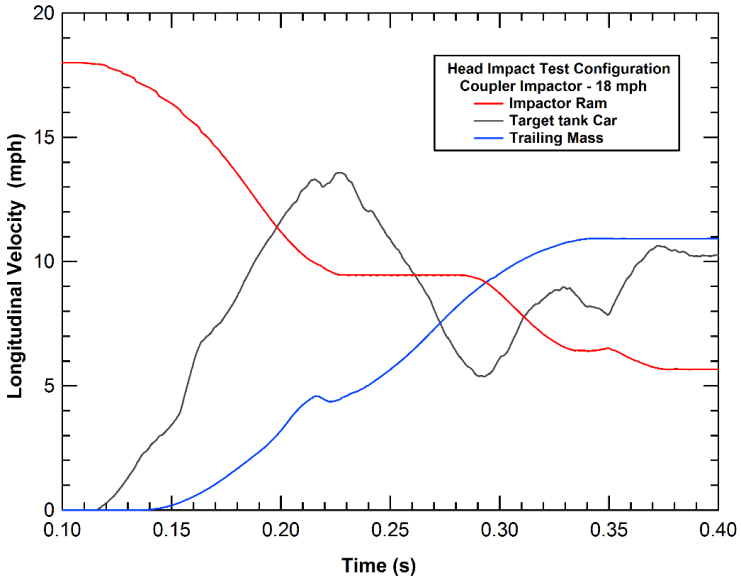

Figure 164. Velocity histories for the 1.3X lading head impact analysis.

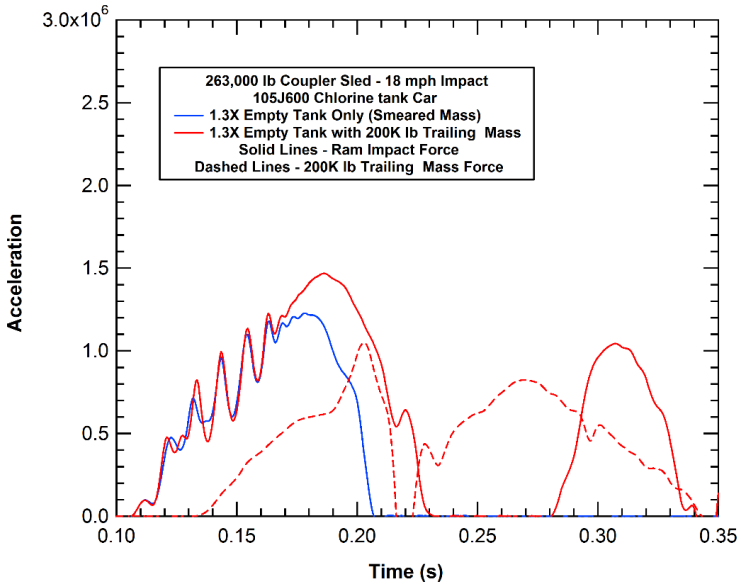

Figure 165. Calculated impact behavior using the 1.3X lading model.

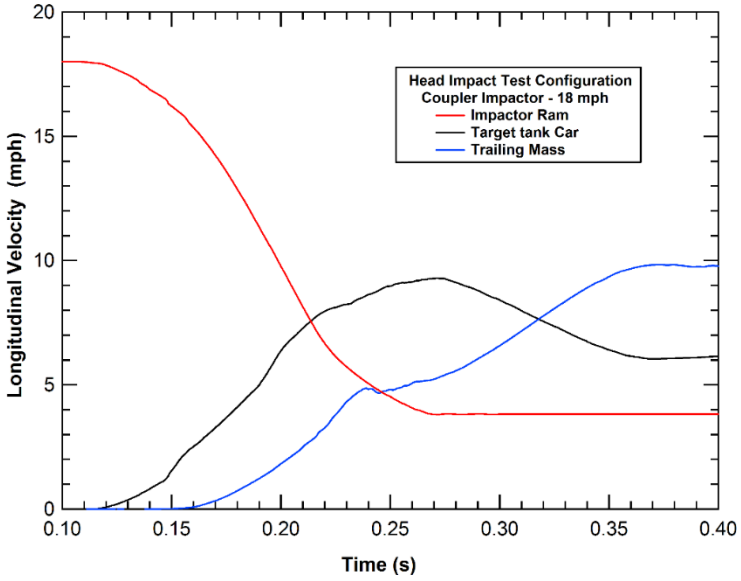

Figure 166. Velocity histories for the smeared full lading head impact analysis.

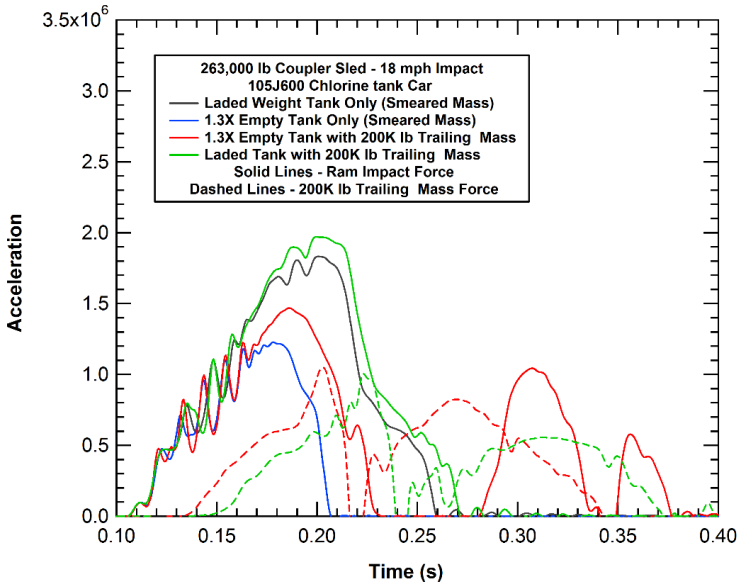

Figure 167. Calculated head impact behavior using the smeared full lading models.

4.5.2 Summary of the Head Impact Test Evaluation

The above analyses, supported by analyses in other sections of this report, allow for observations to be made about the head impact test requirement. The first observation is that the details of the test are not tightly controlled. This includes aspects of the coupler and draft gear geometry and energy absorbing characteristics, tolerances of the coupler and striker clearances that will allow for rotation of the coupler impactor face against the tank head, and the geometry of the impactor and trailing masses. Many features of the test could be changed that would increase or reduce the severity of the impact and the test conditions would still fall within the bounds of the testing specifications.

An example of this test uncertainty is that the test requirements allow for one or more backup cars to be used to provide the inertial resistance to the impact. However, the analyses performed in this study illustrate that a single rigid mass coupled to the target tank car can provide only a modest level of inertial resistance to the initial impact forces. If this coupled mass was replaced by several lighter masses coupled together, each subsequent mass would contribute to a lesser extent and with a delayed effect. As a result, the inertial restraint of the backup cars could be minimized and still be within the allowable testing configuration.

A second general observation is that the test is very complex both for the performance of an experiment and even more so for analysis of the test condition. To accurately model the test condition requires the modeling of the lading sloshing effects, the interaction of the target tank car and coupled “backup” cars, and the modeling of the impactor with a complex coupler impactor face and draft gear behavior. With all these effects, there are many potential modeling assumptions and approximations that could be applied by different analysts that would introduce large errors in the calculated impact forces and puncture resistance.

Ideally, the head impact test condition should be replaced with one where the head is attached to a rigid mass with a well-defined attachment BC. The impactor should also effectively be a rigid mass with a well-defined impactor face geometry. The motions of the two bodies should be

controlled to a one-dimensional translation. With these approximations the test will provide much more repeatable and reproducible results and the analyses will be greatly simplified reducing the potential errors from different modeling methodologies.

4.6 Analysis of Offset Side Impact Effects

4.6.1 Analysis of Vertical Offset Side Impacts

For the idealized side impact analyses, discussed in Section 3, the impact point was always at the center of the tank both along the length and at the vertical mid-height (belt line). In this section, we explore the effects of offsetting the impact position both vertically and longitudinally.

The initial series of offset side impact analyses were performed on the side impact condition where the impact point was offset vertically by different magnitudes. This offset effect is similar to that of the analyses of the head impacts that have typically included the effects of an impact that was offset from the center of the tank head. The offset impact was found to influence the damage development of the tank head under the impactor and reduce the load at the puncture initiation.

The vertical offset side impact analyses were performed using the 9.55-inch-diameter round impactor. In the idealized side impact analyses, described in Section 3.2, the models contained longitudinal and vertical symmetry planes to model one-quarter of the tank. That model reflected about the symmetry plane is shown in Figure 168(a). For the offset analyses, the vertical symmetry plane can no longer be used. As a result, BCs to control the vertical motions of the tank were needed. The methodology used was to apply gravity to the tank and to add a rigid ground model that supports the tank. The corresponding model for the center impact and impact points offset 15 and 25 inches below the centerline are shown in Figure 168(b-d).

The calculated force-deflection histories for the four models shown in Figure 168 are compared in Figure 169. The idealized impact conditions with symmetry (Figure 168a) and the center impact analyses with ground and gravity added (Figure 168b) fail at roughly equivalent puncture forces and energies. There are slight differences introduced by the more complex BCs, but the overall behavior is similar, and the puncture energies are within 10 percent. However, as the impact point is offset, the puncture forces and energies are significantly reduced.

The calculated puncture mode for the 25-inch vertical offset side impact analyses is shown in Figure 170. The puncture behavior looks very similar to the behavior of an offset head impact where the damage is concentrated near the top of the impactor and the puncture forms as a flap that initiates at this top edge. We see for this 25-inch offset that the failure initiates while only the top half of the impactor is significantly interacting with the tank wall. As a result, the forces are concentrated at the upper edge and the total force required to initiate the puncture is reduced.

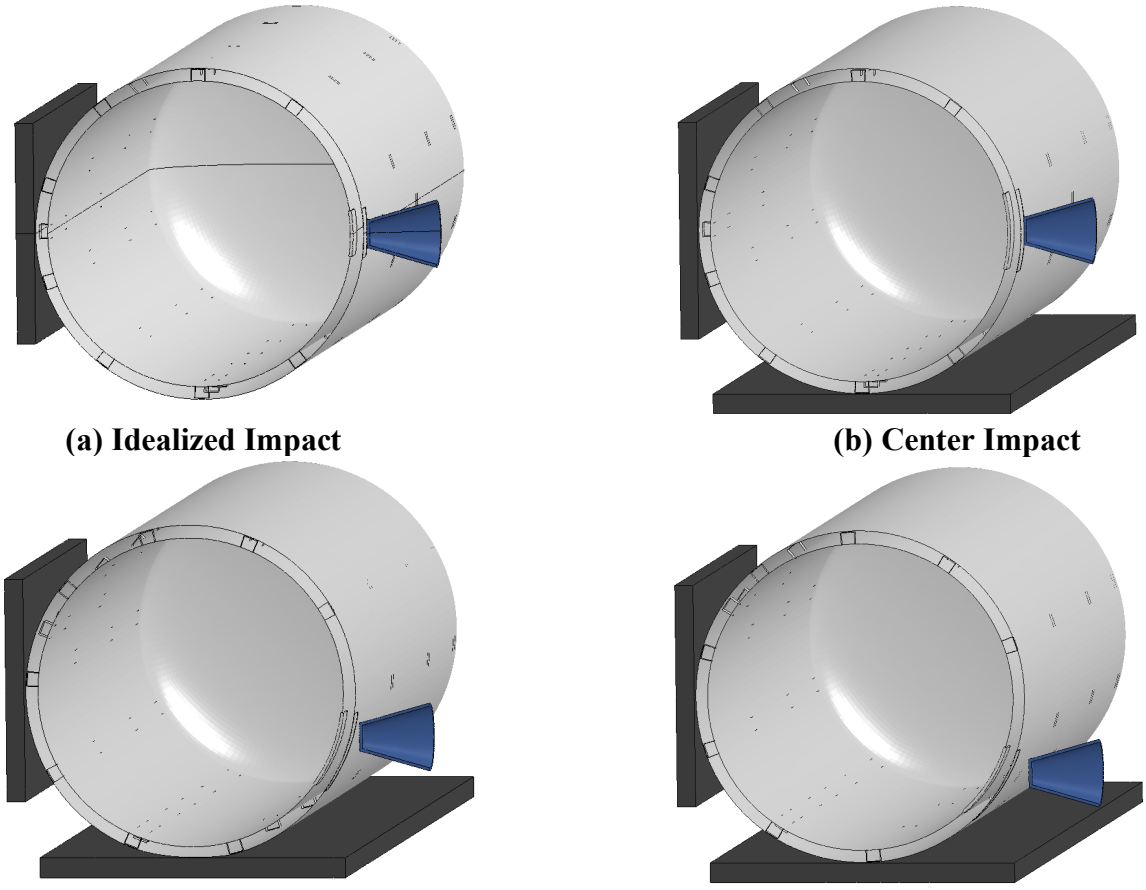

(a) Idealized Impact

(b) Center Impact

(c) 15-inch offset

(d) 25-inch offset

Figure 168. Impact scenarios used in the vertical offset impact analyses.

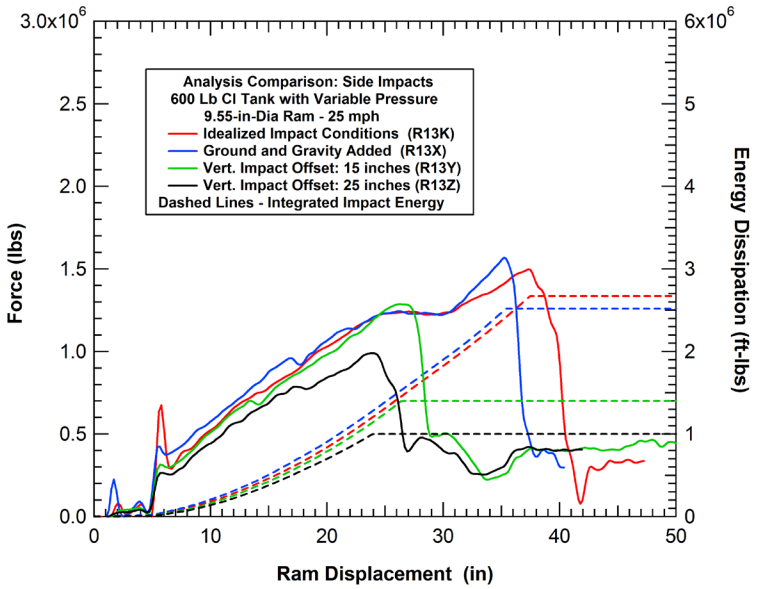

Figure 169. Comparison of the calculated side impact behavior with vertical offsets.

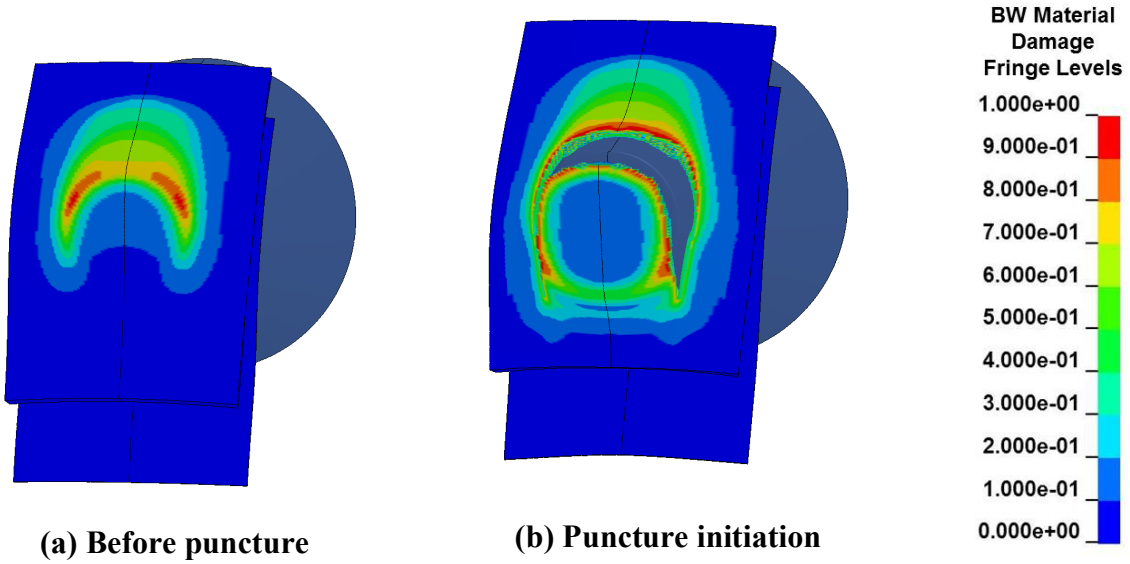

(a) Before puncture **(b) Puncture initiation**

Figure 170. Calculated puncture behavior for the 25-inch vertical offset side impact.

A summary of the calculated puncture response for all the vertical offset side impact analyses is provided in Table 6. The corresponding puncture forces and puncture energies are plotted against the vertical offset distance in Figure 171 and Figure 172, respectively. The comparison shows that a small vertical offset (10 inches or less) has little effect on the puncture force. However, as the offset increases the puncture force drops significantly and a 25-inch offset reduces the puncture force by approximately 35 percent. The trends are similar for puncture energies but are more pronounced. The 25-inch offset reduces the puncture energy by approximately 60 percent. This is because the puncture force reduction is compounded by a corresponding reduction in the ram displacement required to develop that force.

Table 6. Summary of the vertical offset side impact analyses.

Head Impact Calculation	Tank Type	Tank Shell	Jacket	Impact Conditions	Vertical Offset (inches)	Internal Pressure (psi)	Puncture Force (lbs)	Puncture Energy (ft-lbs)
R13X	600 lb Cl	0.981 in TC128B	0.119 in A1011	25 mph 9.55 in. dia.	0.0	100 psi	1,569,000	2,520,000
R13Y	600 lb Cl	0.981 in TC128B	0.119 in A1011	25 mph 9.55 in. dia.	-15.0	100 psi	1.287,000	1,400,000
R13Z	600 lb Cl	0.981 in TC128B	0.119 in A1011	25 mph 9.55 in. dia.	-25.0	100 psi	990,000	1,000,000
R14A	600 lb Cl	0.981 in TC128B	0.119 in A1011	25 mph 9.55 in. dia.	-5.0	100 psi	1,576,000	2,450,000
R14B	600 lb Cl	0.981 in TC128B	0.119 in A1011	25 mph 9.55 in. dia.	-10.0	100 psi	1,467,000	2,060,000
R14C	600 lb Cl	0.981 in TC128B	0.119 in A1011	25 mph 9.55 in. dia.	-20.0	100 psi	1,116,000	1,180,000

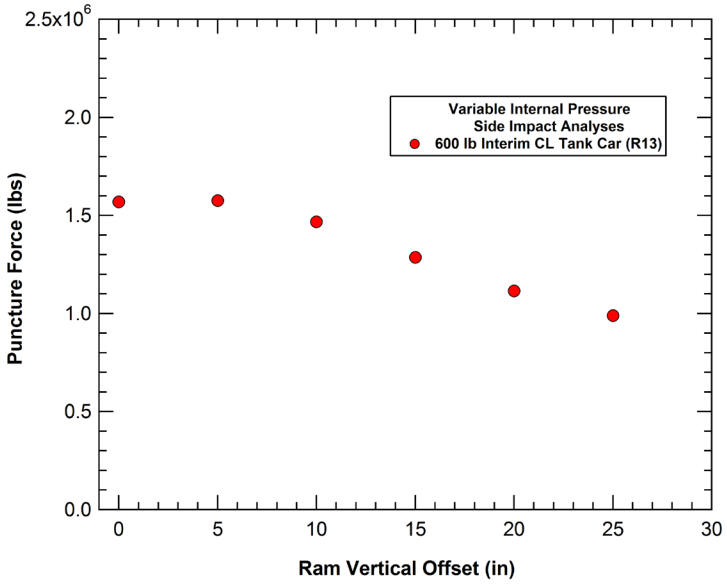

Figure 171. Calculated puncture forces for the various vertical offset side impacts.

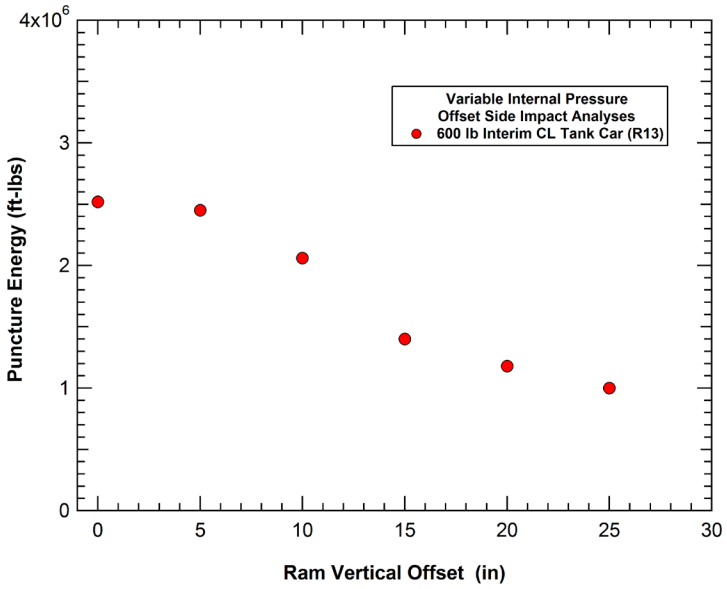

Figure 172. Calculated puncture energies for the various vertical offset side impacts.

4.6.2 Analysis of Longitudinal Offset Side Impacts

A corresponding set of analyses was performed to investigate the effects of a longitudinal offset to the impact point on side impacts. As the impact point move further from the tank center of gravity (CG) the tank motions will include more rotation away from the impact as opposed to the pure translation when the impact is aligned with the tank CG (center impact).

The three primary impact conditions analyzed are shown in Figure 173. In addition to the reference condition of the center impact, the impact locations with longitudinal offsets of 80-inches and 160-inches were also considered. All the analyses used a vertical symmetry plane to constrain the motions of the tank in a two-dimensional plane.

The initial three analyses used a 15-mph constant velocity impact condition on an unconstrained tank. The force-deflection curves for these three analyses are compared in Figure 174. None of the tanks are punctured by these impact conditions. However, the larger the longitudinal offset, the more easily the tank is pushed out of the way from the path of the impactor. As a result, the effect of the longitudinal offset is very similar to the effects of reducing the tank weight. Since the tank can be more easily pushed away from the path of the impacting object, the probability of a given impactor puncturing the tank will be reduced as the impact point moves further from the tank CG.

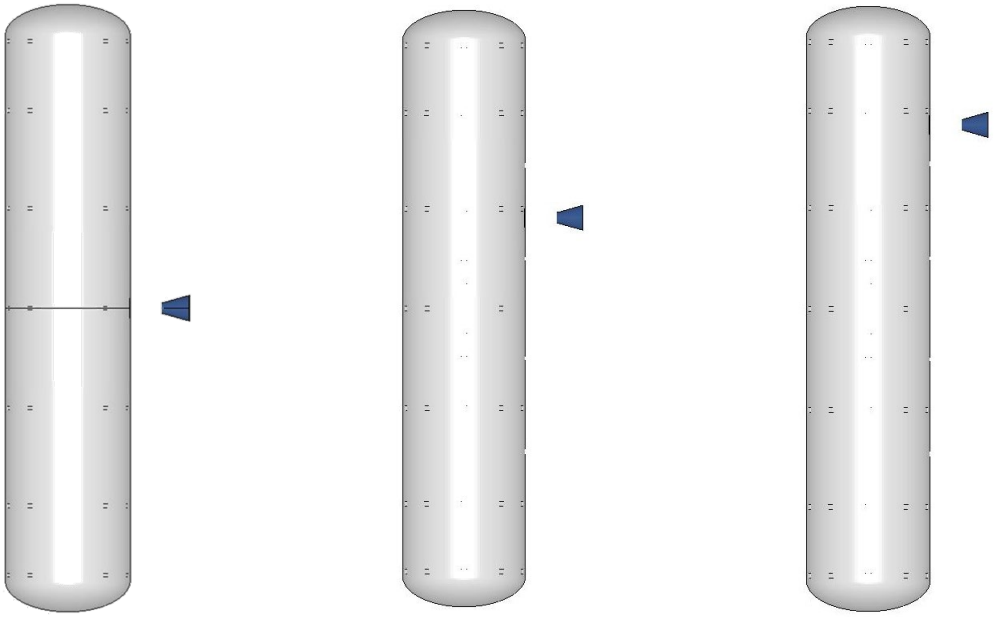

(a) Center Hit **(b) 80-inch offset** **(c) 160-inch offset**

Figure 173. Various impact locations investigated for unconstrained side impacts.

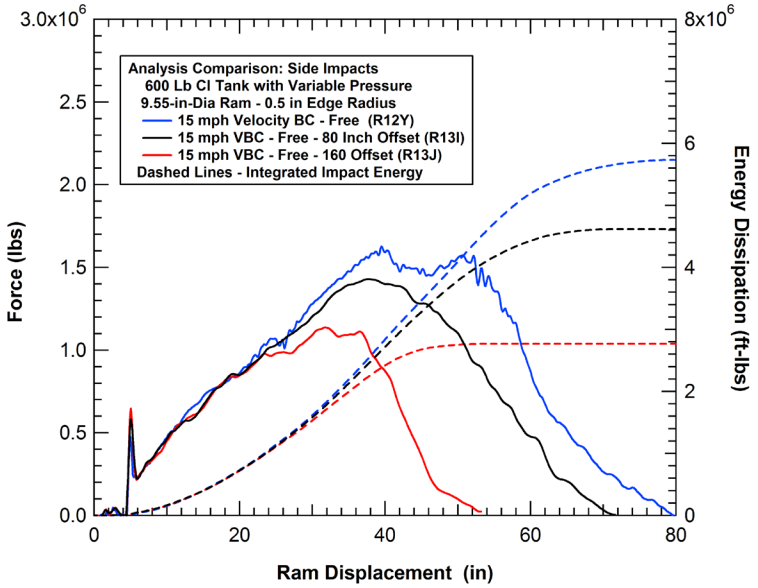

Figure 174. The effects of longitudinal offsets on unconstrained side impact behavior.

The above effects of the offset impact will be reduced as the motions of the tank are more highly constrained. A set of additional impact analyses were performed with a longitudinal offset impact condition and an impact wall behind the tank to constrain the tank motions. The models for the 80-inch and 160-inch offset impacts are shown in Figure 175. Note that the impact wall position is also offset by the same distance to remain aligned with the impactor.

The initial offset impact analyses on the constrained tanks used the 15-mph constant velocity impact condition. The comparison of the force-deflection curves for the center, 80-inch offset, and 160-inch-offset impact conditions is shown in Figure 176. Overall, the differences in these force-deflection curves are relatively small. However, the larger offset distances introduce changes to the tank kinematics, and small asymmetry to the impact behavior that results in failures at slightly less displacement levels and reduced puncture energies.

An additional set of offset impact analyses was performed on the constrained tanks using a 25-mph impact initial condition with the 295,000 lb impactor. The comparison of the force-deflection curves for the center, 80-inch offset, and 160-inch-offset impact conditions is shown in Figure 177. Again, the differences in these force-deflection curves are relatively small. However, for the higher impact speed, the response is more dominated by the inertial constraint. As the offset distance increases the tank more rapidly moves away from the impact and more of the kinematics and interaction with the BC come into play. As a result, the larger offsets cause failures at slightly larger displacement levels and increased puncture energies. This is opposite the trend produced at the slower 15 mph impacts.

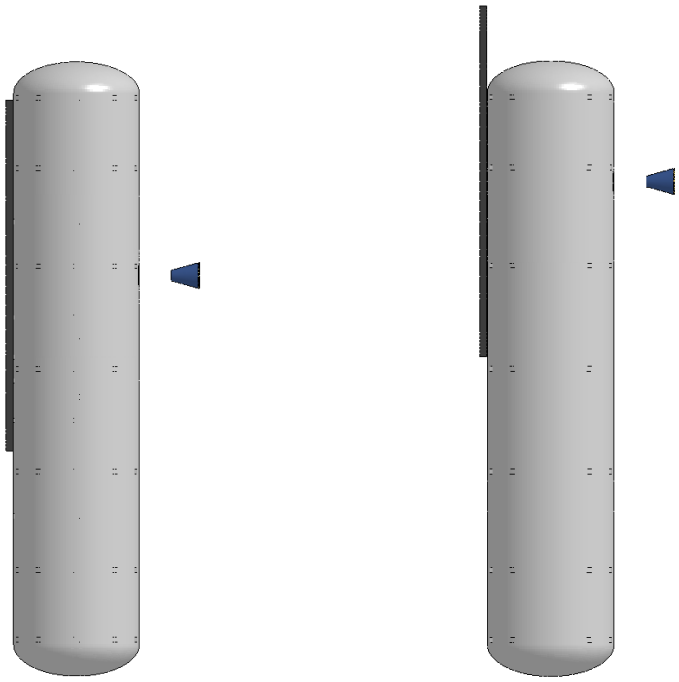

(b) 80-inch offset **(c) 160-inch offset**

Figure 175. Longitudinal offset impact locations investigated for constrained side impacts.

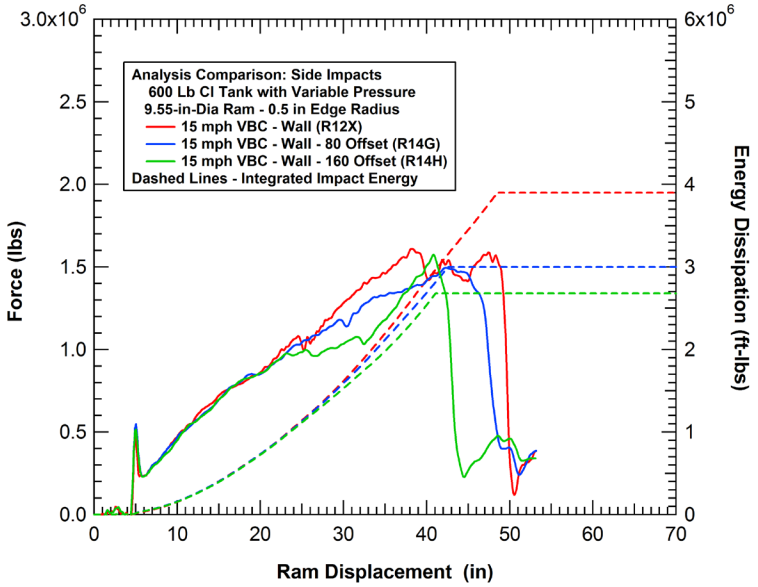

Figure 176. Offset impact effects on a constrained tank, constant 15 mph impact.

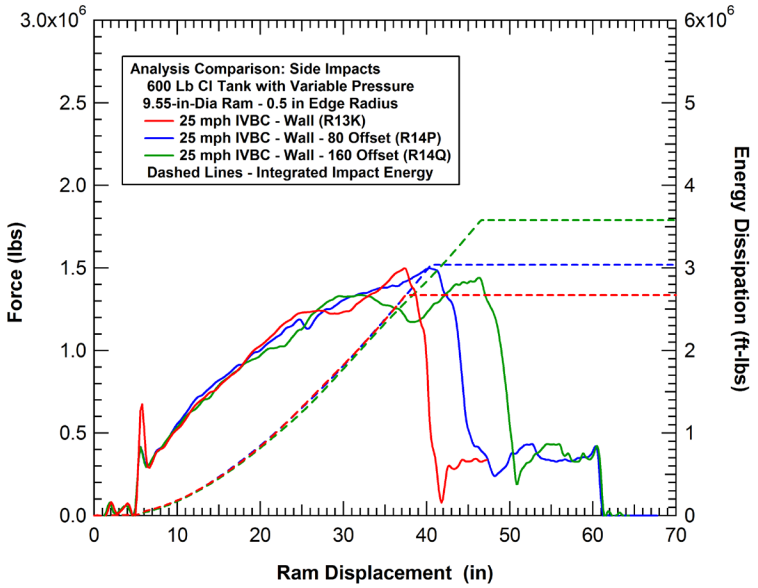

Figure 177. Offset impact effects on a constrained tank, 25 mph initial velocity impact.

5. Impact Analyses on Other Tank Car Designs

5.1 Introduction and Background

One of the significant factors in the puncture resistance of various pressure tank car designs are the effects of the commodities that they carry. The vapor pressure and liquid density of EO, anhydrous ammonia (AA), and chlorine are plotted as a function of temperature in Figure 178. The comparison shows that for a given temperature, AA has a vapor pressure that is approximately 25 percent higher than chlorine and EO has a much lower vapor pressure. However, EO is unique from these other commodities in that nitrogen padding is used for safety considerations. As a result, the typical pressure in an EO tank car during transit is approximately 50 psi and results primarily from the nitrogen padding applied to the tank for safety considerations.

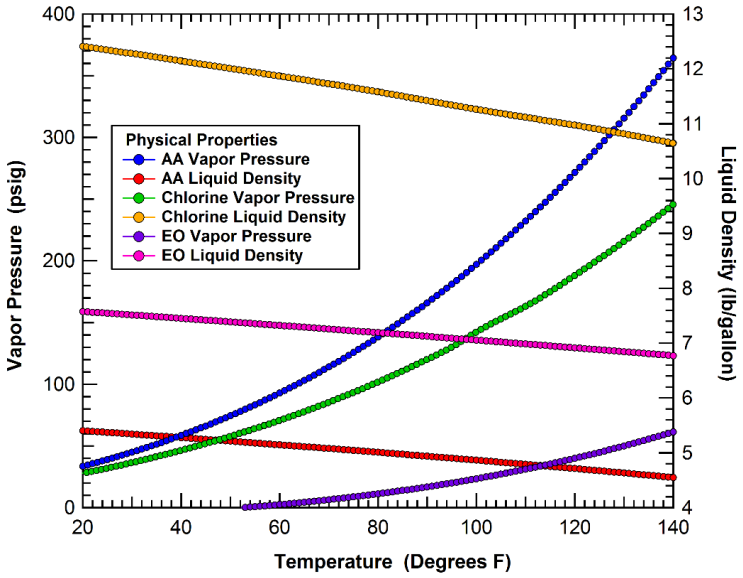

Figure 178. Comparison of physical properties of common pressure tank car commodities.

The resulting pressure-volume relationships used for tank car impact analyses with the three commodities are compared in Figure 179. These assume the tank and lading are at a temperature of approximately 75 degrees F and that the associated outage volume is 10.6 percent. As a result, the internal tank pressure for all three commodities rapidly increases as the tank relative volume approaches a shell full condition (relative volume of 0.896).

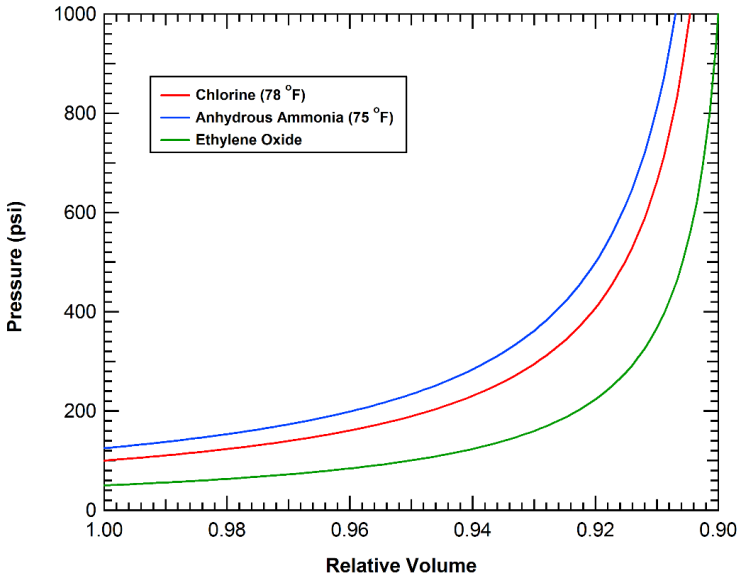

Figure 179. Tank pressure-volume relationships for various commodities (10.6% outage).

5.2 Chlorine Tank Cars

The tank design used in the analyses in Sections 3 and 4 of this report is the 105J600 chlorine tank car required under the interim rule. The TC128B tank shell is 100 inches in diameter and 472 inches long with 2:1 ellipsoidal heads. The tank is covered by a 0.119-inch-thick A1011 jacket with a 4-inch standoff from the tank. In this section, we analyze the puncture performance of the 105J500 chlorine tank car which was the standard prior to the interim rule. The difference between these two designs is that the 0.981-inch-thick tank shell used in the 105J600 is reduced to a 0.777-inch thickness for the 105J500 tank car.

5.2.1 Side Impacts of Chlorine Tank Cars

A series of analyses were performed with the 105J500 chlorine tank car including different size and shape impactors (summarized in Table 7), vertically offset impacts (summarized in Table 8), and 45-degree oblique impacts (summarized in Table 9). The objective of these analyses was to compare the relative puncture performance of the 105J600 chlorine tank car to that of the 105J500 tank car.

Table 7. Summary of the baseline side impact analyses on the 105J500 tank car

Calculation	Tank Type	Tank Shell	Shell Jacket	Impact Conditions	Internal Pressure (psi)	Puncture Force (lbs)	Puncture Energy (ft-lbs)
R18A	500 lb Cl	0.777 in TC128B	0.119 in A1011	15 mph 6"x6" ram	100 psi	8.860E+05	1.050E+06
R18B	500 lb Cl	0.777 in TC128B	0.119 in A1011	25 mph 12"x12" ram	100 psi	1.561E+06	3.560E+06
R18C	500 lb Cl	0.777 in TC128B	0.119 in A1011	20 mph 9"x9" ram	100 psi	1.289E+06	2.280E+06
R18D	500 lb Cl	0.777 in TC128B	0.119 in A1011	10 mph 3"x3" ram	100 psi	4.670E+05	3.220E+05
R18E	500 lb Cl	0.777 in TC128B	0.119 in A1011	15 mph 3"x6" ram	100 psi	6.770E+05	6.910E+05
R18F	500 lb Cl	0.777 in TC128B	0.119 in A1011	25 mph 3"x12" ram	100 psi	1.036E+06	1.330E+06
R18G	500 lb Cl	0.777 in TC128B	0.119 in A1011	15 mph 5.73 in. dia.	100 psi	7.960E+05	9.040E+05
R18H	500 lb Cl	0.777 in TC128B	0.119 in A1011	20 mph 7.64 in. dia.	100 psi	1.040E+06	1.610E+06
R18I	500 lb Cl	0.777 in TC128B	0.119 in A1011	25 mph 9.55 in. dia.	100 psi	1.209E+06	2.220E+06
R18J	500 lb Cl	0.777 in TC128B	0.119 in A1011	25 mph 11.46 in. dia.	100 psi	1.452E+06	2.930E+06
R18K	500 lb Cl	0.777 in TC128B	0.119 in A1011	25 mph 13.37 in. dia.	100 psi	1.629E+06	3.660E+06

Table 8. Summary of the vertical offset side impact analyses on the 105J500 tank car.

Head Impact Calculation	Tank Type	Tank Shell	Jacket	Impact Conditions	Vertical Offset (inches)	Internal Pressure (psi)	Puncture Force (lbs)	Puncture Energy (ft-lbs)
R18L	500 lb Cl	0.777 in TC128B	0.119 in A1011	25 mph 9.55 in. dia.	0.0	100 psi	1.224E+06	2.190E+06
R18M	500 lb Cl	0.777 in TC128B	0.119 in A1011	25 mph 9.55 in. dia.	-15.0	100 psi	9.950E+05	1.000E+06
R18N	500 lb Cl	0.777 in TC128B	0.119 in A1011	25 mph 9.55 in. dia.	-25.0	100 psi	7.590E+05	7.000E+05
R18O	500 lb Cl	0.777 in TC128B	0.119 in A1011	25 mph 9.55 in. dia.	-5.0	100 psi	1.273E+06	2.020E+06
R18P	500 lb Cl	0.777 in TC128B	0.119 in A1011	25 mph 9.55 in. dia.	-10.0	100 psi	1.144E+06	1.350E+06
R18Q	500 lb Cl	0.777 in TC128B	0.119 in A1011	25 mph 9.55 in. dia.	-20.0	100 psi	8.510E+05	7.960E+05

Table 9. Summary of the 45-degree oblique side impact analyses on the 105J500 tank car

Calculation	Tank Type	Tank Shell	Shell Jacket	Impact Conditions	Internal Pressure (psi)	Puncture Initiation Force (lbs)	Puncture Initiation Energy (ft-lbs)
R18R	500 lb Cl	0.777 in TC128B	0.119 in A1011	18 mph 6”x6” ram	100 psi	4.430E+05	3.850E+05
R18S	500 lb Cl	0.777 in TC128B	0.119 in A1011	25 mph 12”x12” ram	100 psi	6.710E+05	6.830E+05
R18T	500 lb Cl	0.777 in TC128B	0.119 in A1011	25 mph 9”x9” ram	100 psi	5.680E+05	4.570E+05
R18U	500 lb Cl	0.777 in TC128B	0.119 in A1011	10 mph 3”x3” ram	100 psi	3.500E+05	2.350E+05
R18V	500 lb Cl	0.777 in TC128B	0.119 in A1011	15 mph 5.73 in. dia.	100 psi	5.070E+05	4.140E+05
R18W	500 lb Cl	0.777 in TC128B	0.119 in A1011	20 mph 7.64 in. dia.	100 psi	6.320E+05	7.120E+05
R18X	500 lb Cl	0.777 in TC128B	0.119 in A1011	25 mph 9.55 in. dia.	100 psi	7.320E+05	8.820E+05
R18Y	500 lb Cl	0.777 in TC128B	0.119 in A1011	25 mph 11.46 in. dia.	100 psi	8.250E+05	1.200E+06
R18Z	500 lb Cl	0.777 in TC128B	0.119 in A1011	25 mph 13.37 in. dia.	100 psi	9.660E+05	1.610E+06

The normal side impact puncture forces and energies for the 105J500 tank car are compared to those of the 105J600 lb tank car for various size and shape impactors in Figure 180 and Figure 181, respectively. The puncture force comparison shows that the puncture forces for the 105J600 tank cars are approximately 30 percent greater than for the 105J500 tank cars. This difference is slightly greater than expected since the 0.981-inch tank shell is 26 percent greater than the 0.777-inch tank shell and both have identical 0.119-inch A1011 jackets. The puncture energy comparison, shown in Figure 181, indicates that the 105J600 tank car has a roughly 40-50 percent increase in puncture energy over the 105J500 tank car for the baseline side impacts.

The offset and 45-degree oblique side impact puncture energies for the 105J500 tank car are compared to those of the 105J600 lb tank car in Figure 182 and Figure 183, respectively. The vertical offset impact comparison shows that the puncture energies for the 105J600 tank cars range between 15-53 percent greater than for the 105J500 tank cars. The puncture energy comparison for the 45-degree oblique impacts, shown in Figure 183, indicates that on average the 105J600 tank car has a roughly 20 percent increase in puncture energy over the 105J500 tank car.

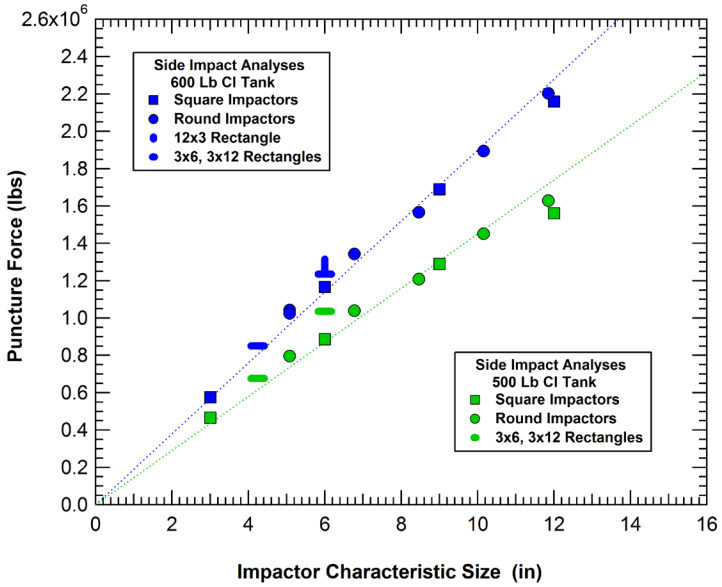

Figure 180. Puncture force comparisons for the 105J500 and 105J600 tank cars.

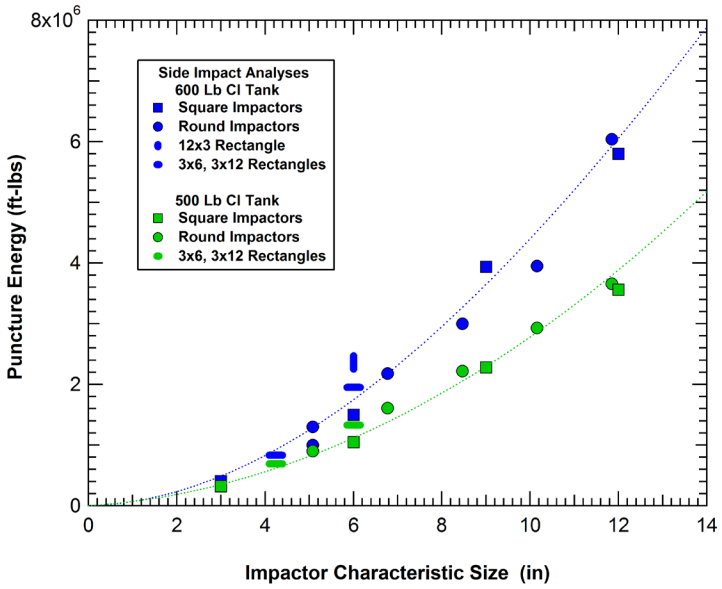

Figure 181. Puncture energy comparisons for the 105J500 and 105J600 tank cars.

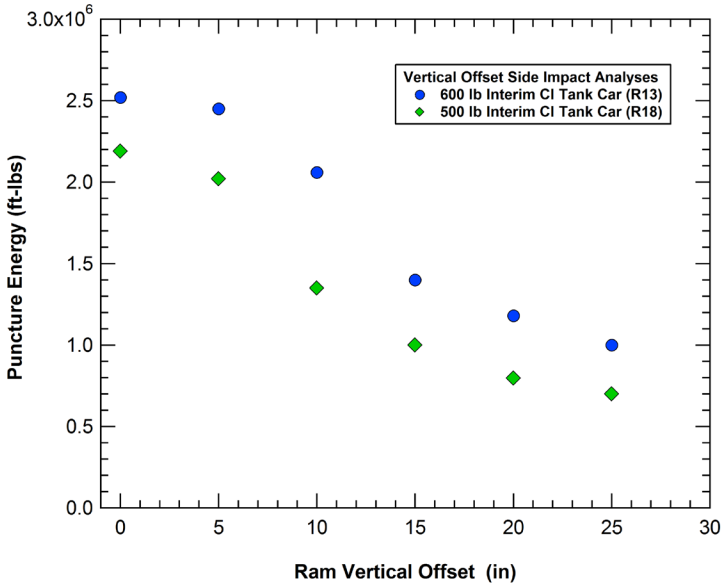

Figure 182. Comparison of the offset impact puncture energies for the 105J500 and 105J600 tank cars.

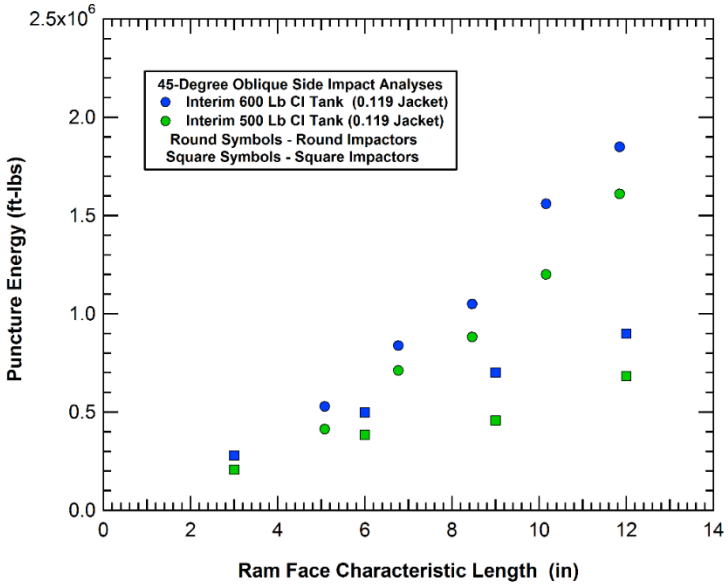

Figure 183. Comparison of the 45-degree oblique impact puncture energies for the 105J500 and 105J600 tank cars.

A summary of the relative side impact puncture energy of the 105J500 and 105J600 tank cars is shown in Figure 184. The summary includes all of the baseline, offset, and oblique impact conditions summarized in Figure 181, Figure 182, and Figure 183. Each point on Figure 184 represents the calculated puncture energy for the 105J600 tank car normalized by the corresponding puncture energy for the 105J500 tank car under identical impact conditions. The individual scenarios result in a range of normalized puncture energies from a minimum of 1.15 to a maximum of 1.85 (15-85 percent higher puncture energies). However, the wide range of impact scenarios considered results in an average increase in puncture energy of 39 percent for the 105J600 over the 105J500 chlorine tank car.

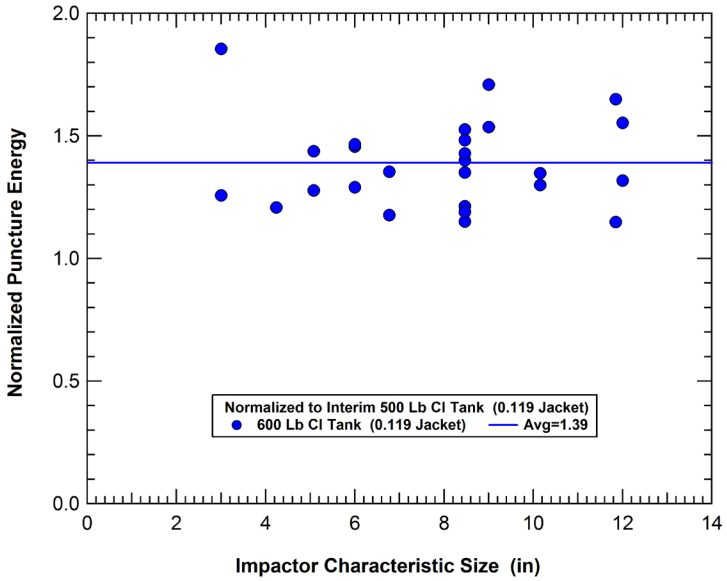

Figure 184. Normalized puncture energy summary for the 105J600 tank cars.

5.2.2 Head Impacts of Chlorine Tank Cars

The head puncture modeling approach was identical to that of the tank side impact puncture analyses. The head impacts analyzed matched the NGRTC Test 1 impact condition (i.e., impact point offset below the tank head center). As a result, the problem has a symmetry plane running vertically through the test specimen. This symmetry plane was used in most of the head impact simulations to reduce the model size by one half compared to the full head model. An example model of a tank head with the BW impact zone mesh used in the head puncture analyses is shown in Figure 185. An example of the impact and puncture behavior for the offset head impact on a chlorine tank head design is shown in Figure 186.

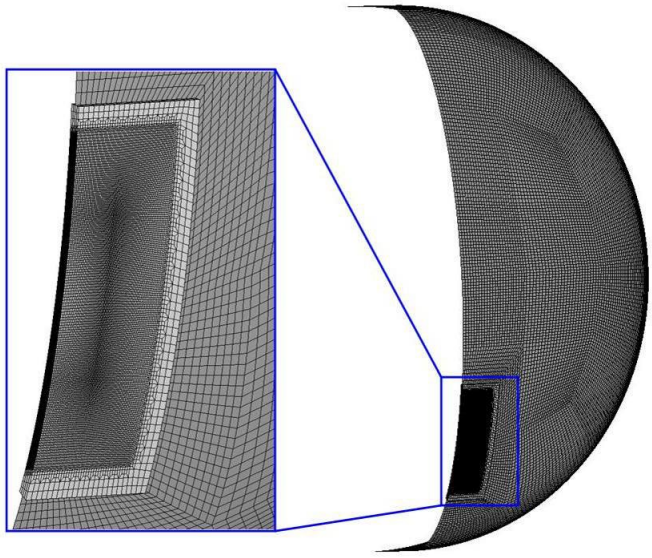

Figure 185. Tank head model and impact zone mesh used for the head impact analyses.

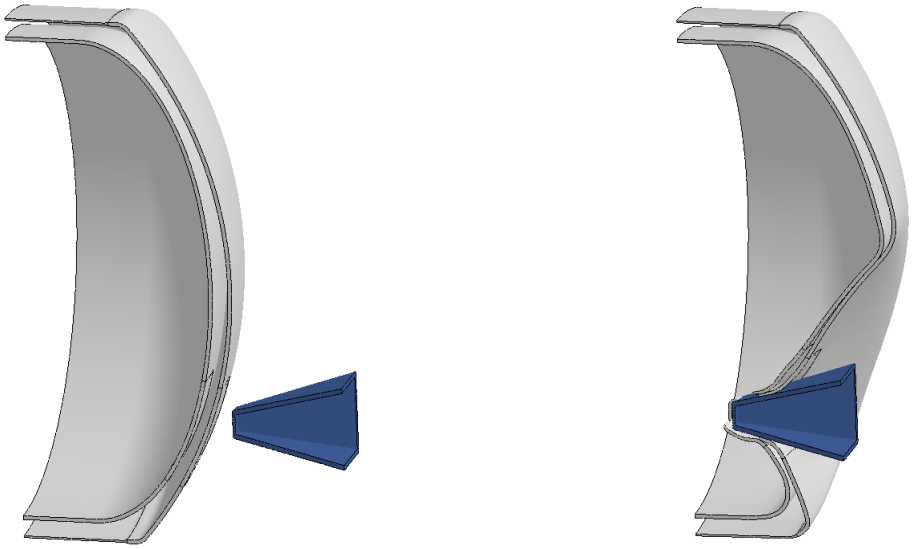

(a) Initial geometry **(b) Puncture behavior**

Figure 186. Calculated behavior of a tank head with the offset impact condition.

A more limited suite of impact conditions was performed on chlorine tank heads compared to the side impacts. A set of four impact analyses were performed using different size impactors in offset head impacts. The analyses are for 3, 6, 9, and 12-inch square impactors in an offset impact condition. A summary of comparative head impact analyses is provided in Table 10. The calculated force-deflection behaviors and integrated puncture energy curves for the 105J500 tank heads is shown in Figure 187. The behaviors for the 105J600 tank heads were similar but with increased impact force levels.

Table 10. Summary of the impact analyses for chlorine tank heads.

Head Impact Calculation	Tank Type	Tank Head	Jacket or Head Shield	Impact Conditions	Impactor Edge Radius	Internal Pressure (psi)	Puncture Force (lbs)	Puncture Energy (ft-lbs)
R95A	600 lb Cl	1.1360 TC128B	0.500" A572-50	15 mph 6"x6" ram	0.50 inch	100 psi	1.347E+06	1.321E+06
R95B	600 lb Cl	1.1360 TC128B	0.500" A572-50	25 mph 12"x12" ram	0.50 inch	100 psi	2.325E+06	3.733E+06
R95C	600 lb Cl	1.1360 TC128B	0.500" A572-50	20 mph 9"x9" ram	0.50 inch	100 psi	1.857E+06	2.464E+06
R95D	600 lb Cl	1.1360 TC128B	0.500" A572-50	10 mph 3"x3" ram	0.50 inch	100 psi	8.110E+05	4.120E+05
R22A	500 lb Cl	0.8281 TC128B	0.500" A572-50	15 mph 6"x6" ram	0.50 inch	100 psi	9.530E+05	8.930E+05
R22B	500 lb Cl	0.8281 TC128B	0.500" A572-50	25 mph 12"x12" ram	0.50 inch	100 psi	1.509E+06	2.740E+06
R22C	500 lb Cl	0.8281 TC128B	0.500" A572-50	20 mph 9"x9" ram	0.50 inch	100 psi	1.227E+06	1.810E+06
R22D	500 lb Cl	0.8281 TC128B	0.500" A572-50	10 mph 3"x3" ram	0.50 inch	100 psi	6.280E+05	3.430E+05

The relative head impact puncture energies of the 105J600 normalized to the corresponding energies of the 105J500 tank cars is shown in Figure 188. Each point on Figure 188 represents the calculated puncture energy for the 105J600 tank head normalized by the corresponding puncture energy for the 105J500 tank head under identical impact conditions. The individual scenarios result in a range of normalized puncture energies from a minimum of 1.20 for the smallest 3-inch impactor to a maximum of 1.73 for the largest 12-inch impactor (20-73 percent higher puncture energies). The four impact scenarios considered results in an average increase in puncture energy of 47 percent for the 105J600 over the 105J500 chlorine tank head.

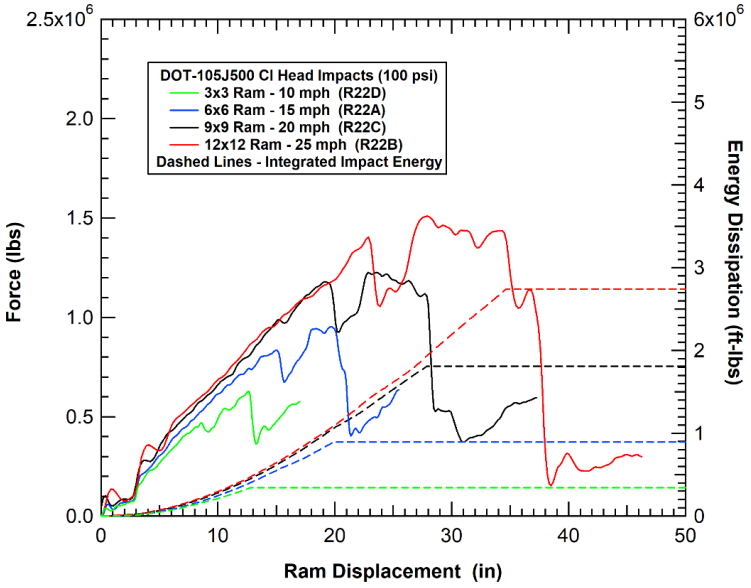

Figure 187. Calculated force-deflection behaviors for the 105J500 tank head impacts.

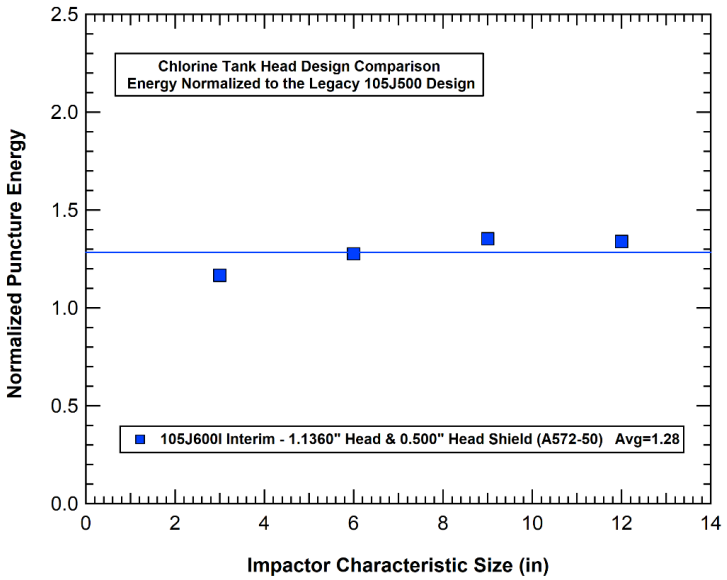

Figure 188. Normalized impact puncture energy summary for the 105J600 tank heads.

5.3 Ethylene Oxide Tank Cars

The baseline ethylene oxide (EO) tank car designs analyzed was the 300 lb EO tank car which is the most common existing design used for EO shipments. Analyses were also performed to evaluate variations on this design that include a proposed increase to a 400 lb design and the 500 lb design specified under the FRA interim rule. A summary of the tank parameters for these analyses are provided in Table 11.

Table 11. Summary of the ethylene oxide tank car design parameters.

Tank Designation	Tank Shell	Tank Jacket	Combined Thickness	Tank Diameter	Jacket Standoff
Baseline 105J300W	0.5625” TC-128B	0.119” A1011	0.6815 inch	111.0 inch	1.0 inch
Baseline 105J400W	0.7350” TC-128B	0.119” A1011	0.8540 inch	111.0 inch	1.0 inch
Interim 105J500W	0.9180” TC-128B	0.119” A1011	1.0370 inch	111.0 inch	1.0 inch

Three sets of analyses were performed for each of the tank designs. These include: (1) normal side impacts with a variety of different size and shape impactors, (2) vertical offset impacts, and (3) oblique side impacts with a variety of different size and shape impactors. The analyses of normal side impacts include 3x3, 6x6, 9x9, 12x12, 3x6, and 3x12 rectangular impactors, all with a 0.50-inch radius around the edges. Additional impact analyses were performed using 5.73-, 7.64-, 9.55-, 11.46-, and 13.37-inch diameter round impactors (ram face perimeter lengths of 18, 24, 30, 36, and 42 inch, respectively). These impactors (shown previously in Figure 69, Figure 73, and Figure 76) provide a significant amount of variation in impactor size and shape.

5.3.1 Normal side Impacts of EO Tank Cars

A summary of the normal side impact puncture forces and puncture energies for the baseline 300, 400, and 500 lb EO tank cars are provided in Figure 189 and Figure 190, respectively. The values for the puncture forces and energies are plotted against the ram face characteristic size (defined as the square root of the area of the impactor face). The comparison of the baseline EO tank car designs show that the puncture forces for the 400 and 500 lb EO tank cars are on average 32 percent and 68 percent greater, respectively, than for the baseline 300 lb EO tank. Similarly, the puncture energies for the 400 and 500 lb EO tank cars are on average 35 percent and 98 percent greater, respectively, than for the baseline 300 lb EO tank. As expected, increasing the thickness of the commodity tank is an effective method for increasing the puncture resistance of a given tank design.

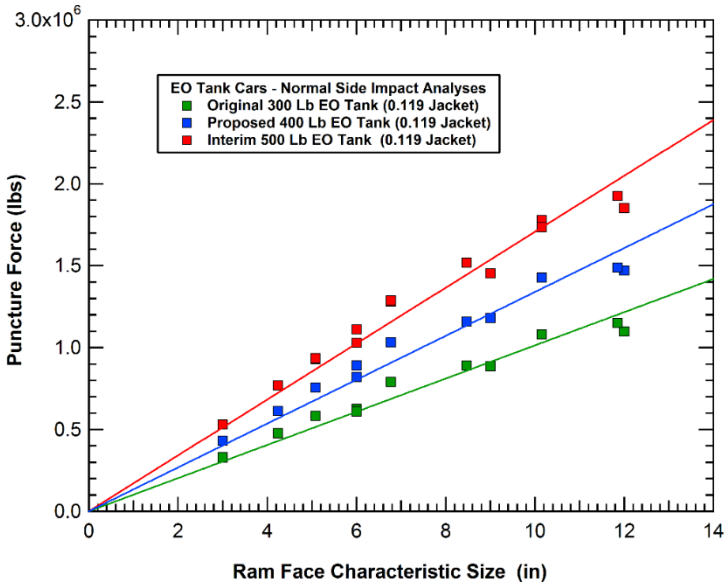

Figure 189. Calculated baseline EO tank puncture forces for various size and shape impactors.

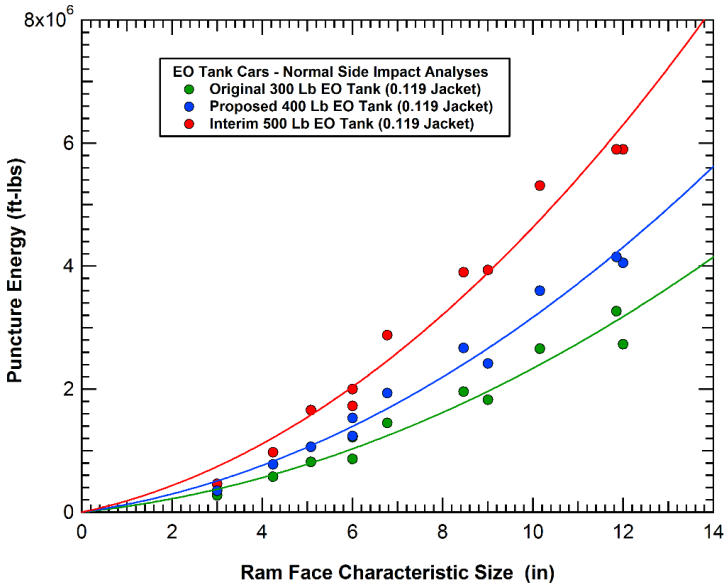

Figure 190. Calculated baseline EO tank puncture energies for various size and shape impactors.

5.3.2 Offset Impacts of EO Tank Cars

The second series of analyses performed for each of the EO tank car designs are the vertical offset impacts. The analyses were performed using conditions identical to those for the chlorine tank car described previously. The vertical offset side impact analyses were performed using the 9.55-inch-diameter round impactor.

A summary of the puncture forces and puncture energies for the various EO tank car designs are plotted against the vertical offset distance in Figure 171 and Figure 172, respectively. The

comparison shows that a small vertical offset (10 inches or less) has little effect on the puncture force. However, as the offset increases the puncture force drops significantly and a 25-inch offset reduces the puncture force by approximately 25 percent. The trends are similar for puncture energies but are more pronounced. The 25-inch offset reduces the puncture energy by approximately 60 percent. This is because the puncture force reduction is compounded by a corresponding reduction in the ram displacement required to develop that force.

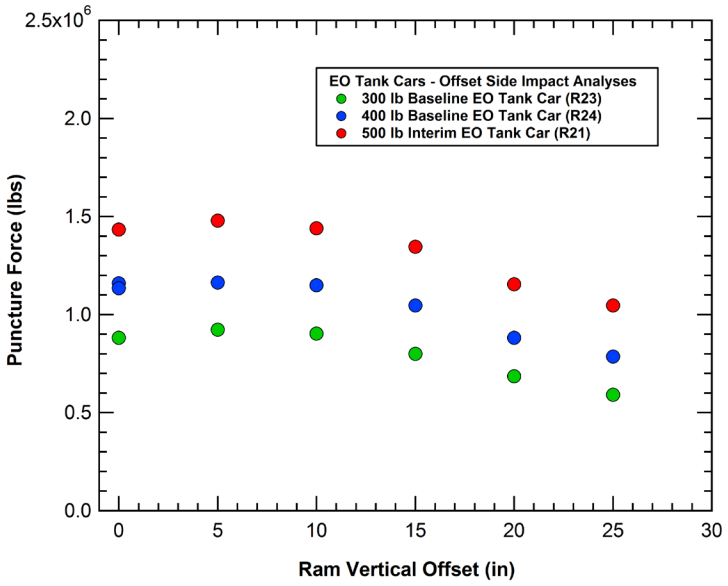

Figure 191. Calculated puncture forces for the various vertical offset side impacts.

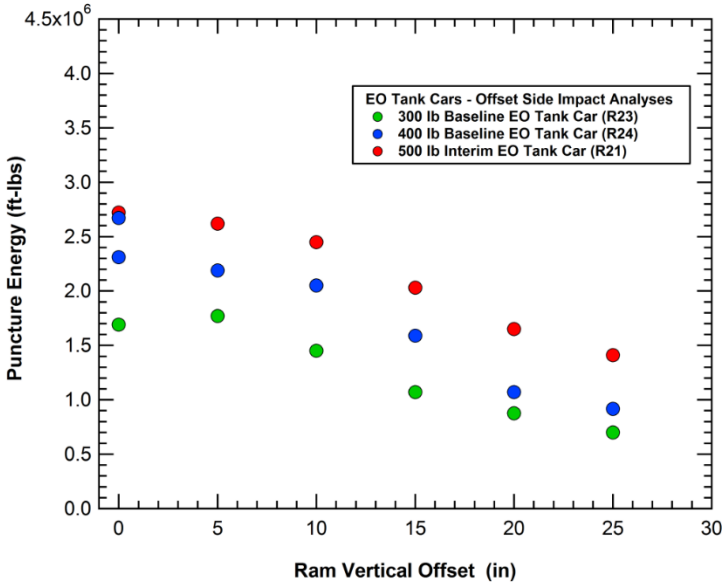

Figure 192. Calculated puncture energies for the various vertical offset side impacts.

5.3.3 Oblique Impacts of EO Tank Cars

In addition to the above normal and offset side impact analyses, a set of analyses was performed with the full range of impactor sizes and shapes at a 45-degree oblique impact angle. The impact scenario is shown in Figure 193.

Figure 193. Impact scenario for the 45-degree oblique side impact analyses.

Comparisons of the normal and oblique impact puncture forces and energies are provided in Figure 194 and Figure 195 for the baseline 300 lb, 400 lb, and 500 lb EO tank cars. The oblique puncture forces are approximately 50 percent of the normal puncture forces for the largest impactors. However, as the impactor size is reduced the differences in puncture force are also reduced. At the smallest 3x3 inch impactor there is very little difference between the normal and oblique impact puncture forces. As a result, a linear fit to the oblique puncture force data would not intercept the origin of the graph as used in the normal impact data.

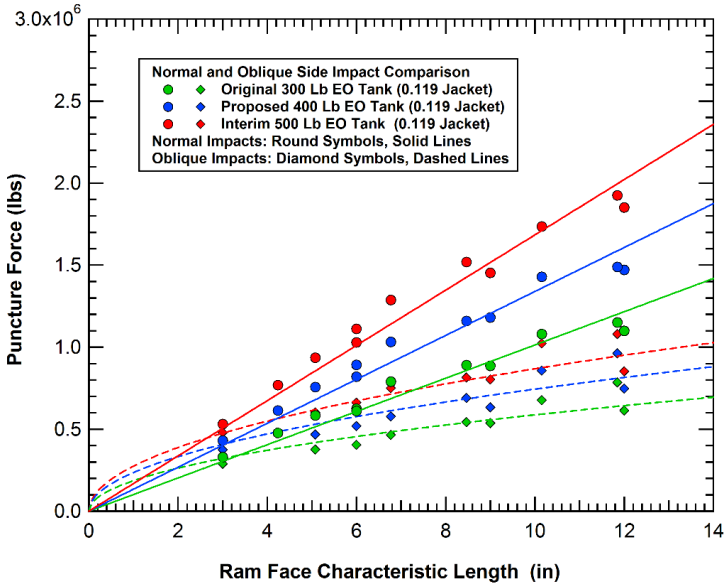

Figure 194. Comparison of puncture forces for normal and oblique impacts.

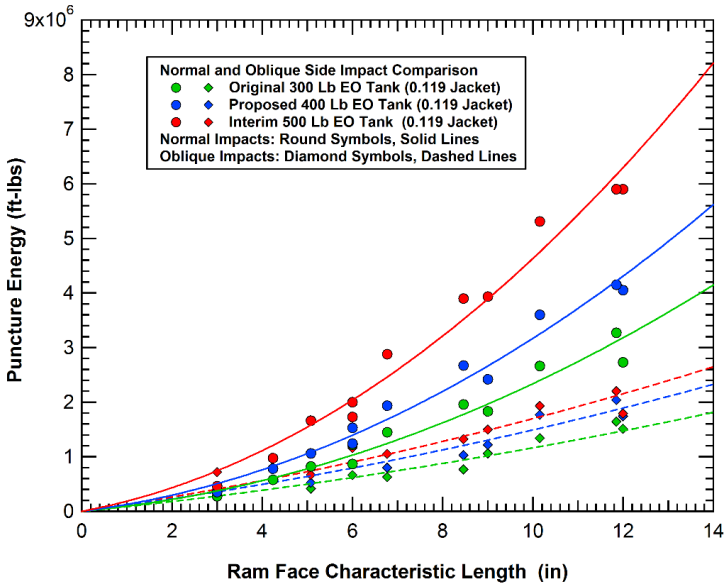

Figure 195. Comparison of puncture energies for normal and oblique impacts.

The puncture energies for the oblique impact show similar trends to the puncture forces. The puncture energies for the largest impactors are reduced by approximately 70 percent. Again, as the impactor size is reduced the differences in puncture energies are also reduced. For the 3x3 inch impactor there is much less difference between the normal and oblique impact puncture energies.

5.3.4 Summary of EO Tank Shell Puncture Performance

The full sets of normal, offset, and oblique impact analyses were performed for all three of the EO tank designs listed in Table 11. Thus, we have 26 different impact conditions analyzed for each of the EO tank designs. In this section, we summarize the relative puncture performance for the various designs.

To assess the relative puncture performance of different designs, we compare the puncture energy for each design under the same impact conditions. In this comparison, we normalize the puncture performance of each of the various designs to the baseline 300 lb EO tank car. Using this approach, the relative performance of the baseline 400 lb and 500 lb EO tank cars are summarized in Figure 196. Each of the symbols in Figure 196 represents the calculated puncture energy from one of the 26 impact scenarios divided by the corresponding puncture energy from the baseline 300 lb EO tank car for the same impact scenario. In addition to the puncture energy data from each of the calculations, an average value line for all 26 impact scenarios is added to the graph for each design. The comparison shows that the 400 lb tank car has on average a 34 percent higher puncture energy than the 300 lb EO tank car for the set of impact conditions analyzed. Similarly, the puncture energies for the 500 lb EO tank car are approximately double those of the 300 lb EO car for these impacts.

An alternative comparison is to compare the performance of the EO tank designs with the chlorine tank designs. For this comparison, the results of the normal and 45-degree oblique side impact analyses were used (20 analyses for each design). The puncture energy of each of the EO tank designs was normalized to the puncture energy for the 105J500 chlorine tank car. These

normalized puncture energies are shown in Figure 197. For comparison the normalized puncture energies for the 105J600 chlorine tank car are added to the graph. In this comparison, the puncture energies for the 105J500W EO tank car design are considerably higher than those of the 105J600W chlorine tank car. The EO tanks have relatively high puncture energies as a result of the lower tank pressures and larger diameter tanks. The 105J500W, 105J400W, and 105J300W EO tank cars have puncture energies on average 82 percent higher, 17 percent higher, and 12 percent lower, respectively, than the 105J500W chlorine tank car. The corresponding puncture energies for the 105J600W chlorine tank car were on average 37 percent higher than the 105J500W chlorine tank car.

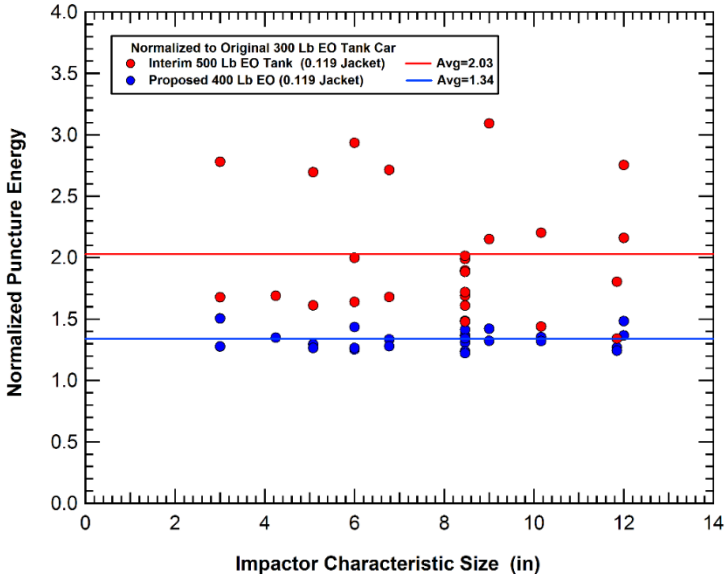

Figure 196. Comparison of relative puncture performance of the baseline EO tank designs.

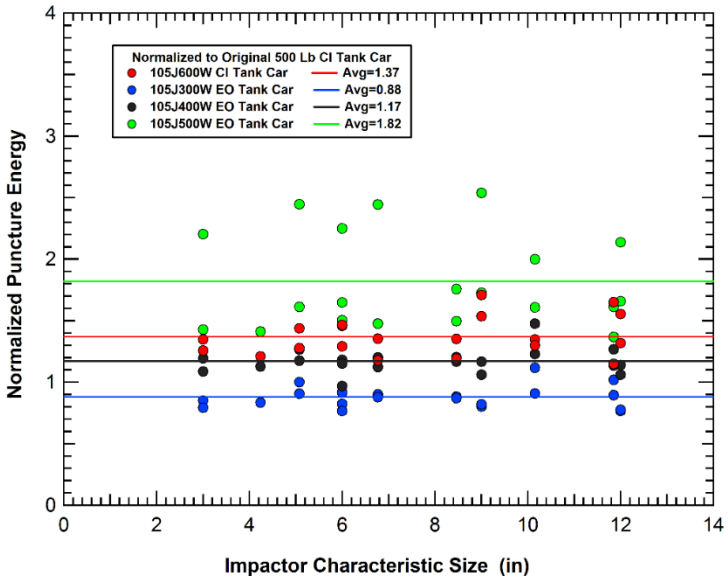

Figure 197. Comparison of relative puncture performance of EO and chlorine tank designs.

5.3.5 Head Impacts of EO Tank Cars

A suite of impact analyses was performed on the various EO tank head designs. For each design, a set of four impact analyses were performed using different size impactors in offset head impacts. A summary of comparative head impact analyses is provided in Table 12.

The relative side impact puncture energy of the 400 lb and interim 500 lb EO tank heads normalized to the corresponding energies of the legacy 300 lb tank head is shown in Figure 198. Each point represents the calculated puncture energy for the 400 or 500 lb tank head normalized by the corresponding puncture energy for the 300 lb tank head under identical impact conditions. The four impact scenarios considered results in an average increase in puncture energy of 37 percent and 49 percent for the 400 lb and 500 lb heads, respectively, over the 300 lb EO tank head.

In an alternative comparison, the relative head impact puncture energy of the 300, 400, and 500 lb EO tank heads are normalized to the corresponding energies of the legacy 105J500 chlorine tank heads, as shown in Figure 199. The four impact scenarios considered result in an average decrease in puncture energy of 18 percent for the 300 lb EO tank head relative to the 500 lb chlorine tank head. The 400 lb and 500 lb EO tank heads have an average increase in puncture energy of 10 percent and 22 percent, respectively, over the 500 lb chlorine tank head.

Table 12. Summary of the impact analyses for EO head impacts.

Head Impact Calculation	Tank Type	Tank Head	Jacket or Head Shield	Impact Conditions	Impactor Edge Radius	Internal Pressure (psi)	Puncture Force (lbs)	Puncture Energy (ft-lbs)
R29A	500 lb EO	0.9784 TC128B	0.500" A572-50	15 mph 6"x6" ram	0.50 inch	50 psi	1.191E+06	1.258E+06
R29B	500 lb EO	0.9784 TC128B	0.500" A572-50	25 mph 12"x12" ram	0.50 inch	50 psi	1,721,000	2.689E+06
R29C	500 lb EO	0.9784 TC128B	0.500" A572-50	20 mph 9"x9" ram	0.50 inch	50 psi	1.49E+06	2.24E+06
R29D	500 lb EO	0.9784 TC128B	0.500" A572-50	10 mph 3"x3" ram	0.50 inch	50 psi	7.31E+05	4.28E+05
R2BA	400 lb EO	0.8500 TC128B	0.500" A572-50	15 mph 6"x6" ram	0.50 inch	50 psi	1.02E+06	1.13E+06
R2BB	400 lb EO	0.8500 TC128B	0.500" A572-50	25 mph 12"x12" ram	0.50 inch	50 psi	1,390,000	1.964E+06
R2BC	400 lb EO	0.8500 TC128B	0.500" A572-50	20 mph 9"x9" ram	0.50 inch	50 psi	1.287E+06	1.988E+06
R2BD	400 lb EO	0.8500 TC128B	0.500" A572-50	10 mph 3"x3" ram	0.50 inch	50 psi	6.730E+05	4.050E+05
R2AA	300 lb EO	0.6030 TC128B	0.500" A572-50	15 mph 6"x6" ram	0.50 inch	50 psi	6.83E+05	7.04E+05
R2AB	300 lb EO	0.6030 TC128B	0.500" A572-50	25 mph 12"x12" ram	0.50 inch	50 psi	1.048E+06	2.381E+06
R2AC	300 lb EO	0.6030 TC128B	0.500" A572-50	20 mph 9"x9" ram	0.50 inch	50 psi	8.840E+05	1.488E+06
R2AD	300 lb EO	0.6030 TC128B	0.500" A572-50	10 mph 3"x3" ram	0.50 inch	50 psi	5.060E+05	3.320E+05

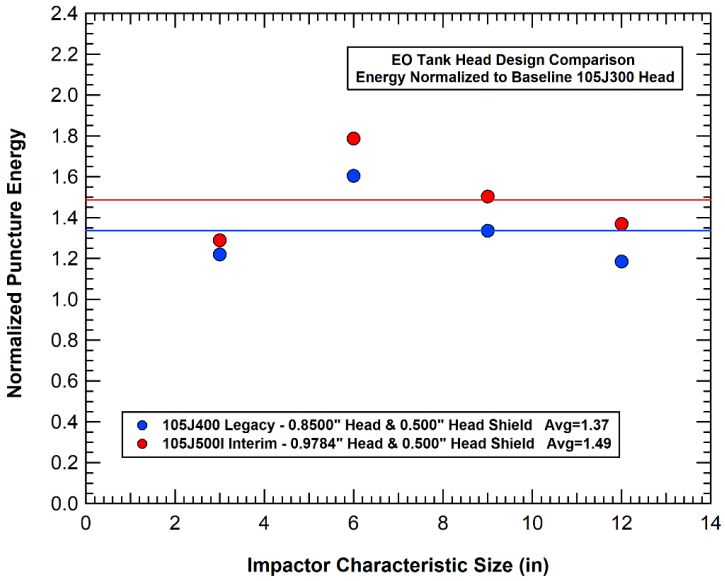

Figure 198. Normalized impact puncture energy summary for the 400 lb and 500 lb EO tank heads.

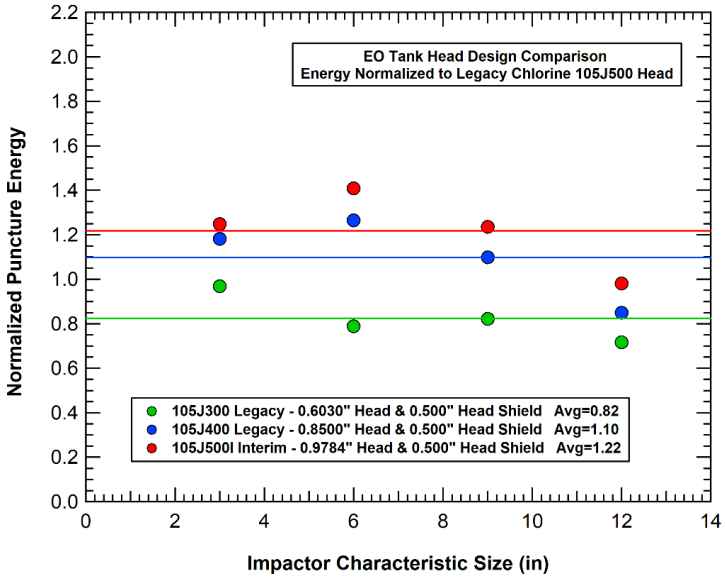

Figure 199. Normalized impact puncture energy summary for various EO tank heads.

5.4 Anhydrous Ammonia Tank Cars

The baseline anhydrous ammonia (AA) tank car designs analyzed was the 340 lb AA tank car which is a common existing design used for AA shipments. Analyses were also performed to evaluate the 500 lb design specified under the FRA interim rule. A summary of the tank parameters for these analyses are provided in Table 13.

Table 13. Summary of the anhydrous ammonia tank car design parameters.

Tank Designation	Tank Shell	Tank Jacket	Combined Thickness	Tank Diameter	Jacket Standoff
Baseline 112J340W	0.6250” TC-128B	0.119” A1011	0.7440 inch	111.0 inch	1.0 inch
Interim 112J500W	0.9180” TC-128B	0.119” A1011	1.0370 inch	111.0 inch	1.0 inch

Two sets of analyses were performed for each of the tank designs. These include the normal side impacts and the 45-degree oblique side impacts with a variety of different size and shape impactors. The impactors include the 3x3, 6x6, 9x9, 12x12, 3x6, and 3x12 rectangular impactors and the 5.73-, 7.64-, 9.55-, 11.46-, and 13.37-inch diameter round impactors. These impactors (shown previously in Figure 69, Figure 73, and Figure 76) provide a significant amount of variation in impactor size and shape.

5.4.1 Normal side Impacts of AA Tank Cars

A summary of the normal side impact puncture forces and puncture energies for the baseline 340 and 500 lb AA tank cars are provided in Figure 200 and Figure 201, respectively. The values for the puncture forces and energies are plotted against the ram face characteristic size defined as the square root of the area of the impactor face. The comparison of the baseline AA tank car designs shows that the puncture forces for the 500 lb AA tank cars are on average approximately 40 percent greater than for the baseline 340 lb AA tank. Similarly, the puncture energies for the 500 lb AA tank cars are on average 85 percent greater than for the baseline 340 lb AA tank. As expected, increasing the thickness of the commodity tank is an effective method for increasing the puncture resistance of the tank design.

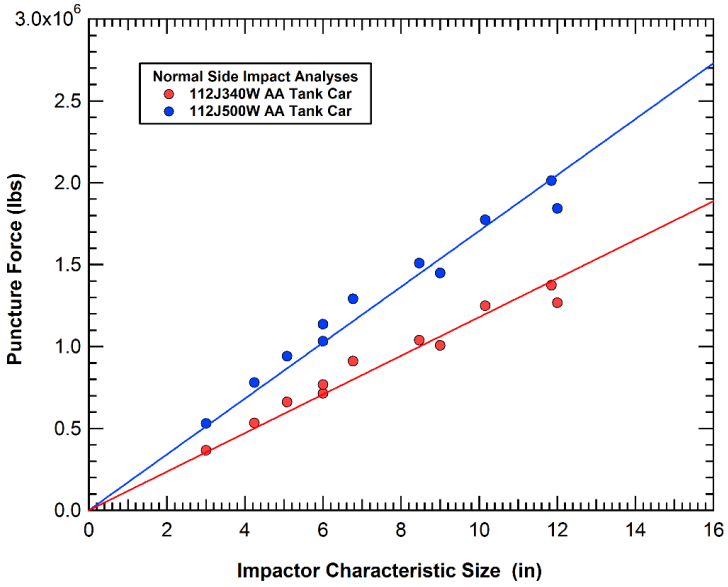

Figure 200. Calculated baseline AA tank puncture forces for various size and shape impactors.

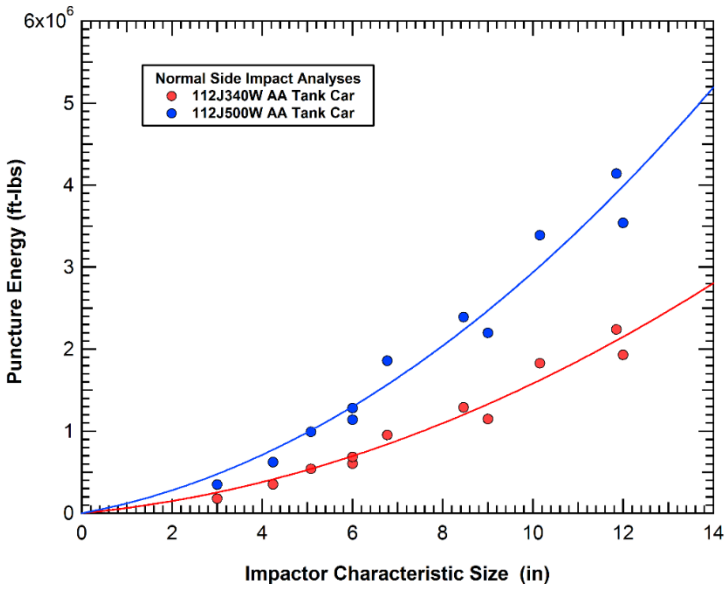

Figure 201. Calculated baseline AA tank puncture energies for various size and shape impactors.

5.4.2 Oblique Impacts of AA Tank Cars

In addition to the above normal side impact analyses, a set of analyses was performed with the full range of impactor sizes and shapes at a 45-degree oblique impact angle. The impact scenario is the same as used for the EO tank cars, shown previously in Figure 130. Comparisons of the normal and oblique impact puncture forces and energies are provided in Figure 202 and Figure 203 for the baseline 340 lb and 500 lb AA tank cars.

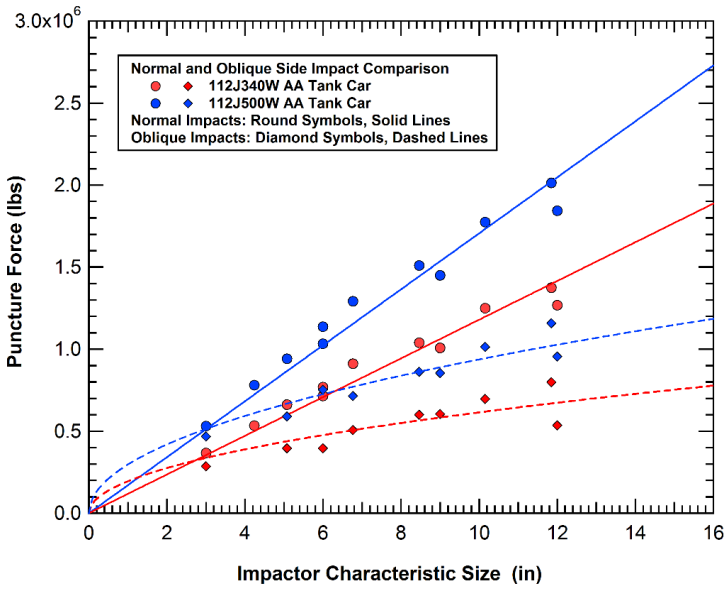

Figure 202. Comparison of puncture forces for normal and oblique impacts.

The oblique puncture forces are approximately 50 percent of the normal puncture forces for the largest impactors. However, as the impactor size is reduced the differences in puncture force are

also reduced. At the smallest 3x3 inch impactor there is very little difference between the normal and oblique impact puncture forces. As a result, a linear fit to the oblique puncture force data would not intercept the origin of the graph as used in the normal impact data.

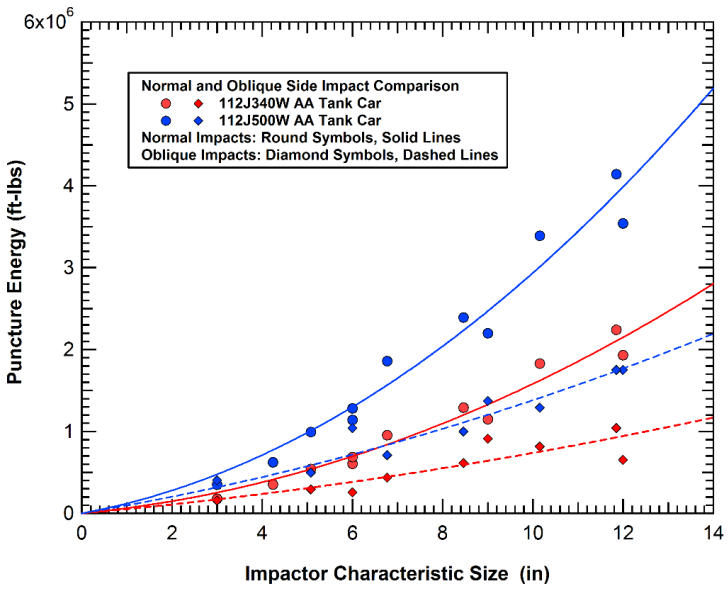

Figure 203. Comparison of puncture energies for normal and oblique impacts.

The puncture energies for the oblique impact show similar trends to the puncture forces. The puncture energies for the largest impactors are reduced by approximately 60 percent. Again, as the impactor size is reduced the differences in puncture energies are also reduced. For the 3x3 inch impactor there is much less difference between the normal and oblique impact puncture energies.

5.4.3 Summary of AA Tank Shell Puncture Performance

The full sets of normal and oblique impact analyses were performed for both of the AA tank designs listed in Table 13. Thus, we have 20 different impact conditions analyzed for both of the AA tank designs. In this section, we summarize the relative puncture performance for the various designs.

The performance of the AA tank designs is compared to the chlorine tank designs in Figure 204. For this comparison, the results of the normal and 45-degree oblique side impact analyses were used (20 analyses for each design). The puncture energy of each of the AA tank designs was normalized to the puncture energy for the 105J500W chlorine tank car. For comparison the normalized puncture energies for the 105J600W chlorine tank car are added to the graph. The 112J500W and 112J340W AA tank cars are on average 10 percent above and 39 percent below the 105J500W chlorine tank car, respectively. The puncture energies for the 105J600W chlorine tank car were on average 37 percent higher than the 105J500W chlorine tank car.

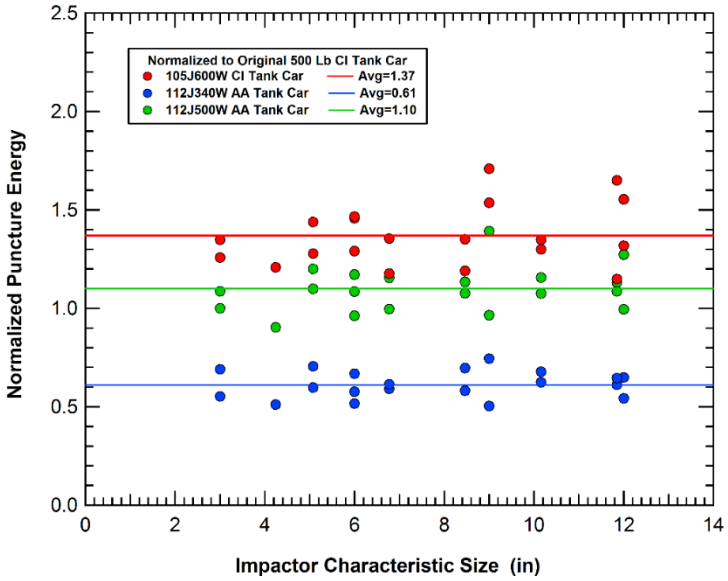

Figure 204. Comparison of relative puncture performance of AA and chlorine tank designs.

5.4.4 Head Impacts of AA Tank Cars

A suite of impact analyses was performed on the legacy 340 lb and interim 500 lb AA tank head designs. For each design, a set of four impact analyses were performed using different size impactors in offset head impacts. A summary of comparative head impact analyses is provided in Table 14.

Table 14. Summary of the impact analyses for AA head impacts.

Head Impact Calculation	Tank Type	Tank Head	Jacket or Head Shield	Impact Conditions	Impactor Edge Radius	Internal Pressure (psi)	Puncture Force (lbs)	Puncture Energy (ft-lbs)
R44A	500 lb AA	0.9784 TC128B	0.500" A572-50	15 mph 6"x6" ram	0.50 inch	125 psi	1.115E+06	1.047E+06
R44B	500 lb AA	0.9784 TC128B	0.500" A572-50	25 mph 12"x12" ram	0.50 inch	125 psi	1.816E+06	2.505E+06
R44C	500 lb AA	0.9784 TC128B	0.500" A572-50	20 mph 9"x9" ram	0.50 inch	125 psi	1.446E+06	1.786E+06
R44D	500 lb AA	0.9784 TC128B	0.500" A572-50	10 mph 3"x3" ram	0.50 inch	125 psi	6.880E+05	3.530E+05
R45A	340 lb AA	0.6720 TC128B	0.500" A572-50	15 mph 6"x6" ram	0.50 inch	125 psi	7.950E+05	6.410E+05
R45B	340 lb AA	0.6720 TC128B	0.500" A572-50	25 mph 12"x12" ram	0.50 inch	125 psi	1.280E+06	1.626E+06
R45C	340 lb AA	0.6720 TC128B	0.500" A572-50	20 mph 9"x9" ram	0.50 inch	125 psi	8.100E+05	1.173E+06
R45D	340 lb AA	0.6720 TC128B	0.500" A572-50	10 mph 3"x3" ram	0.50 inch	125 psi	5.200E+05	2.380E+05

The relative head impact puncture energy of the interim 500 lb AA tank heads normalized to the corresponding energies of the legacy 340 lb tank head is shown in Figure 205. Each point

represents the calculated puncture energy for the 500 lb tank head normalized by the corresponding puncture energy for the 340 lb tank head under identical impact conditions. The four impact scenarios considered results in an average increase in puncture energy of 54 percent over the 340 lb AA tank head.

In an alternative comparison, the relative head impact puncture energy of the 340 and 500 lb AA tank heads are normalized to the corresponding energies of the legacy 105J500 chlorine tank head, as shown in Figure 206. The four impact scenarios considered result in an average decrease in puncture energy of 34 percent for the 340 lb AA tank head relative to the 500 lb chlorine tank head. The 500 lb AA tank head had an average increase in puncture energy of 3 percent over the 500 lb chlorine tank head.

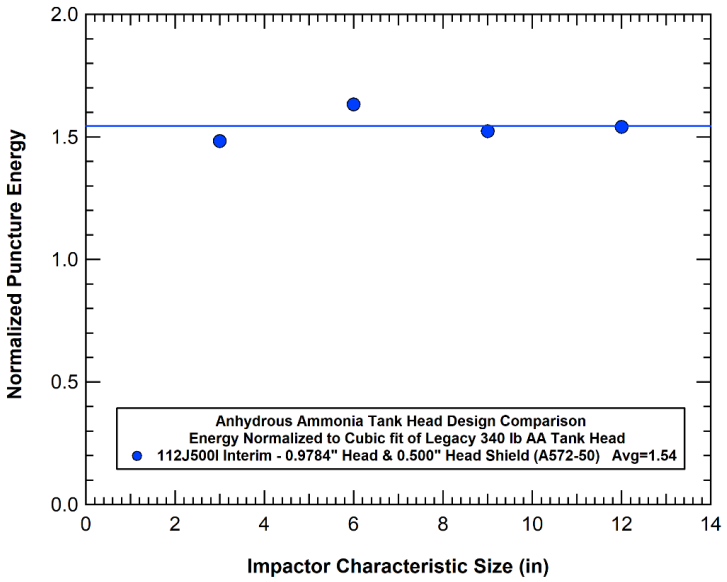

Figure 205. Normalized impact puncture energy summary for the 500 lb AA tank head.

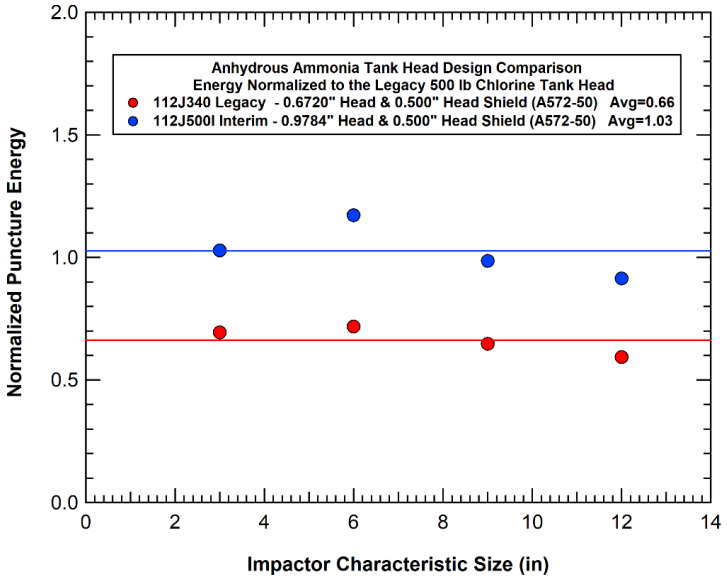

Figure 206. Normalized impact puncture energy summary for various AA tank heads.

5.5 Comparison of the Various Pressure tank Car designs

The full set of normal and 45-degree oblique side impacts were performed for all the chlorine, EO, and AA tank car designs considered. A comparison of the puncture energies for the normal impacts of the various tank cars are compared in Figure 207. The designs include 500 and 600 lb chlorine tank cars, 340 and 500 lb AA tank cars, and 300, 400, and 500 lb EO tank cars. The 112J340W AA tank car has the lowest puncture energies. The 105J300W EO tank car has the second lowest puncture energies. However, the puncture energies for the 105J300W EO tank car are on average approximately 50 percent higher than the 112J340W AA tank car and only 15 percent lower than the 105J500W chlorine tank car. The puncture energies for the 105J400W EO tank car are on average 20 percent greater than the 105J500W chlorine tank car and 10 percent higher than the 112J500W AA tank car. The puncture energies for the 105J500W EO tank car are the highest for any of the designs analyzed and on average 10 percent greater than the 105J600W chlorine tank car.

For a further comparison of the various designs, we added the results of the oblique impacts to the normal impacts and normalized all of the various designs to the puncture energies of the 105J500W chlorine tank car. The comparison for these normalized results is provided in Figure 208. In this comparison, the puncture energies for the 105J500W EO tank car are considerably higher than for any of the other tank car designs. The 105J400W EO tank car puncture performance is above the 112J500W AA tank car and below 105J600W chlorine tank car.

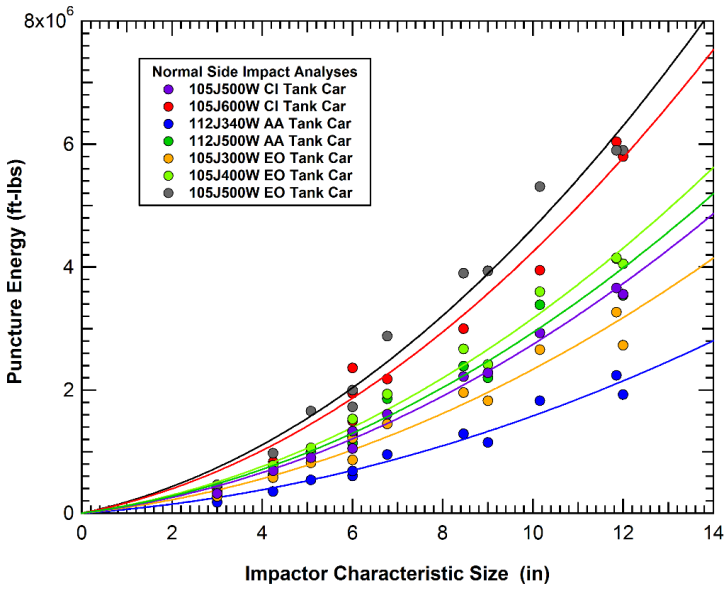

Figure 207. Comparison of relative puncture performance of various tank cars.

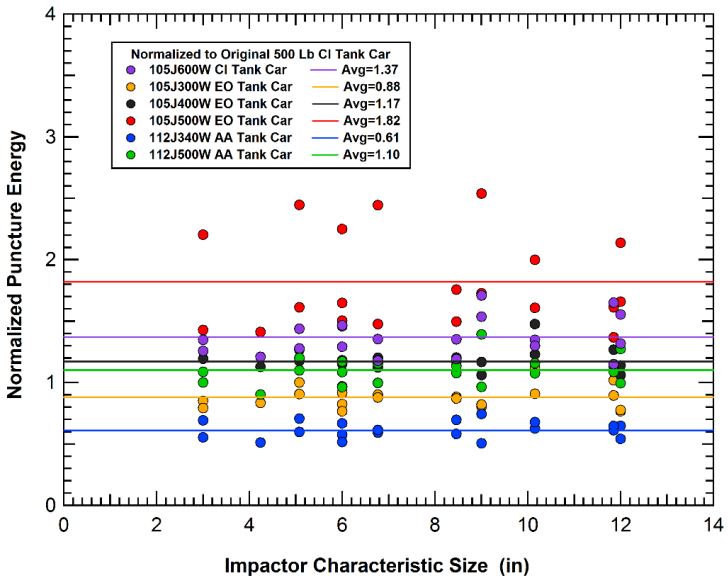

Figure 208. Relative side impact puncture performance of various tank designs.

A similar comparison for the normalized impact resistance in head impacts for the various tank designs is provided in Figure 209. In this comparison, the puncture energies for the 105J600W chlorine tank car are higher than for any of the other tank car designs. The 105J600W chlorine tank head was also somewhat unique in that the relative puncture resistance was much better for the largest impactors and showed significantly less improvement for the smallest impactor. The 105J400W EO tank car puncture performance is above the 112J500W AA tank car and below 105J600W chlorine tank car.

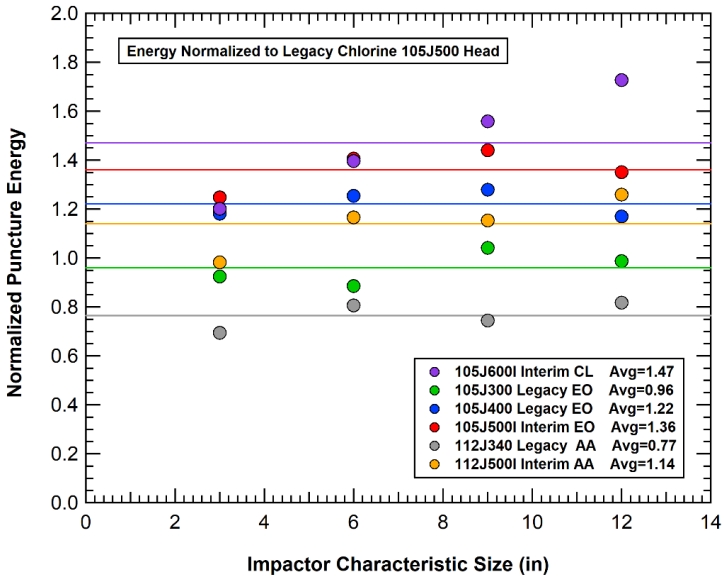

Figure 209. Relative head impact puncture performance of various tank designs.

5.6 DOT Class 111 tank cars

There have been ongoing activities in the tank car community to address safety of general-purpose tank cars. These activities were summarized in the FRA October 2011 regulatory update (FRA, 2011). The background information from that update is summarized below.

On March 9, 2011, the Association of American Railroads (AAR), on behalf of its members and the Tank Car Committee (TCC), jointly petitioned the Pipeline and Hazardous Materials Safety Administration (PHMSA) and Transport Canada (TC) to establish new standards for DOT Class 111 tank cars used to transport hazardous materials in packing groups I and II. The petition (P-1577), which was an outgrowth of a TCC executive working group, proposed new construction standards and specifically recommended no modification for existing tank cars. The AAR agreed to forward the petition to PHMSA on behalf of the TCC as a result of a unanimous decision by the Committee.

On May 10, 2011, FRA met with the Railway Supply Institute's (RSI) Tank Car Safety Committee to discuss improvements to tank cars used for the transportation of crude oil in unit trains. FRA requested this meeting to discuss improving tank car safety specific to crude oil tank cars given the recent increase in demand for these cars. The intent of the meeting was to spur discussion about innovative solutions that improve tank car safety for future changes in the hazardous materials transportation supply chain. The meeting resulted in the RSI members offering to develop an industry standard (non-regulatory) in collaboration with the AAR, the Renewable Fuels Association (RFA), Growth Energy, and the American Petroleum Institute (API). This effort is being conducted through a TCC Task Force led by the FRA.

On June 15, 2011, an Industry Consortium consisting of RSI, AAR, API, Growth Energy and the RFA submitted an action plan for the continuous reduction of risk associated with rail transportation of Crude Oil classified as PG I and II and Ethanol. The objectives of the action plan are to: (1) make recommendations on derailment risk reduction actions that can be quickly implemented; and (2) develop a new specification for tank cars transporting the aforementioned commodities and allowance for new cars for these services to be constructed to the standard proposed in P-1577. The Industry Consortium met with the FRA on July 12, 2011, to review the plan. The FRA concurred with the objectives and supported the proposed approach.

On July 20, 2011, at the summer AAR Tank Car Committee meeting docket T87.6 was created with a dual charge to develop an industry standard for tank cars used to transport crude oil, denatured alcohol, and ethanol/gasoline mixtures; as well as to consider operating requirements to reduce the risk of derailment of tank cars carrying Crude Oil classified as PG I and II, and Ethanol. The task force has been organized into two separate working groups; the first referred to as the design working group, and the second referred to as the operations working group. The 35-member design working group has met three times, August 17, September 9, and September 23 and has made significant progress.

The overarching objective of the working group is to maximize benefits, in this case safety, while minimizing cost. The working group is evaluating numerous design features intended to improve the survivability in accidents of tank cars transporting the referenced commodities. These features will include the new AAR standards outlined in CPC-1230 and petition P-1577, which is currently under review with PHMSA. The additional features will be considered that are based on the findings of forensic evaluations of recent derailments involving tank cars built for ethanol service. The segments of the industry represented in the working group all define cost

differently. The tank car builders/owners define cost in terms of manufacturability, utilization (limited number of commodities), and suitability of design (retrofit requirements to comply with changing regulations). The railroads define cost in terms of imposed operating requirements. The shippers define cost in terms of loss of capacity and compatibility with existing facility and railroad infrastructure.

The analyses described in this section of the report are in support of these T87.6 activities. The objective is to assess the relative puncture performance of existing and proposed designs. The properties of the specific designs analyzed are summarized in Table 15. The initial three designs analyzed were: (1) a baseline 111A100W1 tank car with a 7/15-inch A516-70 tank shell, (2) a CPC-1230 and P-1577 proposed design with a 0.5-inch TC128B tank shell, and (3) a proposed 2-layer concept that had a 3/8-inch TC128B Tank shell with a 1/4-inch jacket. However, for comparison, jacketed versions of the first two designs were added and a final design that considered the 3/8-inch shell and 1/4-inch jacket combined into a single monolithic 5/6-inch TC128B tank shell.

The DOT-117A100W tank car specification did not exist at the time of the original research project in 2013 (Kirkpatrick, 2013), and evaluation of the DOT-117 was outside the scope of this effort. However, the parameters for the DOT-117 tank car are included in Table 15 for comparison. Based on the comparison of parameters in Table 15 the DOT-117 design is similar to the jacketed P1577/CPC1230 tank car design but with an additional 1/16-inch thickness in the tank shell. Thus, we would expect additional puncture resistance above the levels obtained for that design.

Table 15. Summary of the general-purpose tank car design parameters.

Tank Designation	Tank Shell	Tank Jacket	Combined Thickness	Tank Diameter	Jacket Standoff
DOT-111A100W1	7/16” A516-70	N/A	0.4375 inch	111.0 inch	1.0 inch
DOT-111A100W3	7/16” A516-70	0.119 in A1011	0.5565 inch	111.0 inch	1.0 inch
P1577/CPC1230	0.5 in TC-128B	N/A	0.5000 inch	111.0 inch	1.0 inch
P1577/CPC1230(1)	0.5 in TC-128B	0.119 in A1011	0.6190 inch	111.0 inch	1.0 inch
Concept 1 (2-Layer)(2)	3/8” TC-128B	1/4” TC-128B	0.6250 inch	111.0 inch	1.0 inch
Concept 2 (Monolithic)	5/8” TC-128B	N/A	0.6250 inch	111.0 inch	1.0 inch
DOT-117A100W	9/16” A516-70	0.119 in A1011	0.6815 inch	111.0 inch	1.0 inch

Notes: (1) Note that the CPC-1230/P-1577 proposed design allows for a reduced 7/16-inch TC128B tank shell when a jacket is used. However, for these analyses the full 0.5-inch tank thickness was maintained to achieve a combined thickness that is roughly equivalent to the concept 1 and 2 designs.

(2) The 3/8-inch tank thickness is less than the minimum allowable under current regulations (7/16-inch). However, it was included to generate a hypothetical 2-layer design with a total combined thickness close to other designs.

5.6.1 Effects of Outage Volume

The general-purpose tank cars carry commodities in an unpressurized or low-pressure condition. However, with many of the commodities they carry they can typically operate with relatively low outage volumes. As a result, significant pressures can develop as an impactor dents the tank car and reduces the tank volume. A series of analyses were performed on a general-purpose car to analyze the effects of this outage volume and it was found to be a significant factor for the impact response (Kirkpatrick, 2010). The results of these analyses are summarized in this section.

The outage volume effects analyses were performed on an unpressurized DOT-111A100W1 tank car (no jacket). The specific geometry modeled is a 24,000-gallon tank shown in Figure 210. The tank is 111-inches in diameter with a 44-foot 7-inch-long cylindrical shell and 2:1-ellypsoidal heads. The tank is constructed with a 0.4375-inch-thick A516-70 steel tank shell. The tanks are impacted by the standard 6x6 inch impactor (286,000 lbs) at a speed of 16.2 mph.

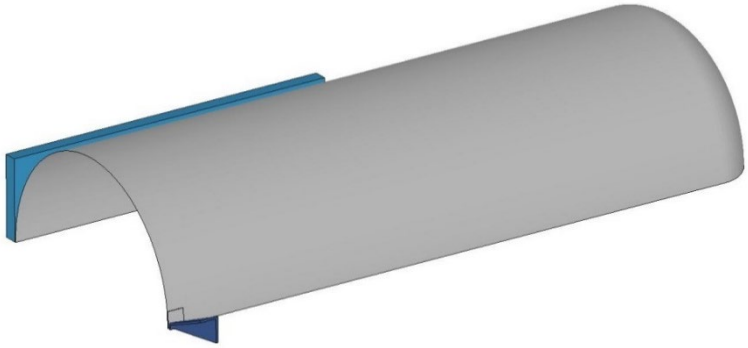

(a) Quarter-symmetry model of tank, ram, and reaction wall

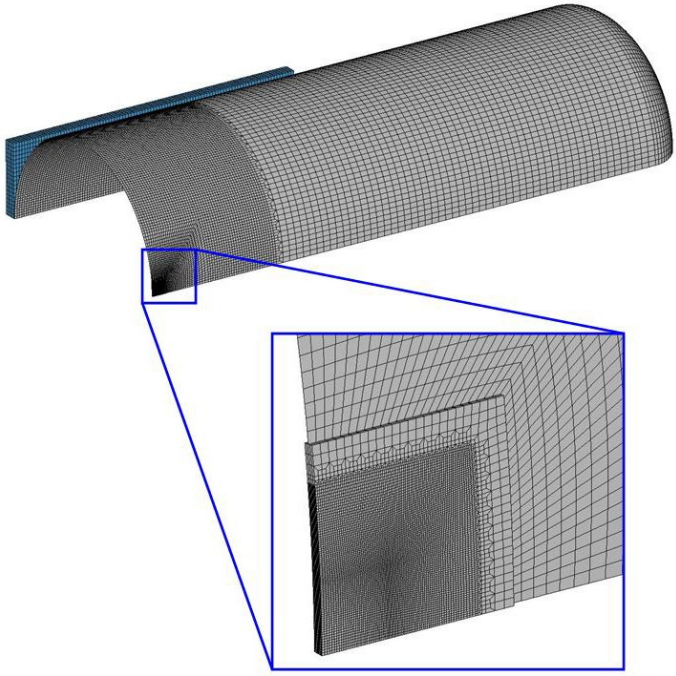

(b) Mesh resolution of the tank and impact patch

Figure 210. Model of a 23,000-gallon DOT-111A100W tank for analysis of outage volume effects.

The tanks in the analyses were modeled as initially unpressurized with a control volume algorithm used to include the pressure-volume effects. Control volume curves were generated representative of a tank filled with an incompressible liquid to various levels up to as much as 99 percent of the tank capacity (1 percent outage). The control volume pressure curves (gauge pressure) for outage volumes between 1 and 18 percent are shown in Figure 211 and are generated assuming the outage volume contains an ideal gas initially at one atmosphere (absolute pressure).

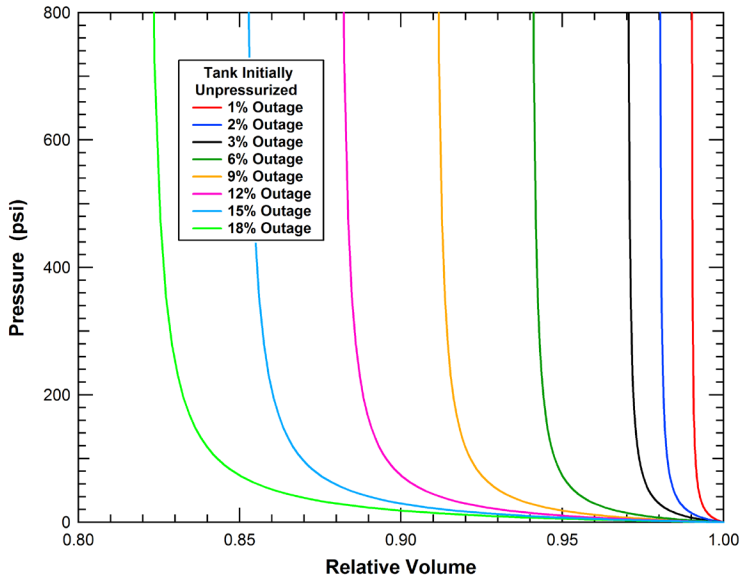

Figure 211. Control volume pressure curves for various outages between 1 and 18 percent.

A comparison of the impact deformations at the point of the tank shell penetration (puncture) for the 1, 3, and 9 percent outage volumes are shown in Figure 212. The comparison clearly shows that the larger outage volumes allow for a larger ram displacement before the tank is punctured. The comparison of the corresponding force-deflection behaviors and puncture energies with the different outage volumes is shown in Figure 213. A summary of the results from all the calculations is provided in Table 16. The comparison shows that tanks with outage volumes between 1 and 18 percent percent are punctured at similar force levels (392,000 to 467,000 lbs) but at significantly different displacements (16 to 65 inches) resulting in puncture energies between 256,000 and 1,370,000 ft-lbs.

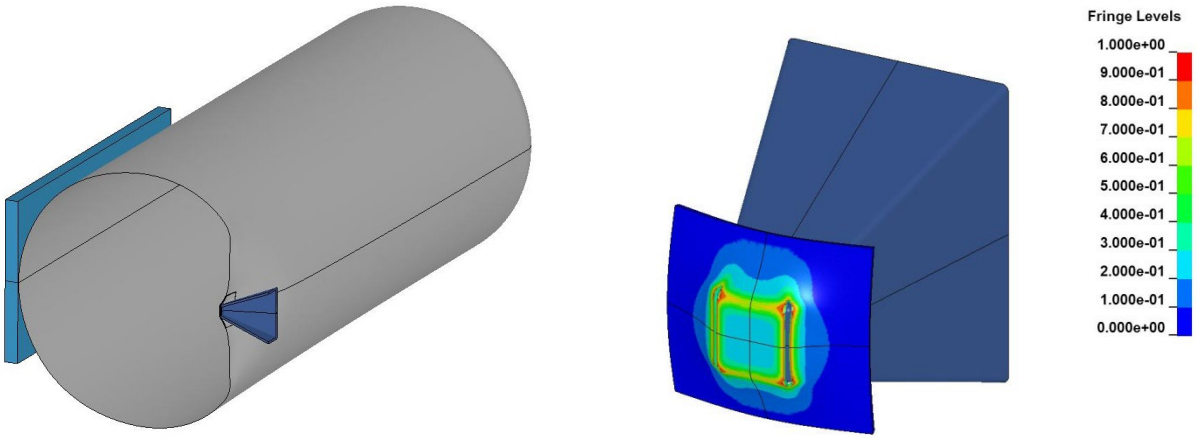

(a) Deformation at puncture for 1% outage

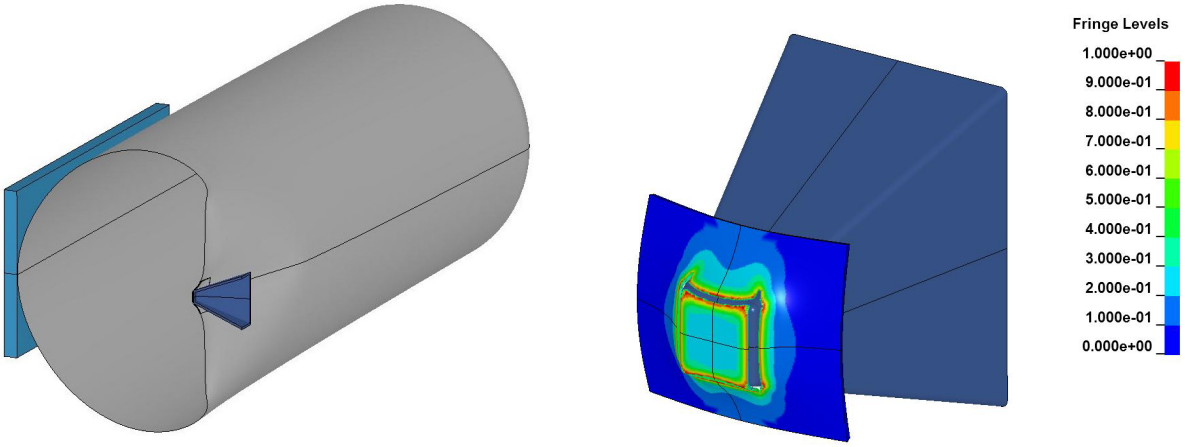

(b) Deformation at puncture for 3% outage

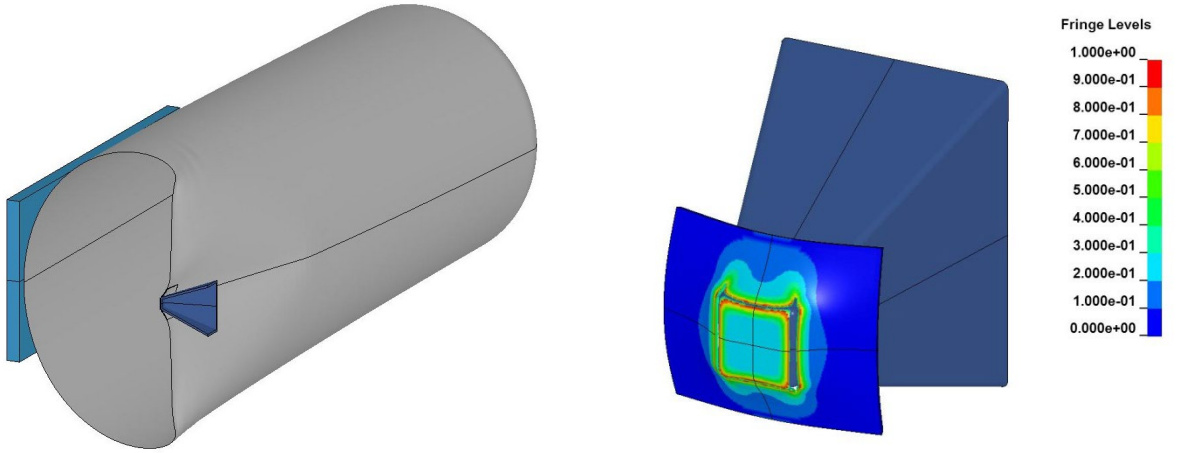

(c) Deformation at puncture for 9% outage

Figure 212. Calculated impact and puncture behaviors for different outage volumes.

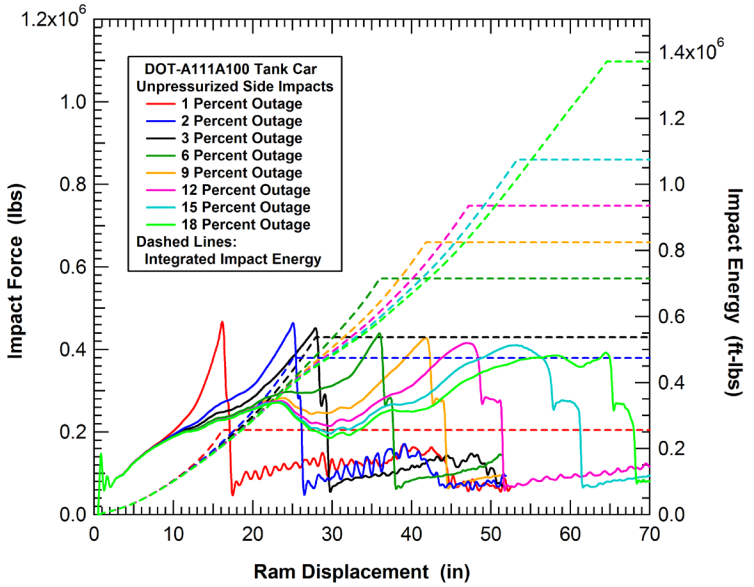

Figure 213. Force-deflection curves and puncture energies for different outage volumes.

Table 16. Summary of impact analyses to assess outage volume effects.

Outage Volume	Tank Shell	Impact Conditions	Ram Puncture Displacement	Puncture Force (lbs)	Puncture Energy (ft-lbs)	Pressure at Puncture
1 %	0.4375 in A516-70	16.2 mph 6”x6” ram	16 inches	467,000	256,000	178 psi
2 %	0.4375 in A516-70	16.2 mph 6”x6” ram	25 inches	464,000	474,000	89 psi
3 %	0.4375 in A516-70	16.2 mph 6”x6” ram	28 inches	452,000	537,000	53 psi
6 %	0.4375 in A516-70	16.2 mph 6”x6” ram	36 inches	439,000	715,000	29 psi
9 %	0.4375 in A516-70	16.2 mph 6”x6” ram	42 inches	428,000	825,000	22 psi
12 %	0.4375 in A516-70	16.2 mph 6”x6” ram	47 inches	415,000	935,000	18 psi
15 %	0.4375 in A516-70	16.2 mph 6”x6” ram	53 inches	410,000	1,075,000	17 psi
18 %	0.4375 in A516-70	16.2 mph 6”x6” ram	65 inches	392,000	1,370,000	21 psi
100 %	0.4375 in A516-70	16.2 mph 6”x6” ram	>110 inches	n/a	>1,800,000	n/a

The calculated control volume pressures in the various analyses are compared in Figure 214 and the corresponding pressures at the time of tank puncture are included in Table 16. As expected, the displacement required to develop an internal pressure increase is significantly larger for the larger outage volumes. Another interesting finding is that the calculated pressure levels at the point of the tank puncture is significantly reduced for the larger outage volumes. Thus, the

fraction of the impact force resulting from the impact deformations is larger as the puncture deformation is increased and the effects of increasing the outage volume would be expected to have a diminishing return.

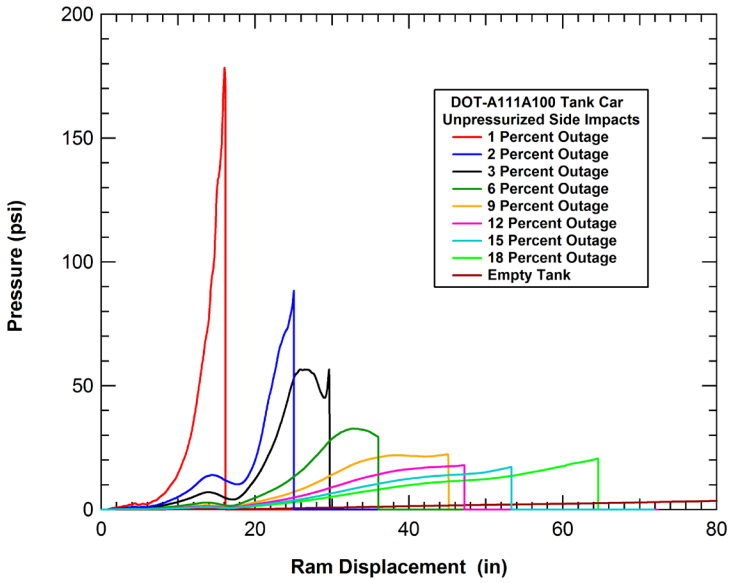

Figure 214. Control volume pressures for impacts with different outage volumes.

The calculated puncture energies are plotted against the outage volume in Figure 215. Also included in the figure is an approximate fit to the calculated energies. The functional form of the fit is a puncture energy that is proportional to the square root of the outage volume. Thus, the effect of an incremental increase of the outage volume results in a corresponding smaller increase in the puncture energy as the outage volume grows larger.

The calculated puncture energies have some natural variability about the functional fit. This variability can be seen by considering the impact behavior of an empty tank as shown in Figure 216. In the empty tank analysis, the impactor dents the side of the tank, and the dent continues to grow until the impactor eventually impacts the far side of the tank and impact wall (greater than 110-inch dent depth. As the side of the tank collapses the resistance of the tank dent oscillates between 150,000 and 300,000 lbs as the dent grows. The timing of the puncture for the different outage levels would be influenced by these natural variations in the impact resistance and as a result the calculated puncture energies do not fall directly on the smooth functional fit.

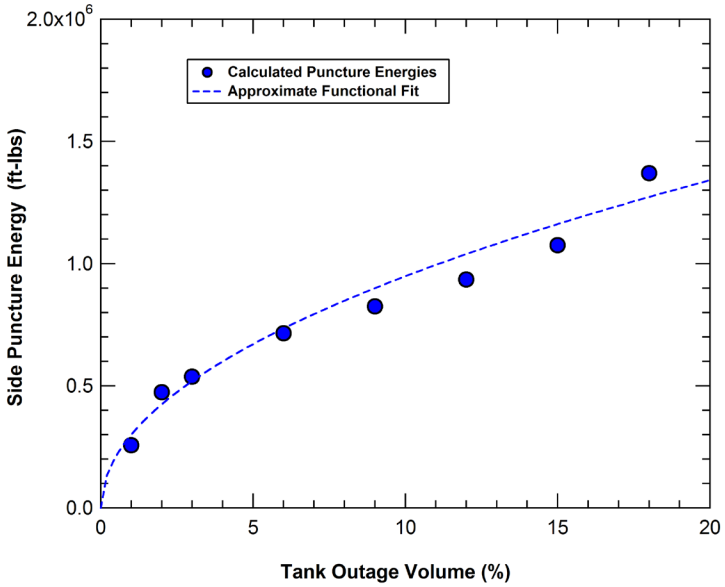

Figure 215. Effect of the outage volume on the puncture energy in side impacts.

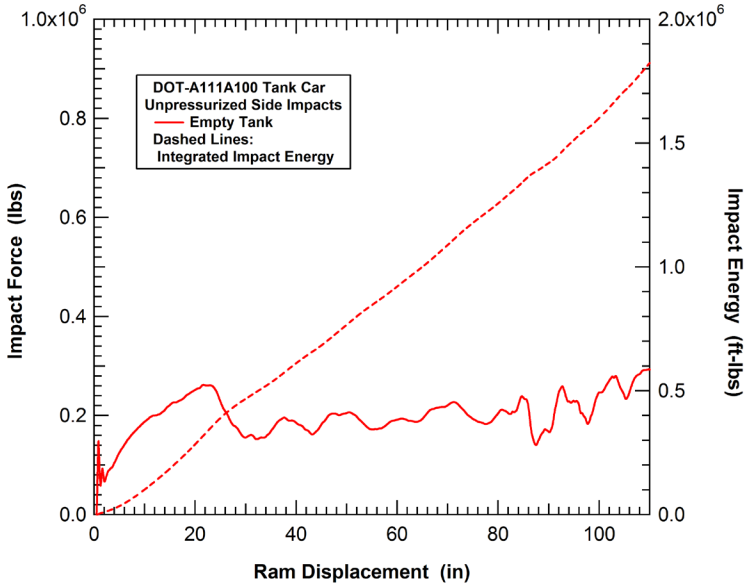

Figure 216. Force-deflection curve and impact energy dissipation for an empty tank.

An inspection of the puncture results in Table 16 indicates a trend of modest reduction in the puncture force as the outage volume is increased. The mechanisms believed responsible for this is the uniformity of the stresses around the edge of the impact face. The profile of the impact damage during the indentation process for both the 1 and 18 percent outage calculations is shown in Figure 217. When the tank has a 1 percent outage volume the damage development is relatively uniform around the perimeter of the contact patch other than the slight concentrations of damage at the corners of the impact face. However, for the 18 percent outage the damage along the top and bottom of the impact face is greater than that along the sides of the impactor. In addition, the larger dent depths would allow for more plastic bending around the edges and corners of the impact face which could result in a less uniform stress state and damage development through the thickness of the tank wall.

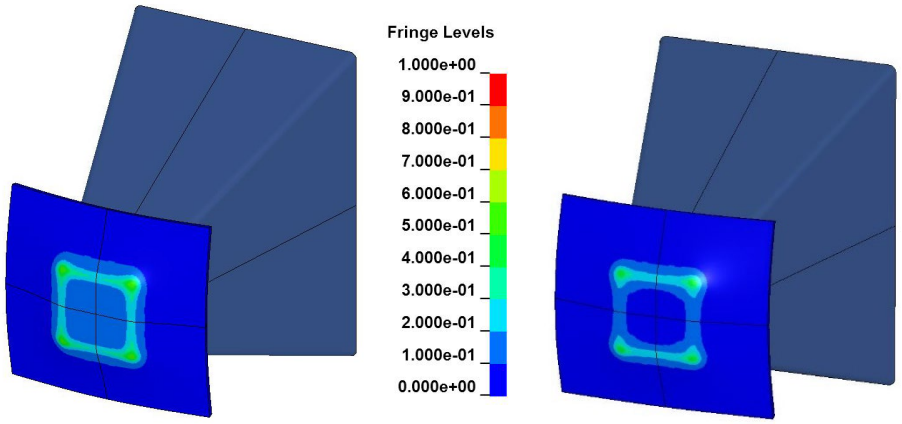

(a) Damage Profile for 1% outage (b) Damage Profile for 18% Outage

Figure 217. Side impact damage distribution for 1% and 18% outage volumes.

5.6.2 Analyses of Different General Purpose Tank Designs

The various general purpose tank car designs, listed in Table 15, were each analyzed with a suite of various size and shape impactors. The baseline analyses include the 3x3, 6x6, 9x9, 12x12, and 3x12 rectangular impactors as well as the 5.73-, 7.64-, 9.55-, 11.46-, and 13.37-inch diameter round impactors. The initial analyses used the 1 percent outage volume since it was the most critical tank condition.

The summary of the puncture forces for the various tank designs is shown in Figure 218. There is an approximately 40 percent increase in the puncture forces for the strongest tank designs (Concepts 1 & 2 and jacketed CPC1230/P1577) compared to the weakest tank design (111A100W1). However, these strong tank car designs have approximately 40 percent more steel in the tank and jacket than the baseline 111A100W1 design.

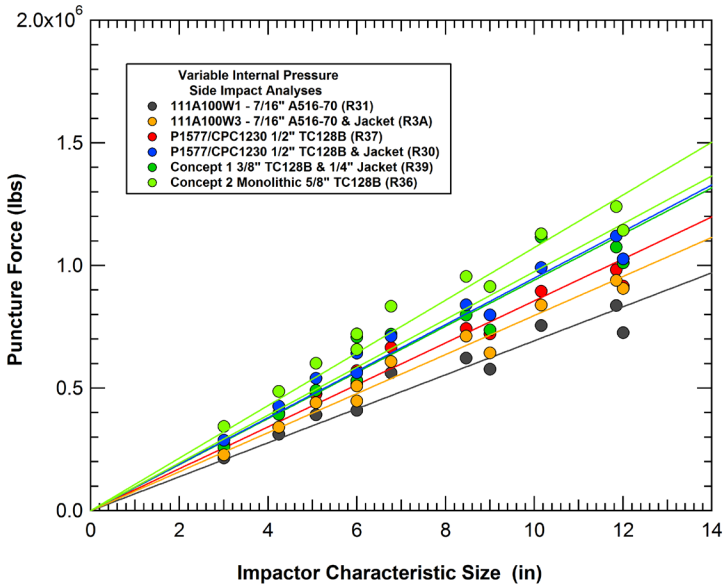

Figure 218. Correlation of the side impact puncture forces with the impactor characteristic size.

To eliminate the tank thickness effect, the puncture forces were normalized by dividing them by the combined tank and jacket thickness, shown in Figure 219. Although there is still some variation in the designs, the correlation of normalized puncture force and impactor size between designs is much closer. Some of the variation in the normalized puncture forces for the various designs comes from the difference between single and two-layer (jacketed) systems. In the two-layer systems the layers can puncture sequentially. If the sequential failures occur at significantly different levels of deformation, the puncture protection is not optimized, and the normalized puncture force is lower than would be achieved by a similar single layer system.

A summary of the puncture energies for the various general purpose tank designs is shown in Figure 220. The comparison shows that there is an approximately 70 percent increase in the puncture energies for the strongest tank designs (Concepts 1&2) compared to the weakest tank design (111A100W1). In addition, these improvements are greater than the 40 percent more steel in the Concept 1 & 2 tank designs compared to the baseline 111A100W1 design. The puncture energies for the jacketed CPC1230/P1577 design (with the 0.5-inch TC128B tank shell) are only about 10 percent lower than the Concept 2 design.

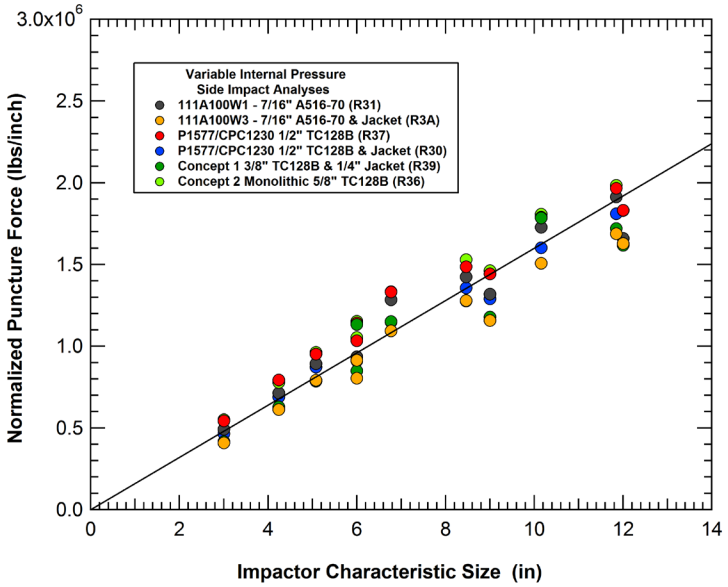

Figure 219. Comparison of the normalized side impact puncture forces.

The puncture energies in Figure 220 show a correlation that is roughly linear with the characteristic size of the impactor. This is in contrast with the comparison of impact energies for the 600 lb chlorine tank car, shown previously in Figure 80, where the shape of the puncture energy correlation is more closely represented by the square of the characteristic size of the impactor.

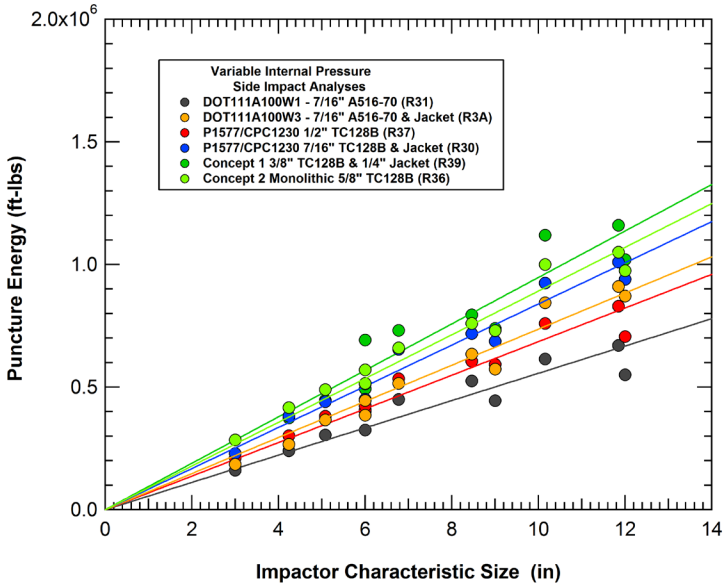

Figure 220. Correlation of the side impact puncture energies with the ram face characteristic size.

The differences in the puncture energy correlations of the 600 lb chlorine and general-purpose tank cars can be seen by a comparison of the response measures. The force deflection curves for the 105J600 and 111A100W3 tank cars and the 3-, 6-, 9-, and 12-inch square impactors are compared in Figure 221. For the 105J600 tank car the ram displacement at puncture is approximately linearly proportional to the puncture forces (and therefore the impactor characteristic size). The 3-inch impactor punctures at approximately 18 inches of ram displacement and the 12-inch impactor punctures at 55 inches of displacement. However, for the general-purpose tank car, the shape of the force deflection curves shows a response that becomes significantly steeper as the displacement increases and, as a result, the corresponding growth in the puncture displacements is reduced. The 3-inch impactor punctures at approximately 21 inches of ram displacement and the 12-inch impactor punctures at 28 inches of displacement with the 111A100W3 general purpose tank car.

A major effect controlling these behaviors of the chlorine and general-purpose tank cars is the initial pressure combined with the pressure buildup as the impactor dents the tank. The pressure displacement curves for the 105J600 and 111A100W3 tank cars and various rectangular impactors are compared in Figure 222. For the 105J600 tank car the initial pressure was 100 psi. The initial pressure helps to increase the initial stiffness of the tank. In addition, the pressure does not increase significantly until approximately 30-40 inches of ram displacement where the 10.6 percent outage volume starts to be significantly reduced. Only the 9- and 12-inch impactors puncture at pressures that are well above the initial pressure (160 and 210 psi respectively for the 9- and 12-inch impactors).

The internal pressure effects are significantly different for the 111A100W3 tank cars. These general-purpose tank cars were initially unpressurized resulting in a more compliant tank car. However, the pressure begins to build up significantly after approximately 15 inches of ram displacement as a result of the much smaller 1 percent outage volume. All the general-purpose tank car analyses are influenced by the buildup of pressure within the tank. The pressure at burst is approximately 25 psi for the 3-inch impactor and increases steadily to approximately 180 psi

for the 12-inch impactors. The effects of these pressures can be compared to the shape of the force-deflection curve for the empty general purpose tank car shown in Figure 216, where the indentation force remains low.

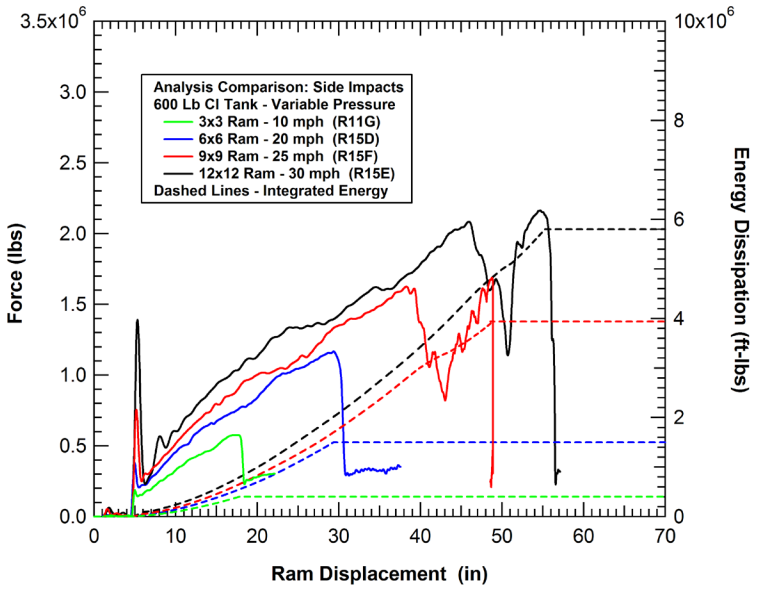

(a) 105J600 chlorine tank car

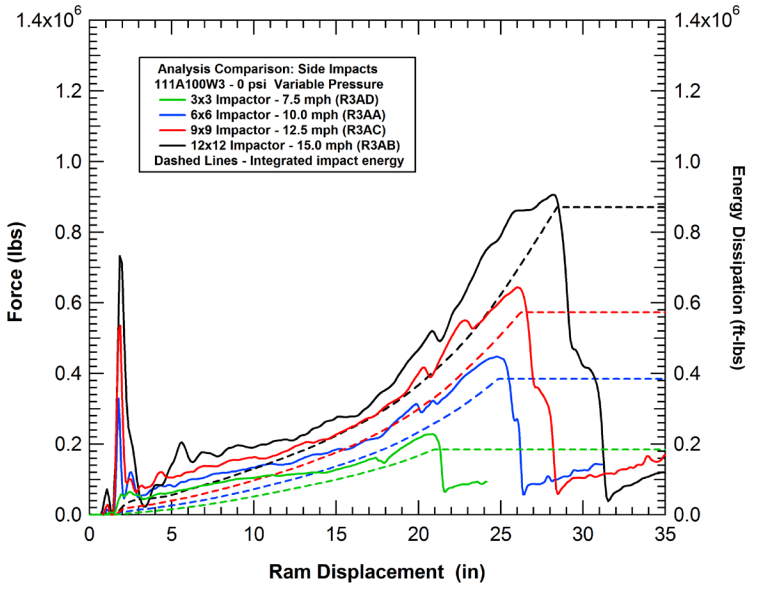

(b) 111A100W3 general purpose tank car

Figure 221. Calculated force-deflection curves for the 105J600 and 111A100W3 tank cars.

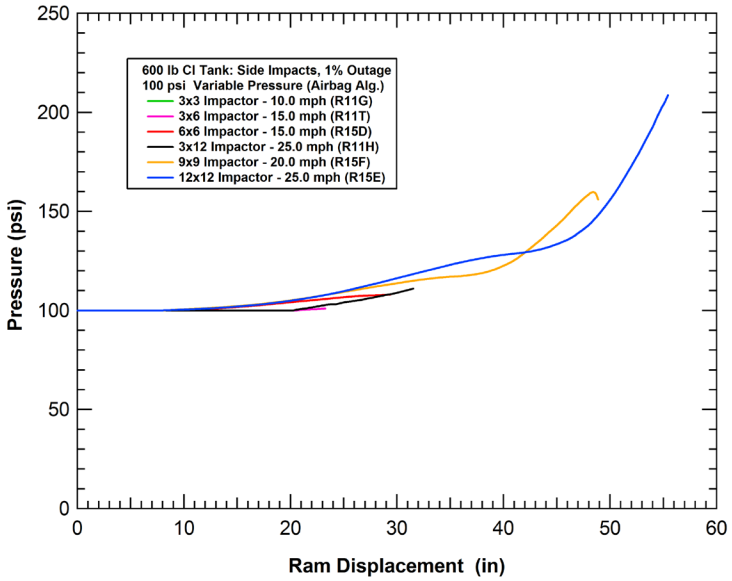

(a) 105J600 chlorine tank car

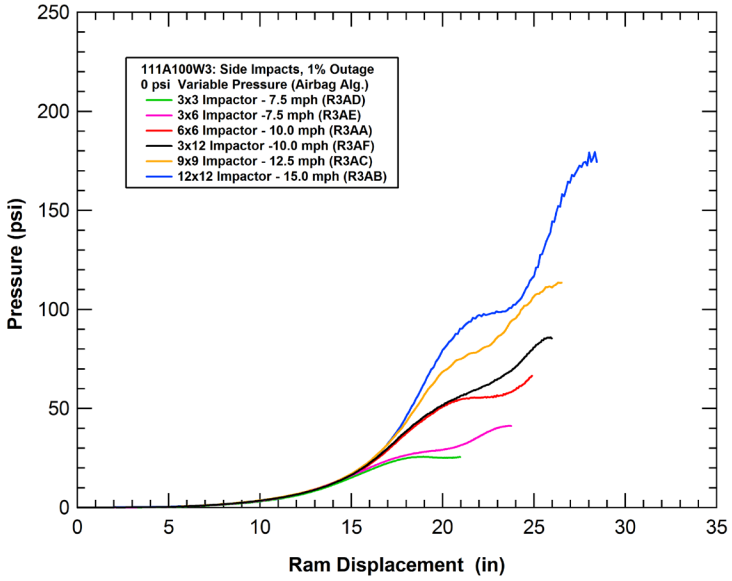

(b) 111A100W3 general purpose tank car

Figure 222. Calculated pressure-deflection curves for the 105J600 and 111A100W3 tank cars.

The above analyses were all performed for the assumed worst-case scenario of a 1 percent outage volume. However, it is desirable to also compare the trends to see if the conclusions hold for a more typical outage volume. To investigate this effect an additional set of analyses was performed with the outage volume increased to 3 percent. The analyses were performed for the jacketed DOT11A100W3 tank car, the P1577/CPC1230 tank car (both with and without a jacket), and the Concept 1 tank car. The comparison of the puncture forces for various size impactors, provided in Figure 223, shows that the outage volume has very little effect on the puncture forces. However, the corresponding comparison of the puncture energies for the various

impactors, provided in Figure 224, shows that the larger outage volumes result in significantly increased puncture energies.

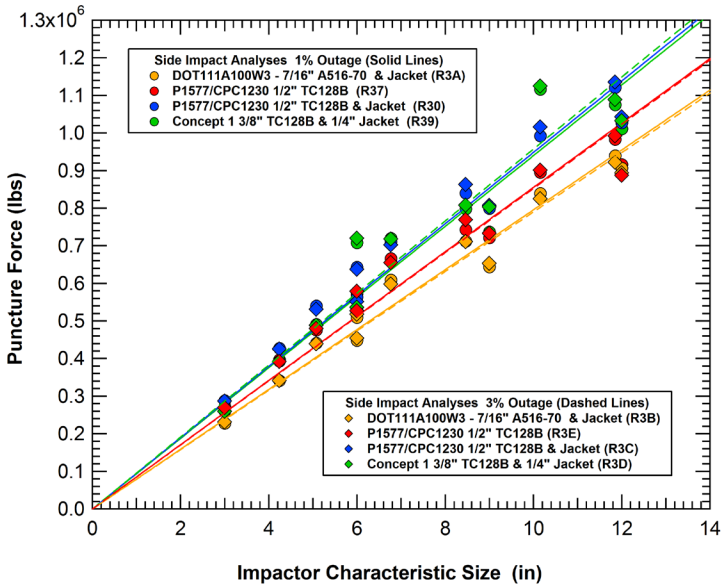

Figure 223. Comparison of calculated puncture forces for 1% and 3% outage.

An example of the corresponding force deflection curves for the 3-, 6-, 9-, and 12-inch square impactors for the 1 and 3 percent outage are shown in Figure 225. The comparison shows that the force deflection characteristics are similar with the exception that the displacement level, where the forces begin to rapidly increase, are significantly larger for the 3 percent outage. This can also be seen in the comparison of the tank pressure histories for various impact conditions, shown in Figure 226. The larger outage volume allows for larger displacements up to the point where the compression of the gasses in the outage volume develops internal pressure levels that are significant.

The relative puncture energy performance for the various tank car designs, summarized in Figure 224, are mostly consistent between the 1 and 3 percent outage calculations. The one notable discrepancy is the Concept 1 design which had clearly the best performance at the 1 percent outage level but was equivalent to the jacketed P1577/CPC1230 car at the 3 percent outage. This illustrates a potential issue associated with multi-layer tank car protection systems. The multiple layers have the potential for protection improvements over an equivalent single layer system when optimized for a given scenario. However, when impacted in alternative non-optimal conditions, the layers can be defeated sequentially, and the performance is degraded below that of the single layer.

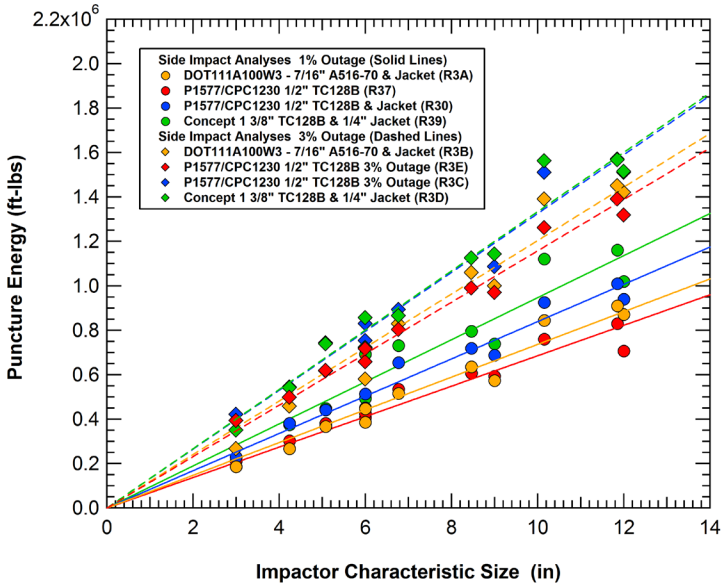

Figure 224. Comparison of calculated puncture energies for 1% and 3% outage.

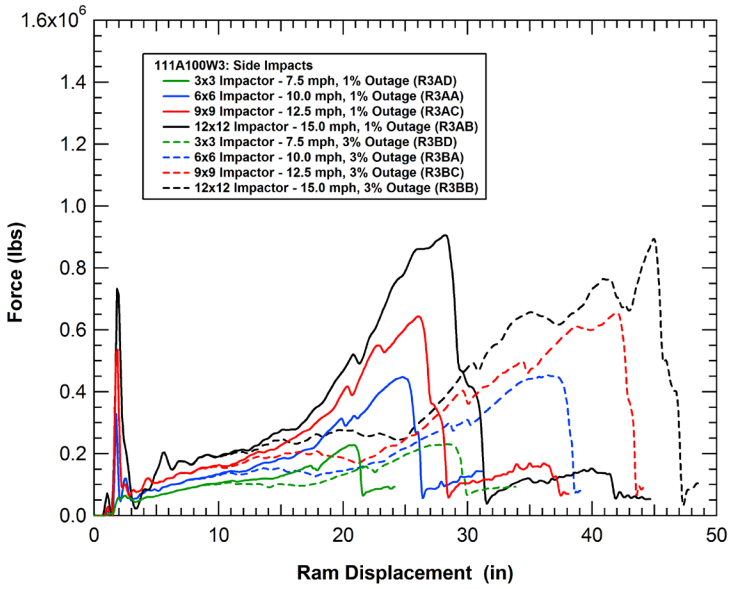

Figure 225. Comparison of force-deflection characteristics for 1% and 3% outage.

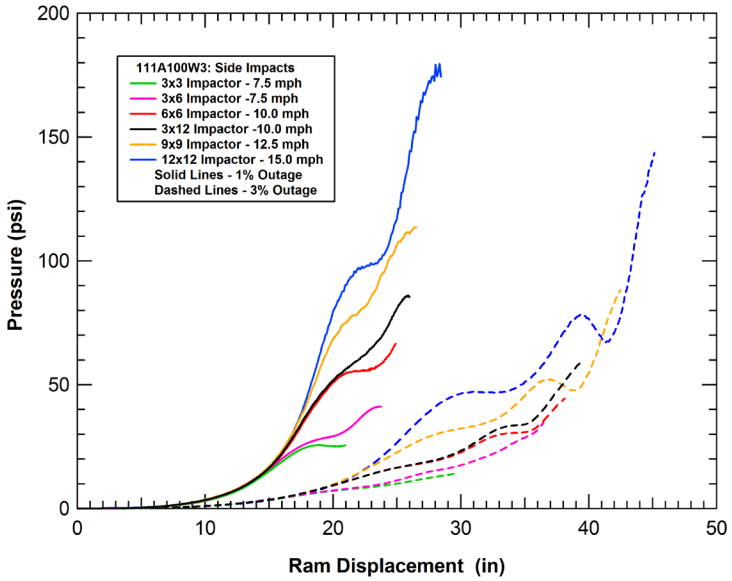

Figure 226. Comparison of calculated tank pressures for analyses with 1% and 3% outage.

5.6.3 Offset Impact Analyses

In addition to the investigation of various impactor sizes and shapes for the general-purpose tank cars, a series of analyses were performed to investigate the effects of a vertically offset impact point. The analyses and BCs were identical to those used for the 600 lb chlorine tank car thoroughly described in Section 4.4.1. The puncture forces and puncture energies for the various general purpose tank car designs and offset impact conditions are shown in Figure 227 and Figure 228, respectively. It is interesting to note that the 25-inch offset impacts result in approximately a 25 percent reduction in the puncture energies for the various general purpose tank car designs. This is in contrast to the 60 percent drop in puncture energy for the 25-inch offset impact on the 105J600 chlorine tank car.

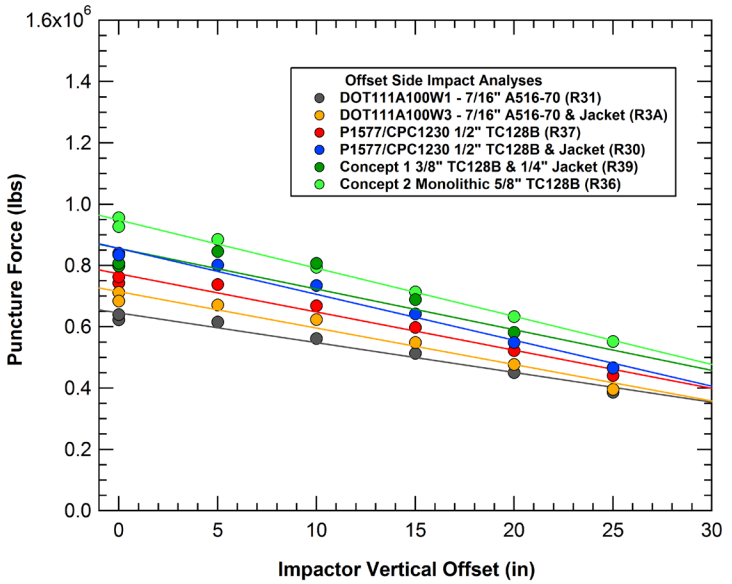

Figure 227. Calculated puncture forces for the various vertical offset side impacts.

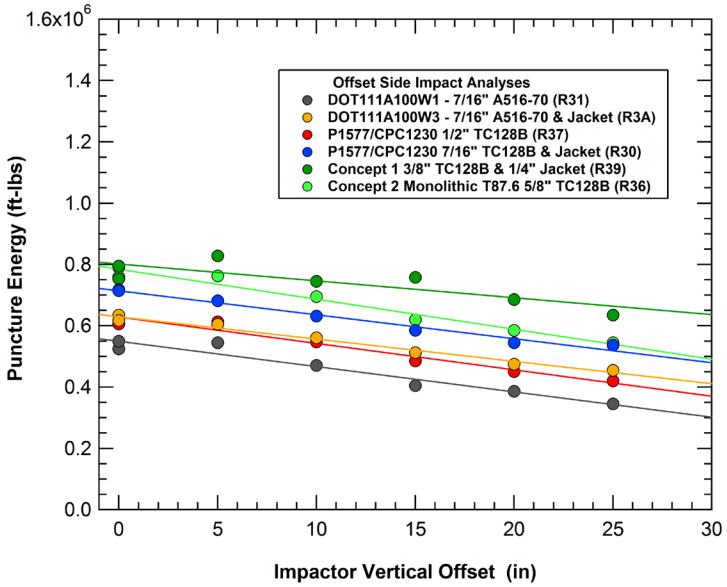

Figure 228. Calculated puncture energies for the various vertical offset side impacts.

Again, in the offset impact analyses, the Concept 1 and 2 designs provide the greatest level of protection. An interesting result of these offset impact analyses is that the performance of the 2-layer Concept 1 design improves relative to the monolithic Concept 2 design as the impact offset increases. This suggests that the 2-layer design has potential for increased puncture resistance in real-world impact conditions that would include primarily offset and oblique impact conditions.

5.6.4 Head Impacts of General-Purpose Tank Cars

A suite of impact analyses was performed on various general purpose tank head designs. For each design, a set of four impact analyses were performed using different size impactors in offset head impacts. A summary of comparative head impact analyses is provided in Table 17.

The relative head impact puncture energies for the general-purpose tank head impacts are summarized in Figure 229. In the figure, the puncture energies for each tank head are normalized to the corresponding energies for the DOT-111A100W1 tank head. Each point represents the calculated puncture energy for the specific tank head normalized by the corresponding puncture energy for the DOT-111A100W1 tank head under identical impact conditions. The comparison shows the four impact scenarios considered resulted in an average increase in puncture energy of 23, 79, 80, and 95 percent respectively for the CPC-1230, DOT-111A100W3, CPC-1230J and DOT-117A100W tank heads.

Table 17. Summary of the analyses for general purpose tank head impacts.

Head Impact Analysis	Tank Type	Tank Head	Jacket or Head Shield	Impact Conditions	Impactor Edge Radius	Internal Pressure (psi)	Puncture Force (lbs)	Puncture Energy (ft-lbs)
R61A	DOT-117	0.5938" TC128B	0.500" A572-50	15 mph 6"x6" ram	0.50 inch	0 psi	6.765E+05	9.160E+05
R61B	DOT-117	0.5938" TC128B	0.500" A572-50	25 mph 12"x12" ram	0.50 inch	0 psi	1.487E+06	2.095E+06
R61C	DOT-117	0.5938" TC128B	0.500" A572-50	20 mph 9"x9" ram	0.50 inch	0 psi	1.031E+06	1.690E+06
R61D	DOT-117	0.5938" TC128B	0.500" A572-50	10 mph 3"x3" ram	0.50 inch	0 psi	4.132E+05	2.338E+05
R62A	111A100W3	0.4688" A516-70	0.500" A572-50	15 mph 6"x6" ram	0.50 inch	0 psi	6.070E+05	8.282E+05
R62B	111A100W3	0.4688" A516-70	0.500" A572-50	25 mph 12"x12" ram	0.50 inch	0 psi	1.329E+06	1.744E+06
R62C	111A100W3	0.4688" A516-70	0.500" A572-50	20 mph 9"x9" ram	0.50 inch	0 psi	7.232E+05	1.285E+06
R62D	111A100W3	0.4688" A516-70	0.500" A572-50	10 mph 3"x3" ram	0.50 inch	0 psi	3.337E+05	3.333E+05
R63A	111A100W1	0.4688" A516-70	N/A	15 mph 6"x6" ram	0.50 inch	0 psi	3.865E+05	4.270E+05
R63B	111A100W1	0.4688" A516-70	N/A	25 mph 12"x12" ram	0.50 inch	0 psi	7.327E+05	9.490E+05
R63C	111A100W1	0.4688" A516-70	N/A	20 mph 9"x9" ram	0.50 inch	0 psi	5.312E+05	7.291E+05
R63D	111A100W1	0.4688" A516-70	N/A	10 mph 3"x3" ram	0.50 inch	0 psi	2.224E+05	2.067E+05
R64A	CPC1230J	0.5625" TC128B	0.500" A572-50	15 mph 6"x6" ram	0.50 inch	0 psi	6.379E+05	9.100E+05
R64B	CPC1230J	0.5625" TC128B	0.500" A572-50	25 mph 12"x12" ram	0.50 inch	0 psi	1.499E+06	1.910E+06
R64C	CPC1230J	0.5625" TC128B	0.500" A572-50	20 mph 9"x9" ram	0.50 inch	0 psi	9.846E+05	1.385E+06
R64D	CPC1230J	0.5625" TC128B	0.500" A572-50	10 mph 3"x3" ram	0.50 inch	0 psi	3.985E+05	2.391E+05
R65A	CPC1230	0.5625" TC128B	N/A	15 mph 6"x6" ram	0.50 inch	0 psi	5.230E+05	6.100E+05
R65B	CPC1230	0.5625" TC128B	N/A	25 mph 12"x12" ram	0.50 inch	0 psi	9.658E+05	1.297E+06
R65C	CPC1230	0.5625" TC128B	N/A	20 mph 9"x9" ram	0.50 inch	0 psi	7.010E+05	8.360E+05
R65D	CPC1230	0.5625" TC128B	N/A	10 mph 3"x3" ram	0.50 inch	0 psi	2.871E+05	2.030E+05

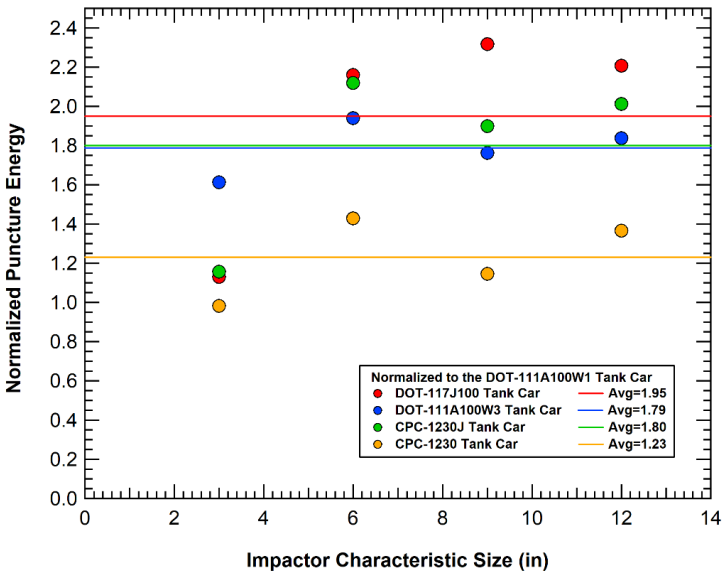

Figure 229. Normalized impact puncture energy summary for the general-purpose tank heads.

5.6.5 Summary of Analyses for General Purpose Tank Cars

The analyses discussed in the previous sections of this report show that the various proposed designs for general purpose tank cars (improved material selection, increased thickness, and/or added jackets) all resulted in increases in the puncture energies compared to the baseline 111A100W1 tank car. To quantify the magnitude of the improvements, the puncture energy obtained from each calculation was normalized by the puncture energy of the 111A100W1 tank car in the identical impact scenario. These normalized puncture energies, along with linear fits through the data, are summarized in Figure 230.

The normalized puncture energies show that the baseline P1577/CPC 1230 tank car (without jacket) results in an approximately 20 percent increase in puncture energy across the full range of impactor sizes. Similarly, the monolithic 5/8-inch-thick TC128B tank car (concept 2) has greater than a 50 percent increase in the puncture energy. Adding a jacket to the baseline tank car (111A100W3) results in on average approximately a 20 percent increase in puncture energy. However, the improvements were less for small impactors and more for large impactors. This was similar to the addition of a jacket on the P1577/CPC 1230 tank car where the average performance was roughly 40 percent above the 111A100W1 tank car but overall, the improvements were greatest for the largest impactors.

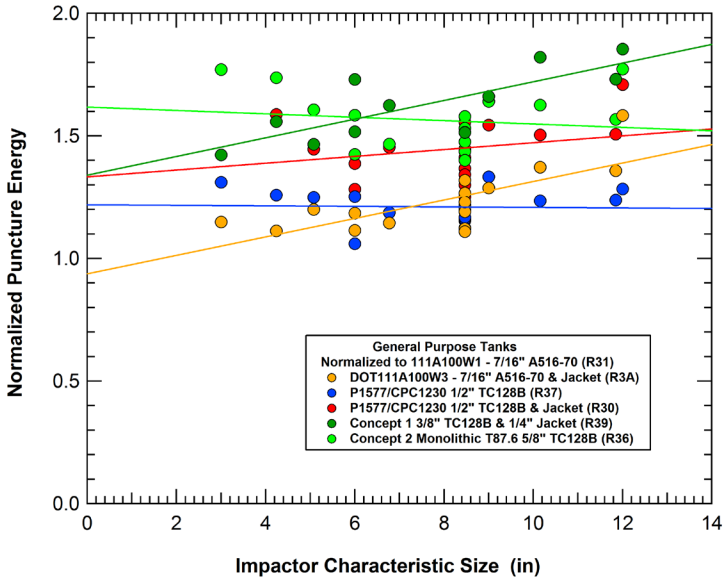

Figure 230. Normalized side impact puncture energies for the various general purpose tank car designs (1% outage).

The normalized puncture energies for the analyses of tank cars with the 3 percent outage are summarized in Figure 231. The normalization for these analyses is still to the reference 111A100W1 tank car at 1 percent outage. The trends are again similar where the multi-layer systems are seen to perform better for large impactor than small impactors. The biggest difference is that the average puncture energy improvements range from approximately 90 percent to more than 130 percent compared to the 111A100W1 tank car at 1 percent outage.

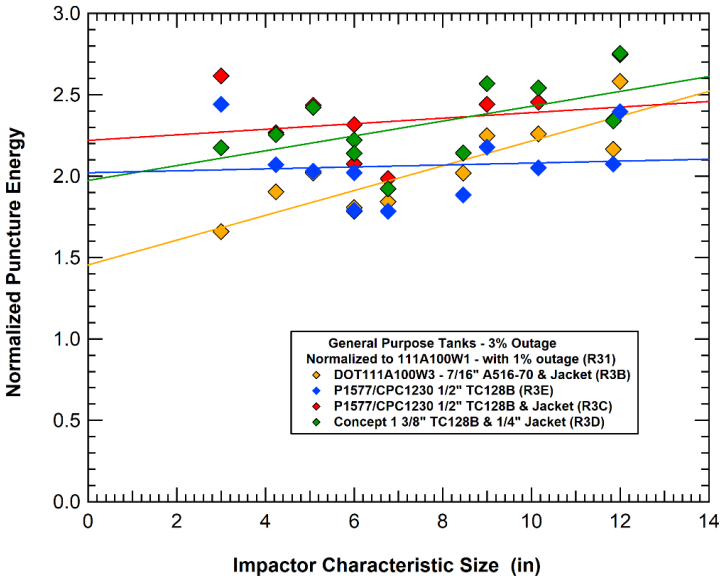

Figure 231. Normalized side impact puncture energies for the various general purpose tank car designs (3% outage).

5.7 DOT Class 113 Cryogenic LNG tank cars

Subsequent the completion of this initial research project in 2013 (Kirkpatrick, 2013), an FRA ruling was made that allows transport of LNG in DOT-113C120W9 tank cars. This will likely result in increasing shipments of LNG by rail in the future. FRA has an ongoing full-scale test program to address the puncture resistance of these tank cars. However, these tests are being performed under ideal impact conditions and to date have applied a relatively large 12-inch by 12-inch impactor. Since these are novel tank designs, there is a risk that under different impact conditions (e.g., smaller impactors) the puncture resistance displayed with these tests of the DOT-113C120W9 tank cars relative to other designs may not be proportional. It was important to identify if this type of vulnerability exists in the design before a significant fleet is put into service. As a result, this study was expanded in 2023 to assess the puncture resistance of the DOT-113C120W9 under a variety of impactors and impact conditions and compare the relative puncture resistance to other designs.

The DOT-113 cryogenic tank car has many characteristics that are significantly different from other tank car designs. It consists of a significantly thicker outer tank (i.e., jacket) that is ring stiffened. The space between the inner and outer tanks is larger than for most traditional tank cars and is insulated by a vacuum state between the inner and outer tanks. Finally, the inner stainless steel tank material at cryogenic temperatures has unique mechanical properties compared to traditional tank car steels, as shown in Section 2.5. As a result, the initial effort in the DOT-113 puncture resistance study was to validate the model against the full-scale puncture test on a DOT-113 tank car with a cryogenic lading.

5.7.1 Summary of Test Results

A full-scale impact test on the DOT-113 tank car was performed by FRA at the Transportation Technology Center (TTC) in Pueblo, CO, on May 14, 2022. The DOT-113 is a double-walled cryogenic tank car with a capacity of approximately 34,500 gallons. During the test, an approximately 297,000-pound ram car equipped with a 12-inch by 12-inch impactor struck the outer shell of the tank car at its mid-height and longitudinally offset 10.8 feet toward the A-end (FRA, 2022). The measured impact speed was 22.1 mph which corresponds to an impact energy of 4.8 million foot-pounds. The tank car and ram position prior to impact is shown in Figure 232.

The measured force-displacement behavior for the ram car during the test is shown in Figure 233. The maximum force of approximately 1.7 million pounds occurs immediately prior to the tank puncture corresponding to an impactor indentation of approximately 60 inches. The tank car absorbed 4.3 million foot-pounds of energy prior to puncture. After puncturing the inner tank, the impactor continued moving at a speed of approximately 7 mph before coming to rest with the head of the impactor lodged inside the inner tank.

Figure 232. Pre-impact configuration of the DOT-113 tank car and ram for Test 13 (FRA, 2022).

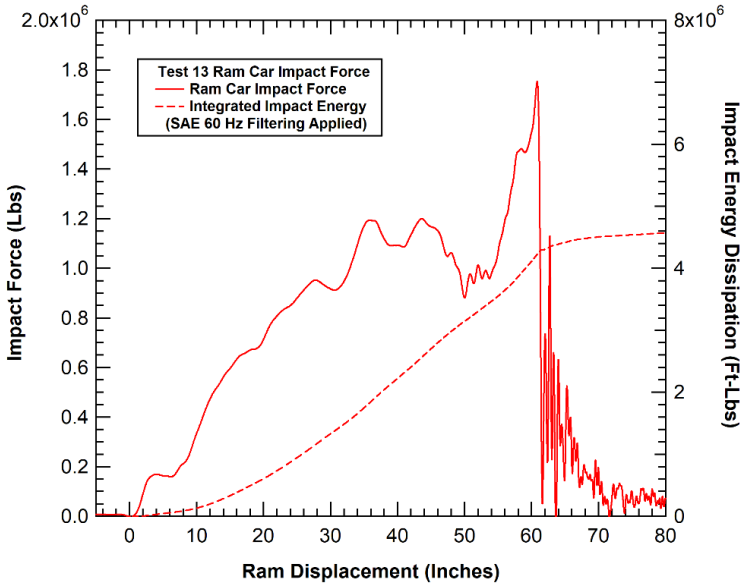

Figure 233. Measured ram car force-displacement and energy dissipation for Test 13.

The test plan was developed with an objective of filling the tank car to approximately 97 percent by volume with liquid nitrogen (LN2). The outage volume contained pressurized gaseous nitrogen (GN2) at a pressure of 21 psig immediately prior to the test (FRA, 2022). The measured pressure history inside the tank during the test is shown in Figure 234. During the initial phase of the impact, the tank is compressed, and the internal pressure begins to rise. After approximately 100 ms the pressure reaches a point at which it stabilizes at approximately 65 psig. It is believed that this pressure level is maintained as subsequent compression results in GN2 condensing to

LN2 and the outage volume is reduced. After approximately 180 ms the pressure begins to rise again as the tank nears a shell-full condition. A peak pressure on the order of 150 psi is achieved immediately prior to tank puncture.

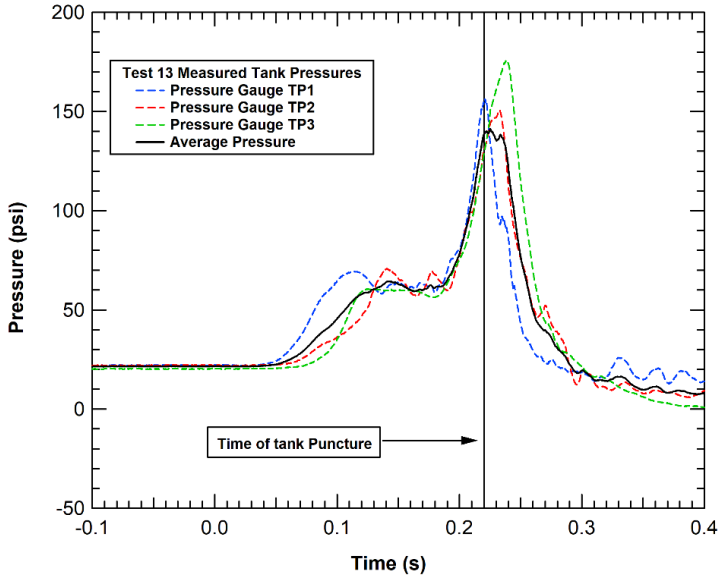

Figure 234. Measured internal tank pressures for Test 13.

5.7.2 Model Validation

The model for the test 13 impact analyses is shown in Figure 235. The model includes the ram car, DOT-113 test car resting on skids, and the impact wall. The model includes 3.9 million nodes with 1.24 million 4-node shell elements and 2.36 million 8-node solid hexahedron (i.e., brick) elements. A significant portion of the model is a highly refined mesh in the impact zone, shown in Figure 236, with solid elements with a characteristic size in the rupture zone of approximately 1 mm.

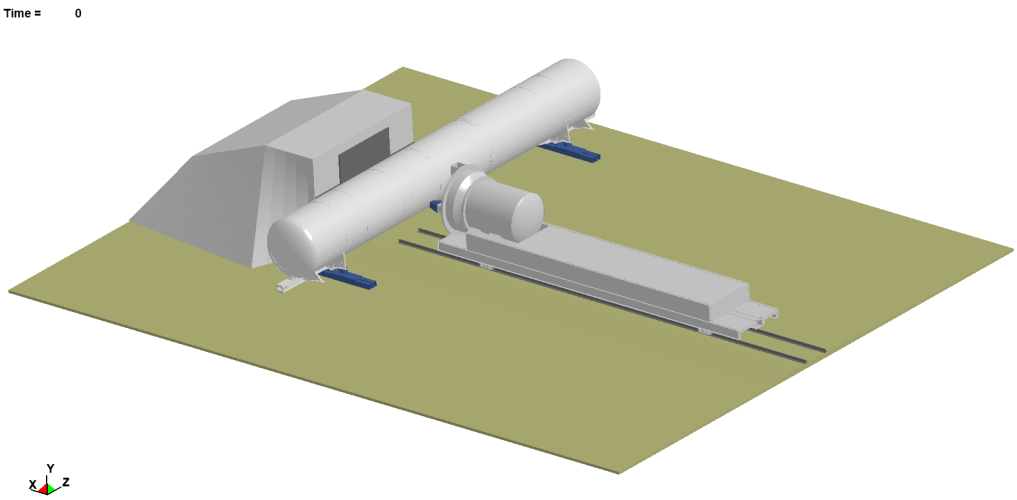

Figure 235. Model of the DOT-113 tank and Test 13 impact configuration.

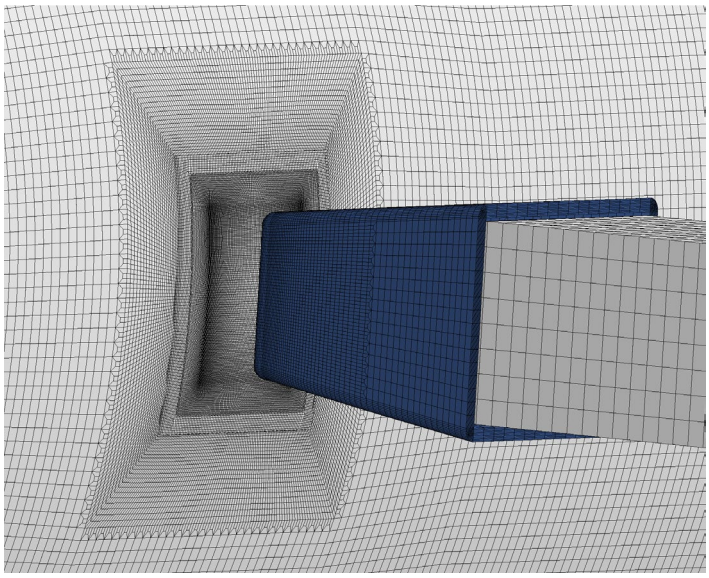

Figure 236. Mesh of the impact zone in the DOT-113 tank car model.

In the analyses, a control volume was established for the tank and the change in volume was used to calculate a corresponding change in pressure (using an airbag algorithm in LS-DYNA). Post-test analyses of the tank indicated that the outage volume was likely closer to 4 percent than the target 3 percent level. The absolute pressure-volume relationship used for the analysis of the test is shown in Figure 237. The figure compares the behavior for an ideal gas constant temperature compression with the modified behavior used that includes a constant pressure region during condensation of the GN2 to LN2. In the modified curve, the pressure reaches a plateau at approximately 80 psi starting at an outage volume of 1.85 percent (relative volume of 0.9785) and remains at that pressure until the outage is reduced to approximately 0.5 percent (relative volume of 0.965) at which point the pressure again continues to increase approaching the shell full condition (relative volume of 0.96).

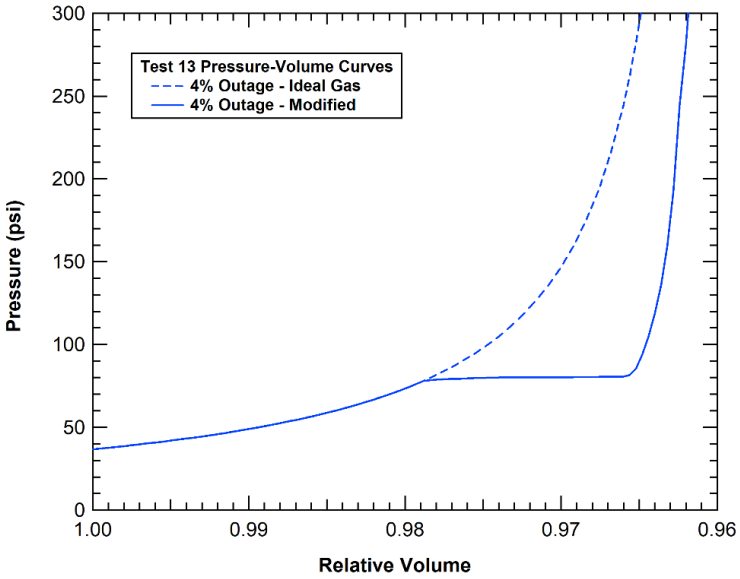

Figure 237. Tank pressure volume relationships used for analysis of Test 13.

The calculated tank impact response just prior to tank rupture (200 ms after impact) is shown in Figure 238. At this time, the ram has indented the tank by 57 inches and the impact force is above 1.5 million lbs. The corresponding calculated force-displacement and energy absorption plots are compared to the measured Test 13 response in Figure 239. The comparison shows a sufficiently good correlation between the force-deflection response and the force and displacement levels at the tank puncture to validate the modeling methodology for assessing the puncture resistance of the DOT-113 tank car.

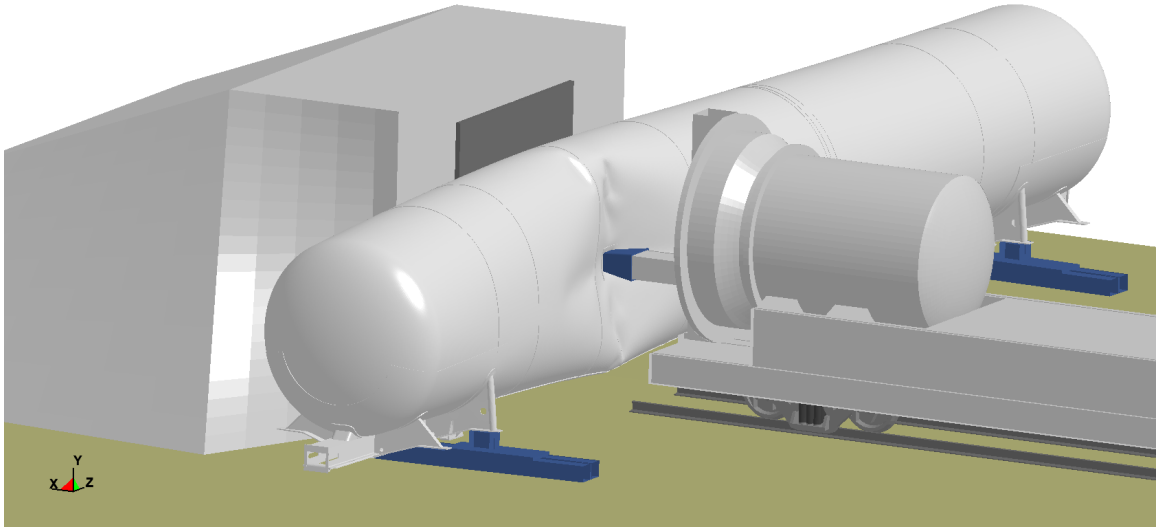

Figure 238. Calculated tank impact response just prior to tank rupture.

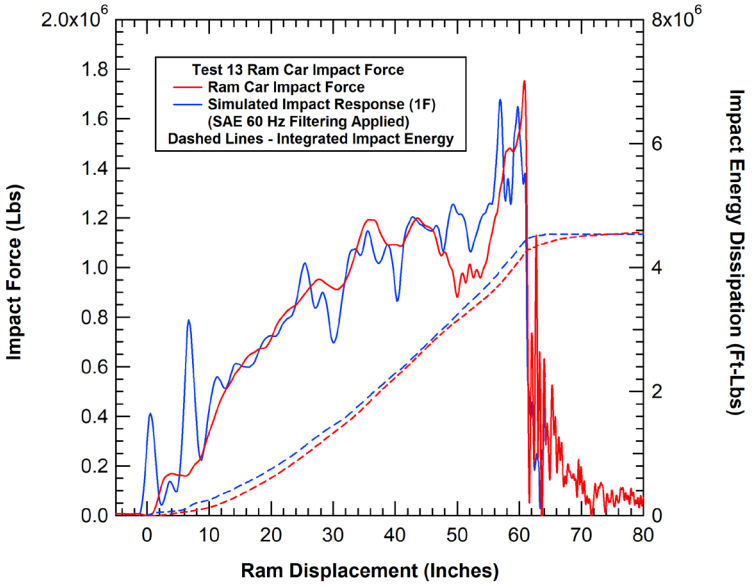

Figure 239. Comparison of the calculated and measured force-displacement behavior in Test 13.

The additional comparison of the measured and calculated tank pressure histories for Test 13 are shown in Figure 240. The agreement in the characteristics of the pressure histories indicates that

the modified pressure curve with a phase change occurring at approximately 80 psi is the likely behavior for the LN2 lading in this test.

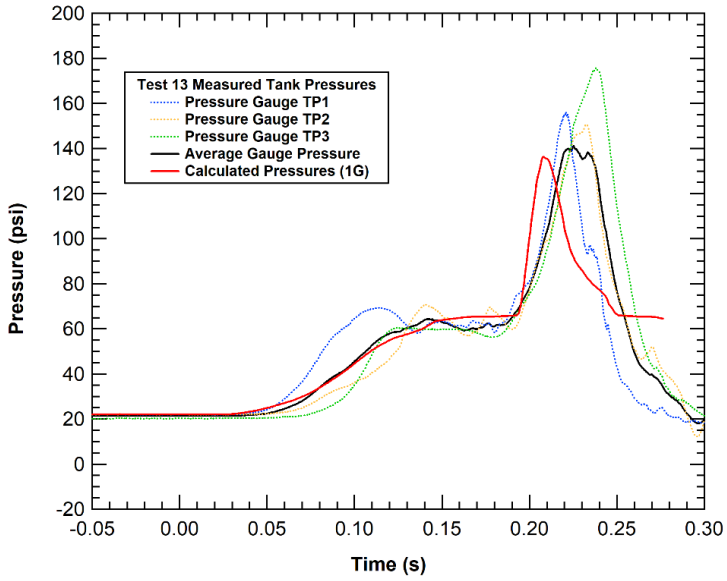

Figure 240. Calculated tank impact response just prior to tank rupture.

5.7.3 DOT Class 113 LNG Tank Model

The full model of the DOT-113 tank car used for the model validation efforts described above was not considered to be appropriate for the subsequent assessment of the relative puncture resistance. First, the tank car design had proprietary design features that do not allow for any symmetry planes to be incorporated. In addition, it includes features such as the detailed sill and bolster models which do not have a significant effect on the puncture response. As a result, a simplified generic DOT113 tank model was developed for the following assessments of the relative puncture resistance.

The generic DOT113 Tank model developed for the tank puncture resistance assessment is shown in Figure 241. The tank model is again a double tank construction with a stiffened outer tank and cryogenic inner tank with vacuum insulation between tanks. The tank diameters and thicknesses were the same as those of the Test 13 DOT-113 tank car. However, the geometry is simplified such that the model includes both vertical and longitudinal symmetry planes. In addition, the material model for the inner tank was swapped to that of the A240 304 stainless steel at LNG cryogenic temperature (-260F, 110K).

The other significant modification required for analysis of a DOT-113 tank car for LNG service is the definition of appropriate outage volume and the pressure-volume relationship during impact. Multiple sources were used to develop a nominal pressure-volume relationship for a DOT-113 tank car transporting LNG. From the PHMSA LNG by rail final rule (PHMSA, 2020), the loading pressure when offered for transportation must be a maximum of 15 psi. The corresponding maximum start to discharge pressure is 75 psi (safety relief valve setting). The corresponding outages for these pressures are approximately 9 percent at loading and 2 percent at the start to discharge condition.

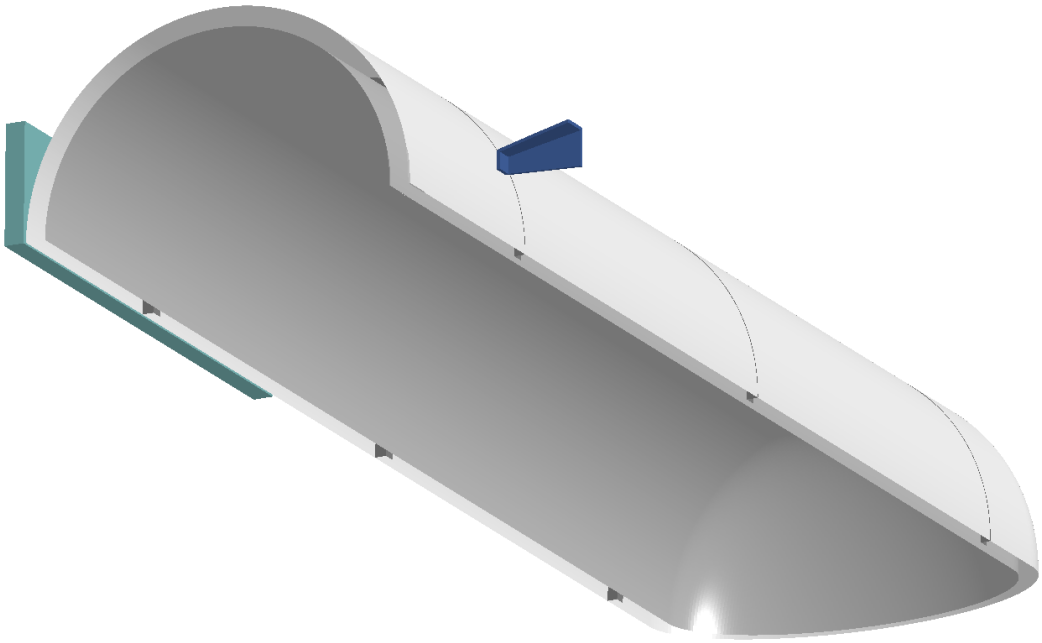

(a) Quarter-symmetry model of tank, ram, and reaction wall

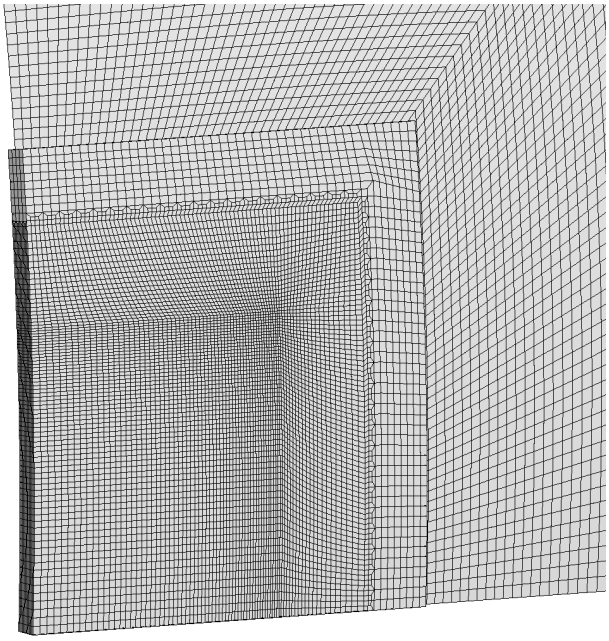

(b) Mesh resolution of the outer tank impact patch

Figure 241. Model of a generic DOT-113 tank for analysis of puncture resistance.

Expected pressure conditions during shipment were provided in an example by the National Academies (National Academies of Sciences, Engineering, and Medicine, 2022): “These materials must be shipped in tank cars designed to minimize heat input so as to limit pressure rise to 3 pounds per square inch gauge (psig) (1.2 bar) per day. For example, ethylene is

authorized to be offered for transportation at 20 psig and a corresponding temperature of −125°F (−87°C). Because the lading will continue to warm until delivery and the daily pressure rise of a DOT-113 tank car is 0.5 to 0.75 psig (1.05 to 1.07 bar), the temperature and pressure at the end of a 10-day trip is expected to be about −117°F (–83°C) and 27.5 psig (2.9 bar)." If we apply upper bound LNG transport conditions of 15 psi loading pressure and a maximum increase of 3 psi per day that would still limit the pressure at arrival to the destination to 45 psi for a 10-day transit.

Since the risk of a derailment/impact is uniform over the transit, the average condition at impact would be the midpoint between the loading condition and the arrival condition. However, a lower outage volume and higher initial pressure would result in a more conservative estimate of the puncture resistance. As a result, we selected a 30-psig initial pressure and a corresponding outage of approximately 7.5 percent for the nominal condition in the puncture resistance assessment.

The final consideration for the LNG pressure volume behaviors in impact is the shape of the pressure-volume curve. The two possibilities are an ideal gas pressure-volume curve, like the behaviors used for other hazmat commodities [e.g., (Kirkpatrick, 2009a), (2013)] or a curve that allows for a gas-to-liquid phase change as seen in the Test 13 LN2 response (Figure 237). A comparison of these two possible behaviors is shown in Figure 242.

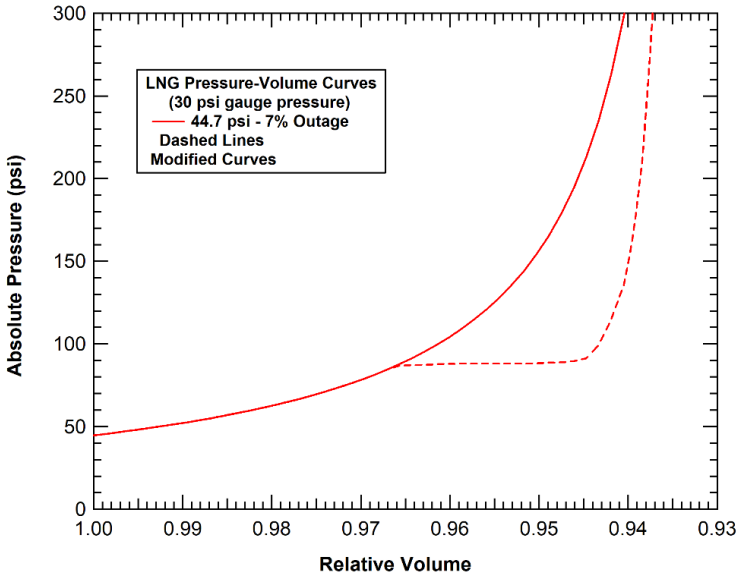

Figure 242. Tank pressure volume relationships used for puncture analysis of the DOT-113 LNG tank car.

To support the selection of a pressure-volume relationship to use on the DOT-113 puncture resistance assessment, a set of preliminary analyses was performed using both behaviors. The puncture behaviors for both a 30-mph impact with the 12x12-inch impactor and 20 mph impact with the 6x6-inch impactor are shown in Figure 243 and Figure 244, respectively. During the initial impact response, the pressure curves are identical, so the resulting impact response is identical. For the 12x12-inch impactor the response diverges after approximately 45 inches of ram displacement. The pressure behavior with phase change allows for somewhat reduced forces during the subsequent impact but a corresponding increase of displacement to puncture of 2.6

inches. As a result, the analysis with the phase change dissipates 0.5 percent more of the impact energy at puncture.

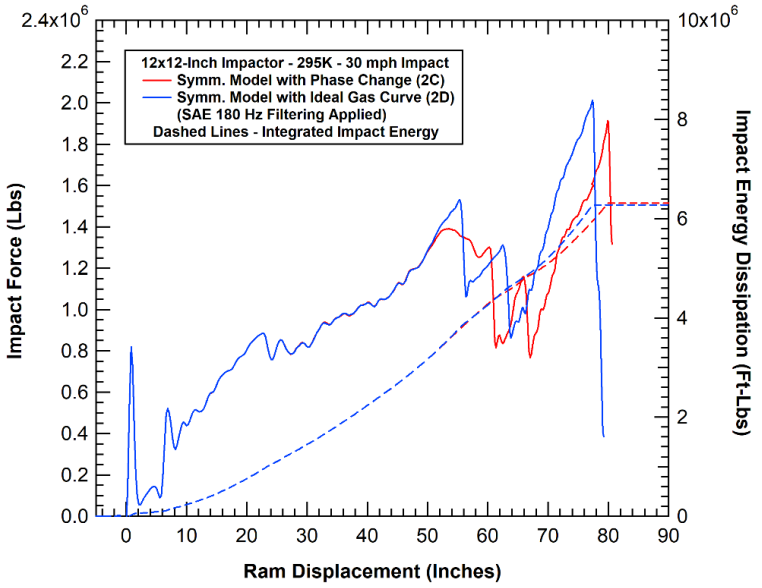

Figure 243. Calculated and measured force-displacement behaviors for the Test 13 impact condition.

For the 6x6-inch impactor the response is identical until immediately preceding the puncture response. This is because the tank only reaches a compression of the volume to reach the gas-to-liquid transition pressure at the point near the puncture condition. As a result, the analysis with the phase change dissipates 1.2 percent more of the impact energy at puncture.

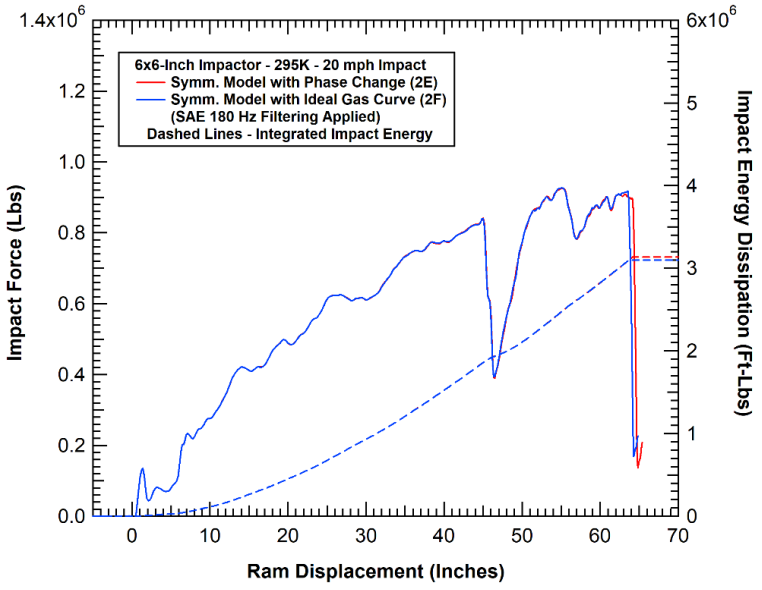

Figure 244. Calculated and measured force-displacement behaviors for the Test 13 impact condition.

Preliminary Analysis of Validation Test Conditions

Prior to performing the full assessment of the baseline DOT-113 tank car design under a range of impact conditions, a pair of analyses were performed with the simplified generic DOT-113 tank impact model using the approximate Test 13 impact conditions. In these analyses, the pressure volume relationships for the LN2 in Test 13, shown previously in Figure 237, were applied. To evaluate the effects of the gas-to-liquid phase change, analyses were performed both with the ideal gas pressure behavior as well as the modified behavior including the phase change effect. In addition, these analyses maintained the constitutive behavior of the inner tank for the A240 304 stainless steel at the colder LN2 cryogenic temperature (-321F, 77K), described in Section 2.5.2.

The calculated response for the Test 13 impact condition with the generic DOT-113 model is shown in Figure 245. In the figure, the model has been reflected about the vertical plane to present a cross-sectional half model view. The deformed shape, shown in Figure 245(b) is at the point of inner tank puncture and the ram is seen to have fully penetrated the outer tank. In this analysis the ram displacement (i.e., tank indentation) is slightly more than 60 inches when puncture occurs.

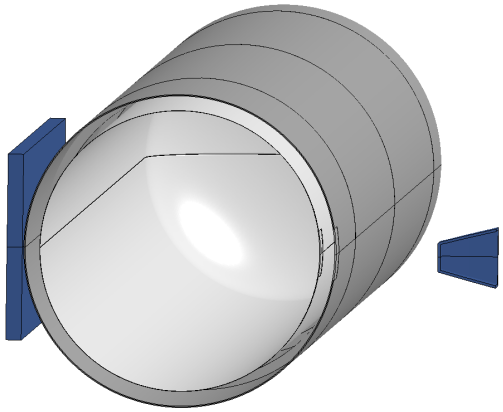

(a) Cross section of the tank, ram, and reaction wall model

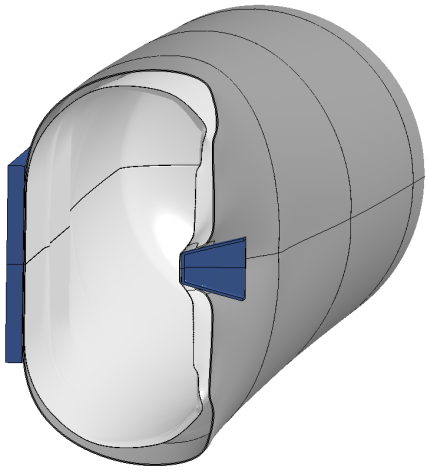

(b) Tank deformation at puncture

Figure 245. Analysis of the generic DOT-113 tank in the Test 13 impact conditions.

The comparison of the calculated force-deflection behaviors with the generic DOT-113 tank geometry are compared to the measured Test 13 behavior in Figure 246. As expected, the analyses provide an identical response for the initial 35 inches of ram displacement (approx. 0.1 s) where the pressure curves are identical. Some differences are observed in the subsequent impact response resulting from internal pressure differences. Again, the phase change allows for lower forces after the initiation of phase change stabilizes internal pressure and a slightly larger displacements prior to reaching the puncture condition. As a result, puncture energy is increased by 1.6 percent by including the phase change response.

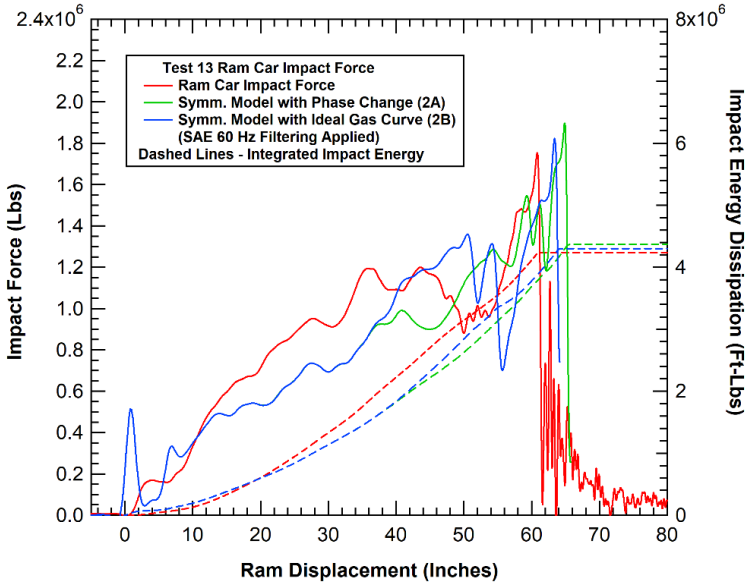

Figure 246. Calculated and measured force-displacement behaviors for the Test 13 impact condition.

5.7.4 Baseline DOT Class 113 LNG Tank Analyses

The generic DOT-113 tank car model was applied to analyze puncture conditions for the standard suite of side impact conditions. The baseline analyses normal impacts include the 3x3, 6x6, 9x9, 12x12, and 3x12 rectangular impactors as well as the 5.73-, 7.64-, 9.55-, 11.46-, and 13.37-inch diameter round impactors. The calculated impact force-deflection and puncture energy dissipation curves for these impacts on the DOT-113C120W9 tank car are summarized in Table 18 and shown in Figure 247.

As a baseline comparison of the puncture resistance for the DOT-113C120W9 LNG tank car, the puncture energies for each impact scenario were normalized against the corresponding puncture energies for the DOT-105J500W chlorine tank car. These normalized tank car puncture energies are then plotted against those of the other TIH pressure tank car designs (previously summarized in Section 5.5) in Figure 248. The average puncture energy for the DOT-113C120W9 tank car is 126 percent higher than the DOT-105J500W chlorine tank car. In addition, the average puncture energy for the DOT-113C120W9 tank car is higher than those of all the TIH pressure tank car designs that have been analyzed.

Table 18. Summary of the baseline side impact analyses on the DOT-113C120W9 tank car

Calculation	Tank Type	Tank Shell	Shell Jacket	Impact Conditions	Internal Pressure (psi)	Puncture Force (lbs)	Puncture Energy (ft-lbs)
RL3A	DOT-113	0.29 in SS304L	0.5625 in TC128B	20 mph 6”x6” ram	30 psi	9.172E+05	3.098E+06
RL3B	DOT-113	0.29 in SS304L	0.5625 in TC128B	30 mph 12”x12” ram	30 psi	2.020E+06	6.278E+06
RL3C	DOT-113	0.29 in SS304L	0.5625 in TC128B	25 mph 9”x9” ram	30 psi	1.461E+06	4.651E+06
RL3D	DOT-113	0.29 in SS304L	0.5625 in TC128B	15 mph 3”x3” ram	30 psi	4.857E+05	8.629E+05
RL3E	DOT-113	0.29 in SS304L	0.5625 in TC128B	15 mph 3”x6” ram	30 psi	6.439E+05	1.919E+06
RL3F	DOT-113	0.29 in SS304L	0.5625 in TC128B	25 mph 3”x12” ram	30 psi	1.184E+06	3.449E+06
RL3G	DOT-113	0.29 in SS304L	0.5625 in TC128B	20 mph 5.73 in. dia.	30 psi	8.416E+05	1.957E+06
RL3H	DOT-113	0.29 in SS304L	0.5625 in TC128B	20 mph 7.64 in. dia.	30 psi	1.046E+06	3.214E+06
RL3I	DOT-113	0.29 in SS304L	0.5625 in TC128B	25 mph 9.55 in. dia.	30 psi	1.296E+06	4.193E+06
RL3J	DOT-113	0.29 in SS304L	0.5625 in TC128B	30 mph 11.46 in. dia.	30 psi	1.590E+06	5.492E+06
RL3K	DOT-113	0.29 in SS304L	0.5625 in TC128B	35 mph 13.37 in. dia.	30 psi	1.618E+06	6.190E+06

To evaluate the factors that lead to the high puncture resistance of the DOT-113C120W9 tank car compared to other pressure tank car designs, the calculated force-deflection behaviors are compared to those of the DOT-105J500 EO and DOT-105J600 CL tank cars for the 6- and 12-inch square impactors in Figure 249 and Figure 250, respectively. The comparison shows that the puncture forces of the pressure tank car designs are equivalent or higher to that of the DOT-113 tank car. However, the DOT-113 tank car has a significantly more compliant impact response with higher displacement, and thus higher impact energy dissipation, prior to puncture.

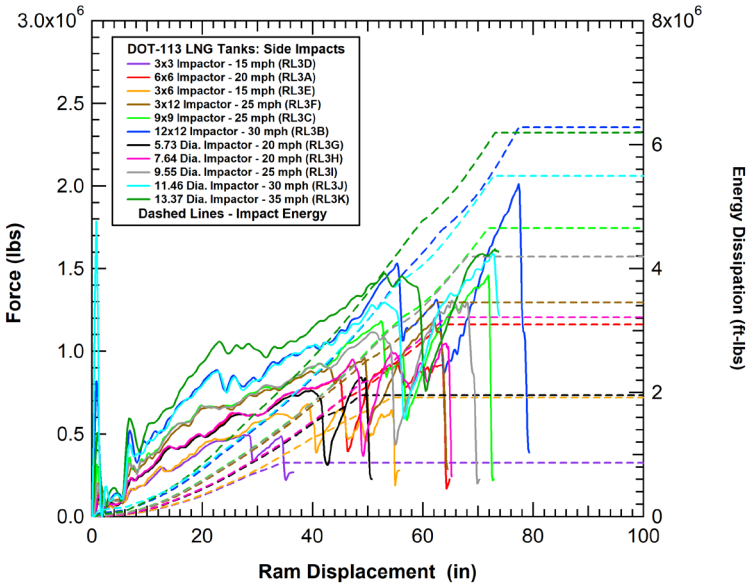

Figure 247. Force-deflection response and energy absorption for the DOT-113 tank in normal side impacts.

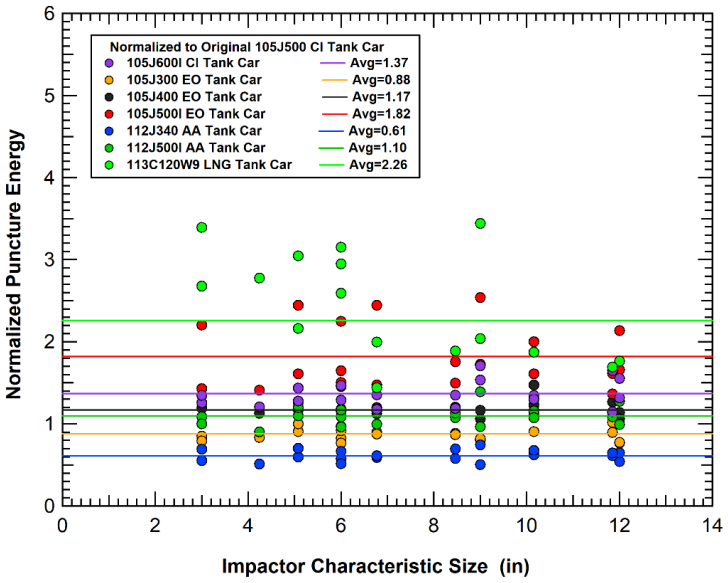

Figure 248. Comparison of the DOT-113 LNG tank car to various TIH commodity pressure tank car designs.

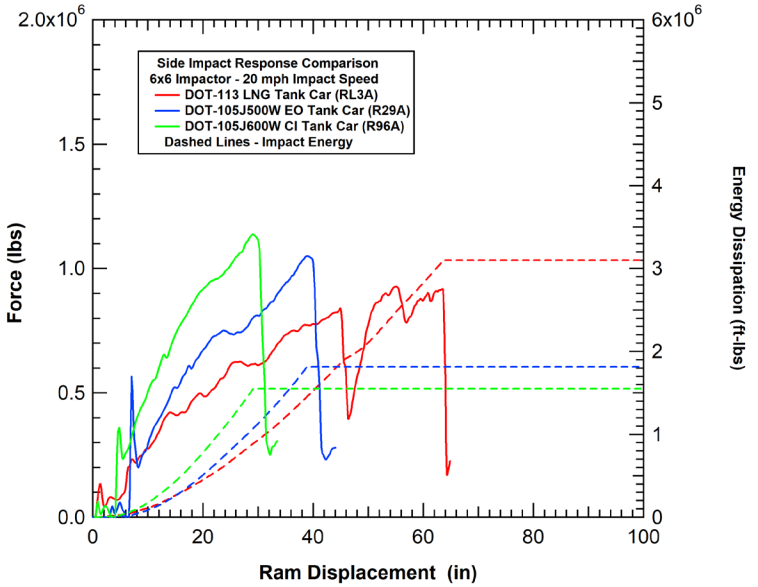

Figure 249. Comparison of the DOT-113 tank with other pressure tanks (6x6 impactor).

Another relevant comparison for the DOT-113C120W9 LNG tank car is to compare to the general-purpose tank cars that have traditionally been used to carry other flammable commodities (e.g., crude oil and ethanol). In this comparison, the DOT-113C120W9 tank car puncture energies for each impact scenario were normalized against the corresponding puncture energies for the DOT-111A100W1 tank car. These normalized tank car puncture energies are then plotted against those of the other general purpose tank car designs (previously summarized in Section 5.6.5) in Figure 251. The average puncture energy for the DOT-113C120W9 tank car is 8.46 times higher than that of the DOT-111A100W1 tank car. In addition, the average puncture energy for the DOT-113C120W9 tank car is much higher than those of all the general-purpose tank car designs that have been analyzed.

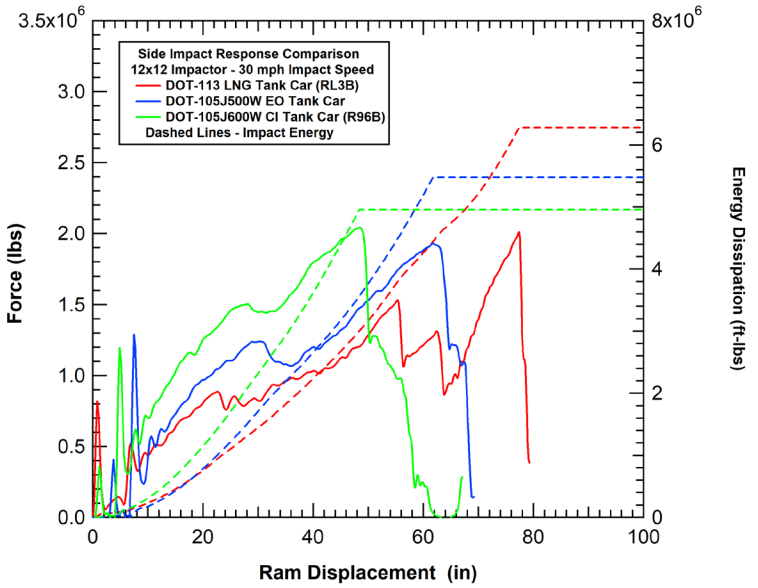

Figure 250. Comparison of the DOT-113 tank with other pressure tanks (12x12 impactor).

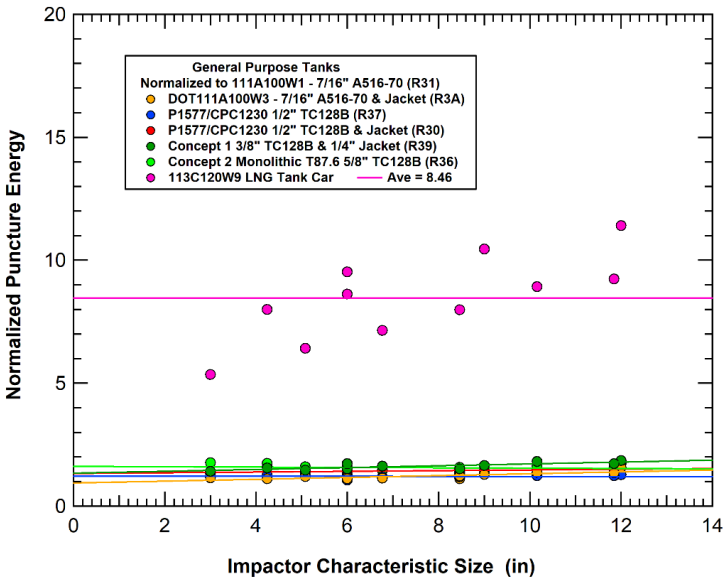

Figure 251. Comparison of the DOT-113 tank puncture resistance to non-pressure general purpose tank designs.

5.7.5 Modified DOT Class 113 LNG Tank Analyses

Although the puncture resistance of the baseline DOT-113 LNG tank design was quite high, additional analyses were performed to evaluate potential DOT-113 enhancements designed to increase the puncture resistance. In this section, we evaluate design variations with increased inner and outer tank thicknesses to assess as optimum design for increased puncture resistance.

Preliminary Analyses to Select Design Modification

Preliminary analyses were performed with both small (6x6-inch) and large (12x12-inch) impactor on proposed designs with additional thickness applied independently to the inner and outer shells. Based on the results of these preliminary analyses, a modified design was selected, and a full puncture assessment performed.

In these preliminary comparisons, the inner and outer tank shells were separately increased in thickness by an additional 1/8-inch. The calculated force-deflection and impact energy dissipation curves for these preliminary proposed modifications are compared to the baseline DOT-113 tank design for the 6- and 12-inch square impactors in Figure 252 and Figure 253, respectively. For both scenarios, the concept with the increased inner tank shell thickness results in the greatest increase in puncture resistance. Note that due to the smaller diameter of the inner tank, this modification would also result in a smaller increase in the tank light weight.

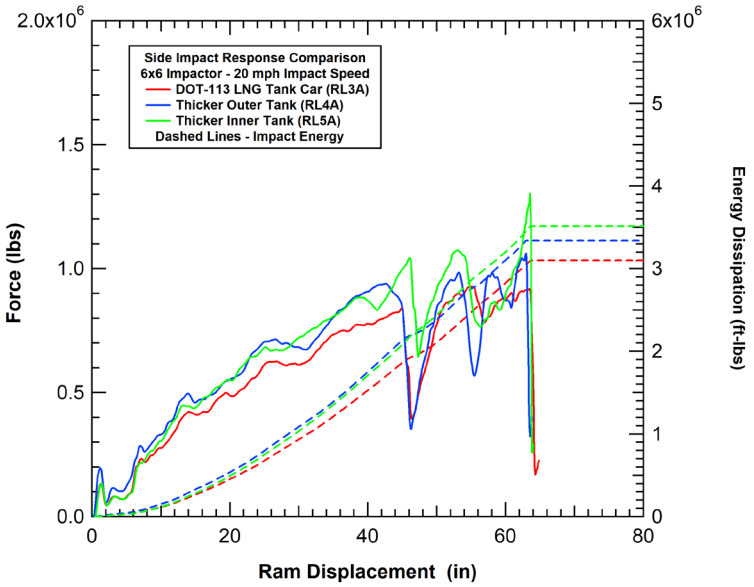

Figure 252. Preliminary mitigation analyses for the DOT-113 tank car (6x6 impactor).

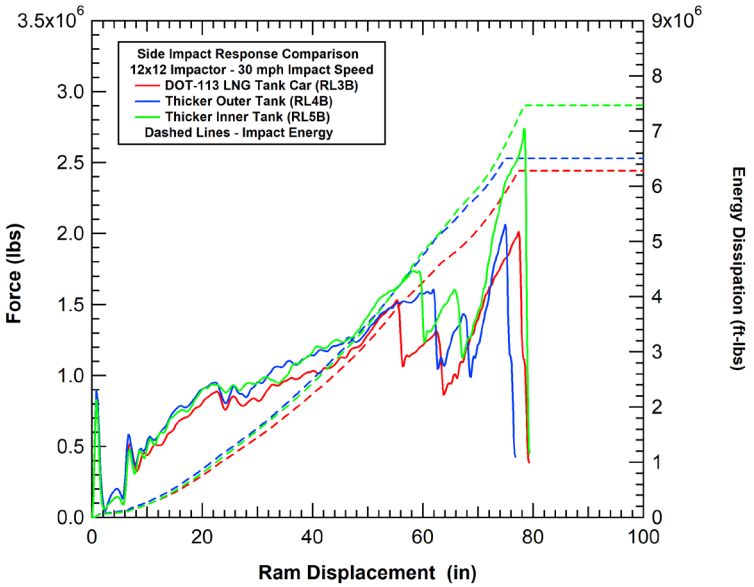

Figure 253. Preliminary mitigation analyses for the DOT-113 tank car (12x12 impactor).

Analyses of the Modified Design

Based on the preliminary analyses of the design modification, researchers selected the one with an increased thickness of the internal tank shell. However, the appropriate magnitude of the increase in the tank shell still needed to be determined. The final decision was based on a consideration of the AAR Specification M-1004 which covers LNG fuel tenders. By increasing the internal tank thickness to 0.50 inch, the tank design would be equivalent to an LNG tender tank that is M-1004 compliant. A summary of the tank shell parameters for this tank compared to the baseline DOT-113 tank is provided in Table 19.

Table 19. Summary of the LNG tank car design parameters.

Tank Designation	Tank Shell	Tank Jacket	Combined Thickness
Baseline DOT-113C120W9	0.29-inch SS304L	0.5625-inch TC128B	0.8525 inch
M-1004 Compliant DOT-113	0.50-inch SS304L	0.5625-inch TC128B	1.0625 inch

The modified M-1004 tank was similarly evaluated using the same suite of side impact conditions used for the baseline DOT-113 LNG tank car. The calculated puncture energies for the M-1004 LNG tank normalized to those of the baseline DOT-113 LNG tank are shown in Figure 254. The M-1004 compliant tank design has on average a 44 percent increase in the puncture energy. The puncture resistance improvements are also seen to be higher for the small and medium size impactors.

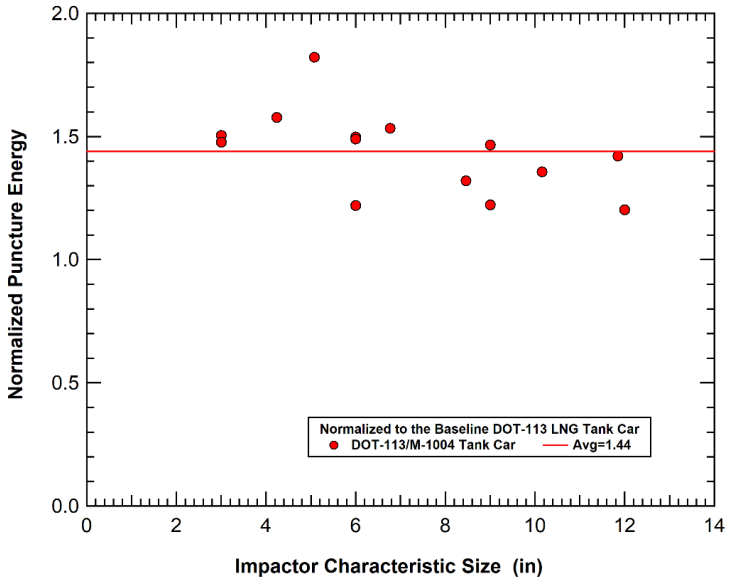

Figure 254. Comparison of the M-1004 compliant LNG tank car to the baseline DOT-113 tank car design.

A comparison of the puncture resistance for the M-1004 compliant LNG tank car to TIH pressure tank cars is obtained through normalization against the corresponding puncture energies for the DOT-105J500W chlorine tank car. These normalized tank car puncture energies are then plotted against those of the baseline DOT-113 tank car and other TIH pressure tank car designs (previously summarized in Section 5.5) in Figure 255. The average puncture energy for the DOT-113C120W9 tank car is approximately 3 times that of the DOT-105J500W chlorine tank car. In addition, the average puncture energy for the M-1004 compliant LNG tank car is significantly higher than those of all the TIH pressure tank car designs that have been analyzed.

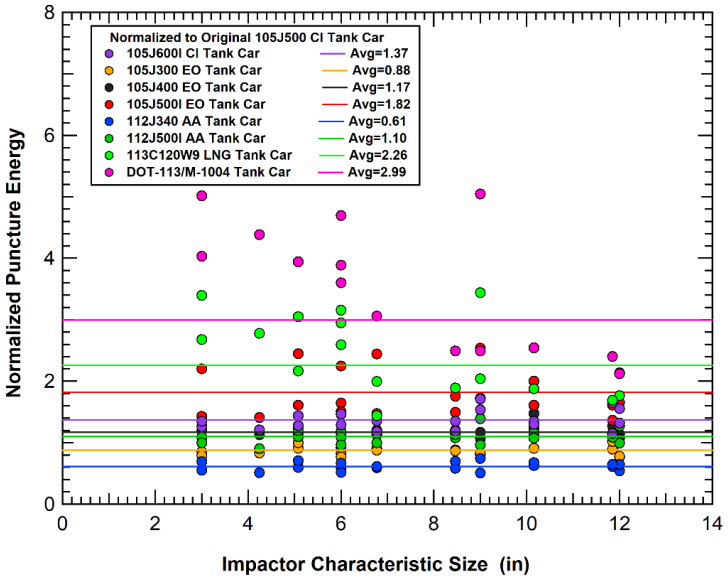

Figure 255. Comparison of the M-1004 compliant LNG tank car to various TIH commodity pressure tank car designs.

5.7.6 Head Impacts of DOT Class 113 LNG Tank Cars

A suite of impact analyses was performed on both the baseline DOT-113 and the modified M-1004 compliant LNG tank head designs. A set of four impact analyses were performed for each design using different size impactors in offset head impacts. A summary of comparative head impact analyses is provided in Table 20. The calculated force-deflection behaviors and integrated puncture energy curves for the baseline and modified DOT-113 tank heads is shown in Figure 256 and Figure 257, respectively.

Table 20. Summary of the impact analyses for baseline DOT-113 head impacts.

Head Impact Calculation	Tank Type	Tank Head	Jacket or Head Shield	Impact Conditions	Impactor Edge Radius	Internal Pressure (psi)	Puncture Force (lbs)	Puncture Energy (ft-lbs)
R71A	DOT-113 LNG	0.300” SS-304	0.5625” TC128B	15 mph 6”x6” ram	0.50 inch	30 psi	9.234E+05	2.181E+06
R71B	DOT-113 LNG	0.300” SS-304	0.5625” TC128B	25 mph 12”x12” ram	0.50 inch	30 psi	1.891E+06	3.917E+06
R71C	DOT-113 LNG	0.300” SS-304	0.5625” TC128B	20 mph 9”x9” ram	0.50 inch	30 psi	1.139E+06	2.685E+06
R71D	DOT-113 LNG	0.300” SS-304	0.5625” TC128B	10 mph 3”x3” ram	0.50 inch	30 psi	6.258E+05	9.430E+05
R72A	M-1004 LNG	0.510” SS-304	0.5625” TC128B	15 mph 6”x6” ram	0.50 inch	30 psi	1.453E+06	2.471E+06
R72B	M-1004 LNG	0.510” SS-304	0.5625” TC128B	25 mph 12”x12” ram	0.50 inch	30 psi	2.069E+06	4.865E+06
R72C	M-1004 LNG	0.510” SS-304	0.5625” TC128B	20 mph 9”x9” ram	0.50 inch	30 psi	1.526E+06	3.265E+06
R72D	M-1004 LNG	0.510” SS-304	0.5625” TC128B	10 mph 3”x3” ram	0.50 inch	30 psi	8.335E+05	9.383E+05

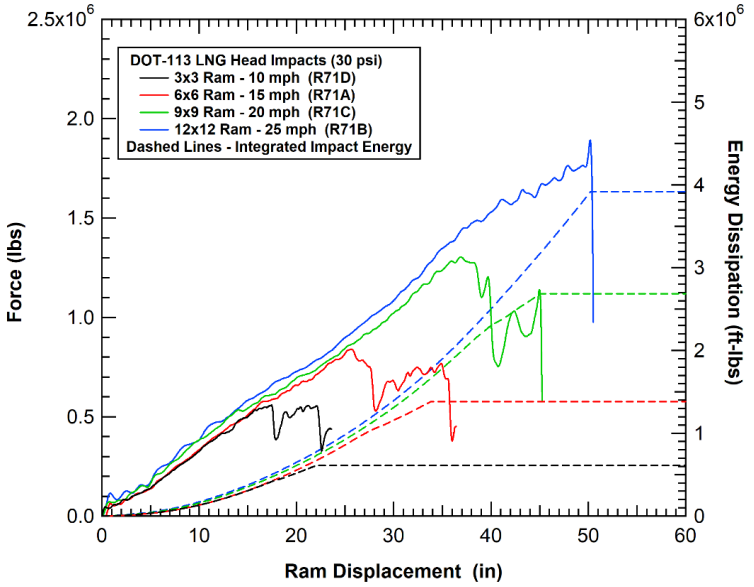

Figure 256. Calculated force-deflection behaviors for DOT-113 tank head impacts.

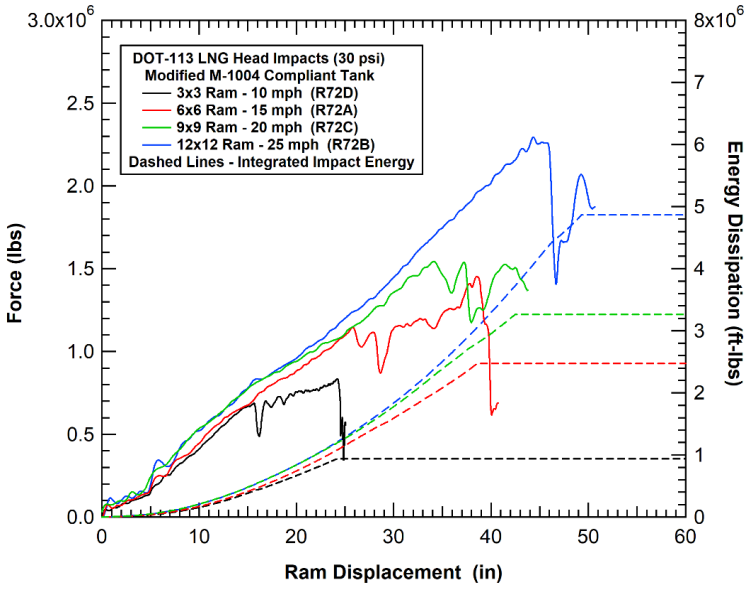

Figure 257. Calculated force-deflection behaviors for the modified DOT-113 tank head impacts.

The relative head impact puncture energies of the baseline DOT-113 normalized to the corresponding energies of the modified M-1004 compliant DOT-113 tank head is shown in Figure 258. Each point on Figure 258 represents the calculated puncture energy for the modified DOT-113 tank head normalized by the corresponding puncture energy for the baseline DOT-113 tank head for the same impactor. The individual scenarios result in a range of normalized puncture energies from a minimum of 1.22 for the 9-inch impactor to a maximum of 1.79 for the smallest 3-inch impactor (22-79 percent higher puncture energies). The four impact scenarios considered results in an average increase in puncture energy of 45 percent for the modified DOT-

113 over the baseline DOT-113 LNG tank head. This magnitude is consistent with the 44 percent average impact energy increase obtained for the side impacts.

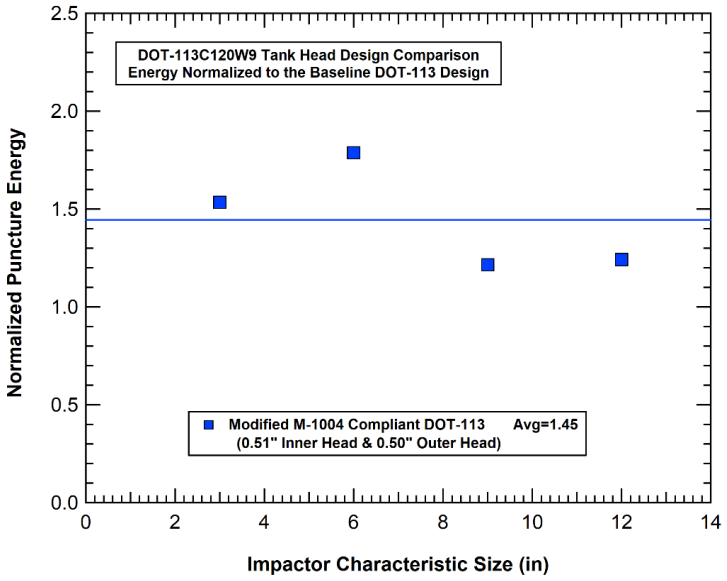

Figure 258. Normalized impact puncture energy summary for the DOT-113 tank heads.

The relative head impact puncture energies of the DOT-113 LNG tank heads normalized to the corresponding energies of the legacy 105J500 chlorine tank head are shown in Figure 259. The four impact scenarios considered result in an average increase in puncture energy of 56 percent and 127 percent for the baseline and modified DOT-113 tank heads, respectively, relative to the 500 lb chlorine tank head. The puncture resistance for both designs is also significantly greater than those of the other pressure tank car designs that were evaluated, as shown in Figure 259.

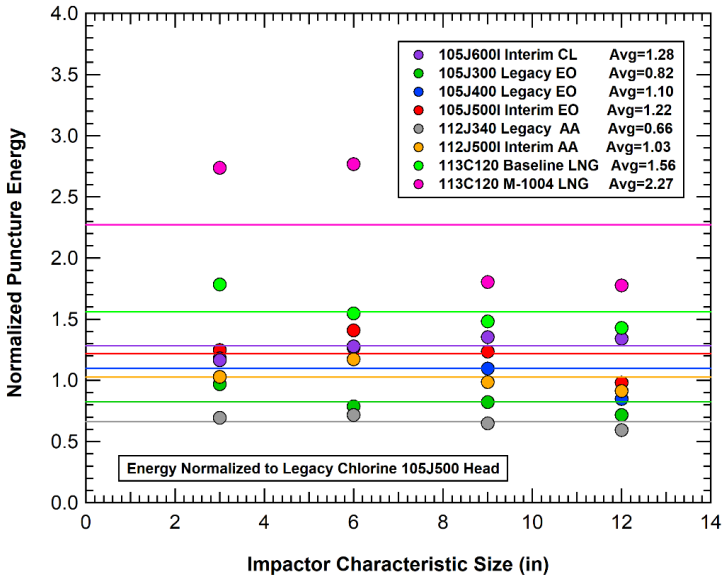

Figure 259. Normalized puncture energy summary for the baseline DOT-113 tank heads.

6. Analytical Models for Tank Car Impacts

6.1 Introduction

The detailed FE impact analyses and BW failure have been extensively applied to assess various tank impact conditions as described in Sections 3 through 5 of this report. The FE modeling approach is very useful for understanding the mechanics of tank impacts and punctures. However, at times, a simplified analysis methodology or impact algorithm is useful for the assessment of various factors on tank impact safety. As a result, other researchers have developed similar analytical approaches for tank impacts [e.g., (Jeong, Tang, & Pearlman, 2001a), (2001b), (Jeong, Tang, Yu, & Pearlman, 2006)]. However, these have typically been developed and applied to very limited sets of impact conditions. In this chapter, we describe the development of tank impact algorithms.

When assessing appropriate analysis methodologies, we examined the response characteristics of both head and side impacts. We found that the behaviors for these two impact conditions are sufficiently unique that different analysis methodologies were appropriate for the head and side impacts. These will be described in separate sections of this chapter.

6.2 Head Impact Analyses

The head impact response has several characteristics that influenced the methodology applied for the simplified impact algorithm. The tank head is a stiffer structure under impact and the impact behavior for a constrained head is relatively independent of the impact speed (minimal dynamic effects – see Section 3.4). The most common head impact scenario is with the motions and orientations of the impacted and impacting cars nearly aligned with the original direction of travel. As a result, the motions can be assumed to be primarily one dimensional. In addition, the effects of the lading model assumptions are much more significant for head impacts on unconstrained tanks. As a result, a unique analytical methodology was used to develop an algorithm for head impacts.

6.2.1 Head Impact Analysis Algorithm

The initial methodology for the head impact response algorithm was developed and validated against the analyses of head impacts with different constraint conditions described previously in Section 1.1.1. The constraint effects in head impacts are bounded by analyses of the fully constrained tank head and an unconstrained tank. The unconstrained tank model includes the entire tank which is free to translate. To bounds the lading effects on the unconstrained tank analyses were performed where, in the first analyses, none of the weight of the lading was added to the tank, and in the second analysis, all the lading mass was smeared into the tank.

The force-deflection curves for initial set of impact analyses used in the assessment of the 1D impact algorithm are shown in Figure 260. The analyses are for an 18-mph impact of the 9.55-inch-diameter round impactor. The three analyses are the constrained tank head impact and the two unconstrained tank models at the different tank weights.

A simple 1D algorithm was developed for the head impact tank motions with the different constraint conditions. The algorithm uses a known force-deflection curve of the fully constrained tank head as a characteristic property of the tank structure. The forces are then used to update the

tank and impactor motions. The relative displacement of the impactor and tank are used to calculate an updated tank depth and corresponding change in impact force.

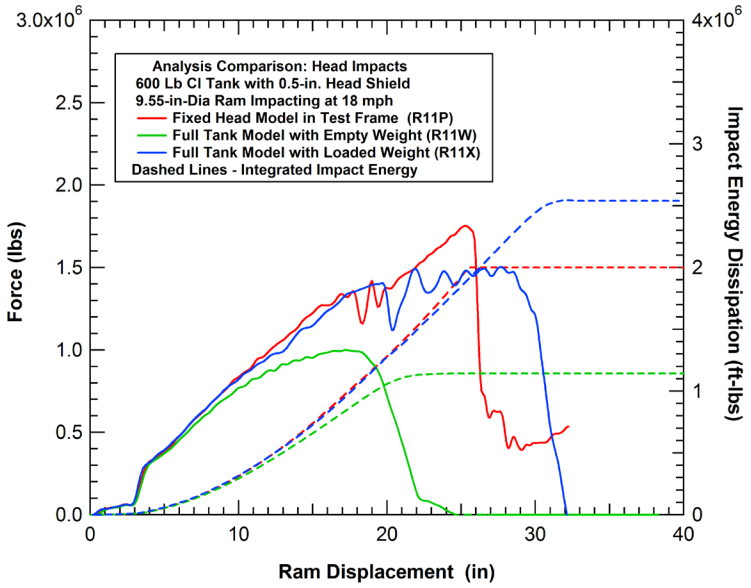

Figure 260. The effects of BC restraint on head impact response.

The 1D head impact algorithm was developed as a set of equations that are solved for a given impact using a time stepping methodology. The equations governing the motion are:

Time Stepping: $$t_{i+1} = t_i + \Delta t \quad (8)$$

Impactor Displacement: $$X^i_{i+1} = X^i_i + \Delta t * V^i_i \quad (9)$$

Tank Displacement: $$X^t_{i+1} = X^t_i + \Delta t * V^t_i \quad (10)$$

Relative Penetration Depth: $$\delta_{i+1} = X^i_{i+1} - X^t_{i+1} \quad (11)$$

Updated Impactor Force: $$F(\delta_{i+1}) \quad (12)$$

Impactor Velocity: $$V^i_{i+1} = V^i_i - \frac{\Delta t}{2M_1} * [F(\delta_i) + F(\delta_{i+1})] \quad (13)$$

Tank Velocity: $$V^t_{i+1} = V^t_i + \frac{\Delta t}{2M_2} * [F(\delta_i) + F(\delta_{i+1})] \quad (14)$$

Where: M_1 = impactor mass, M_2 = tank mass, and Δt = time step

The initial application of the algorithm uses the calculated force-deflection curve of the fully constrained tank head as a characteristic property of the tank structure. The forces are used by a tabular lookup to update the impact forces based on the current dent depth of the unconstrained tank. An approximate value such as a linear stiffness could also be used.

The force-deflection behaviors predicted by this simple one-dimensional (1D) algorithm for the two unconstrained tank impacts with the empty and full tank weights of 61,300 and 263,000 lbs

respectively are compared to the detailed FE analyses in Figure 261. The comparison shows that the simple approach of an uncoupled force versus dent depth interaction and tank motions describe most of the impact behavior. The largest deficiency of the 1D algorithm is that the nonlinear unloading behavior was not included in the analyses. In the detailed FEA a residual dent is maintained in the unloading process as the tank separates from the impactor. In the preliminary development of the algorithm the dent displacement unloads along the original loading curve.

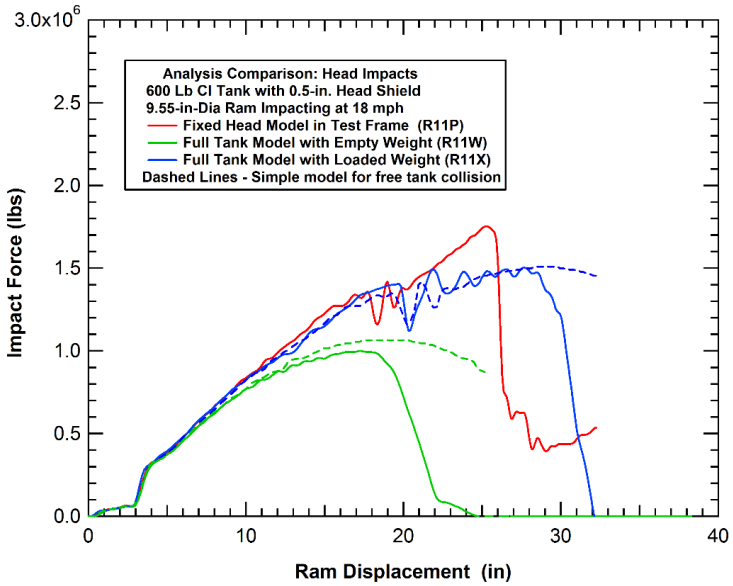

Figure 261. Comparison of the 1D model and FEA predictions for tank impact forces (18 mph impacts).

A modification was made to the model to include the unloading effects. The approach uses a linear unloading modulus when the relative motions between the tank and the ram are negative. To estimate the unloading modulus, the plots of force versus relative displacement for the 18 mph impacts of the loaded and empty tanks are compared in Figure 262. The comparison shows that a linear unloading behavior is a reasonable approximation and the unloading modulus of approximately 2 million lbs/in is a good average value for the 600 lb tank head.

Using the modified model with unloading, the force-deflection behaviors predicted by the simple 1D algorithm for the two unconstrained tank impacts with the empty and full tank weights are compared to the detailed FE analyses in Figure 263. The comparison shows that the simple algorithm accurately reproduces the force versus dent depth interaction and tank motions for the full impact and unloading behavior.

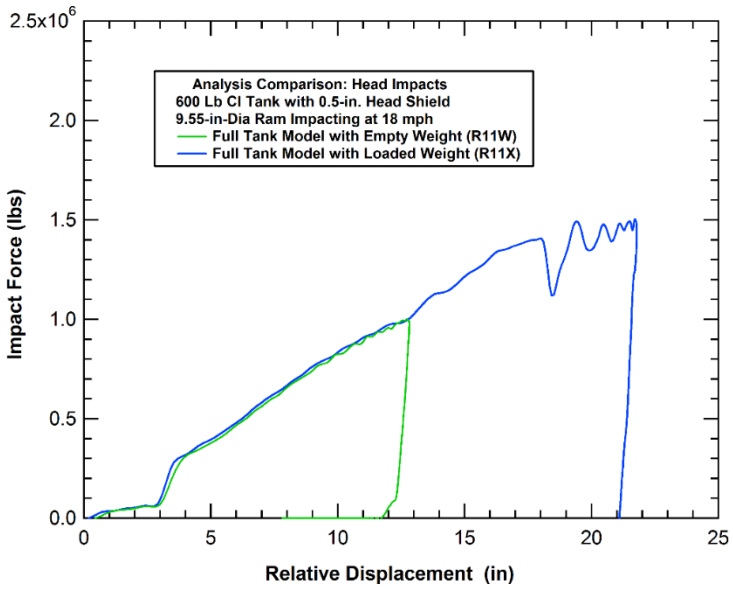

Figure 262. Comparison of the FEA analyses with unloading behaviors.

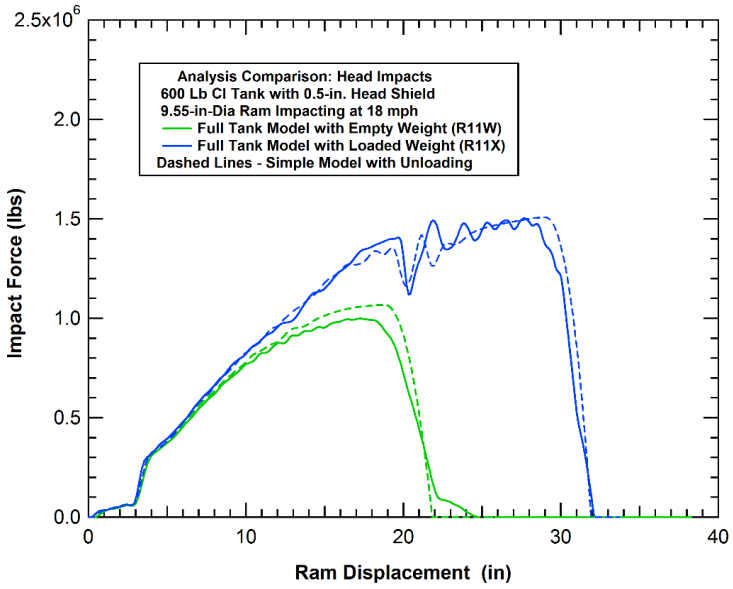

Figure 263. Comparison of the 1D model and FEA predictions with unloading (18 mph impacts).

To confirm the performance of the algorithm, we applied it to a similar set of analyses using the coupler impactor model and an impact speed of 25 mph. The force deflection curves for these analyses are compared in Figure 264. The comparison of the detailed FEA and the simplified 1D head impact algorithm is shown in Figure 265. The comparison shows again that the simplified 1D algorithm does a good job of predicting the force-deflection curves for the head impacts on the tank.

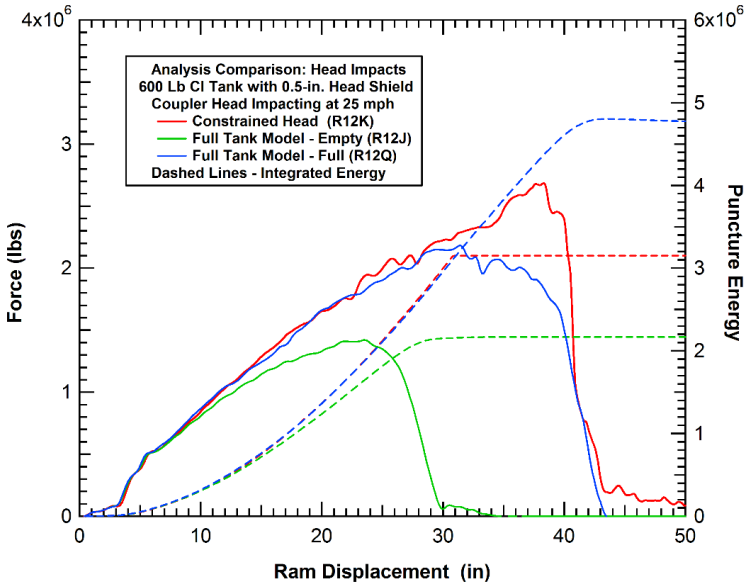

Figure 264. The effects of BC restraint on head impact response (25 mph coupler impacts).

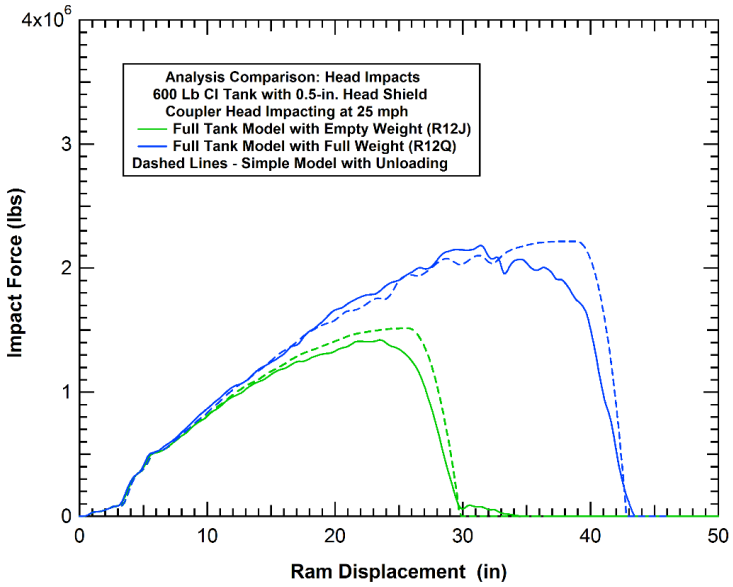

Figure 265. Comparison of the 1D model and FEA predictions with unloading (25 mph coupler impacts).

One of the complexities of this approach is that the detailed force-deflection curve for a fixed tank head was obtained from a detailed FEA and applied in a tabular lookup to obtain the interaction forces. An alternative approach is to use a simplified linear stiffness for the force-deflection behavior of the tank head. We can approximate the indentation stiffness of the 600 lb chlorine tank head and head shield at 80,000 lb/in. A comparison of this constant stiffness approximation to the fixed head force-deflection curves is shown in Figure 266. Using this constant stiffness value in the 1D algorithm we can recalculate the force-deflection behaviors for the empty and full tanks for the 18 and 25 mph impacts. The comparison of the constant stiffness 1D algorithm approximation to the detailed FEA results is shown in Figure 267. Again, the

overall agreement is quite good. The largest discrepancies are for the late time impacts on the loaded tanks where the force reduction from the head shield damage is not captured by the constant stiffness approximation.

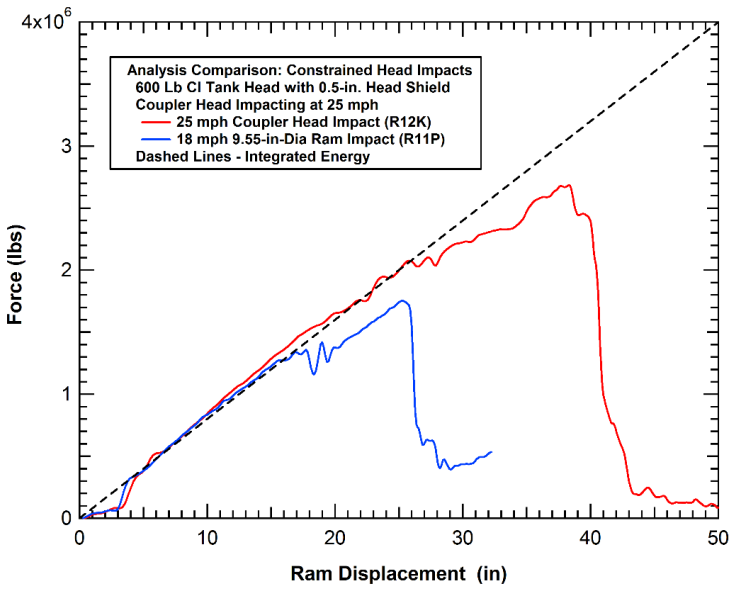

Figure 266. Comparison of the FEA and constant stiffness approximation.

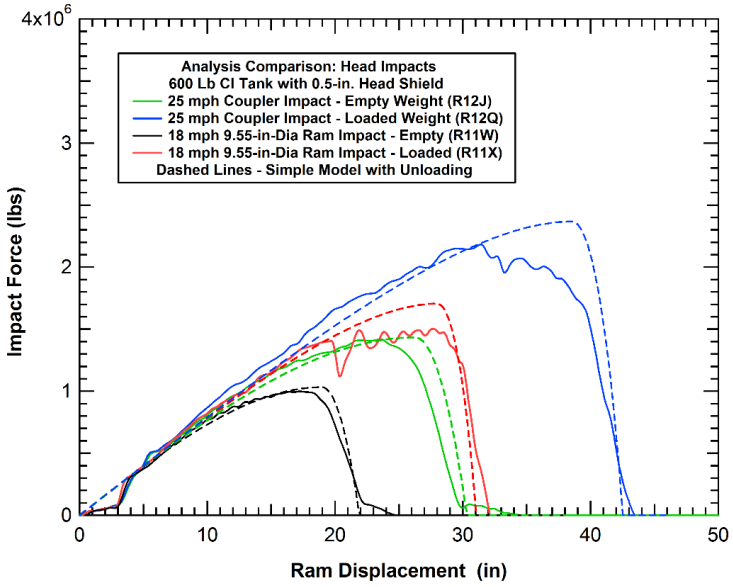

Figure 267. Comparison of the 1D model and FEA predictions with unloading (fixed head stiffness - 18 and 25 mph impacts).

6.3 Side Impact Analyses

The side impact response has several characteristics that influenced the methodology applied for the simplified impact algorithm. The tank is a more compliant structure under side impacts and the impact behavior is not independent of the impact speed (dynamic effects – see Section 3.4). The impact scenarios under side impacts are also typically occurring in large scale lateral

buckling behaviors of a derailment where the motions of the various cars are chaotic. As a result, the side impacts will include a greater range of variability in impact location and orientation. As a result, the motions will be at least two dimensional. As a result, a unique analytical methodology was used to develop an algorithm for side impacts.

6.3.1 Supporting FE Tank Analyses

In the previous sections of the report, many of the possible behaviors of tank cars in various side impact conditions have been analyzed. This information will be used to assist in the development and validation of the side impact model. However, there are other aspects of the tank response that are difficult to extract from the complex impact analyses. As a result, a series of idealized tank side loading analyses were performed to address some of the physics of tank behaviors.

An example of the type of additional analysis performed to assist the development of the analytical model is an analysis of the effects of different BCs. A series of analyses were previously performed to assess different tank constraint conditions as described in Section 4.3.1 of this report. Initially, a series of side impact analyses were performed where the impacted tank was placed against a wall, against another tank, and free to translate. The effects of the BCs could be detected but under the dynamic impact conditions the effects are seen only at late times in the response.

To more clearly evaluate the effects of the boundary constraints, idealized impact scenarios were analyzed where the tank was loaded at slow rates and under symmetrically conditions between two rams or two walls. Under these loading conditions, the tank has relatively linear force deflection curves and both fail at roughly equivalent puncture forces, as shown in Figure 268.

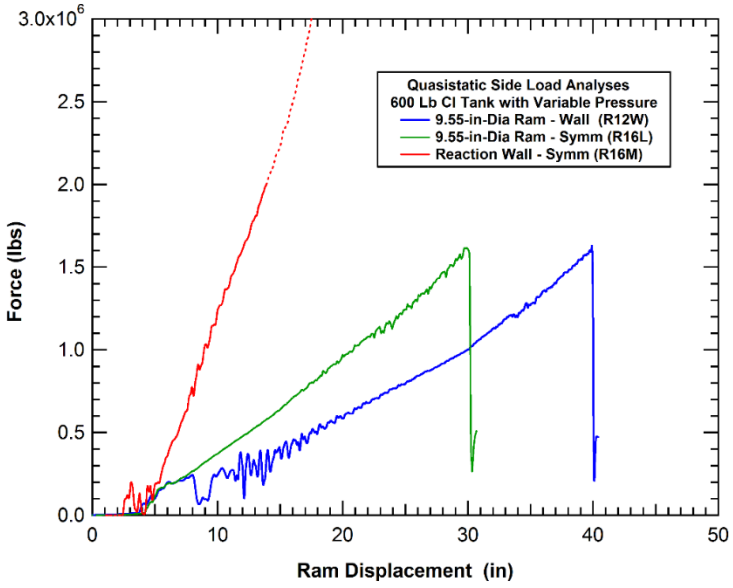

Figure 268. The effects of constraint BCs on the side impact response.

The quasistatic loading with a 9.55-in.-diameter rams of a tank against the wall fails at a force of approximately 1.5 million lbs and a ram displacement of approximately 40 inches. The symmetric loading between two 9.55-in.-diameter rams fails at a similar load level and a corresponding ram displacement of approximately 30 inches. However, the symmetric condition assumes that the tank is between two moving rams. Thus, the total compaction of the tank

between the two ram faces is approximately 60 inches. The calculated force-deflection for the symmetric wall loading develops a 1.5 million lb reaction load over a displacement of approximately 10 inches (after the initial 4-inch standoff distance of the jacket from the tank is crushed).

The significant difference in the compliance of the tank against either an impactor or the reaction wall is a result of the load application over a much larger area with the wall. This suggests that the size of the wall would have a significant effect on the wall reaction forces and tank deformations against the wall. To investigate this effect, a series of analyses were performed where the tank is quasistatically compressed between walls of different sizes (symmetric loading analyses).

In the initial series of analyses, the length of the wall was varied. The height of the wall is 6 feet and centered on the tank height. This dimension is sufficiently large that it exceeded the height of the contact patch of the tank and jacket for all the analyses. The baseline width of the wall was 25 feet to match the width of the impact wall at the transportation Technology Center Inc. (TTCI) test facilities where the NGRTC tests were performed (Kirkpatrick, 2009a). Additional widths analyzed included 1, 4, 8, 16, and 32 feet. This ranges from a very narrow width that will behave as if the tank were resting against a structural column to a wide width that extends nearly the full length of the tank shell. The models for the 1-foot and 32-foot wall length analyses are shown in Figure 269.

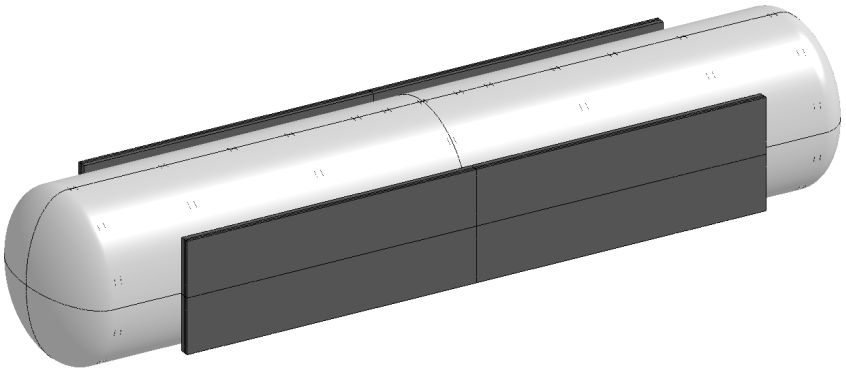

(a) 32-foot wall length

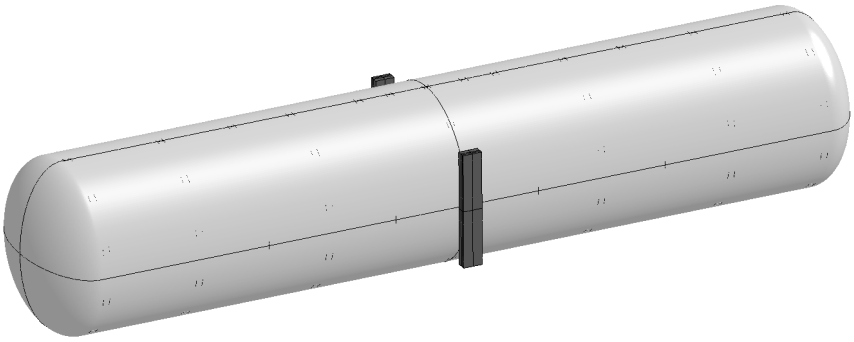

(b) 1-foot wall length

Figure 269. Comparison of models used to investigate reaction wall size effects.

The comparison of the force-deflection curves for the analyses with the different wall lengths is shown in Figure 270. The comparison shows that the wall length has a significant influence on the stiffness of the reaction forces. This effect is not too surprising since a longer section of the tank cylinder is being compressed with the longer wall. To quantify the effect, we plot the approximate steady state stiffness of the tank compression against the wall width as shown in Figure 271. The comparison shows a relatively linear increase in the tank stiffness as the width of the wall is increased. The non-zero intercept of the ordinate in Figure 271 is probably an indication of the magnitude of the edge effect for the tank denting outside the direct load application region against the wall.

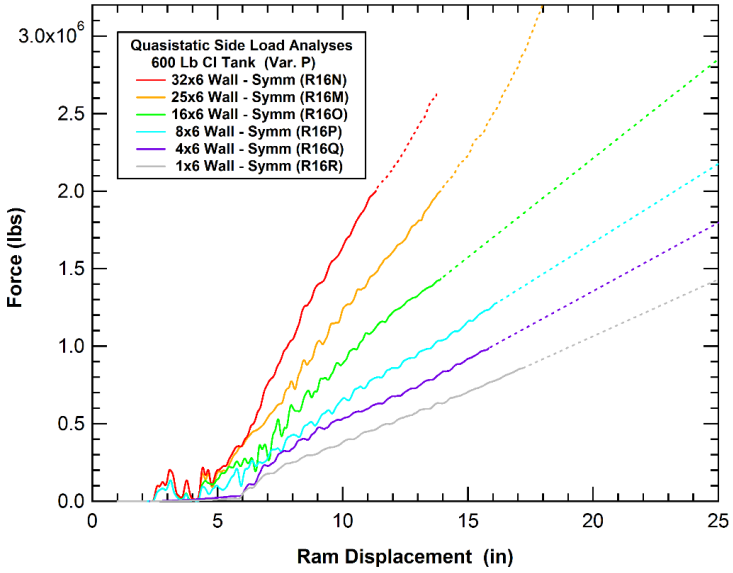

Figure 270. The effects of constraint wall width on the reaction loads.

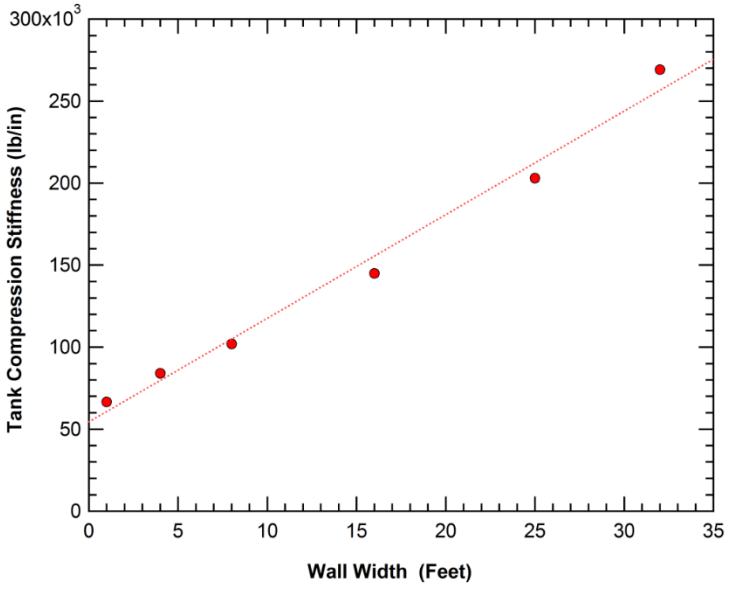

Figure 271. The effects of wall width on the tank compression stiffness.

These effects of the reaction wall width can be seen in an impact analysis where the tank dynamics and wall interaction are significant. A series of analyses were performed for a 15-mph impact of the 9.55-in-diameter round impactor. This impact condition is below the puncture threshold for the 105J600W chlorine tank car. The three BCs analyzed were a free tank (no wall) and a tank against the 1-foot-wide and 25-foot-wide reaction walls. The force-displacement curves for these three analyses are shown in Figure 272. The initial loading behaviors for all three analyses are identical but the tank dynamics (unloading and reloading) at the large displacement levels are significantly different.

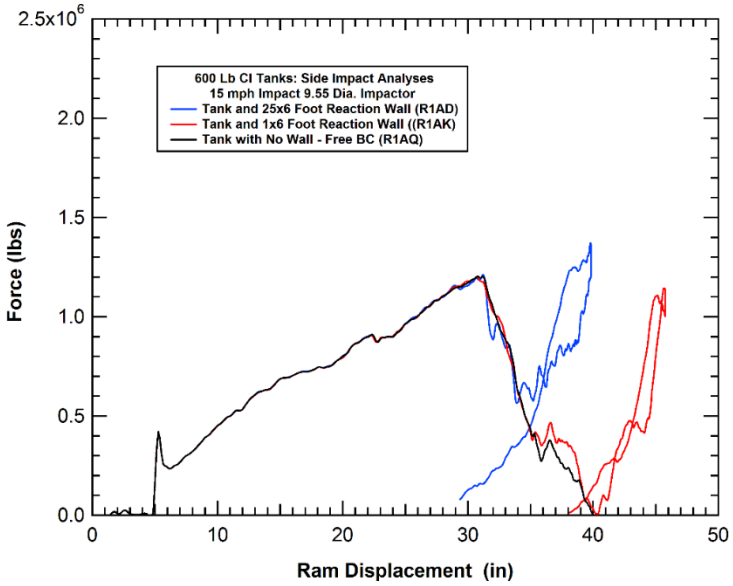

Figure 272. The effects of wall width on the tank impact behavior.

The effects of the wall interaction can be seen more clearly in the force-time histories for the three impact analyses, shown in Figure 273. With no wall, the tank loads up against the impactor over the initial 150 ms followed by an unloading over the next 80 ms as the tank is pushed away from the impactor. With the 25-foot-wide wall, the motions of the tank interact with the stiff wall to resist the tank motions and the rebound off the wall and reloading process starts at a time of approximately 180 ms (approximately halfway through the unloading). The reloading behavior reaches a peak force that is approximately 10-15 percent higher than the peak force in the initial loading.

The impact with the 1-foot-wide reaction wall allows for a much more compliant behavior of the tank against the wall. As a result, the wall reaction forces develop more slowly, and the tank rebound off the wall and reloading process starts at a time of approximately 250 ms after the initial impact force has completely unloaded. As a result of the longer overall impact duration, there is less residual impact energy and the peak force in the reloading behavior is approximately 5 percent lower than the peak force in the initial loading.

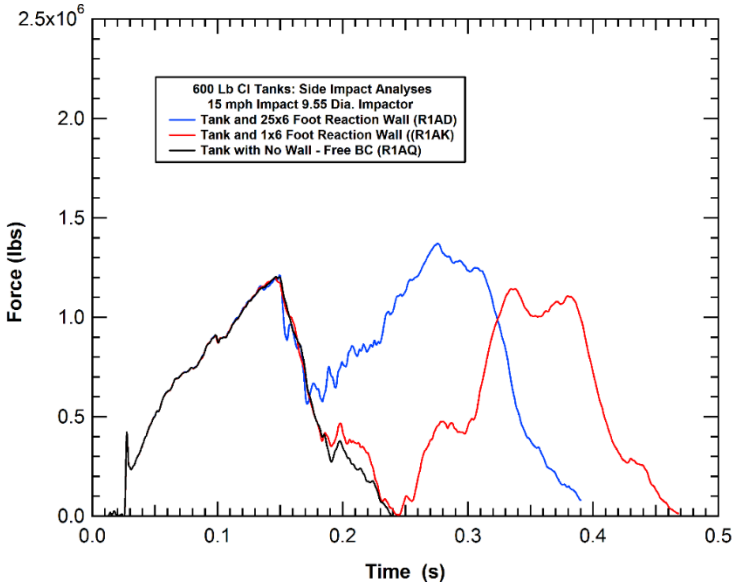

Figure 273. The effects of wall width on the impact force histories.

An additional series of analyses was performed to investigate the effects of the wall height. The 32-foot-wide wall was used for these analyses. The 6-foot height is sufficiently large that it exceeded the height of the contact patch of the tank and jacket for all the analyses. As a result, smaller heights of 1, 2, and 4 feet were also investigated. The comparison of the force-deflection curves for the analyses with the different wall heights is shown in Figure 274. The comparison shows that the wall height has a small influence on the stiffness of the reaction forces. This suggests that the shape of the tank deformations against the wall do not vary significantly with much smaller wall heights. A comparison of the 1-foot and 6-foot wall height deformations is provided in Figure 275. There are differences in the deformations of the outer jacket, but the deformations of the commodity tanks are very similar.

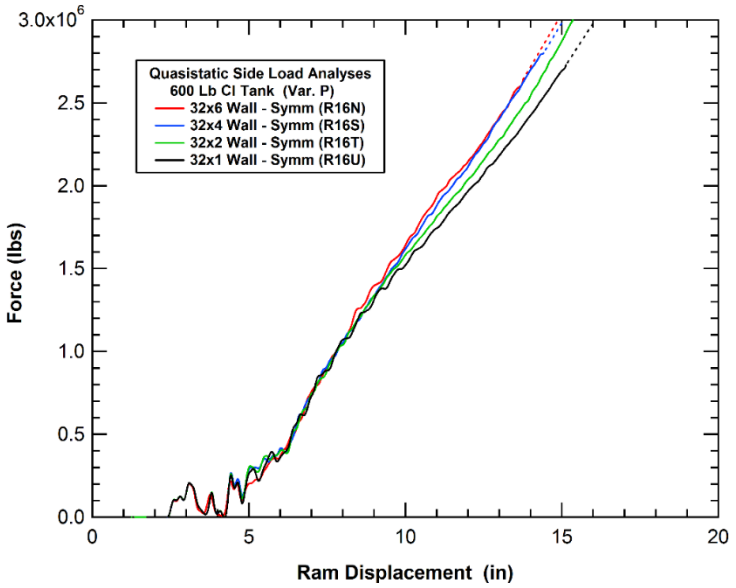

Figure 274. The effects of constraint wall height on the reaction loads.

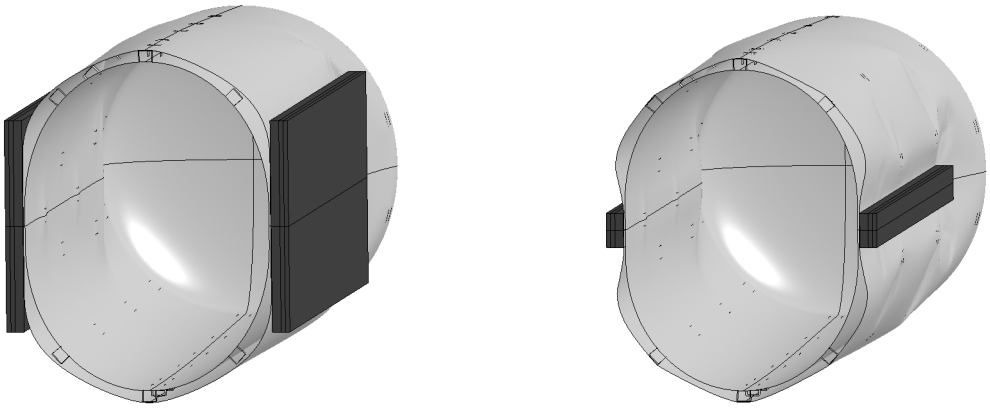

(a) 1-foot wall height **(b) 1-foot wall height**

Figure 275. Comparison of Tank Deformations with different wall heights.

The baseline side impact algorithm development was performed for the 600 lb chlorine tank car (105J600W) at a 100-psi internal pressure. However, for the algorithm to have greater utility, it needs to be applicable to other tank car designs and pressure levels. One approach to extending the analysis to other tank cars or pressure conditions is to develop scale factors for the system stiffness base on the tank design parameters. To assess these potential scale factors, a series of quasistatic compression analyses were performed on a tank where the thickness, radius, and pressure were varied independently.

The analyses were performed for the quasistatic symmetric compression loading of a tank between two 25-foot-wide walls. In the initial series of analyses, the diameter of the tank and the initial internal pressure were held constant, and the thickness of the tank shell was varied. The thickness variations evaluated were 1/2, 2/3, and 5/6 of the original 600 lb tank shell thickness. The calculated force deflection curves for these different thickness tanks are shown in Figure 276. The thickness has a moderate influence on the tank stiffness under the side loading.

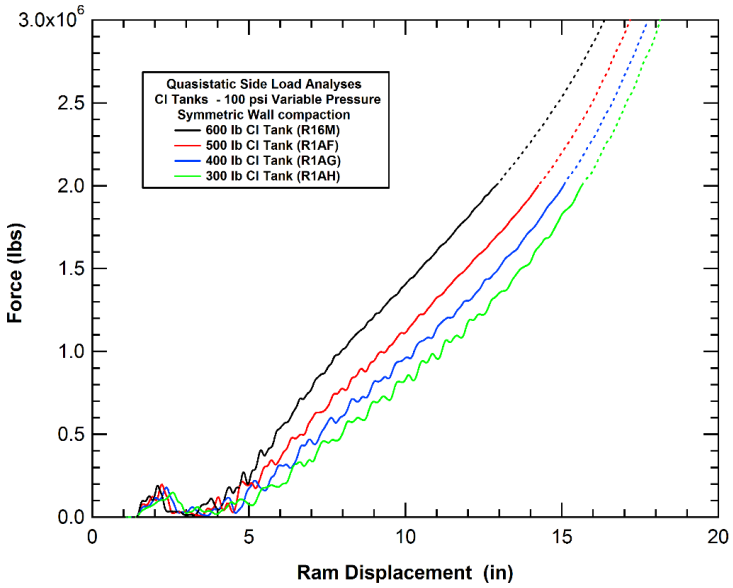

Figure 276. The effects of tank thickness on quasistatic compression loads.

To quantify the effect, we determined the relative stiffness of the various tanks between 8 and 12 inches of displacement. This is a relatively linear portion of the response after the initial jacket compaction is complete and before the variable pressure effects become large. A plot of this effective tank stiffness against the tank wall thickness is shown in Figure 277 A fit shows a relatively linear increase in the tank stiffness with changes to the tank shell thickness.

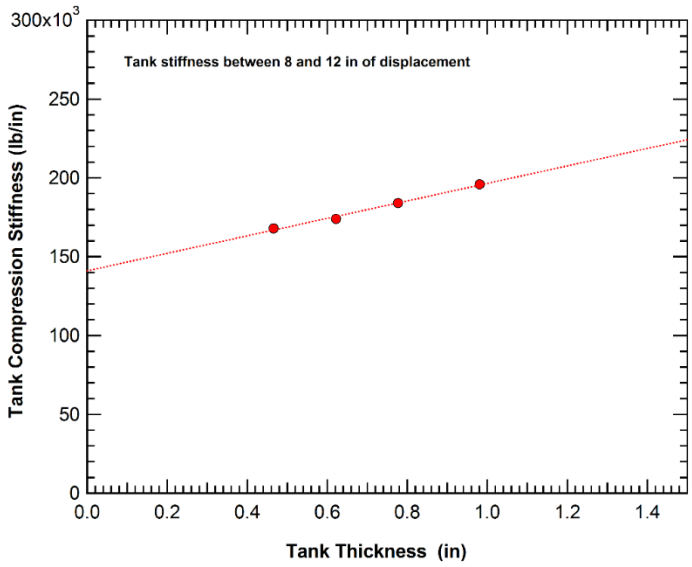

Figure 277. The effects of tank thickness on quasistatic compression stiffness.

In the second series of analyses, the tank shell thickness was fixed (0.981-in-thick TC128B) and the initial internal pressure was held at 100 psi while the diameter of the tank was varied at 80, 100, and 120 inches. The calculated force deflection curves for these different pressure tanks are shown in Figure 278. The comparison shows that the tank diameter has a very small influence on the tank stiffness under the side compression loading.

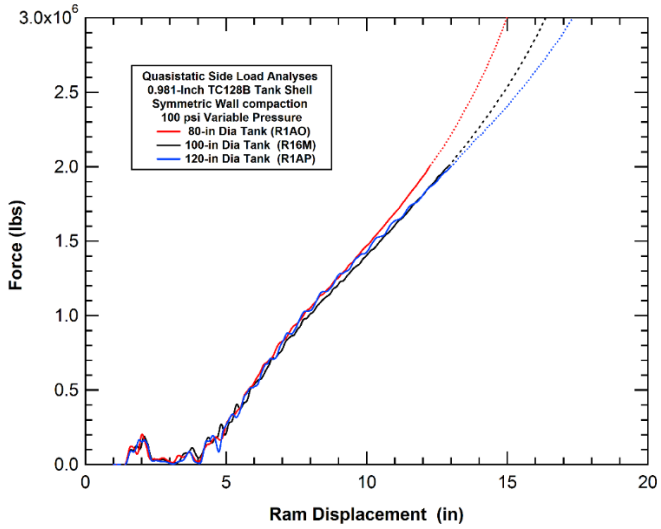

Figure 278. The effects of tank radius on quasistatic compression loads.

In the final series of analyses, the tank design was fixed (600 lb Cl tank) and initial internal pressures of 0, 50, 100, and 150 psi were analyzed. The calculated force deflection curves for

these different pressure tanks are shown in Figure 279. The pressure has a large influence on the tank stiffness under the side compression loading. This is seen clearly by the comparison to the force-deflection behavior of the unpressurized tank. Without the pressure the force deflection curve is very nonlinear with reductions in the compaction stiffness at increased deflection levels.

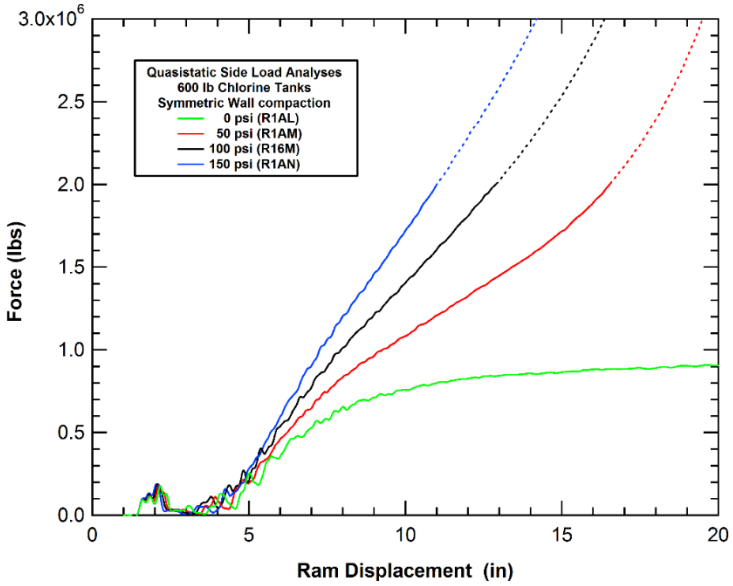

Figure 279. The effects of tank pressure on quasistatic compression loads.

To quantify the effect of the internal pressure, we determined the relative stiffness of the various tanks between 8 and 10 inches of displacement. This is a portion of the response after the initial jacket compaction is complete and before the variable pressure effects become large. A plot of this effective tank stiffness against the tank pressure level is shown in Figure 280. A fit shows a relatively linear increase in the tank stiffness with the internal pressure levels. At 100 psi the compaction stiffness of the tank is nearly four times that of the unpressurized tank.

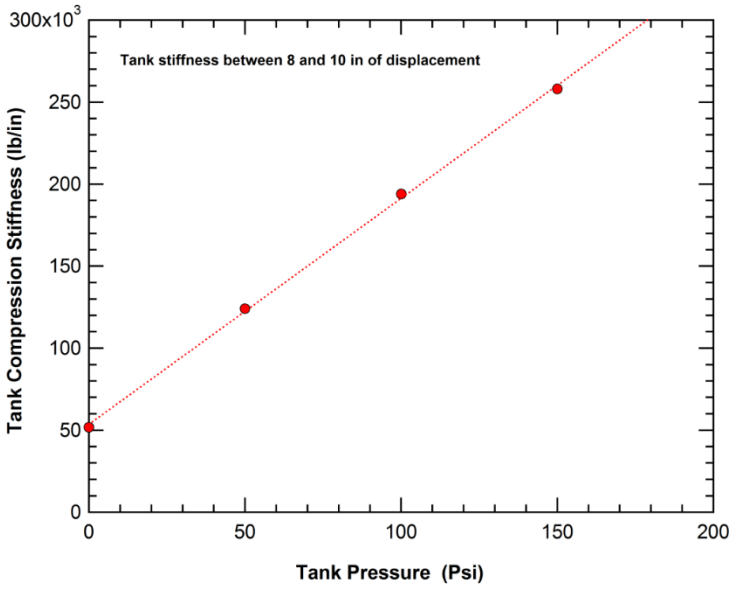

Figure 280. The effects of tank pressure on quasistatic compression stiffness.

6.3.2 Side Impact Analysis Algorithm

The approach used to develop a side impact analysis algorithm is to develop a spring-mass model for the tank that can replicate the force-deflection characteristics for side loading against various objects (e.g., impactor, reaction wall). These loads can then be applied with equations for the tank kinematics under the combined actions of the loads.

The side impact algorithm was developed with Python coding language (van Rossum, 2012) using the NumPy scientific computing package (NumPy, 2012). The equations of motion were written in matrix form as a series of first-order differential equations and integrated with a fixed time step. The objective is to fit the mode across multiple trials (impact conditions) and develop optimized spring constants & tank mass distribution. Wherever possible, information about the tank known physical behaviors are used as constraints.

A schematic of the spring-mass system used for the side impact algorithm is shown in Figure 281. The tank is represented by a series of five symmetric masses connected by springs. The outer masses (M_1) are small and represent a small region of the tank that is involved with the initial interaction with the impactor or reaction structures. The secondary masses (M_2) represent the region of the tank in the deformation zone around the impactor or reaction structures that become significant as the deformation progresses. The central mass (M_3) is the remainder of the tank mass.

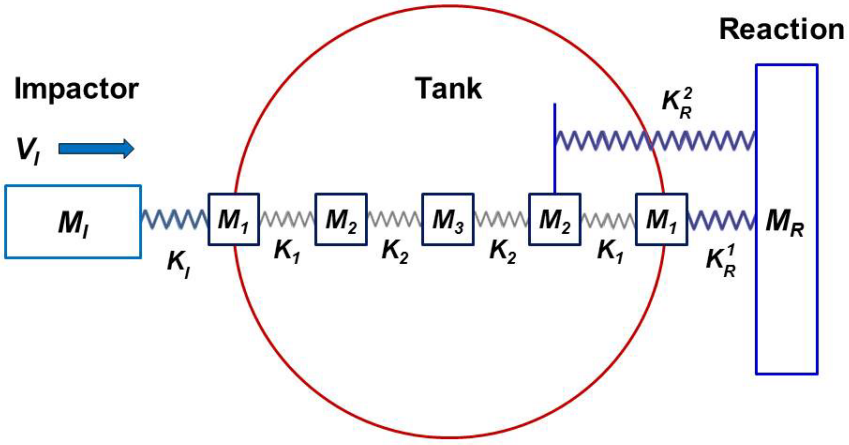

Figure 281. Idealized schematic of the side impact spring mass model.

The impact is modeled using a rigid impactor mass (M_I) and an external nonlinear spring (K_I) between the impactor and the outer tank mass on the impactor side. The impactor mass can be given different BCs such as a constant velocity or bee free to decelerate based on the interaction forces with the tank. The general characteristics of the external spring are a relatively low stiffness over the initial 4 inches of travel (the initial engagement and crushing of the jacket standoff) followed by a high stiffness spring. This effectively produces a constraint where the motions of the impactor and the outer mass under the impactor have equivalent displacements as long as the interaction force is compressive.

The approach used for the reaction on the back side of the tank is similar to the approach used on the front side of the tank. The reaction mass (M_R) can be given various displacement BCs (e.g., fixed or free to translate). For a stiff object, such as the reaction wall, the spring interacting with

the external tank mass (M_1) will be similar to the external impactor spring. This will allow for a small amount of tank displacement at low interaction forces while the standoff distance from the tank to the jacket is crushed. After the standoff is eliminated, the high external spring stiffness will effectively result in a displacement constraint against the reaction for the external tank mass.

A significant difference of the reaction model is the addition of a secondary spring between the reaction mass and the secondary tank mass (M_2) on the reaction side. This additional spring was necessary to model the interaction of a much larger contact area (such as the reaction wall). The properties of this secondary spring will be a function of the reaction wall size and if the reaction is localized to a small contact area this secondary spring is eliminated.

Another physical characteristic of the impact response that was added to the spring-mass model is the effects of nonlinear elastic-plastic unloading behavior. When the forces between the tank and impactor (or reaction wall) begin to unload, they do not follow the initial loading curve. This is a result of the plastic deformations of the tank shell around the impact zone. The springs were modified to be elastic-plastic springs where they load along an initial linear path with the spring displacements divided into elastic and plastic components. When the interaction begins to unload, the unloading occurs with the elastic components of the displacement only. The model uses a ratio of 70 percent plastic and 30 percent elastic deformations during the loading process. A comparison of the idealized elastic-plastic spring behavior with a calculated force-deflection curve for an impact response with unloading is shown in Figure 282. The comparison shows that the 70 percent plasticity approximation is reasonable for the tank impact response.

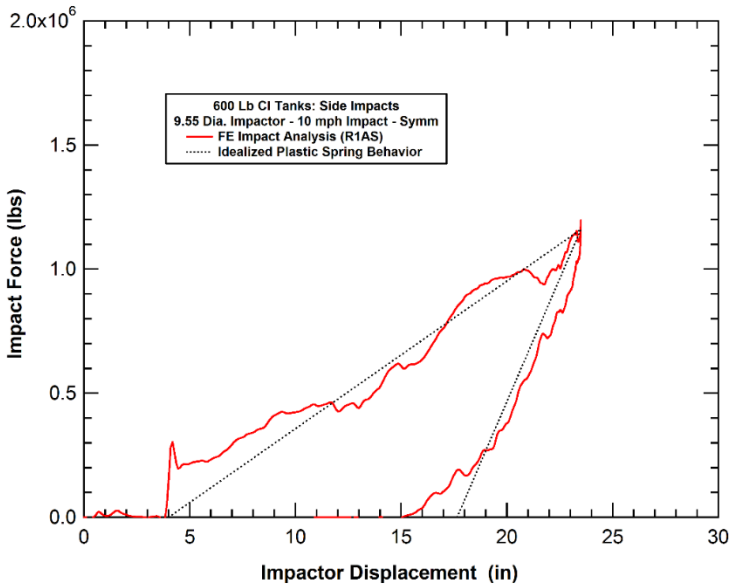

Figure 282. Idealized elastic-plastic spring behavior and calculated unloading response.

The values used for the spring-mass model parameters were derived in a two-step fitting process. Initially, a series of Monte-Carlo analyses were performed where the parameters were allowed to vary randomly, within ranges determined by physical constraints. Results were compared to a series of FE impact analyses and the correlation for each set of parameters was determined. Subsequently, the parameters that provided the best fit to the impact data were optimized by finding the minimum error in the parameter space around the initial Monte Carlo parameter set. The values that were selected based on this methodology are summarized in Table 21.

The resulting model was then applied to simulate a series of impact behaviors and the results were compared to the corresponding FE analyses. For example, a series of impacts with the 9.55-in-diameter impactor at different impact speeds are compared in Figure 283. The comparison shows that the spring-mass model does a good job of reproducing the variations in impact behaviors produced by different speed impacts. Note that the spring-mass model does not include puncture prediction, so the comparison of the higher speed impacts is only appropriate up to the point of the calculated tank punctures in the FEA.

Table 21. Parameter values for the spring-mass side impact algorithm

Component	Subcomponent	Value
105J600 Tank	Mass 1 (M_1)	39 lbs
105J600 Tank	Mass 2 (M_2)	4.432×10^4 lbs
105J600 Tank	Mass 3 (M_3)	1.745×10^5 lbs
105J600 Tank	Spring 1 (K_1)	3.465×10^5 lb/in
105J600 Tank	Spring 2 (K_2)	2.046×10^5 lb/in
Impactor	Mass (M_I)	2.950×10^5 lbs
Impactor	Spring (K_I)	9.020×10^2 lb/in
Reaction Wall 25'x6'	Spring (K_R^1)	1.955×10^5 lb/in
Reaction Wall 25'x6'	Spring (K_R^2)	2.590×10^5 lb/in
Reaction Wall 25'x1'	Spring (K_R^1)	1.955×10^5 lb/in
Reaction Wall 25'x1'	Spring (K_R^2)	2.590×10^5 lb/in

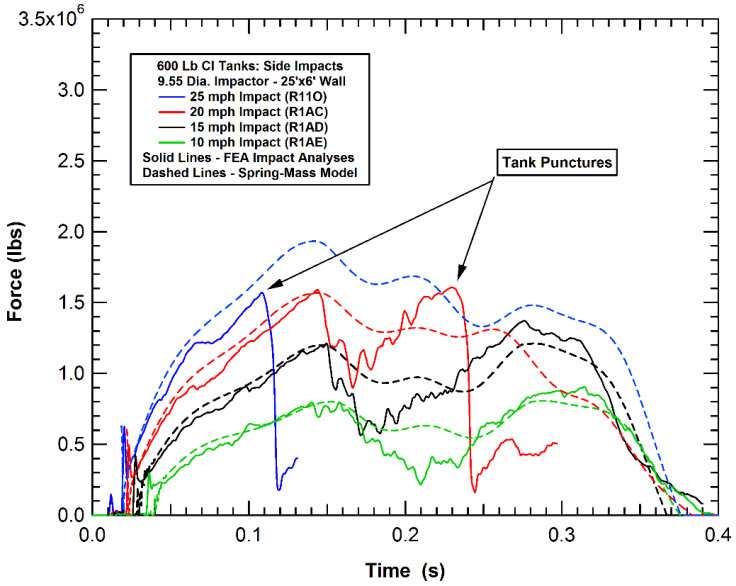

Figure 283. Comparison of the FEA and impact algorithm for different speed impacts.

A similar comparison of analyses with different BCs is shown in Figure 284. In this example, a series of 15 mph impacts were analyzed with the 9.55-in-diameter impactor and different restraint conditions on the far side of the tank. The BCs included both a free tank with no restraint conditions and tanks reacted by both a 25-foot-wide and 1-foot-wide reaction wall. The comparison shows that the spring-mass model does a good job of reproducing the variations in impact behaviors produced by different reaction BCs on the far side of the tank.

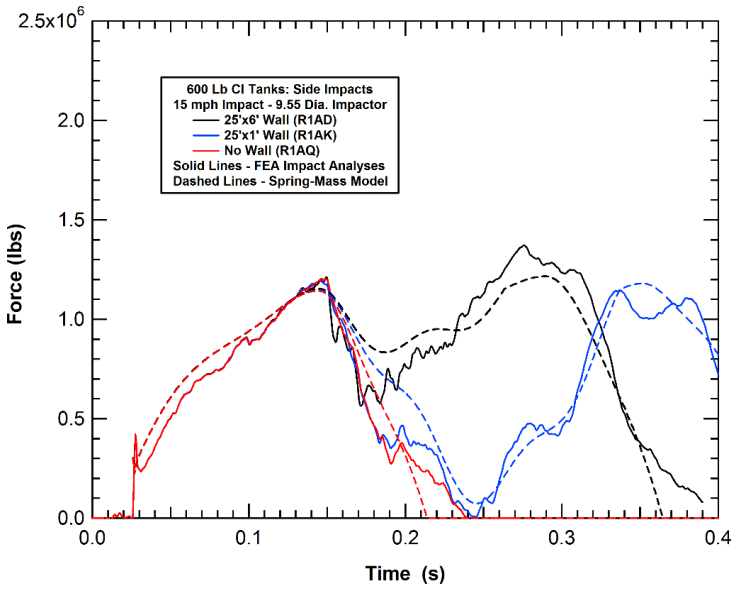

Figure 284. Comparison of the FEA and impact algorithm for different BCs.

The initial formulation of the spring mass system was developed for a center side impact scenario. However, the model can be easily modified to account for an off-center impact. The methodology for the offset impact scenario is illustrated in Figure 285. The local tank deformation and development of reaction forces are assumed to be identical to the center impact scenario. However, the tank motions relative to the impact point are now a combination of tank translation and rotation about the tank center of gravity (CG). Thus, the inertial characteristics of the tank are used to solve for the 2D tank motions and applied to determine the relative motions and dent depth at the impact point.

Using this methodology, a series of impacts was analyzed for the tank with a center impact and impacts with both 80-inch and 160-inch longitudinal offsets. The impactors used the 9.55-inch-diameter round impactor at a 15mph constant velocity impact condition. The tank was free to translate and rotate as a result of the impact forces. A comparison of the calculated behaviors with the FEA and spring-mass models for the three different impact conditions is shown in Figure 286. Again, the spring-mass model agrees well with the FEA predictions of the impact behaviors.

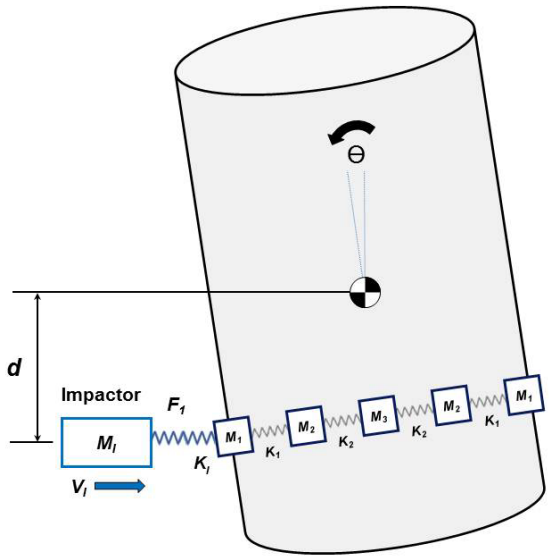

Figure 285. Idealized schematic of the offset side impact model kinematics.

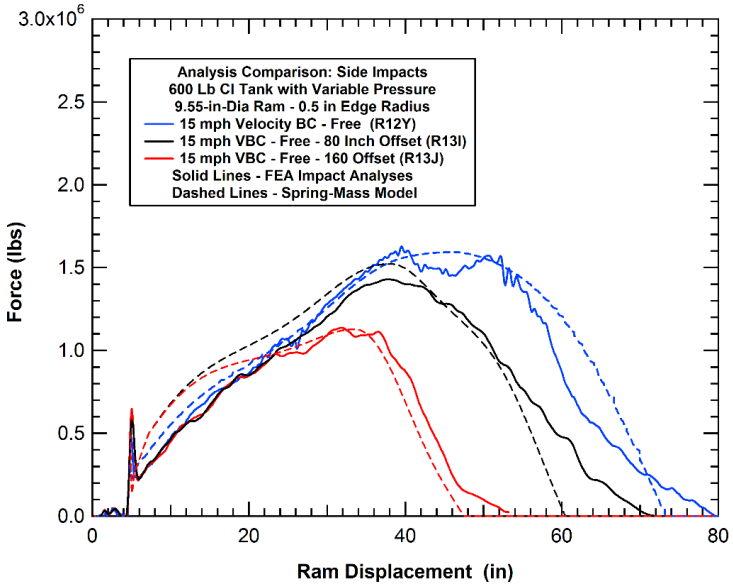

Figure 286. Comparison of the FEA and impact algorithm for offset side impacts.

A final comparison was made for the side impact analyses of a 500 Lb EO tank car at different impact speeds. In the above comparisons, the model was developed and optimized for the 600 lb chlorine tank car pressurized to 100 psi. For the EO tank car, the parameters were modified based on the results of analyses from Section 6.3.1. The larger radius of the tank does not significantly modify the algorithm, as shown in Figure 278. The tank shell thickness for the 500 lb EO tank car is 0.918-inch and the corresponding thickness for the 600 LB chlorine tank car is 0.981-inch. This results in a thickness correction in the tank stiffness of approximately 2 percent from Figure 277. Finally, the tank pressure of 50 psi for the EO tank car compared to the 100 psi for the chlorine tank car results in a reduction of the tank stiffness of 36 percent. As a result, all

the spring stiffness values for the EO tank car were scaled to 63 percent of the original stiffness in the chlorine tank car model. The values for the masses were maintained from the chlorine tank model to the EO tank model.

A comparison force deflection curves from detailed FE and simplified spring mass analyses of side impacts on an EO tank car at different impact speeds are provided in Figure 287. Overall, the agreement is quite good for model parameters scaled using this approximate methodology. This level of correlation would be suitable for many applications. However, if an improved fit is desired, a secondary optimization process could be performed for alternative tank car designs.

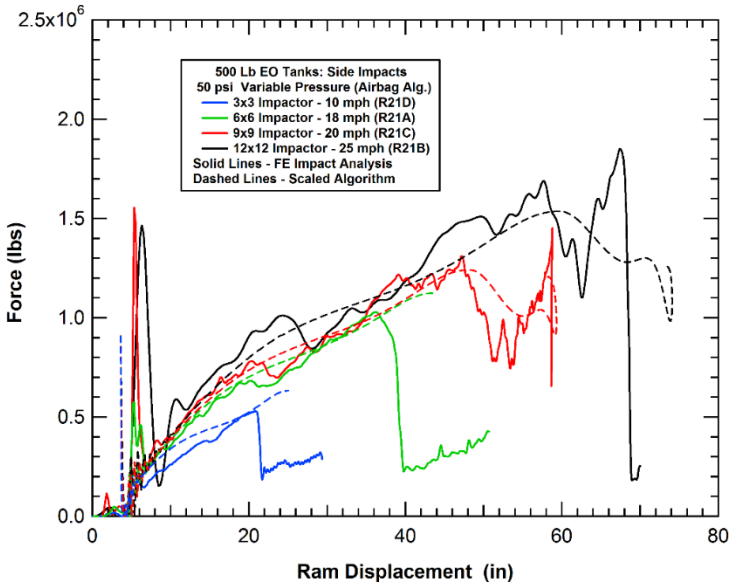

Figure 287. Comparison of the FEA and impact algorithm for an EO tank car.

6.4 Development of the Characteristic Puncture Force

The above sections describe analyses that can predict the force-deflection behaviors. However, the point along the force-deflection curve at which the tank is punctured also needs to be determined. This puncture force will be dependent on both tank geometry (materials and thicknesses) and the impact conditions (impactor size and impact orientation).

Our approach to developing a tank puncture criterion for the tank impact algorithm(s) was to use puncture data from all the detailed FE puncture analyses described in this report and develop a "characteristic puncture force" parameter that is a function of the impactor characteristic size (defined in Section 3.2.2). A collection of the calculated puncture forces for various tank and impact conditions is shown in Figure 288. As expected, there is a general trend in the data with increasing puncture loads for increasing ram characteristic size. However, for any given ram characteristic size, there is a large spread in puncture forces. This is because the puncture force for an oblique impact against a 111A100W1 tank car will be much lower than the puncture force for a normal impact against a 105J600 tank car.

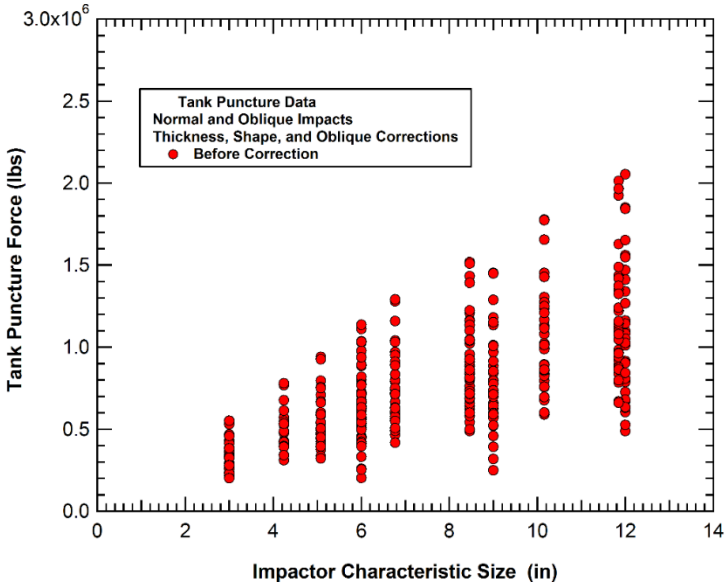

Figure 288. Initial set of tank puncture forces under various impact conditions.

The first correction that can be made to the data is to correct for the tank design. Previous analyses of tank car puncture behavior have established that the puncture force for a given impact scenario scales approximately linearly with the combined thickness of the tank and jacket. This trend is consistent in the analyses performed in this study, as shown in Figure 289. The figure plots the puncture forces for the normal impact analyses with the different rectangular impactors and all the different tank cars analyzed in this study. The comparison shows that the puncture forces correlate well to a linear fit against the combined tank and jacket thickness. A similar correlation was also seen for the round impactor geometries.

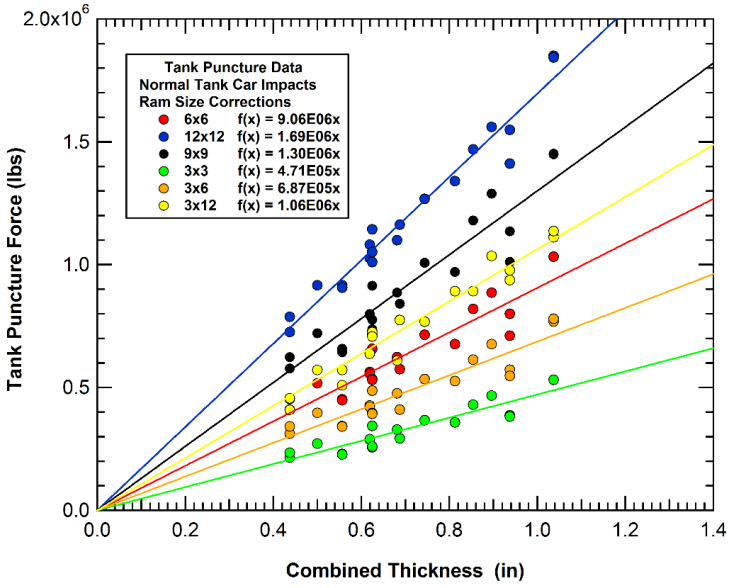

Figure 289. Effects of tank thickness on puncture force for various size impactors.

One potential modification to the thickness correction is to assess the puncture performance of the tank and jacket thickness independently. The assumed form of the thickness correction was:

Thickness Correction:

$$\bar{F}_p = F_p/(T_t + AT_j) \quad (15)$$

Where:

$\bar{F}_p$ =corrected puncture force

F_p = calculated puncture force

T_t = tank thickness

T_j = jacket thickness

A = jacket thickness correction coefficient

The evaluation of the thickness correction found that the best correlation was obtained using a value of the 0.7 for the jacket thickness correction coefficient. Thus, the jacket material was found to be 30 percent less effective at resisting punctures than the material in the tank. However, this result may be influenced by the fact that the vast majority of the analyses used a 0.119-inch-thick A1011 steel jacket. If we analyzed a series of double tank concepts where the outer tank is thicker and fabricated with a higher strength steel (e.g., TC128B) these results may change. The thickness corrected puncture force data for the normal side impact analyses is shown in Figure 290.

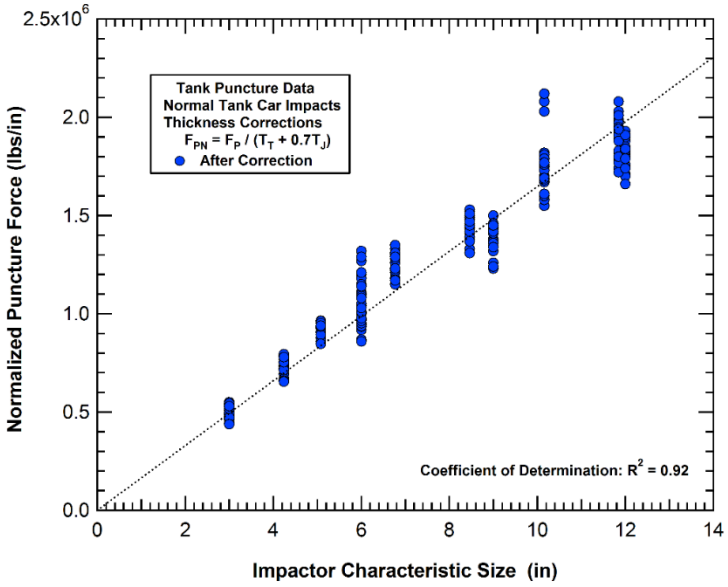

Figure 290. Tank thickness correction for the characteristic puncture force.

A second correction that can be made to the puncture force data is to correct for the relative orientation of the tank and impactor face. Analyses of the effect of the impactor orientation on the tank puncture force were described previously in Section 3.2.5. Similarly, the effect of impact obliquity on the puncture force has been evaluated as described in Section 4.2. Figure 291 provides the puncture forces for the rotated and oblique impacts for the 12x12 impactor normalized by the corresponding force of the normal impact scenario. As the angle between the impactor and tank increases, the stress concentrations at the edge of the impactor increases and the puncture force drops. The reduction in puncture force can be fit by the following correction function:

Impactor Angle Correction: $$\bar{F}_p = F_p[1.0 - 0.60Sin(2\theta)] \quad (16)$$

Where: θ =Angle between the impactor face and tank wall normal

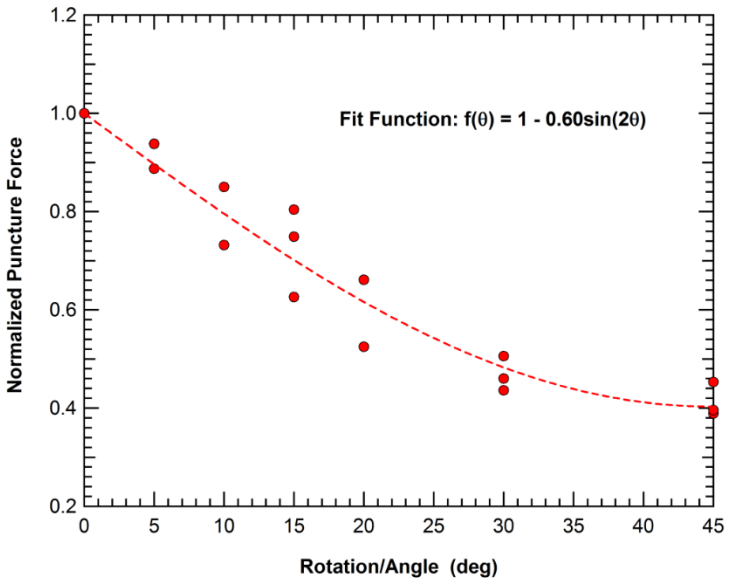

Figure 291. Effects of impact face orientation on puncture force.

An additional correction factor observed for the oblique impacts is an effect of the impactor shape. The thickness corrected 45-degree oblique impact puncture force data is shown in Figure 292. The data shows that there are different trends for the rectangular and round impactor shapes. We believe this is a result of the increased concentrations in loads and deformations for the rectangular impactors when rotated to apply primarily an edge load. As a round impactor is rotated for an oblique impact there is still a relatively smooth uniform loading along the length of the contact zone. When we look at similar sets of analyses for 30-degree and 15-degree impacts we see similar trends as shown in Figure 293 and Figure 294, respectively (analyses performed for the 105J600 tank car only).

The equation for the shape correction in oblique impacts is:

Shape Correction: $$\hat{\bar{F}}_p = \begin{cases} \bar{F}_p & \text{Round impactors} \\ [(\bar{F}_p - 4x10^5)x(0.88 - 0.008\theta) + 4x10^5] & \text{Square impactors} \end{cases} \quad (17)$$

Where: $\bar{F}_p$ =thickness corrected puncture force

$\hat{\bar{F}}_p$ =thickness and shape corrected puncture force

The correlation of the shape corrected 45-defree oblique impact data is shown in Figure 295. With this shape adjustment the normalized puncture forces for the various oblique impacts all agree. Similarly, the shape corrected data for the 15-degree-30-degree, and 45-degree oblique impacts are all compared to the normal impact data in Figure 296. With this shape correction the calculated puncture force for each impact angle obliquity correlate to a linear fit.

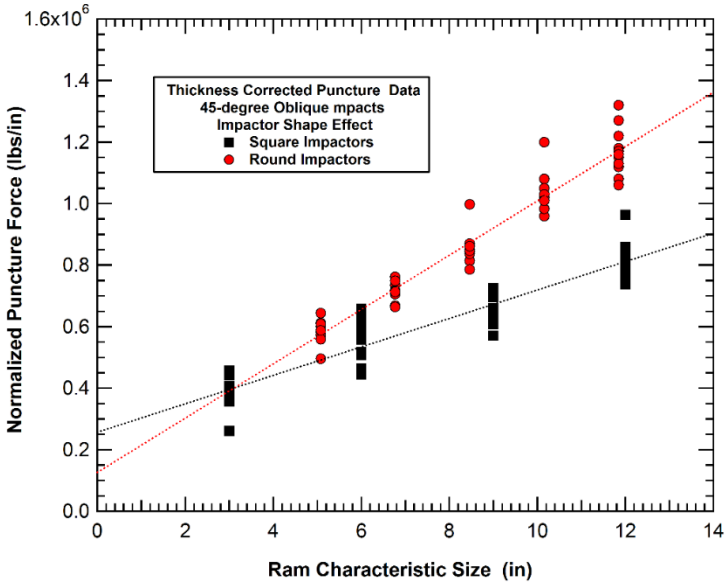

Figure 292. Effects of impactor shape on puncture force in 45-degree oblique impacts.

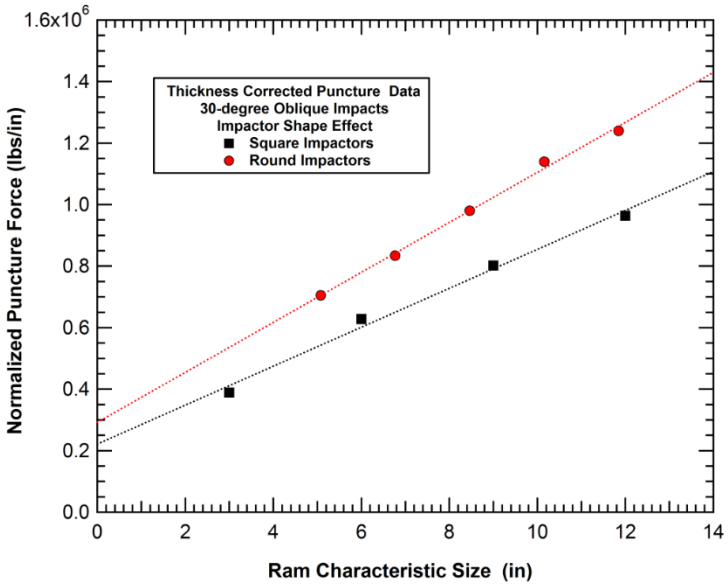

Figure 293. Effects of impactor shape on puncture force in 30-degree oblique impacts.

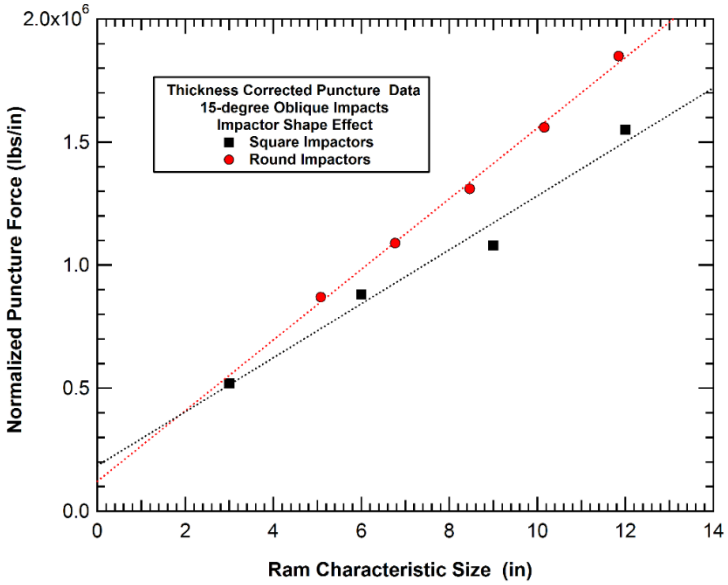

Figure 294. Effects of impactor shape on puncture force in 15-degree oblique impacts.

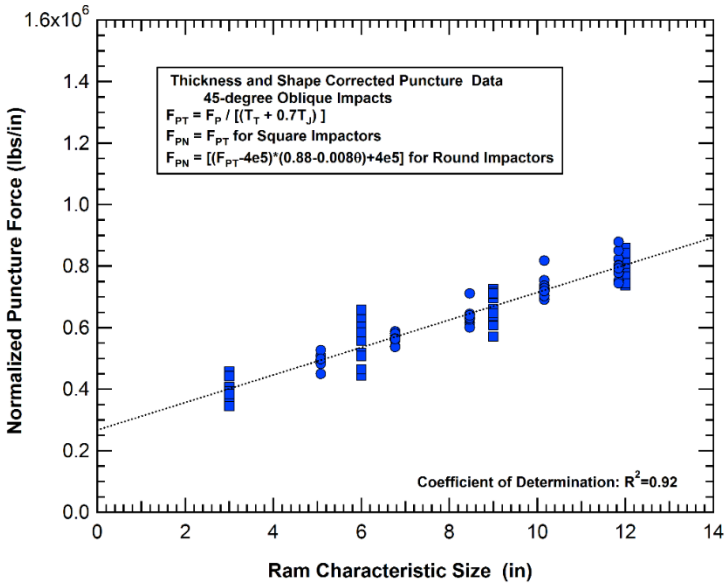

Figure 295. Impactor shape corrected puncture forces for 45-degree oblique impacts.

A final correction factor observed for the oblique impacts is an effect of the impactor size. The angle correction factor, shown in Figure 291, were developed using the 12x12 inch square impactor. At this size, the 45-degree oblique impact puncture forces were reduced by approximately 60 percent. However, when a wider range of impactors are analyzed in oblique impacts, as shown in Figure 296, we see that the drop in puncture force is much less for small impactor sizes.

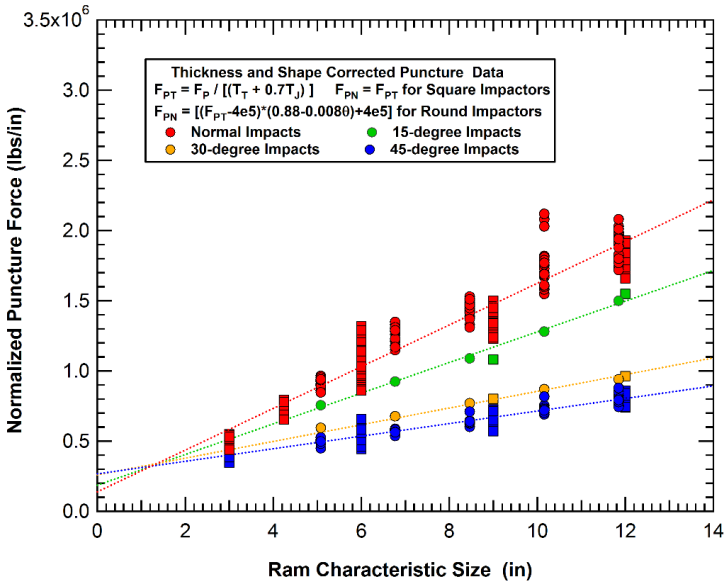

Figure 296. Impactor shape corrected puncture forces for various oblique impacts.

The size correction for oblique impacts was developed by comparing the average (fit) puncture force for the 45-degreee oblique impacts to the average normal impacts for various impactor sizes. The correction was normalized to the correction for the large 12-inch impactors. A fitting function was then developed for the oblique size effects data as shown in Figure 297. The resulting equation for the size correction in oblique impacts is:

Size Correction:
$$f(x) = \frac{1.0}{1.0 + exp(2.3 - 0.58x)} \tag{18}$$

Where: x =ram characteristic size

When we apply all the corrections, we obtain the characteristic puncture force correlation as shown in Figure 298. Using this characteristic puncture force allows us to assess the puncture conditions for a wide range of tank and impact parameters. The uncertainties in the puncture force can be assessed by comparing the range of errors in the corrected data for the detailed FE analyses to the puncture data fitting line.

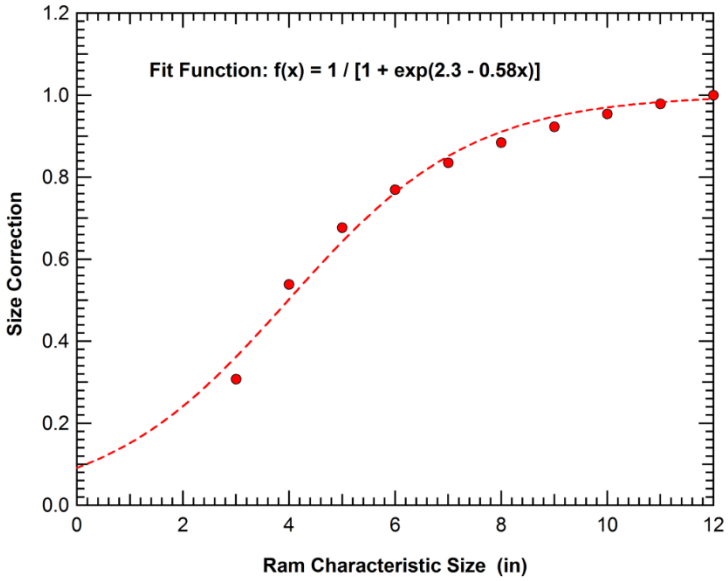

Figure 297. Impactor size correction for oblique impact puncture forces.

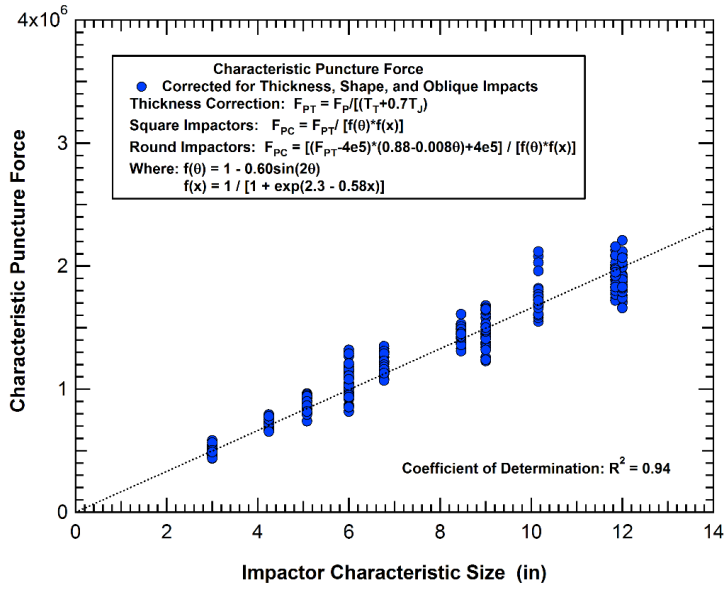

Figure 298. Correlation of characteristic puncture forces for various impact conditions.

7. Analysis of Real-World Threats

7.1 Introduction and Background

The other chapters of this report are focused on the safety of tank cars in accidents and derailments. These events that occur as part of normal rail operations are the most common events that lead to releases of hazardous materials in rail operations. However, the security of tank car from an intentional attack is also a consideration for these designs. The Department of Homeland Security (DHS) has done several small- and full-scale tests of components and tank cars subjected to different acts of terrorism. The objective of the analyses described in this section is to assess the puncture performance in impacts (safety) of a protection concept developed by DHS for security against various threats.

7.2 Protection System Design

The DHS, in collaboration with the Army Research Laboratory (ARL) evaluated a range of different tank car protection concepts against multiple security threats (Yen, Kaste, Montgomery, Cheeseman, & Scott, 2011). One of the best performing concepts, that also appeared to have potential for improving performance in accidents and derailments (safety applications) was the punched plate configuration illustrated in Figure 299. The system consists of two ¼-inch-thick perforated panels made of High Hard Steel (HHS). The perforations were 3/8-inch diameter holes in a hexagonal pattern with ½-inch spacing between the nearest neighbor hole positions. The two panels are used in an offset configuration as illustrated in Figure 299(b).

Material test data for the HHS was not made available for this study. Instead, DHS/ARL provided parameters for a simplified Johnson-Cook constitutive model in LS-DYNA (LSTC, 2003) which they claimed was validated against test data (Jeong, et al., 2009) This validated constitutive model was used to simulate a tensile test which was used as the material "test" data to develop the constitutive and failure parameters that were used in the puncture analyses. The simulated tensile test behavior for the HHS is shown in Figure 300. The methodologies used to develop the constitutive and failure parameters were described in Section 2.

The analyses of the HHS show that it has a very high yield strength compared to typical tank car structural materials. The yield strength for the HHS is approximately 230 ksi and the elongation calculated for the round bar tensile test was approximately 16 percent. The greatest uncertainty in the calculated tensile behavior is the elongation value which is sensitive to the specimen geometry and gauge length used in the test or analyses (a 2-inch gauge length was used for the analysis). A confirmation of the elongation for this configuration cannot be made without access to material test data.

For analysis of the impact and puncture behavior of a tank with the punched plate protection system some additional model development was required. In the detailed impact zone, the geometry of the punched plates will be explicitly modeled. However, outside the impact zone, an effective material is needed that will have the equivalent stiffness and strength of the punched plates but can be modeled with larger shell elements. To create the "effective" material model we simulated a tensile test on a section of punched plate material. The simulation of the tensile test on the punched plate specimen is shown in Figure 301. The calculated engineering stress-strain curve for the punched plate tensile test is compared to that of the solid HHS material in Figure 302. The comparison shows that the punched plate geometry both significantly reduces the

stiffness and strength compared to the solid material. The effective elastic modulus is less than 20 percent of that for the solid steel. The effective yield stress is reduced to approximately 40 ksi and the engineering ultimate stress for the punched plate material is approximately 65 ksi with an elongation of 20 percent.

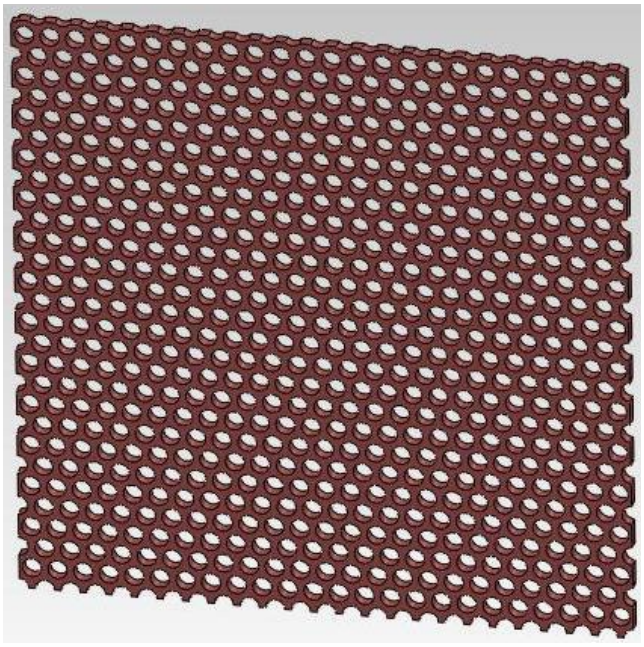

(a) Punched plate geometry

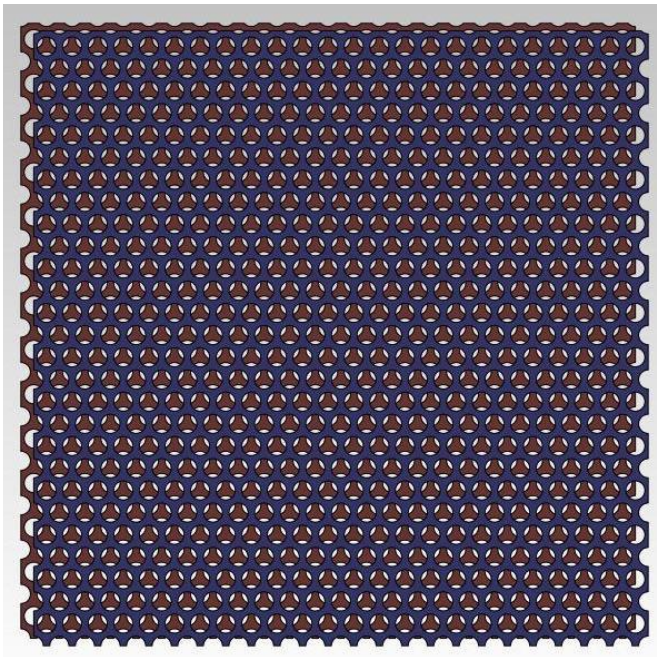

(b) layered punched plates

Figure 299. Configuration of the layered punched plate protection concept (Yen, Kaste, Montgomery, Cheeseman, & Scott, 2011).

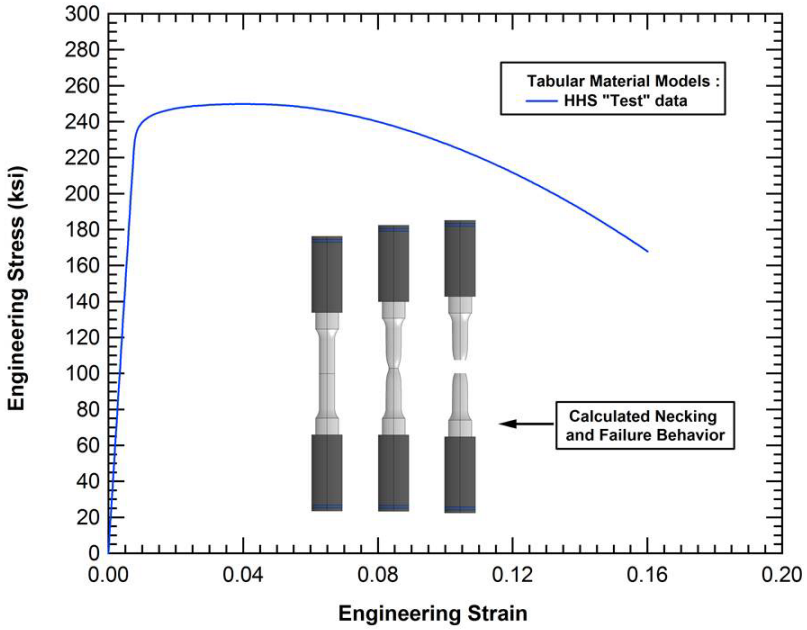

Figure 300. Simulated tensile test behavior for the High Hard Steel.

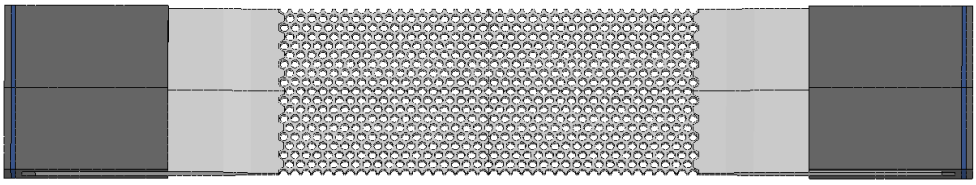

(a) Initial configuration

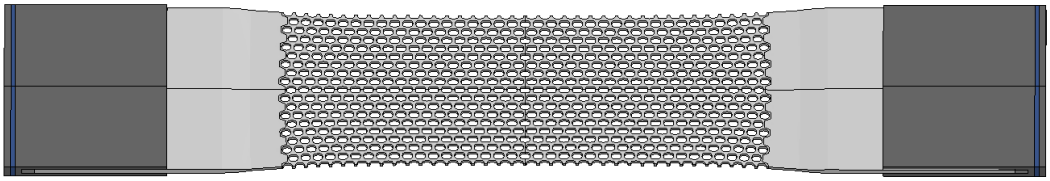

(b) Deformed specimen (before failure)

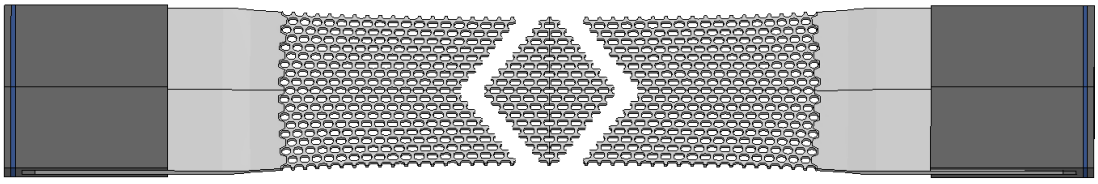

(c) Calculated failure mode

Figure 301. Simulated tensile behavior of the punched plate material.

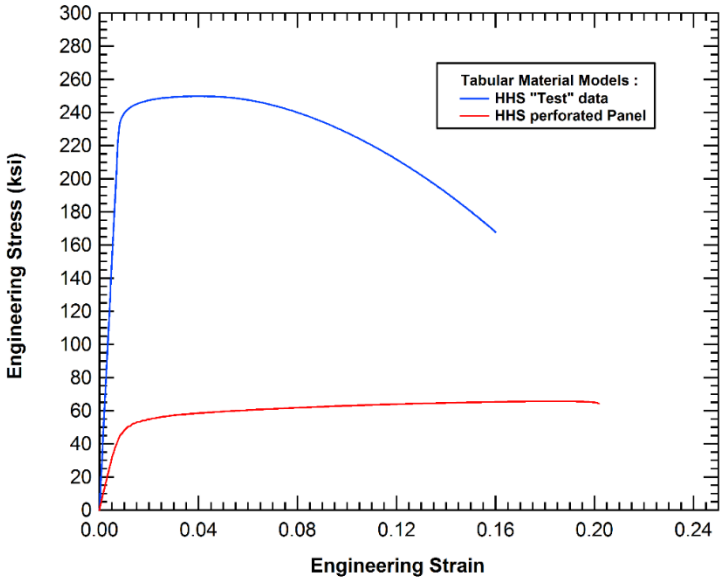

Figure 302. Comparison of the solid and punched plate tensile behavior.

7.3 Side Impact Puncture Analyses

The side impact puncture analyses were performed for a 105J500 chlorine tank car protected with the punched plate system. The impact and puncture analyses use the methodologies described previously in Section 3 of this report. The model for a representative normal side impact analysis with the punched plate system is shown in Figure 303. The model has been reflected about the two symmetry planes used for the normal impacts. The detail of the impact patch shown in the figure illustrates the region of the impact patch where the punched plate geometry is explicitly modeled. Within that region, the model has a uniform mesh density with a characteristic element size of approximately 0.040 inches (1 mm), as shown in Figure 304. Each layer of the punched plate has 6 elements through the 0.25-inch-thickness. This results in elements with an approximate 1:1 aspect ratio.

The puncture behavior of the tank with the punched plate protection system is shown in Figure 305. The example shown is for the 6x6-inch square impactor at an impact speed of 20 mph. The puncture response is very similar to that of tank cars with more traditional jackets. The side of the tank and punched plate system are dented inward by the impact. At sufficiently large displacements and forces the impactor punctures the tank.

More detailed images of the impact zone and damage development for the 6x6-inch impactor and the punched plate system are shown at corresponding times in Figure 306 and Figure 307. The images in Figure 306 show both the tank wall and punched plate layers and the images in Figure 307 show only the punched plate layers. The comparison shows that the punched plate system is penetrated by the impactor prior to the failure of the tank wall. This is common of most tank designs that the jacket fails at a time before the tank wall.

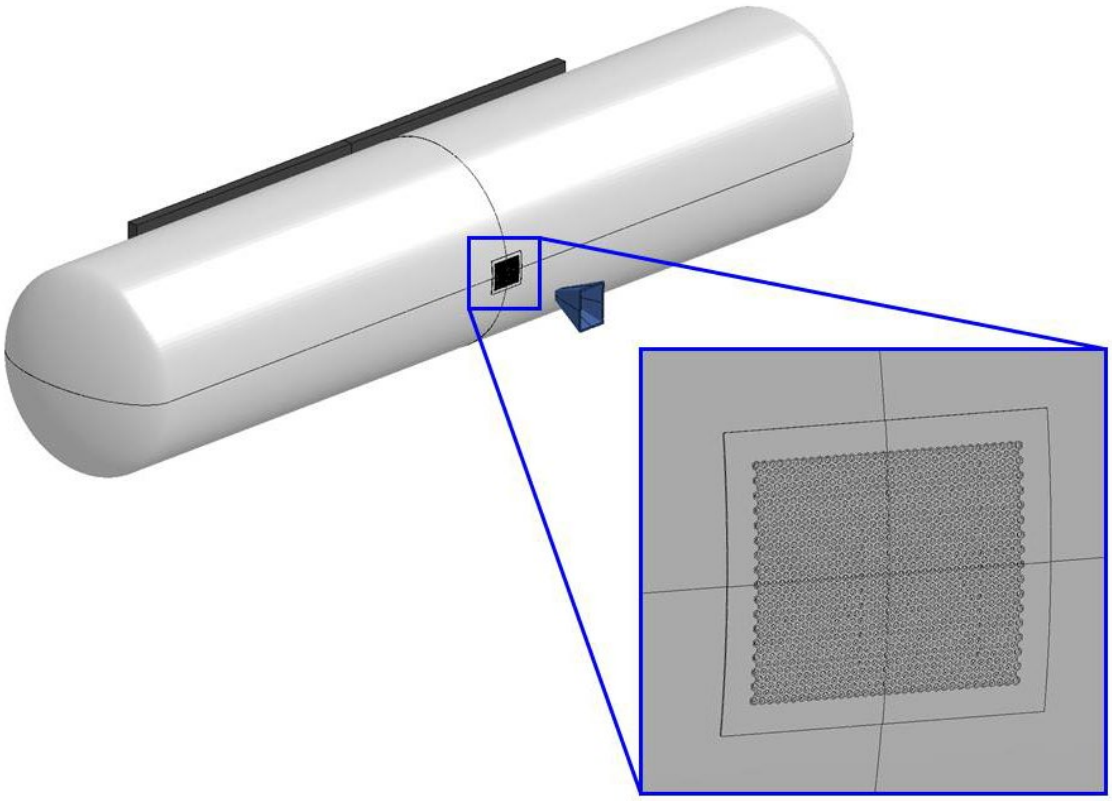

Figure 303. Model for the punched plate concept impact analyses.

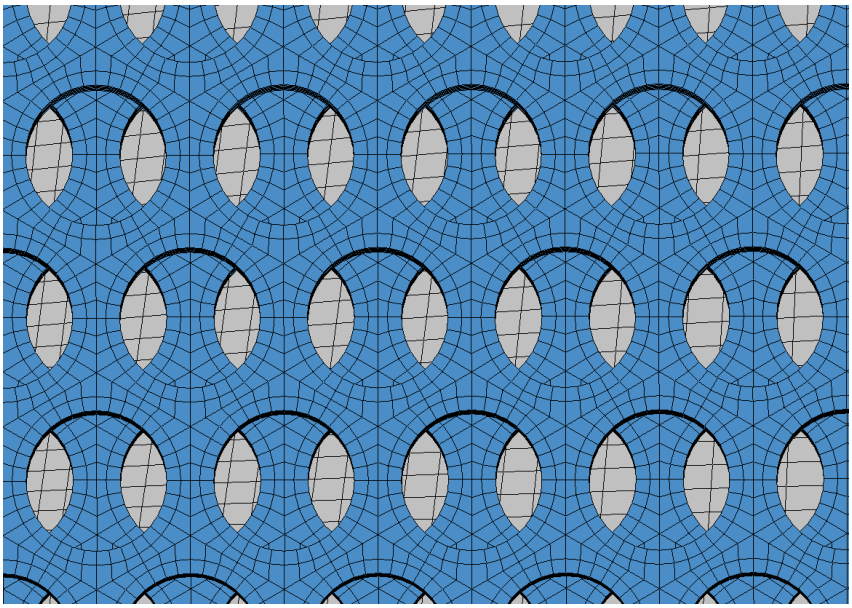

Figure 304. Details of the model for the punched plate impact patch.

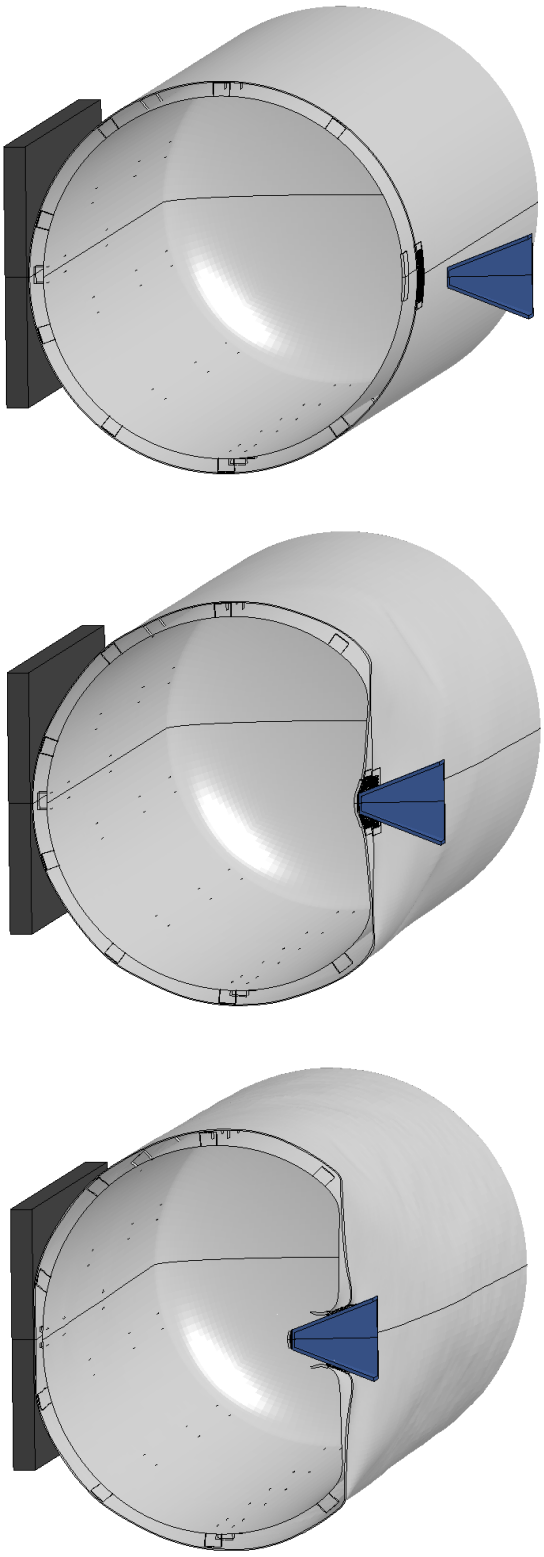

Figure 305. Impact and puncture of the 500 lb chlorine car and punched plate protection.

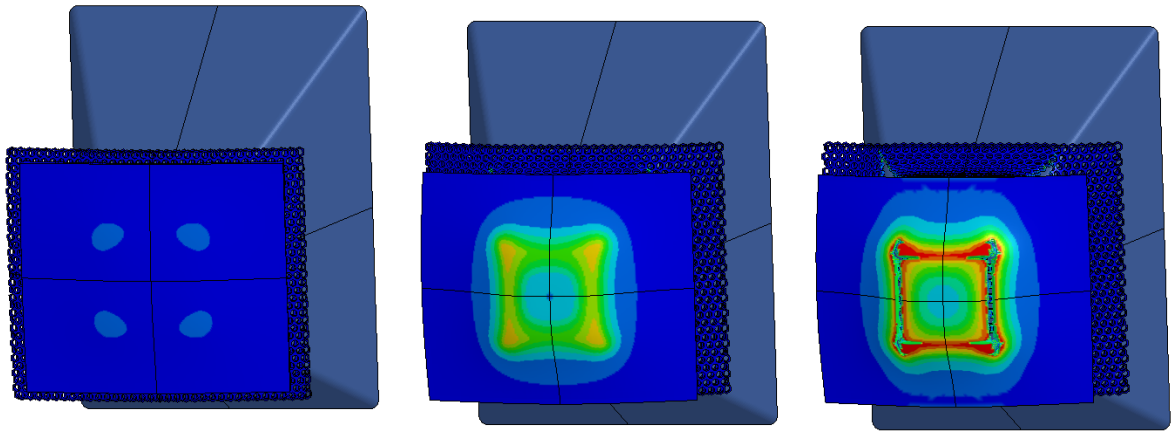

(a) Early impact **(b) After jacket failure** **(c) tank puncture**

Figure 306. Calculated tank impact damage and puncture initiation.

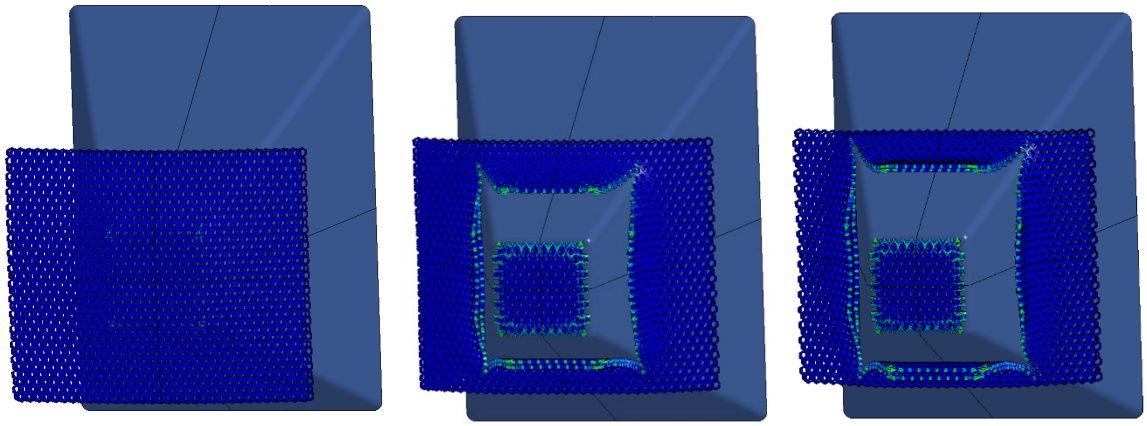

(a) Early impact **(b) After jacket failure** **(c) tank puncture**

Figure 307. Calculated punched plate impact damage and puncture behavior.

A summary of the side impact analyses performed for the 105J500 chlorine commodity tank protected by the punched plate concept is provided in Table 22. The table summarized the impact conditions and calculated puncture forces and energies for the analyses. A comparison of the puncture forces and puncture energies for the 500 lb tank with the punched plate protection are compared to those of traditional 500 lb and 600 lb tanks in Figure 308 and Figure 309, respectively. The comparisons are for normal side impacts using the full range of impactor sizes and shapes as described in Section 3.2.1. For the 600 lb tank car both the lower and higher impact speeds, discussed in Section 3.3 of this report, are included in this comparison. The impact velocities selected for the punched plate concept analyses are the same as the higher speed analyses of that section.

The comparison of the puncture forces for the different tank car designs, shown in Figure 308, shows that the punched plate protection system increases the puncture forces over the 11-gauge jacket for the 500 lb commodity tank. However, the increase in puncture forces is approximately 10 percent. The puncture forces for the 500 lb tank and punched plate system are still

approximately 15 percent lower than those of the 600 lb commodity tank with the 11-gauge jacket.

Table 22. Summary of side impact analyses for the 105J500 tank and punched plate concept

Calculation	Tank Type	Tank Shell	Shell Jacket	Impact Conditions	Internal Pressure (psi)	Puncture Force (lbs)	Puncture Energy (ft-lbs)
R91A	500 lb Cl	0.777 in TC128B	Punched Plate	20 mph 6”x6” ram	100 psi	9.530E+05	1.390E+06
R91B	500 lb Cl	0.777 in TC128B	Punched Plate	30 mph 12”x12” ram	100 psi	1.848E+06	4.260E+06
R91C	500 lb Cl	0.777 in TC128B	Punched Plate	25 mph 9”x9” ram	100 psi	1.402E+06	2.770E+06
R91D	500 lb Cl	0.777 in TC128B	Punched Plate	15 mph 3”x3” ram	100 psi	4.910E+05	3.260E+05
R91E	500 lb Cl	0.777 in TC128B	Punched Plate	15 mph 3”x6” ram	100 psi	8.090E+05	9.770E+05
R91F	500 lb Cl	0.777 in TC128B	Punched Plate	25 mph 3”x12” ram	100 psi	1.199E+06	2.130E+06
R91G	500 lb Cl	0.777 in TC128B	Punched Plate	20 mph 5.73 in. dia.	100 psi	8.350E+05	8.600E+05
R91H	500 lb Cl	0.777 in TC128B	Punched Plate	20 mph 7.64 in. dia.	100 psi	1.125E+06	1.820E+06
R91I	500 lb Cl	0.777 in TC128B	Punched Plate	25 mph 9.55 in. dia.	100 psi	1.318E+06	2.720E+06
R91J	500 lb Cl	0.777 in TC128B	Punched Plate	30 mph 11.46 in. dia.	100 psi	1.535E+06	3.110E+06
R91K	500 lb Cl	0.777 in TC128B	Punched Plate	35 mph 13.37 in. dia.	100 psi	1.725E+06	3.400E+06

The comparison of the puncture energies for the different tank car designs, shown in Figure 309, shows that the punched plate protection system is again closer to those of the 500 lb chlorine tank car than the 600 lb tank car. This result is roughly consistent with the amount of steel added to the various systems. The pinched plate geometry removes roughly 50 percent of the steel in each plate. Thus, the total system is roughly equivalent in weight to a monolithic 0.25-inch-thick steel jacket. Thus, the punched plate system adds only 0.13 inches to the effective jacket and tank combined thickness. By comparison the increase from the 500 lb to the 600 lb commodity tank adds 0.204 inches to the tank thickness.

This comparison shows that the punched plate system is reasonably effective for tank car safety applications. It does not result in significant improvements in puncture resistance, but the performance is consistent with the modest levels of added weight for the concept. None of the analyses indicate that the punched plate protection system would introduce new damage modes that could result in reductions in the tank puncture resistance.

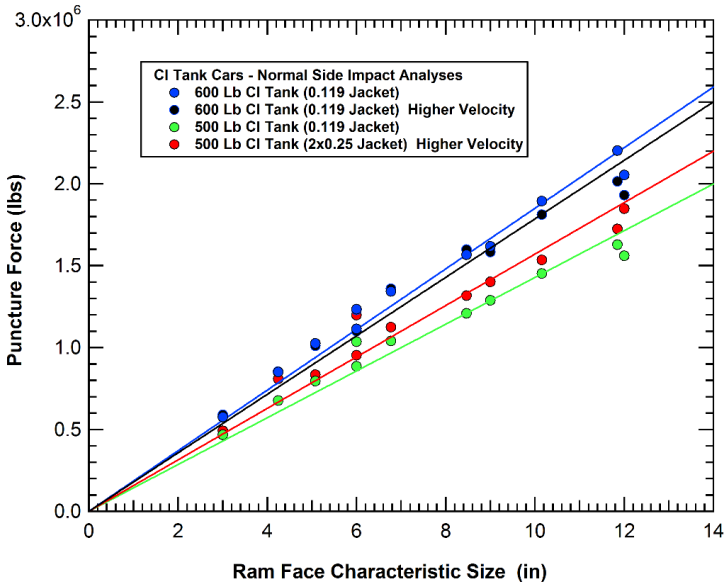

Figure 308. Comparison of side impact puncture forces for different tank designs.

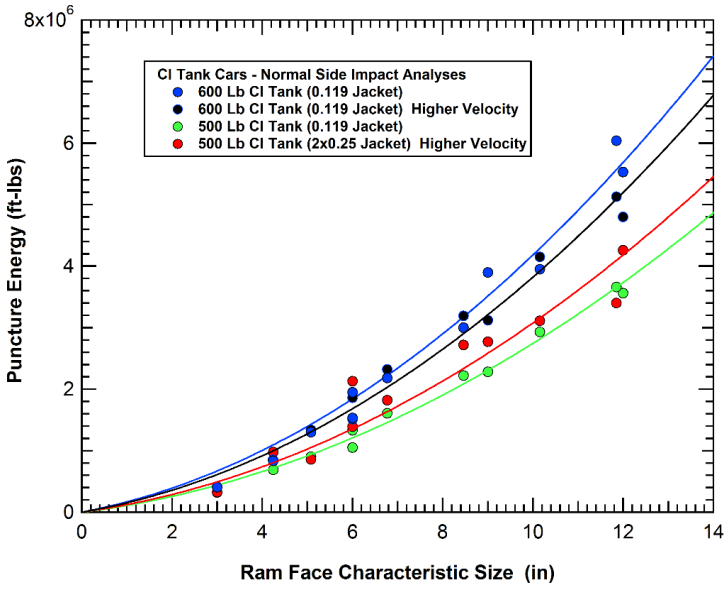

Figure 309. Comparison of side impact puncture energies for different tank designs.

To evaluate the effectiveness of the punched plate at increasing the tank resistance, additional analyses were performed where the punched plate system was replaced by ¼-inch jackets that have roughly equivalent weight. The jacket materials considered were TC128B and HHS. A comparison of the 6x6 inch square impactor force-deflection behavior for these two jacket designs with those of the baseline 11-gauge jacket and the punched plate system is shown in Figure 310. The comparison shows that the punched plate system has a higher puncture energy than the ¼-inch TC128B jacket but a lower puncture energy than the monolithic ¼-inch HHS jacket.

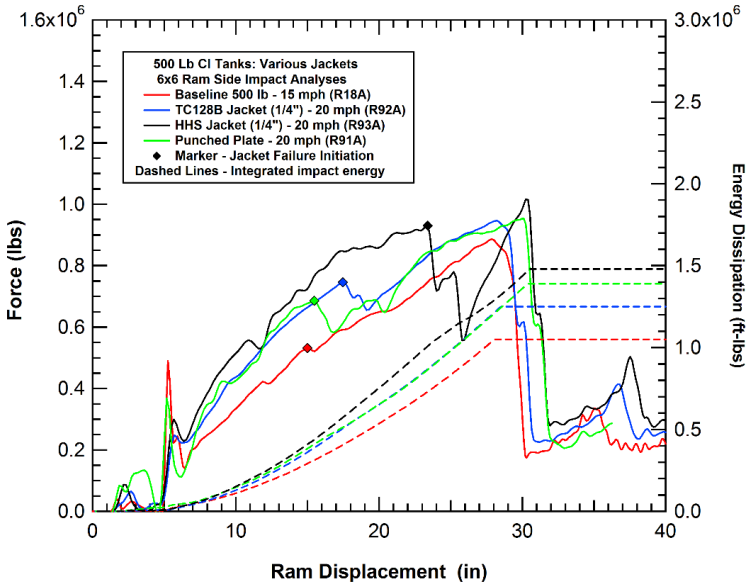

Figure 310. Comparison of side impact puncture energies for different tank designs.

8. Conclusions

This report describes a research program to improve the safety and security of railroad tank cars. The approach used in the research and development program was to apply a tank impact and puncture prediction capability using detailed finite element analyses. The capability was developed and validated previously in the NGRTC program. In this study, the analyses were applied to investigate the tank puncture behaviors for a wide range of impact conditions.

In the initial phase of this program, different size and shape impactors were investigated. A new parameter was developed to characterize the effective size of the impactor. This impactor characteristic size is the square root of the area of the impactor face. The impactor characteristic size parameter provides a good correlation for the different impactor sizes and shapes analyzed and is a useful parameter for quantifying the puncture potential for various impactors. For example, a rail section impactor has a characteristic size of approximately 5 inches. Alternatively, a more complex impactor, such as a coupler head can be assessed. Here the behavior is complicated by an impactor face profile that is not flat. As a result, the puncture force can vary significantly with relatively small changes in the orientation of the impact. For a limited set of impact orientations analyzed, the coupler head was found to have a characteristic size as small as 5 inches and as large as 12 inches.

Two different series of analyses were performed to investigate the effects of the impactor orientation. The first series of analyses rotated the impactor orientation and maintained the normal impact trajectory. The second series of analyses used an oblique impact configuration. Both sets of analyses found that the rotation of the impactor face relative to the tank surface results in load concentrations at the edge of the impactor and significant reductions in the puncture force. As a result, the characteristic size of the 12x12 impactor drops from 12 inches in the normal impact to approximately 4.5-5 inches in an edge impact. The characteristic size is further reduced to approximately 3 inches for the corner impact. These results show that impacting objects with corners and edges can have the penetration potential of a much smaller object if the orientation of the impactor concentrates the loading to the edge or corner.

A series of analyses were performed to investigate the effects of the constraint level on the tank side impact response. The analysis of the different tank boundary constraints shows that the effects on the late time behavior and puncture energy can be significant. However, the initial portion of the loading is dominated by the inertial resistance of the tank and the puncture will occur in this initial phase of the impact for many combinations of impactor sizes and impact speeds. Thus, for many side impacts, the constraint on the back side of the tank is not significant.

A corresponding series of analyses were performed to investigate the effects of the constraint level on the tank head impact response. The constraint conditions were found to be more significant for head impacts. The tank constraint effects for head impacts are observed much earlier in the response than for side impacts for two reasons. The first is that the tank cylinder is much stiffer in axial loading compared to lateral loading. Thus, the head impact forces are very rapidly transmitted to translations of the tank center of gravity (CG). The second reason for increased constraint effects in head impacts is the behavior of the lading in head impacts. During the duration of the impact, only a fraction of the total lading mass is coupled to the motions of the unconstrained tank. Analyses to quantify the lading effect show that less than 10 percent of the lading is coupled to the motion of the tank for a typical head impact scenario.

A set of analyses was performed to assess the effects of the temperature of the tank and lading for a chlorine tank car. As the equilibrium temperature of the tank rises, the vapor pressure increases, and the liquid density is reduced. A decrease in the liquid density will produce an increase in the liquid volume with a corresponding reduction in the outage volume. Both increasing the pressure and reducing the outage can reduce the puncture resistance of a tank car. The condition analyzed is a 105J600W chlorine tank car at an equilibrium temperature of 105º F. This temperature increases the internal vapor pressure for the tank to 155 psi and lowers the corresponding outage volume for a tank loaded to the specified limit to 7.5 percent. These are compared to the 100-psi internal pressure and outage volume of 10.6 percent at a tank temperature of 78 degrees F. On average, the increase in temperature dropped the puncture energies by 20 percent. However, the puncture energies for smaller impactor sizes are more similar at the two temperatures. This is because the impact response for small impactors is dominated more by the structural stiffness. The internal pressure (and pressure increase) plays a smaller roll for the small dent sizes from small impactors prior to puncture.

In addition to the analyses performed on the 105J600 tank car, a series of other tank car types were analyzed. The evaluations of TIH pressure tank cars were performed for the 500 lb chlorine tank car, the 340 and 500 lb AA tank cars, and 300, 400, and 500 lb EO tank cars. In addition, evaluations of various general purpose tank cars and DOT-113 LNG tank car designs were also evaluated. For the side impact evaluations, a full set of normal and 45-degree oblique side impacts were performed for each of the tank car designs considered. For the head impact evaluations, offset impacts using various size square impactors was used. For comparison of the various designs, we normalized the calculated puncture energies from all the various designs against an appropriate reference tank car.

In the comparison of TIH pressure tank cars, the side impact puncture energies for the 105J500W EO tank car are considerably higher than for any of the other tank car designs. The EO tanks have relatively high puncture energies as a result of the lower tank pressures and larger diameter tanks. The 105J500W, 105J400W, and 105J300W EO tank cars have puncture energies on average 82 percent higher, 17 percent higher, and 12 percent lower, respectively, than the 105J500W chlorine tank car. The puncture energies for the 105J600W chlorine tank car were on average 37 percent higher than the 105J500W chlorine tank car. The 112J500W and 112J340W AA tank cars are on average 10 percent above and 39 percent below the 105J500W chlorine tank car, respectively.

The head impact puncture energies for the TIH pressure tank cars show different trends in the puncture resistance. Due to the doubly curved geometry, the structural stiffness and tank thickness plays a larger role in the behavior and the internal pressure levels plays a lesser role in the impact energy dissipation. The head impact puncture energies for the 105J600W chlorine tank car were highest and, on average, 28 percent higher than the 105J500W chlorine tank car. The 105J500W, 105J400W, and 105J300W EO tank heads have puncture energies on average 22 percent higher, 10 percent higher, and 18 percent lower, respectively, than the 105J500W chlorine tank head. The 112J500W and 112J340W AA tank heads are on average 3 percent above and 34 percent below the 105J500W chlorine tank head, respectively.

The analyses of the side impacts for the DOT-111 class of general-purpose tank cars investigated a range of tank designs and design concepts. The P1577/CPC 1230 tank car (0.50-inch-thick TC128B tank shell) with a jacket and head shield provided an approximately 40 percent increase in average puncture energy over a DOT-111A100W1 tank car when the worst-case outage

volume of 1 percent is applied. When the outage volume is increased to 3 percent, the jacketed P1577/CPC 1230 tank car provided an approximately 120 percent increase in average puncture energy over a DOT-111A100W1 tank car. In head impacts, the P1577/CPC 1230 tank head with a head shield provided an approximately 80 percent increase in average puncture energy over the DOT-111A100W1 tank head. Similarly, the DOT-117A100W tank head (with a head shield) provided an approximately 95 percent increase in average puncture energy over the DOT-111A100W1 tank head (or 8 percent increase over the P1577/CPC 1230 tank head with a head shield). Although the DOT-117A100W tank car was not evaluated for side impacts, we would expect similar increases in the side impact puncture resistance over the jacketed P1577/CPC 1230 tank car design.

The DOT-113C120W9 LNG tank cars were found to have very good side impact puncture resistance. The average puncture energy for the DOT-113C120W9 tank car is 126 percent higher than the DOT-105J500W chlorine tank car. In addition, the average puncture energy for the DOT-113C120W9 tank car is higher than those of all the TIH pressure tank car designs analyzed. Additionally, the average puncture energy for the DOT-113C120W9 tank car is 8.46 times higher than that of the DOT-111A100W1 tank car and much higher than those of all the general-purpose tank car designs analyzed. An evaluation was also performed for a modified DOT-113 tank design with a 0.50-inch-thick tank shell meeting the requirements of the AAR Specification M-1004 for LNG fuel tenders. This M-1004 compliant DOT-113 tank car was found to have an additional 44 percent increase in average side impact puncture resistance over the baseline DOT-113 tank design.

The DOT-113C120W9 LNG tank again was found to have very good head impact puncture resistance. The average puncture energy for the DOT-113C120W9 tank head is 127 percent higher than the DOT-105J500W chlorine tank car and higher than those of all the TIH pressure tank car designs that have been analyzed. This M-1004 compliant DOT-113 tank head was found to have an additional 45 percent increase in average head impact puncture resistance over the baseline DOT-113 tank head design.

The FE modeling approach used for all the above impact analyses is very useful for understanding the mechanics of tank impacts and punctures. However, at times, a simplified analysis methodology or impact algorithm is useful for the assessment of various factors on tank impact safety. In this study, we developed analytical tank impact algorithms that can be applied for future analyses of tank car safety. When assessing appropriate analysis methodologies, we examined the response characteristics of both head and side impacts. We found that the behaviors for these two impact conditions are sufficiently unique that different analysis methodologies were appropriate for the head and side impacts. The resulting models were compared to the FE analyses of different impact conditions and found to provide good correlation to the FE results.

9. References

Anderson, T. L., & Kirkpatrick, S. W. (2006). *Quantifying and Enhancing Puncture Resistance in Railroad Tank Cars Carrying Hazardous Materials: Phase I – Preliminary Study.* Prepared for The Chlorine Institute.

Anderson, T. L., Rose, B., McKeighan, P. C., & Kirkpatrick, S. W. (2007). *Quantifying and Enhancing Puncture Resistance in Railroad Tank Cars Carrying Hazardous Materials: Phase II – Development and Validation of a Puncture Resistance Evaluation Methodology.* The Chlorine Institute.

Arcan, M., Hashin, Z., & Voloshin, A. (1978). A Method to Produce Uniform Plane-stress States with Applications to Fiber-reinforced Materials. *Experimental Mechanics*, 141-146.

Bao, Y., & Wierzbicki, T. (2004a). On Fracture Locus in the Equivalent Strain and Stress Triaxiality Space. *International Journal of Mechanical Sciences*, 46, 81-98.

Bao, Y., & Wierzbicki, T. (2004b). A Comparative Study on Various Ductile Crack Formation Criteria. *Journal of Engineering Materials and Technology*, 126, 314-324.

Barkan, C. P., Ukkusuri, S. V., & Waller, S. T. (2005). Optimizing the design of railway tank cars to minimize accident-caused releases. In *Computers & Operations Research.* Elsevier Ltd.

Beremin, F. M. (1981). Study of Fracture Criteria for Ductile Rupture of A508 Steel. In E. D. François, *Advances in Fracture Research (ICF5)* (pp. 809-816). Pergamon Press.

Blandford, R. K., Morton, D. K., Snow, S. D., & Rahl, T. E. (2007). Tensile Stress-Strain Results for 304L and 316L Stainless Steel Plate at Temperature. *Proceedings of the PVP2007, ASME Pressure Vessel and Piping Division Conference, Paper No. PVP2007-26096.* San Antonio, TX: American Society of Mechanical Engineers.

FRA. (2011). *Regulatory Update, October 2011, T59.1.* Federal Railroad Administration.

FRA. (2022). *Full-Scale Shell Impact Test of a DOT-113C120W9 Tank Car Filled with Liquid Nitrogen.* FRA office of Research, Development, and Technology, Research Reports RR22-10.

FRA. (2023). *Railroad Accident/Incident Reporting System (RAIRS).* Federal Railroad Administration.

Giovanola, J. H., & Kirkpatrick, S. W. (1992). Applying a Simple Ductile Fracture Model to Fracture of Welded T-Joints. *Advances in Local Fracture/Damage Models for the Analysis of Engineering Problems, ASME AMD Vol. 137* (pp. 285-303). New York: American Society of Mechanical Engineers.

Giovanola, J. H., & Kirkpatrick, S. W. (1993). Methodology for Evaluating Strength and Fracture Resistance of Weldments Using a Local Approach to Fracture. *Pressure Vessel Integrity-1993, ASME PVP-Vol. 250* (pp. 157-171). New York: American Society of Mechanical Engineers.

Giovanola, J. H., Kirkpatrick, S. W., & Crocker, J. E. (1996). Investigation of Scaling Effects in Elastic-Plastic Ductile Fracture Using the Local Approach. *Proceedings of the First*

European Mechanics of Materials Conference on Local Approach to Fracture, Euromech-Mechamat '96. Fontainebleau-France: Euromech-Mechamat '96.

Gurson, A. (1977). Continuum Theory of Ductile Rupture by Void Nucleation and Growth: Part 1—Yield Criteria and Flow Rules for Porous Ductile Media. *Journal of Engineering Materials and Technology, Vol. 99*, 2-15.

Hancock, J. W., & Mackenzie, A. C. (1976). On the Mechanisms of Ductile Failure in High-Strength Steels Subjected to Multiaxial Stress States. *Journal of the Mechanics and Physics of Solids*, Vol. 24, pp. 147-169.

Jeong, D., Tang, Y., & Pearlman, A. (2001a). *Evaluation of Semi-Empirical Analyses for Railroad Tank Car Puncture Velocity, Part I: Correlations with Experimental Data.* Federal Railroad Administration, Report No. DOT/FRA/ORD-01/21.1 .

Jeong, D., Tang, Y., & Pearlman, A. (2001b). *Evaluation of Semi-Empirical Analyses for Railroad Tank Car Puncture Velocity, Part II: Correlations with Engineering Analysis.* Federal Railroad Administration, Report No. DOT/FRA/ORD-01/21.II.

Jeong, D., Tang, Y., Yu, H., & Pearlman, A. (2006). Engineering Analyses for Railroad Tank Car Head Puncture Resistance. *Proceedings of IMECE2006, Paper No. IMECE2006-13212.*

Jeong, D., Tang, Y., Yu, H., Lyons, M., Gordon, J., Orringer, O., & Perlman, A. (2009). *Engineering Studies on Structural Integrity of Railroad Tank Cars Under Accident Loading Conditions.* FRA Report No. DOT/FRA/ORD-09/18.

Kim, J.-H., Kang, K.-Y., Kim, M.-H., & Lee, J.-M. (2012). Elasto-Visco-Plastic-Damage Model for Pre-Strained 304L Stainless Steel subjected to Low Temperature. *World Academy of Science, Engineering and Technology, Vol. 61*, 195-200.

Kirkpatrick, S. W. (2009a). *Detailed Puncture Analyses of Various Tank Car Designs.* ARA Final Technical Report, Prepared for the Next Generation Railroad Tank Car (NGRTC) Project.

Kirkpatrick, S. W. (2009b). Detailed Impact Analyses for Development of the Next Generation Rail Tank Car - Part 1 – Model Development and Assessment of Existing Tank Car Designs. *Proceedings of the ASME 2009 Rail Transportation Division Fall Conference, Paper No. RTDF2009-18016.* Ft. Worth, TX: ASME.

Kirkpatrick, S. W. (2009c). Detailed Impact Analyses for Development of the Next Generation Rail Tank Car - Part 2 –Development of Advanced Tank Car Protection Concepts. *Proceedings of the ASME 2009 Rail Transportation Division Fall Conference, Paper No. RTDF2009-18017.* Fort Worth, TX: ASME.

Kirkpatrick, S. W. (2010). *Analyses of Outage Volume Effects on Puncture Energy for Unpressurized DOT-111A100W Tank Cars.* Applied Research Associates, Technical Note, January 4, 2010.

Kirkpatrick, S. W. (2013). *Detailed Puncture Analyses Tank Cars - Analysis of Different Impactor Threats and Impact Conditions.* Federal Railroad Administration, Report No. DOT/FRA/ORD-13/17.

Kirkpatrick, S. W. (2017). *TWP-4 Assessing Puncture Resistance for Sandwich Tank Car Designs; TWP-5 Composite Materials for Protection Systems; TWP-22 Advanced Head Protection Concepts.* Advanced Tank Car Collaborative Research Program (ATCCRP) Research Report, Draft Final Technical Report for Projects TWP-4, TWP-5, and TWP-22.

Kirkpatrick, S. W. (2018). *Advanced Tank Car Collaborative Research Program (ATCCRP) – Executive Summary and Conclusions.* ATCCRP Final Report.

Kirkpatrick, S. W., & McKeighan, P. C. (2018). *Correlating Material Properties to Puncture Resistance to Enhance the Safety and Security of Tank Cars.* Advanced Tank Car Collaborative Research Program (ATCCRP) Research Report, Final Technical Report for Project TWP-10, Revision 1.

Kirkpatrick, S. W., Barkan, C. P., T., T. T., Lin, C.-Y., Iannacone, L., Gharzouzi, P., & Gardoni, P. (2022). mproving Understanding of Railroad Tank Wagon Performance in Accidents Through Simulation-Based Derailment Analyses. *2022 World Conference on Railroad Research (WCRR).* Birmingham, UK.

Kirkpatrick, S. W., Lin, C., Iannacone, L., Gharzouzi, P., Treichel, T., Barkan, C. P., & & Gardoni, P. (2023). Derailment Analysis for Prediction of Damage and Probability of Release for Novel Railroad Tank Car Designs. *Transportation Research Record*, 2677(5), 812–828.

Kirkpatrick, S. W., Wagner, C., & Northrup, C. (2019). *Crashworthiness and Puncture Protection Analyses of LNG Tenders.* Applied Research Associates, Prepared for the Association of American Railroads (AAR) in support of the Natural Gas Fuel Tender Technical Advisory Group (NGFT TAG).

Krishnamurthy, A., Trevithick, S., Carolan, M., Spangenberg, U., Wilson, N., Eshraghi, S., & Kirkpatrick, S. W. (2022). *Review of Tank Car Side Impact Tests and Analyses 2007-2020.* Federal Railroad Administration Office of Research Development and Technology, Report No. DOT/FRA/ORD-22/14.

Lee, Y.-W., & Wierzbicki, T. (2004). *Quick Fracture Calibration for Industrial Use.* Massachusetts Institute of Technology Impact & Crashworthiness Laboratory, Report No: 115.

Lemaitre, J. (1986). Local Approach of Fracture. *Engineering Fracture Mechanics*, Vol. 25, pp. 523-537.

LSTC. (2003). *LS-DYNA Keyword User's Manual - Version 970.* Livermore, CA: Livermore Software Technology Company.

Mackenzie, A. C., Hancock, J. W., & Brown, D. K. (1977). On the Influence of State of Stress on Ductile Failure Initiation in High-Strength Steels. *Engineering Fracture Mechanics, Vol. 9*, 167-188.

Malvern, L. (1969). *Introduction to the Mechanics of a Continuous Medium.* Prentice-Hall.

McKeighan, P. C. (2007a). *Tensile Properties and Stress-Strain Behavior of Various Steel Products Used in Fabricating Test Specimen for the NGRTC Program.* Southwest Research Institute, NGRTC Project Memorandum.

McKeighan, P. C. (2007b). *Notched Tensile Properties of Tank Car Material from Full Scale Test No. 1 (Car No. 3069) and Test No. 2 (3074) Oriented in the Transverse Direction.* Southwest Research Institute, NGRTC Project Memorandum.

McKeighan, P. C. (2007c). *Shear Tests on TC128B Normalized Material of Two Different Thicknesses.* Southwest Research Institute, NGRTC Project Memorandum.

McKeighan, P. C. (2007d). *Puncture Tests on Jacket Material (A1011, 90X) and Normalized TC128B Shell Material (two thicknesses)- Revised.* Southwest Research Institute, NGRTC Project Memorandum.

McKeighan, P. C. (2008a). *Puncture Behavior of 0.48-inch Thick A516 Material.* Southwest Research Institute, NGRTC Project Memorandum.

McKeighan, P. C. (2008b). *Puncture Properties of Different 90x Stacked Layers and a Composite Structure.* Southwest Research Institute, GRTC Project Memorandum.

Mudry, F. (1985). Methodology and Applications of Local Criteria for Prediction of Ductile Tearing. In e. L. H. Larson, *Elastic-Plastic Fracture Mechanics* (pp. 263-283). Brussels and Luxembourg, Belgium: ECSC, EEC, EAEC.

Mudry, F. (1985). Methodology and Applications of Local Criteria for Prediction of Ductile Tearing. In e. L. H. Larson, *Elastic-Plastic Fracture Mechanics* (pp. 263-283). Luxembourg, Belgium: ECSC, EEC, EAEC.

National Academies of Sciences, Engineering, and Medicine. (2022). *Preparing for LNG by Rail Tank Car: A Readiness Review.* Washington, DC: The National Academies Press.

NTSB. (2003). *Draft of NTSB Material Laboratory Factual Report [In reference to Canadian Pacific Railway Derailment and Anhydrous Ammonia Release, Minot, ND, January 18, 2002, DCA-02-MP-002].* National Transportation Safety Board.

NTSB. (2004). *Derailment of Canadian Pacific Railway Freight Train 292-16 and Subsequent Release of Anhydrous Ammonia Near Minot, North Dakota; January 18, 2002.* National Transportation Safety Board.

NTSB. (2005). *Collision of Norfolk Southern Freight Train 192 with Standing Norfolk Southern Local Train P22 with Subsequent Hazardous Materials Release at Graniteville, South Carolina, January 6, 2005.* National Transportation Safety Board, Railroad Accident Report NTSB/RAR-05/04.

NTSB. (2006). *Collision of Union Pacific Railroad Train MHOTU-23 with BNSF Railway Company Train MEAP-TUL-126-D with Subsequent Derailment and Hazardous Materials Release, Macdona, Texas, June 28, 2004.* National Transportation Safety Board, Railroad Accident Report NTSB/RAR-06/03.

NTSB. (2013). *Railroad Accident Brief: Derailment and hazardous materials release and fire, Tiskilwa, Illinois, October 7, 2011.* National Transportation Safety Board, NTSB/RAB-13/02.

NumPy. (2012). *NumPy User Guide - Release 1.7.0.dev-36681eb.* http://docs.scipy.org/doc/.

PHMSA. (2020). *Hazardous Materials: Liquefied Natural Gas by Rail.* Pipeline and Hazardous Materials Safety Administration, Final Rule, Federal Register, Vol. 85, No. 143, July 24, 2020.

Railway Supply Institute. (2009). *Railroad Tank Cars – Safely Transporting Hazardous Materials.* RSI-AAR Railroad Tank Car Safety Research and Test Project.

Saat, M. R., & B. C. (2005). Release Risk and Optimization of Railroad Tank Car Safety Design. *Transportation Research Record: Journal of the Transportation Research Board*.

Tang, Y. H., Yu, H., Gordon, J., Jeong, D., & Perlman, A. (2008). Analysis of Railroad Tank Car Shell Impacts using Finite Element Method. *Proceedings of the 2008 IEEE/ASME Joint Rail Conference, JRC2008, Paper JRC2008-63014.* Wilmington, Delaware: IEEE/ASME.

Tang, Y. H., Yu, H., Gordon, J., Priante, M., Jeong, D., Tyrell, D., & Perlman, A. (2007). Analyses of Full-Scale Tank Car Shell Impact Tests. *roceedings of the 2007 ASME Rail Transportation Division Fall Technical Conference, RTDF2007, Paper RTDF2007-46010.* Chicago, Illinois: American Society of Mechanical Engineers.

Tang, Y., Yu, H., Gordon, J., Jeong, D., & Perlman, A. (2008). nalysis of Railroad Tank Car Shell Impacts Using Finite Element Method. *Proceedings of the 2008 ASME/IEEE Joint Rail Conference, Paper no. JRC2008-63014.*

Treichel, T. T., Ghosh, L., Saat, M. R., Barkan, C. P., Liu, X., Kirkpatrick, S. W., . . . Zhou, X. (2019). *Conditional Probability of Release (CPR) Estimates for Railroad Tank Cars in Accidents.* RSI-AAR Railroad Tank Car Safety Research and Test Project Report RA-19-01.

Tvergaard, V. (1982). On Localization in Ductile Materials Containing Spherical Voids. *International Journal of Fracture, Vol. 18*, 237-252.

Tvergaard, V. (1990). Material Failure by Void Growth to Coalescence. *Advances in Applied Mechanics, Vol. 27*, 83-151.

van Rossum, G. (2012). *The Python Language Reference - Release 2.7.3.* Python Software Foundation, Fred L. Drake, Jr., editor.

Wakulchik, P. (2017). *Test Report No. AR20472.* Touchstone Testing Labs .

Wilson, N., Carolan, M., Trevithick, S., & Eshraghi, S. (2021). *Side Impact Test and Analyses of a DOT-113 Surrogate Tank Car with Water.* Federal railroad Administration, Report No. DOT/FRA/ORD-21/35.

Witte, M., & Anankitpaiboon, S. (2007). *Fully Instrumented Side Impact Test of Tank Car 3069.* Transportation Technology Center, Inc. Report No. P-07-033.

Yen, C.-F., Kaste, R., Montgomery, J., Cheeseman, B., & Scott, B. (2011). *Rail Car Mitigation Technology Development, Test and Evaluation.* Washington, DC: Department of Homeland Sevurity, Rail Tank Car Briefing.

Appendix A.
Tank Head Puncture Resistance Performance Standards

49 CFR § 179.16

Tank-head puncture-resistance systems.

(a) Performance standard. When the regulations in this subchapter require a tank-head puncture-resistance system, the system shall be capable of sustaining, without any loss of lading, coupler-to-tank-head impacts at relative car speeds of 29 km/hour (18 mph) when:

(1) The weight of the impact car is at least 119,295 kg (263,000 pounds);

(2) The impacted tank car is coupled to one or more backup cars that have a total weight of at least 217,724 kg (480,000 pounds) and the hand brake is applied on the last "backup" car; and

(3) The impacted tank car is pressurized to at least 6.9 Bar (100 psig).

(b) Verification by testing. Compliance with the requirements of paragraph (a) of this section shall be verified by full-scale testing according to appendix A of this part.

Appendix A to Part 179—Procedures for Tank-Head Puncture-Resistance Test

1. This test procedure is designed to verify the integrity of new or untried tank-head puncture-resistance systems and to test for system survivability after coupler-to-tank-head impacts at relative speeds of 29 km/hour (18 mph). Tank-head puncture-resistance is a function of one or more of the following: Head thickness, jacket thickness, insulation thickness, and material of construction.
2. **Tank-head puncture-resistance test**. A tank-head puncture-resistance system must be tested under the following conditions:
   a. The ram car used must weigh at least 119,295 kg (263,000 pounds), be equipped with a coupler, and duplicate the condition of a conventional draft sill including the draft yoke and draft gear. The coupler must protrude from the end of the ram car so that it is the leading location of perpendicular contact with the impacted test car.

   b. The impacted test car must be loaded with water at six percent outage with internal pressure of at least 6.9 Bar (100 psig) and coupled to one or more "backup" cars which have a total weight of 217,724 kg (480,000 pounds) with hand brakes applied on the last "backup" car.

   c. At least two separate tests must be conducted with the coupler on the vertical centerline of the ram car. One test must be conducted with the coupler at a height of 53.3 cm (21 inches), plus-or-minus 2.5 cm (1 inch), above the top of the sill; the other test must be conducted with the coupler height at 79 cm (31 inches), plus-or-minus 2.5 cm (1 inch), above the top of the sill. If the combined thickness of the tank head and any additional shielding material is less than the combined thickness on the vertical centerline of the car, a third test must be conducted with the coupler positioned so as to strike the thinnest point of the tank head.

3. One of the following test conditions must be applied:

Minimum weight of attached ram cars in kg (pounds)	**Minimum velocity of impact in km/hour (mph)**	**Restrictions**
119,295 (263,000)	29 (18)	One ram car only.
155,582 (343,000)	25.5 (16)	One ram car or one car plus one rigidly attached car.
311,164 (686,000)	22.5 (14)	One ram car plus one or more rigidly attached cars.

4. A test is successful if there is no visible leak from the standing tank car for at least one hour after impact.

Abbreviations and Acronyms

ACRONYM	DEFINITION
1D	One Dimensional
AA	Anhydrous Ammonia
AAR	Association of American Railroads
ALE	Arbitrary Lagrangian Eulerian
API	American Petroleum Institute
ARL	Army Research Laboratory
ATCCRP	Advanced Tank Car Cooperative Research Program
BC	Boundary Condition
BW	Bao-Wierzbicki
CG	Center of Gravity
DHS	Department of Homeland Security
DOT	Department of Transportation
EO	Ethylene Oxide
EPFM	Elastic-Plastic Fracture Mechanics
FE	Finite Element
FEA	Finite Element Analysis
FRA	Federal Railroad Administration
FMVSS	Federal Motor Vehicle Safety Standards
GN2	Gaseous Nitrogen
HHS	High Hard Steel
LEFM	Linear Elastic Fracture Mechanics
LFM	Local Fracture Mechanics
LN2	Liquid Nitrogen
LNG	Liquid Natural Gas
NGRTC	Next Generation Railroad Tank Car
PHMSA	Pipeline and Hazardous Materials Safety Administration
RAIRS	Railroad Accident and Incident Reporting System
RFA	Renewable Fuels Association
SPH	Smoothed Particle Hydrodynamics

ACRONYM	DEFINITION
SS	Stainless Steel
TC	Transport Canada
TIH	Toxic Inhalation Hazard
TCC	Tank Car Committee
TTCI	Transportation Technology Center, Inc.
TWP	Technical White Papers